Dissertation
submitted to the
Naturwissenschaftlich-mathematische Gesamtfakultät
of the
Ruprechts-Karl-Universität of Heidelberg, Germany
for the degree of
Doctor of Natural Sciences

Put foward by
Gabriel-Dominique Marleau, M. Sc.
born in Verdun, Québec (Canada)

Oral examination: 1st February 2016

The post-formation entropy of gas giants: Radiative properties of the accretion shock and constraints from observations

Referees: Priv.-Doz. Dr. Hubert Klahr
Priv.-Doz. Dr. Simon Glover

Kurzfassung

Wir untersuchen den Strahlungstransport und insbesondere die Strahlungsverlusteffizienz η bei der planetarischen Akkretionsstoßfront mittels strahlungshydrodynamischer Simulationen der obersten Schichten eines Planeten und wählen dafür Momentaufnahmen während seiner Entstehung aus. Wir benutzen den PLUTO-Code in sphärischer Symmetrie und flußbegrenzte Diffusion mit den Ein- und Zweitemperaturenverfahren (1- und 2-T). Tabellierte Gas- und Staubopazitäten werden herangezogen und eine konstante Zustandsgleichung wird benutzt um Strahlungstransporteffekte zu isolieren.

Die Simulationen zeigen, daß in einem bedeutsamen Teil des Entstehungsparameterraumes die Stoßfront isotherm ist und die ganze kinetische Energie in Strahlung umgewandelt wird und daß der in den Planeten hineingebrachte Anteil mit der internen Leuchtkraft verglichen vernachlässigbar ist. Der Befund scheint zu sogenannten Kalten Anfängen zu führen.

Wir untersuchen auch die Frage aus der Perspektive der Beobachtungen und bestimmen, welche Informationen Direktbeobachtungen über die Anfangsentropie liefern können. Erstens versuchen wir, genaue Kühlungskurven durch eine selbstkonsistente Einbindung der komplexen BT-Settl-2010-Atmosphärenmodelle zu berechenen. Wir stellen jedoch fest, daß dies aufgrund unkonvergierter Staubphasenübergänge bei $T_{\rm eff} \approx 1500$ K unmöglich ist. Zweitens benutzen wir einfache Kühlungskurven um Niedrigstwerte der Anfangsentropie von Gasriesen herzuleiten. Wir finden, daß die untersuchten Beispiele wahrscheinlich nicht als klassiche Kalte Anfängen entstanden sind, aber daß κ Andromeda b möglicherweise einen 'Deuteriumblitz' erlebt.

Abstract

We study the radiative properties and in particular the radiation loss efficiency of the planetary accretion shock by performing radiation-hydrodynamics simulations of accretion onto a planet at snapshots during its formation. We use the state-of-the-art code PLUTO in spherical symmetry and both one- and two-temperature flux limited diffusion. We take tabulated gas and dust opacities and use a constant equation of state to isolate radiation transport effects.

We find that, for a significant subset of the formation parameter space, the schock is isothermal and essentially the entire kinetic energy is converted to radiation. The fraction brought into the planet is negligible compared to the internal luminosity, which appears to favour the so-called 'cold-start' assumption.

We also study what constraints direct detections can provide on the post-formation entropy. First, we attempt to produce accurate cooling tracks by using self-consistently the sophisticated BT-Settl-2010 atmospheric models. However, we find that this is not possible because of due to dust phase transitions at $T_{\rm eff} \approx 1500$ K. Secondly, we set lower bounds on the post-formation entropy of some well-studied gas giants. We find that they most likely did not form as classical coldest starts, but that κ Andromeda b may be undergoing a 'deuterium flash'.

Contents

We are so small between the stars,
so large against the sky

— Leonard Cohen

1 Introduction

Of all fields of astrophysical research, the science of extrasolar planets (exoplanets) is a relatively new and particularly interesting one. While philosophical musings about the nature and origin of the planets can be traced back to ancient Greece, it has only recently become possible to start addressing these issues observationally. Detailed research on our Solar System planets, which are rocky (Mercury, Venus, Earth, Mars), gaseous (Jupiter, Saturn), or icy (Uranus, Neptune), only became possible in the second half of the 20th century with probes passing by some planets or even entering into their atmosphere. This has brought a wealth of information and allowed detailed studies, but it was only with the discovery of the first exoplanet orbiting a main-sequence star twenty years ago (Mayor & Queloz, 1995) that the current, modern era of exoplanet science began. This has revealed an even richer diversity of planet types and system architectures and also allows statistically meaningful statements about these characteristics and, still in its early phase, about the physical processes which shape them (e.g., Ford, 2014). Moreover, exoplanet discoveries usually elicit a particularly positive response across wide segments of society, also from some who are not typically attracted to science. This is due perhaps to the fact that many exoplanetary physical parameters can be, relative to other subfields of astrophysics, more easily brought in relation with our experience as inhabitants of a planet, and to the possibility of discovering that life does exist somewhere else in the cosmos.

As supported by strong observational evidence, planets form in young stars' dust and gas discs, which are leftover material from their formation. Both bottom-up (hiarchical) and top-down formation processes are considered: core accretion (CA), in which a solid protoplanetary core of several Earth masses ($M_\oplus = 5.97 \times 10^{28}$ g) first forms and triggers runaway gas accretion (Pollack et al., 1996, described in more detail below), and gravitational instability (GI), in which the local self-gravity of a region of the gas disc begins to dominate over its pressure support and collapse ensues (e.g., Boss, 1997). Most planets, in particular planets close to their hosts, seemed to be formed by CA (Janson et al., 2012; Grether & Lineweaver, 2006). A number of observational diagnostics can help distinguish between the two modes, both population-wide and, tentatively, at the planet level (Dodson-Robinson et al., 2009), but most are uncertain and a robust interpretation of observations does not yet seem possible.

There are several open questions in planet formation, one of which concerns the accretion of gas in CA's runaway gas accretion phase. In this model, which reproduces quite well observations of several independent observables (e.g., mass–period distribution, frequency as a function of host-star metallicity, etc.; Mordasini et al., 2009, 2015), the accretion rate onto a planet starts increasing exponentially once the solid core has accreted a gaseous envelope equal roughly to its mass (the 'crossover' mass) (Pollack et al., 1996; Hubickyj et al., 2005). This early envelope is still connected

to the surrounding disc, the 'nebula' (Stevenson, 1982), and the planet is able to accrete more mass as it contracts on its Kelvin–Helmholtz timescale

$$t_{\mathrm{KH}} = \frac{G{M_{\mathrm{p}}}^2}{L_{\mathrm{p}} R_{\mathrm{p}}}, \tag{1.1}$$

where M_{p}, L_{p}, and R_{p} are the planet's mass, radius, and luminosity. The outer radius of the planet is thus on order of the Hill or Bondi radii, defined below, and equal to several tens to hundreds of Jupiter radii R_{J} ($R_{\mathrm{J}} = 7.15 \times 10^9$ cm). Soon after the start of the runaway accretion, however, the planet is contracting faster than the local disc is able to provide material, and it shrinks down to a new equilibrium with a much smaller radius. This state is that of a gaseous body in hydrostatic equilibrium which is accreting gas in free-fall from the accretion radius the Hill or Bondi radius. Thus there is a *shock* defining the planet's surface, with boundary conditions provided by this infalling gas. The important unanswered question concerning this stage is therefore the following (Marley et al., 2007): *What fraction of the kinetic energy of the gas is not radiated away but added to the planet instead?* To the best of our knowledge, this question has not yet been studied in the context of planet formation.

Indeed, the two extreme situations, where all the kinetic energy is kept or, conversely, fully radiated away, lead to very different outcomes in terms of planetary properties. One convenient parameterisation of this is in terms of the entropy S of the gas giant (Marley et al., 2007; Spiegel & Burrows, 2012). Classically, and to a very good approximation, gas giants are thought to have an isentropic (i.e., adiabatic) interior (e.g., Baraffe et al., 2014), and both their luminosity and effective temperature T_{eff} as well as their cooling $L_{\mathrm{p}}(t)$ depend solely on their mass and entropy. Thus the traditional and useful way of framing the question is: *What is the post-formation entropy of a gas planet of a given mass?* This post-formation entropy is also termed 'initial', as it is the value the planet has at the beginning of its cooling phase.

Marley et al. (2007) drew attention to the fact that the consequences of the assumption about the post-shock state of the gas are dramatic at early ages, with differences of several orders of magnitude in luminosity. Since direct observations, which began in the last decade (the first examples being Chauvin et al., 2004; Lafrenière et al., 2008; Marois et al., 2008; Lagrange et al., 2009), provide only a brightness measurement, determining a directly-observed object's mass requires a conversion through planetary cooling curves, which need to assume some initial value for the entropy. However, what this should be has not yet been predicted by theory and, before the author's Master's thesis, (Marleau, 2012), not constrained by observations. We therefore approach the question from both sides in the present dissertation.

This thesis is structured as follows: The remainder of this chapter presents basic shock theory which will be needed in the first few chapters. Then, Chapter 2 presents shock calculations using one-temperature radiation transport, followed by selected comparison cases for two-temperature radiation transport in Chapter 3. In Chapter 4, we present efforts to produce self-consistent planetary cooling curves which use a state-of-the-art and popular set of detailed atmosphere models since they are needed to interpret direct observations. Finally, Chapter 5 presents published work on deriving information about the post-formation entropy of planets from observational data, and a summary and outlook are presented in Chapter 6. Background on and tests of the radiation-hydrodynamics code used in Chapters 2 and 3 are presented in Appendix A, and additional material is given in Appendix B.

1.1. Shock physics

A shock is characterised by an abrupt change in velocity of the fluid, from supersonic to subsonic. Radiative shocks are shocks in which at least the radiation flux F_{rad} and, at higher temperatures, also the radiation energy density E_{rad} and pressure P_{rad} play a role. They are common in astrophysics, whether in stellar explosions (novæ, supernovæ) or in envelopes of pulsating stars (see, e.g., Drake, 2006 and references therein). Usually, the radiation energy density may be neglected because

$E_{\rm rad} \ll E_{\rm int}$, whereas the flux ratio, the Boltzmann number

$$\mathrm{Bo} = \frac{E_{\rm int} v}{F_{\rm rad}} \sim \frac{E_{\rm int}}{E_{\rm rad}} \times \frac{v}{c}, \tag{1.2}$$

may be close to unity since we are considering non-relativistic flows ($v \ll c$). For the approximate second equation, we used the free-streaming case $F_{\rm rad} = cE_{\rm rad}$ (i.e., that the photons effectively move at the speed of light; in general, the flux of quantity X can always be written as the density of X times the propagation velocity). $E_{\rm int}$ is the internal energy density, with dimensions of energy per volume, with $E_{\rm int} = \varrho c_{\rm v} T$ only in the case that the heat capacity at constant volume $c_{\rm v}$ is constant.

One must distinguish between 'one-' and 'two-temperature' (1- and 2-T) radiation transport, also known as the equilibrium and non-equilibrium approaches. In both cases, one is solving moments of the radiative transfer equation, but makes different assumptions about the radiation field (as discussed in more detail in Appendix A). In 2-T radiation transport, $E_{\rm rad}$ is taken to be independent of the gas temperature $T_{\rm gas}$ (hereafter usually denoted with T), whereas 1-T assumes that the radiation and gas couple sufficiently well that $E_{\rm rad} = aT^4$, where $a = 7.5657 \times 10^{-15}$ erg cm^{-3} K^4 is the radiation constant. One could also go one step further and consider 3-T radiation transport, where the electron and ion temperatures are not assumed to be equal, but for the densities relevant to the astrophysical context (and here in particular) both equilibrate in the downstream region of a shock over a small distance (Zel'dovich & Raizer, 1967; Mihalas & Mihalas, 1984; Drake, 2006) and they will be assumed equal. The 'radiation temperature' is defined as the equilibrium temperature corresponding to the radiation energy density, i.e., $T_{\rm rad} = (E_{\rm rad}/a)^{0.25}$.

1.1.1. Shock structure

The schematic structure of a radiative shock is shown in Figure 1.1. In the frame in which the shock is at rest, gas in an initial state (T_0, ϱ_0) flows in from the right in the upstream (or pre-shock) region, passes through a precursor region (described below) before encountering the hydrodynamical shock, and flows away in the downstream (or post-shock) region in a final state $(T_1, \varrho_1) > (T_0, \varrho_0)$, i.e., heated up and compressed. The hydrodynamical shock occurs over the viscous length scale, which is equal to a few gas mean free paths $\ell = 1/n\sigma$ (where n is the volume number density and σ is the cross-section of the gas constituents) and is therefore embedded in the much larger 'radiation exchange zone' (Mihalas & Mihalas, 1984) of several optical depths $\lambda_{\rm phot} = 1/\kappa\varrho$, where κ is the opacity (with dimensions of cross-sectional area per mass).

The radiation precursor arises because the hot post-shock (downstream) region, which in the planetary or stellar context is optically thick as it corresponds to the planetary or stellar interior, emits radiation which penetrates into the upstream material and pre-heats it. The radiation and gas temperatures are decoupled in the 'transmissive' parts of the precursor, where radiation flows at close to the streaming limit ($F_{\rm rad} \approx cE_{\rm rad}$), as well as in the optically thin cooling layer behind the shock (see Figure 1.1). The increase of temperature in the precursor leads to a small pressure gradient which slightly slows down the gas; in turn, its density must increase slightly to have a spatially constant accretion mass flux $\dot{m} = \varrho v$ (neglecting non-planar geometric effects here). In the downstream region and in the 'diffusive' parts of the precursor, where $F_{\rm rad} \ll cE_{\rm rad}$, matter and radiation are in equilibrium.

The classical shock literature distinguishes between 'subcritical' and '(super)critical' shocks depending on the strength of the shock (e.g., Zel'dovich & Raizer, 1967; Mihalas & Mihalas, 1984; Drake, 2006, see also Heaslet & Baldwin, 1963). As the post-shock temperature T_1 increases, so does the generated flux $F \propto \sigma {T_1}^4$, and for sufficiently strong shocks (i.e., for a velocity equal to or greater than the 'critical velocity'), this flux is able to raise the temperature of the gas in the precursor to approximately the value it would have attained downstream. This is the supercritical regime, which is a is a limiting case (Drake, 2007). While in both sub- and supercritical shocks the immediate post-shock temperature T_+ is larger than the equilibrium value T_1 due to preheating, any increase above the critical velocity only serves to increase T_+ but cannot drive T_- to be higher than

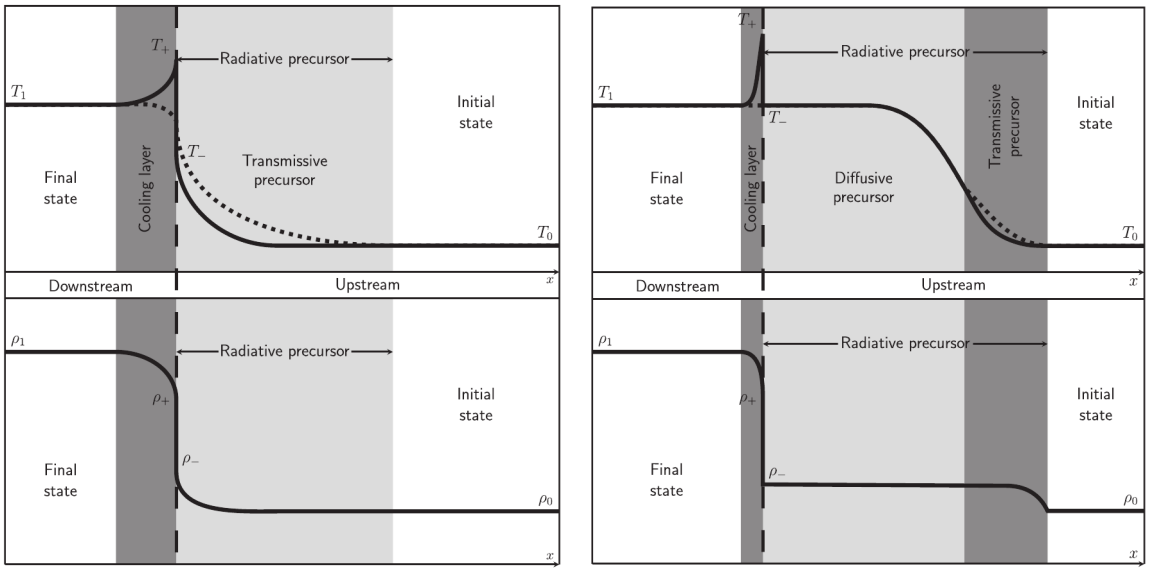

Fig. 1.1.: Schematic structure of radiative shocks, showing the temperature (*top halves*) of the gas (*solid line*) and the radiation (*dotted line*), as well as the density (*bottom halves*). *Left panel*: Subcritical shock ($T_- < T_1$). *Right panel*: Supercritical shock ($T_{\approx} T_1$). The hydrodynamical shock is highlighted (*vertical dashed line*). The relative sizes of the regions are only illustrative. Figure reproduced from Vaytet et al. (2013).

T_1. (As discussed in Drake (2007) and Vaytet et al. (2013), there is however a number of interesting refinements which can be made to this description but they are left out for the sake of brevity.)

A 1-T analysis of the shock yields essentially the same profiles, except in the regions where both temperatures would not be equal. In particular, the immediate post-shock temperature T_+, known as the Zel'dovich spike, cannot be modeled. Also, in the subcritical case, the pre-shock gas temperature T_- will in general be different from that of the 2-T case.

We now derive useful conservation relations for steady-state shocks, which will lead to the definition of an efficiency.

1.1.2. Conservation equations across the shock

Consider the usual equations of radiation hydrodynamics, expressing conservation of mass, momentum, and total energy along the one-dimensional flow (Mihalas & Mihalas, 1984, see also Appendix A):

$$\frac{\partial \varrho}{\partial t} + \nabla(\varrho v) = 0 \tag{1.3a}$$

$$\frac{\partial \varrho v}{\partial t} + \nabla\left(\varrho v^2 + P\right) = -\varrho g \tag{1.3b}$$

$$\frac{\partial E_{\text{tot}}}{\partial t} + \nabla\left(\left[E_{\text{int}} + E_{\text{kin}} + P\right] v + F_{\text{rad}}\right) = -\varrho v g, \tag{1.3c}$$

where as usual ϱ, P, v, g, $E_{\text{int}} = \varrho e_{\text{int}}$, $E_{\text{kin}} = \frac{1}{2}\varrho v^2$, and F_{rad} are respectively the density, pressure, velocity, magnitude of the gravitational acceleration, internal and kinetic energy volume density (e_{int} and e_{kin} being the massic energy densities), and radiative flux, and where in spherical coordinates the divergence operator $\nabla(\cdot) = \partial(\cdot)/\partial r$ for scalars and $\nabla(\cdot) = 1/r^2 \partial(r^2 \cdot)/\partial r$ for vectors, with r the radial coordinate. The total energy density is $E_{\text{tot}} = E_{\text{int}} + E_{\text{int}} + E_{\text{rad}}$ but we assumed that E_{rad} is negligible compared to E_{int} in the other terms.

It is easy to show that the shock front[1] is moving out in the laboratory frame with velocity

$$v_{\rm front} = \frac{\varrho_1 v_1 - \varrho_- v_-}{\varrho_1 - \varrho_-}. \tag{1.4}$$

Jumping into the shock frame and assuming steady-state (i.e., on the downstream side, this implies looking only close to the shock, before the $r_{\rm min}$ boundary is felt), the mass, momentum, energy conservation Equations (1.3) yield (Marshak, 1958; Mihalas & Mihalas, 1984; Commerçon et al., 2011)

$$\varrho_- v_- = \varrho_1 v_1 \tag{1.5a}$$

$$\varrho_- {v_-}^2 + P_- = \varrho_1 {v_1}^2 + P_1 \tag{1.5b}$$

$$\dot{m}\left(h_- + \frac{1}{2}{v_-}^2\right) + F_- = \dot{m}\left(h_1 + \frac{1}{2}{v_1}^2\right) + F_1, \tag{1.5c}$$

where h is the specific enthalpy (per unit mass) and $\dot{m} = \varrho v$, and where the '$-$' subscript denotes immediately upstream of the shock and the '1' subscript denotes downstream of the radiative relaxation (cooling) layer (see Figure 1.1)[2]. As mentioned above, the radiation flux plays in general an important role. Note that these equations are valid in general, independently of the details of the radiation transfer. The enthalpy is given by $h = \gamma/(\gamma-1)P/\varrho = \gamma e_{\rm int}$ and we will work with a constant equation of state (EOS), which means in particular that the mean molecular weight μ and the heat capacity ratio γ are assumed constant.

Following Commerçon et al. (2011), we divide the momentum conservation equation (Equation 1.5b) by the upstream pressure P_- to obtain

$$\Pi = 1 + \gamma {\mathcal{M}_-}^2\left(1 - \frac{1}{r}\right), \tag{1.6}$$

where the pressure and compression ratios are defined as $\Pi = P_1/P_-$ and $r = \varrho_1/\varrho_-$, respectively. Similarly, making the energy conservation equation (Equation 1.5c) dimensionless yields

$$\frac{\Delta F}{\frac{1}{2}\varrho_- {v_-}^3} = 1 - \frac{1}{r^2} - \frac{2}{(\gamma-1){\mathcal{M}_-}^2}\left(\frac{\Pi}{r} - 1\right), \tag{1.7}$$

where $\Delta F = F_- - F_1$ is the jump in flux at the shock, i.e., the net amount of radiation lost at the shock and an important quantity in this work. These derivations have made use of mass conservation (Equation 1.5a) and the definition of the Mach number $\mathcal{M}$,

$$\mathcal{M}^2 = \frac{v^2}{{c_{\rm s}}^2} = \frac{v^2\varrho}{\gamma P}, \tag{1.8}$$

where $c_{\rm s}$ is the sound speed. Note that at low Mach numbers, it becomes important to distinguish between the laboratory and shock frames since $v_{\rm front}$ approaches v_-. Finally, the dimensionless momentum and energy conservation expressions (Equations 1.6 and 1.7) can be combined to yield

$$\eta^{\rm kin} \equiv \frac{\Delta F}{\frac{1}{2}\varrho_- {v_-}^3} = 1 + \frac{2}{(\gamma-1){\mathcal{M}_-}^2}\frac{r-1}{r} + \frac{\gamma+1}{\gamma-1}\frac{1}{r^2}. \tag{1.9}$$

This defines the *kinetic-energy-normalised shock loss efficiency* $\eta^{\rm kin}$, the central quantity of the first few chapters of this thesis. It is the efficiency with which the incoming kinetic energy is converted to radiation, which is then lost from the shock into the upstream region, nevertheless interacting with the incoming gas to generate a precursor.

[1] This expression is redundant, since a shock is already a front, but helps distinguish the velocity of the shock in the laboratory frame from that of the material upstream of the shock in its frame.

[2] Note that in equation (3) of Commerçon et al. (2011) ϱ_1 and ϱ_2 should both be replaced by $\frac{1}{2}$ but that this is only a typesetting error, their following equations being correct.

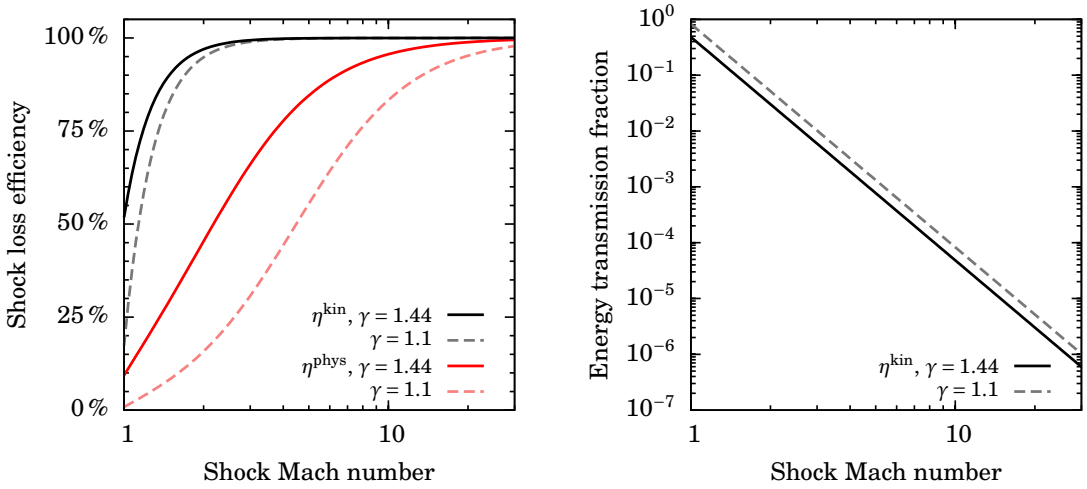

Fig. 1.2.: *Left panel:* Shock loss efficiency against the shock-frame Mach number according to the classical, kinetic-energy normalised definition (Equation 1.11, as in Commerçon et al. 2011; *upper two curves*) and according to the physical, total-energy definition (Equation 1.13; *bottom two curves*), for a constant $\gamma = 1.44$ (*solid curves*) and $\gamma = 1.1$ (*dashed*). *Right panel:* Fraction $(1-\eta^{\rm kin})$ of the kinetic energy not lost as radiation and thus transmitted to the downstream region; $(1-\eta^{\rm kin})L_{\rm acc,\,max}$ is the shock heating.

Anticipating that our simulation results will always show (very nearly) isothermal shocks, we can look at the case where the pre- and post-shock temperatures are the same ($T_1 = T_-$). We recall that this is classically referred to as the supercritical case. In that case, the compression ratio depends quadratically on the Mach number:

$$r = \gamma \mathcal{M}_-{}^2, \tag{1.10}$$

since $\Pi = r$, so that the efficiency becomes

$$\eta^{\rm kin}_{\rm isoth} = 1 - \frac{1}{\gamma^2 \mathcal{M}^4}, \tag{1.11}$$

one of the key equations of this work. Note that there is effectively no dependence on γ when the Mach number is written out since $c_{\rm s} \propto \sqrt{\gamma}$. The basic theory was presented by Marshak (1958) and Mihalas & Mihalas (1984), and Drake (2006) gave a derivation but without writing down the explicit form of Equation (1.11). While he showed efficiency curves as a function of the shock velocity for examples in high-energy research, credit for providing and plotting the general $\eta^{\rm kin}_{\rm isoth}(\mathcal{M})$ function goes, to the best of our knowledge, to Commerçon et al. (2011). It is shown in Figure 1.2. As pointed out by Commerçon et al. (2011), $\eta^{\rm kin}_{\rm isoth} \approx 100$ per cent for $\mathcal{M} \gtrsim 2$. This is valid only for isothermal shocks but since our shocks are always isothermal, we will drop the subcript for convenience.

Of course, the gas flowing into the shock brings not only kinetic but also internal energy with it, and this total energy flux is

$$\varrho v e_{\rm tot} = \varrho v \left(\frac{1}{2} v^2 + h \right) \tag{1.12a}$$

$$= \frac{1}{2} \varrho v^3 \left(1 + \frac{2}{\gamma - 1} \frac{1}{\mathcal{M}^2} \right). \tag{1.12b}$$

Naively, one might expect in supersonic flows ($\mathcal{M} = v/c_{\rm s} \gg 1$) the internal energy (measured by ${c_{\rm s}}^2$) to be negligible compared to the kinetic energy (measured by v^2), but the $2/(\gamma - 1)$ factor can change somewhat the qualitative situation, especially for low γ values; e.g., for $\gamma = 1.1$ and even a

high Mach number $\mathcal{M} = 10$, the factor $2/\mathcal{M}^2(\gamma - 1) = 0.2$, i.e., a 20 per cent contribution. From this, one can then define a 'physical' shock efficiency in the isothermal case as

$$\eta_{\text{isoth}}^{\text{phys}} = \eta_{\text{isoth}}^{\text{kin}} \times \left(1 + \frac{2}{\gamma - 1}\frac{1}{\mathcal{M}^2}\right)^{-1}, \tag{1.13}$$

which expresses what fraction of the total (kinetic and internal) energy is converted to radiation. This is also shown in Figure 1.2. However, this efficiency definition is only of limited use since an isothermal shock is not able to tap into the internal energy when the heat capacity is constant. The 'physical efficiency' will therefore only be used for pragmatic display purposes, as the dependence on γ of the efficiency is quite clear on a linear scale even for $\mathcal{M} \sim 30$ (see Figure 1.2).

In the planetary (or, similarly, stellar) formation context, the maximal 'accretion luminosity' can be written as

$$L_{\text{acc, max}} = 4\pi {R_{\text{p}}}^2 \frac{1}{2}\varrho v^3 = \frac{1}{2}\dot{M}v^2 \approx \frac{GM_{\text{p}}\dot{M}}{R_{\text{p}}}, \tag{1.14}$$

where $\dot{M} = 4\pi r^2 \varrho v$ is the mass accretion rate (neglecting the sign of v) and the last expression is valid for free fall from a large radius (see Equation 2.7). Therefore, the energy actually radiated away at the shock is usually defined as

$$L_{\text{acc}} = \eta^{\text{kin}} \frac{GM_{\text{p}}\dot{M}}{R_{\text{p}}}, \tag{1.15}$$

with η^{kin} set to 1 (e.g., Hartmann et al., 1997; Baraffe et al., 2012; Zhu, 2015). (For completeness, note that our loss efficiency η^{kin} corresponds to the quantity $(1 - \eta)$ of Spiegel & Burrows (2012), α_{h} of Mordasini et al. (2012), $(1-\alpha)$ of Hartmann et al. (1997), and X of Commerçon et al. (2011).) The case $\eta^{\text{kin}} = 1$ is termed a 'cold start' and $\eta^{\text{kin}} = 0$ a 'hot start', as the resulting planets are then respectively colder or hotter (Marley et al., 2007). In this work, we set out to determine η^{kin} by radiation hydrodynamical simulations.

While L_{acc} escapes from the shock and is therefore relevant for the disc structure and observations of this accretion luminosity (Zhou et al., 2014; Eisner, 2015; Sallum et al., 2015), the quantity of interest for the planetary structure is the amount of energy which goes into the planet. By energy conservation, this 'shock heating' is $Q^+_{\text{shock}} = (1 - \eta^{\text{kin}})L_{\text{acc, max}}$ (see Figure 1.2b). The internal energy being the same across the shock for a constant-heat capacity gas, this energy remains as kinetic energy, in the (subsonic) settling velocity. The increase of η^{kin} with $\mathcal{M}$ is due to the fact that higher Mach numbers lead to higher compression ratios, which, by mass conservation, imply smaller settling velocities. As the gas is brought to rest in the settling region and compresses, it gives up its energy as volume work, which is thus spread over a small region of the atmosphere. The detailed structure of this heating will not be important when one is interested only in the energetics of the shock for coupling purposes.

1.1.3. Estimate of the shock temperature

We return to shock physics to derive an estimate of the shock temperature which will prove very useful for interpreting the numerical results. When all the incoming kinetic energy is converted to radiation, i.e., $\eta^{\text{kin}} = 1$, the jump in radiative flux is given by

$$\Delta F_{\text{rad}} = \frac{1}{2}\varrho {v_{\text{shock}}}^3. \tag{1.16}$$

If the upstream region is in the free-streaming limit (discussed also in the next section), as should be the case for sufficiently optically thin gas, we have $F_{\text{rad}} = cE_{\text{rad}}$; but in general

$$F_{\text{rad}} \leqslant cE_{\text{rad}} = ac{T_{\text{shock}}}^4, \tag{1.17}$$

where T_{shock} is the temperature at the shock (which is the same up- and downstream) and we assumed equilibrium radiation transport ($T_{\text{gas}} = T_{\text{rad}}$). If the luminosity L_{downstr} downstream of the

shock is positive (i.e., radiation is flowing in the positive r direction), $F_{\rm rad} \geqslant \Delta F_{\rm rad}$. Combining these results, one obtains

$$\sigma {T_{\rm shock}}^4 \geqslant \frac{\varrho {v_{\rm shock}}^3}{8}, \tag{1.18}$$

since $ac = 4\sigma$, with σ the Stefan–Boltzmann radiation constant. This thus provides an approximate lower bound on the shock temperature. Commerçon et al. (2011) give a similar formula but based only on heuristic arguments and do not include the factor of 4 (their equation 22 or 53), which makes their lower bound higher. It is approximate because $\eta^{\rm kin}$ can be smaller than 1 and because $L_{\rm downstr}$ might not be negligible compared to the upstream luminosity.

For reference, the strong-shock, pure-hydrodynamical limit of the shock temperature is given by (Drake, 2006)

$$k_{\rm B} T = 2\frac{\gamma - 1}{(\gamma + 1)^2} \mu m_{\rm H} {v_{\rm shock}}^2, \tag{1.19}$$

where $v_{\rm shock}$ is the pre-shock velocity. For $\gamma = 5/3$, appropriate for a monoatomic gas, the prefactor has the commonly quoted value of $2(\gamma - 1)/(\gamma + 1)^2 = 3/16$ (e.g., Stahler et al., 1980).

1.2. Radiative flux

The energy equation (Equation 1.3c) involves the zeroth moment $E_{\rm rad}$ and the first moment $F_{\rm rad}$ of the radiation intensity (see Equation A.7) and thus requires a further relation to close the system. One common choice for this is to assume flux-limited diffusion, in which the radiative flux is written as a diffusion (Fick-like) equation for the radiation density with diffusion coefficient $D_{\rm F}$:

$$F_{\rm rad} = -D_{\rm F} \nabla E_{\rm rad}, . \tag{1.20}$$

To prevent superluminal propagation speeds when the $E_{\rm rad}$ gradient becomes steep enough and to recover the free-streaming limit, a 'flux limiter' λ is introduced:

$$D_{\rm F} \equiv \frac{\lambda c}{\kappa_{\rm R} \varrho}, \tag{1.21a}$$

$$\lambda = f(R), \tag{1.21b}$$

$$R \equiv \frac{\|\nabla \ln E_{\rm rad}\|}{\kappa_{\rm R}\, \varrho}, \tag{1.21c}$$

where the radiation quantity R is discussed in more detail in Section 1.3. There is some freedom in the choice of the flux limiter but it is required to behave asymptotically as

$$\lambda(R) \to \begin{cases} \frac{1}{3}, & R \ll 1 \quad \text{(diffusion limit)} \\ \frac{1}{R}, & R \gg 1 \quad \text{(free-streaming limit)} \end{cases} \tag{1.22}$$

to recover the diffusion and free-streaming limits. In this work, we take the flux limiter from Levermore & Pomraning (1981) given by

$$\lambda = \frac{2 + \lambda}{6 + 3R + R^2}, \tag{1.23}$$

but note that a simpler expression, with the same required limits, is given by (e.g., Ensman, 1994)

$$\lambda = \frac{1}{3 + R}. \tag{1.24}$$

They differ only up to some tens of per cent in the transition region between the optically thin and thick limits (see Section B.1).

1.3. The radiation quantity R and the reduced flux

The local radiation quantity $R(\varrho, T, E_{\rm rad})$ defined in Equation (1.21c) compares the photon mean free path $\lambda_{\rm phot} = 1/\kappa\varrho$ to the 'radiation energy density scale height' $H_{E_{\rm rad}}$; in spherical coordinates it is given by

$$R \equiv \frac{1}{\kappa\varrho E_{\rm rad}} \frac{\partial E_{\rm rad}}{\partial r} = \frac{\partial \ln E_{\rm rad}}{\partial \tau} \tag{1.25a}$$

$$= \frac{1/\kappa\varrho}{E_{\rm rad}/(\mathrm{d}E_{\rm rad}/\mathrm{d}r)} \tag{1.25b}$$

$$= \frac{\lambda_{\rm phot}}{H_{E_{\rm rad}}}. \tag{1.25c}$$

Large R values mean that the radiation energy density (which can be identified with temperature in the 1-T approximation) changes over a shorter distance than photons get absorbed and re-emitted.

In spherical geometry, a radially constant luminosity in the free-streaming regime implies $L \propto r^2 F \propto r^2 E_{\rm rad} =$ constant, so that

$$R_{\text{free stream}} = \frac{1}{\kappa\varrho} \left| \frac{\partial \ln E_{\rm rad}}{\partial r} \right| = \frac{2}{\kappa\varrho r} \gg 1. \tag{1.26}$$

Therefore, $\kappa\varrho r$, which is usually used as a crude estimate of the optical depth of a region as discussed around Equation (2.15), is in fact a diagnostic quantity which indicates whether the radiation is locally propagating by free streaming ($\kappa\varrho r \ll 1$) or not. That the local quantity R depends on an absolute coordinate r may appear at first surprising but only reflects the geometry.

The 'reduced flux' is defined as

$$f_{\rm red} \equiv \frac{F_{\rm rad}}{cE_{\rm rad}} = R\lambda(R) \tag{1.27}$$

and is a (local) measure of the extent to which radiation is streaming freely ($f_{\rm red} \to 1$) or diffusing ($f_{\rm red} \to 0$), with the effective speed of propagation of the photons $c_{\rm eff} = f_{\rm red}c$. Obviously, $f_{\rm red} \leqslant 1$. Note that $f_{\rm red}$ is different from the optical depth between two points, although there exists a relation between both as discussed around Equation (2.16a).

Finally, note that in the case of diffusion, whether the luminosity is spatially constant or not, R simply becomes three times the reduced flux:

$$R_{\rm diffusion} = 3\frac{F_{\rm rad}}{cE_{\rm rad}} = 3f_{\rm red} \ll 1, \tag{1.28}$$

and the flux can be written as

$$F_{\rm rad} = \frac{4}{3} R\sigma T^4. \tag{1.29}$$

This concludes our presentation of the necessary background material.

– I'm shocked, shocked to find that gambling is going on in here!
– Your winnings, sir.
– (sotto voce) Oh, thank you very much.

— *Casablanca* (1942)

2

The gas giant accretion shock with one-temperature radiation transport

2.1. Methods

For our one-temperature radiation hydrodynamics simulations, we use the static-grid version of the versatile and modular (magneto-)hydrodynamics code `PLUTO` (version 3; Mignone et al., 2007, 2012) combined (by R. Kuiper) with the grey, one-temperature flux-limited diffusion (FLD) radiation transport module `Makemake` described in Kuiper et al. (2010), without ray tracing. The only significant difference from Kuiper et al. (2010) is an update of the energy scheme, which is described and tested in Appendix A.

2.1.1. Model

Each simulation is meant as a snapshot of the accretion process when the planet has grown to $R_\mathrm{p} = r_\mathrm{shock}$. To follow gas accretion onto a growing planet which is detached from the nebula (see Chapter 1), we let our simulation box extend from the top-most layers of the planet to a large fraction of its accretion radius R_acc, defined through (Bodenheimer et al., 2000)

$$\frac{1}{R_\mathrm{acc}} = \frac{1}{R_\mathrm{Hill}} + \frac{1}{R_\mathrm{Bondi}}, \tag{2.1}$$

where

$$R_\mathrm{Hill} = a\left(\frac{M_\mathrm{p}}{3M_*}\right)^{1/3}, \quad R_\mathrm{Bondi} = \frac{GM_\mathrm{p}}{{c_\infty}^2} \tag{2.2}$$

are the Hill and Bondi radii, respectively, with a the semi-major axis of the planet to the star of mass M_* and c_∞ the sound speed in the disc at the planet's location. R_acc is thus the approximate region where gas should be bound to the planet, both in terms of gravitational force compared to the star (R_Hill) and thermal energy compared to the planet's potential (R_Bondi). While global and local disc simulations have shown that the accretion onto the protoplanet is highly three-dimensional (Ayliffe & Bate, 2009; Tanigawa et al., 2012; D'Angelo & Bodenheimer, 2013; Ormel et al., 2015; Fung et al., 2015) and possibly affected by magnetic fields in the gap and protoplanetary disc (e.g., Uribe et al., 2013; Keith & Wardle, 2015), we take a first step here by using a spherically-symmetric set-up and neglecting magnetic fields.

Note that, in the detached runaway phase, the continued accretion of solids (dust and planetesimals) by the planet is important for setting the final mass of the core (Mordasini, 2013). However, this accretion rate of solid is several orders of magnitude smaller than that of gas and is therefore neglected here.

2.1.2. Initial set-up

Concretely, we use a semi-open box fixed at some height in the atmosphere of the planet, with a closed left, inner edge (towards the centre of the planet) at $r = r_{\min}$, and start with an atmosphere of some arbitrary small height (e.g., 0.5 R_J), onto which gas falls from the outer edge of the grid at $r_{\max}$. For the initial set-up, we calculate an atmosphere in hydrostatic equilibrium with a constant luminosity $L_p = 10^{-3}\ L_\odot$ using the usual equations of stellar structure (but Equation 2.3d as appropriate for an atmosphere)

$$\frac{\mathrm{d}m_r}{\mathrm{d}r} = 4\pi r^2 \varrho, \tag{2.3a}$$

$$\frac{\mathrm{d}T}{\mathrm{d}r} = \nabla_{\mathrm{act}} \frac{T}{P} \frac{\mathrm{d}P}{\mathrm{d}r}, \tag{2.3b}$$

$$\frac{\mathrm{d}P}{\mathrm{d}r} = -\varrho \frac{G m_r}{r^2}, \tag{2.3c}$$

$$\frac{\mathrm{d}L}{\mathrm{d}r} = \frac{\mathrm{d}m_r}{\mathrm{d}r}\left(\varepsilon - T\frac{\mathrm{d}S}{\mathrm{d}r}\right), \quad = 0, \tag{2.3d}$$

where m_r is the mass interior to r (dominated by the M_p), S the entropy, and ε the energy generation rate, and where the actual, adiabatic, and radiative gradients are given respectively by

$$\nabla_{\mathrm{act}} = \min(\nabla_{\mathrm{ad}}, \nabla_{\mathrm{rad}}) \tag{2.4a}$$

$$\nabla_{\mathrm{ad}} = \frac{\gamma - 1}{\gamma}, \tag{2.4b}$$

$$\nabla_{\mathrm{rad}} = \frac{3LP\kappa}{64\pi\sigma G m_r T^4}. \tag{2.4c}$$

Equation (2.4a) is the Schwarzschild criterion and could have been replaced with $\nabla_{\mathrm{act}} = \nabla_{\mathrm{rad}}$ since the actual simulations do not include convection (see also the discussion in Section 2.7). We use an adaptive step size Δr for the integration to resolve accurately the pressure and temperature gradients. This atmosphere is then smoothly joined onto a calculated accretion flow for ϱ and v. (See Equations 2.7ff below.) The goal of these efforts is (i) to provide a numerically sufficiently smooth initial profile while (ii) beginning with a certain atmospheric mass to speed up the computation. 'Production data' is measured only after an adjustment phase, once the actual accretion rate at the shock is equal to the one set through the outer boundary conditions, described below.

We take a uniform grid segment from $r_{\min}$ to $r_{\min} + \Delta r$ to resolve sufficiently well the pressure gradient in the innermost part, using by default $\Delta r = 0.5\ R_J$ and $N = 500$ cells there. The other grid patch is a stretched segment out to $r_{\max}$, with usually also $N = 500$, i.e., a much smaller resolution. This has proven to be stable and accurate.

2.1.3. Boundary conditions

For the hydrodynamics, reflective boundary (zero-gradient) conditions are used in the density, pressure, and velocity, i.e.,

$$\frac{\mathrm{d}P}{\mathrm{d}r} = 0 \tag{2.5a}$$

$$\frac{\mathrm{d}\varrho}{\mathrm{d}r} = 0 \tag{2.5b}$$

$$\frac{\mathrm{d}v}{\mathrm{d}r} = 0. \tag{2.5c}$$

It proved numerically not feasible to enforce hydrostatic equilibrium at $r_{\min}$, i.e., to set $\mathrm{d}P/\mathrm{d}r$ to $-\varrho g$, where $g = Gm_r/r^2$ is the local gravitational acceleration. Since g acts in all grid cells,

Equation (2.5a) implies an acceleration at $r_{\min}$. However, this is unproblematic as Equation (2.5c) ensures that no mass flows over the boundary. In the radiation transport also, we prevent flow of energy over $r_{\min}$ by using (since the flux limiter $\lambda = 1/3$ always)

$$\frac{\mathrm{d}E_{\mathrm{rad}}}{\mathrm{d}r} = 0. \tag{2.6}$$

The outer edge of the grid $r_{\max}$ is set well outside of the atmosphere and away from the shock. For the hydrodynamics, we choose an accretion rate and approximate the velocity as the free-fall velocity:

$$v_{\mathrm{ff}}(r_{\max}) = \sqrt{2GM_{\mathrm{p}}\left(\frac{1}{r_{\max}} - \frac{1}{R_{\mathrm{acc}}}\right)}, \tag{2.7}$$

with R_{acc} defined in equation (2.1). Mass conservation then determines the 'free-fall density':

$$\varrho_{\mathrm{ff}}(r_{\max}) = \frac{\dot{M}}{4\pi r^2 |v(r_{\max})|}. \tag{2.8}$$

The pressure gradient here too is required to vanish:

$$\left.\frac{\mathrm{d}P}{\mathrm{d}r}\right|_{r_{\max}} = 0, \tag{2.9}$$

although for some simulations we considered a Dirichlet boundary condition with $P = P(\varrho_{\mathrm{ff}}(r_{\max}), T_{\mathrm{neb}})$ for a nebula temperature T_{neb}, taken as $T_{\mathrm{neb}} = 150$ K (e.g., Mizuno, 1980) unless stated otherwise.

Finally, the radiation outer boundary condition is usually set to the flux-divergence-free condition

$$\frac{\partial r^2 E_{\mathrm{rad}}}{\partial r} = 0, \tag{2.10}$$

which corresponds to a constant luminosity if f_{red} is sufficiently close to 1. However, even when the flux at the outer edge is rather in the diffusion regime, we obtain similar results for a simple Dirichlet boundary condition on the radiation temperature.

2.2. Microphysics

In this chapter, we use a constant equation of state, but we still present in this section the effective heat capacity ratio γ_{eff} (usually abbreviated to γ) and the mean molecular weigth μ of a hydroden-helium mixture as a function of density and temperature. This will serve to justify our choice for values of γ and μ. We take a helium mass fraction $Y = 0.25$.

2.2.1. Equation of state

Figure 2.1 shows the effective heat capacity ratio γ, computed with the ideal-gas equation of state (e.g., Black & Bodenheimer, 1975; D'Angelo & Bodenheimer, 2013) as implemented Vaidya et al. (2015), as function of density and temperature. At hydrogen dissociation and ionisation, γ is seen to sink, and one can also see the effect of helium ionisation at higher temperatures. Below roughly 40–100 K, depending on the assumption for the ratio of the ortho- to parahydrogen (e.g. Vaytet et al., 2014), rotational degrees of freedom of molecular hydrogen are frozen (not shown), with $\gamma \approx 1.4$ for higher temperatures until 1000–2000 K (increasing with density). There, H_2 dissociation lets γ drop to 1.1 (for $\varrho = 10^{-8}$ g cm^{-3}, but $\gamma = 1.07$ for $\varrho = 10^{-13}$). Moving further up in temperature, it reincreases to $\gamma = 1.2$ only[1] before hydrogen ionisation again sinks it. At $T = 3 \times 10^4$ K, the adiabatic index has reincreased to $\gamma \approx 1.3$. Thus, values of $\gamma = 1.1$ and $\gamma = 1.44$ bracket the relevant range for planet formation given the densities and temperatures found later.

[1] While these figures agree with Saumon et al. (1995) and Vaytet et al. (2013), they contrast with figure 1 of Tomida et al. (2013) and figure 2 of Vaytet et al. (2014), who apparently find that $\gamma = 5/3$ is reached again between hydrogen dissociation and hydrogen ionisation and helium ionisation. The source of this is not clear, and their slightly higher helium mass fraction ($Y = 0.28$ or $Y = 0.30$ with unaccounted-for metals) cannot explain the discrepancy.

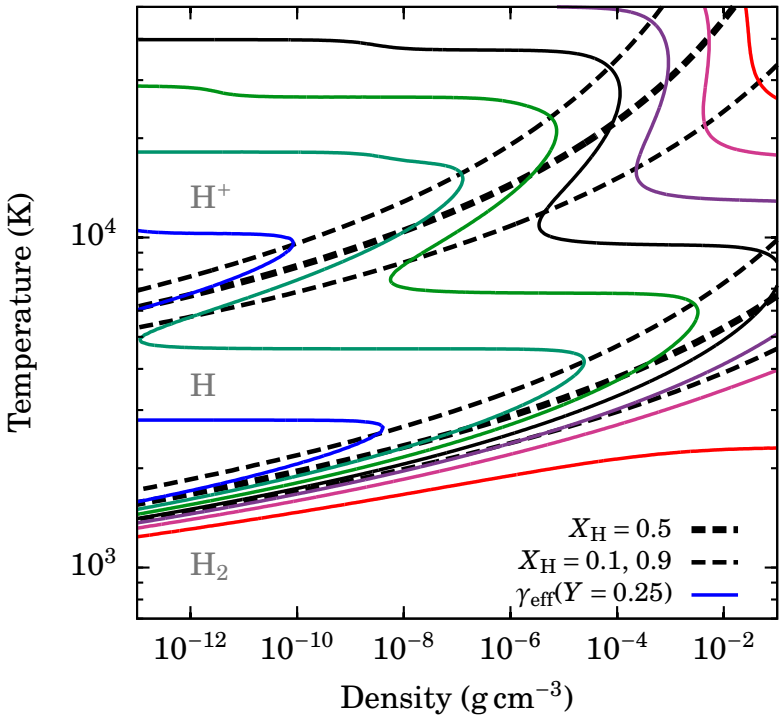

Fig. 2.1.: Contours of constant effective heat capacity ratio $\gamma_{\rm eff}$ for an ideal hydrogen–helium gas with $Y = 0.25$ (*solid lines*) and ionisation or dissociation fraction for hydrogen $X_{\rm H}$ (*dashed lines*). Heat capacity ratio contours are for $\gamma_{\rm eff} = 1.10$–1.40 (*blue to red*) in steps of 0.05, starting at $\varrho = 10^{-13}$ g cm^{-3} near 3000 K or 10^4 K and increasing to higher densities. The shift in the $\gamma_{\rm eff}$ curves at low densities and high temperatures are due to helium ionisation. The dominant hydrogen species (H$_2$, H I, H$^+$) is indicated in each region separated by the dashed lines.

2.2.2. Opacities

We consider both constant and tabulated opacities. The contribution of the dust to the opacity dominates below approximately 1400–1600 K, at which temperature its refractory components (olivine, silicates, pyroxene, etc.) evaporate (Pollack et al., 1994; Semenov et al., 2003). The standard opacity tables we use are the smoothed Bell & Lin (1994, hereafter BL94) tables. We can also make use of the Malygin et al. (2014) gas opacities combined with the dust opacities from Semenov et al. (2003) and compare these in Figure 2.2.

BL94 model the destruction of dust (metal grains) with a very steep slope of $\kappa(T) \propto T^{-24}$ between two temperatures obtainable analytically from their table,

$$T_{\rm dest,\,beg} = 813\ {\rm K} \left(\frac{\varrho}{10^{-11}\ {\rm g\,cm^{-3}}} \right)^{1/24.5}, \tag{2.11a}$$

$$T_{\rm dest,\,end} = 1485\ {\rm K} \left(\frac{\varrho}{10^{-11}\ {\rm g\,cm^{-3}}} \right)^{1/81}, \tag{2.11b}$$

where the dust begins melting at $T = T_{\rm dest,\,beg}$ and is completely removed at $T_{\rm dest,\,end}$. Using directly the tabulated dust opacity at a given temperature effectively assumes that the dust melts instantaneously but, in reality, this melting process might be time-dependent, so that the opacity in this region is not certain. This destruction region is shown as a grey band in the ϱ–T diagrams in the following sections where appropriate. Note however that above it (i.e, at higher T) and up to roughly 4000 K, the BL94 opacity is unrealistically low compared to more recent opacities (cf. with the Malygin et al., 2014 data in Figure 2.2; Helling et al., 2000; Ferguson et al., 2005), due to missing H_2O lines or alkali line wings (M. Malygin, priv. comm.).

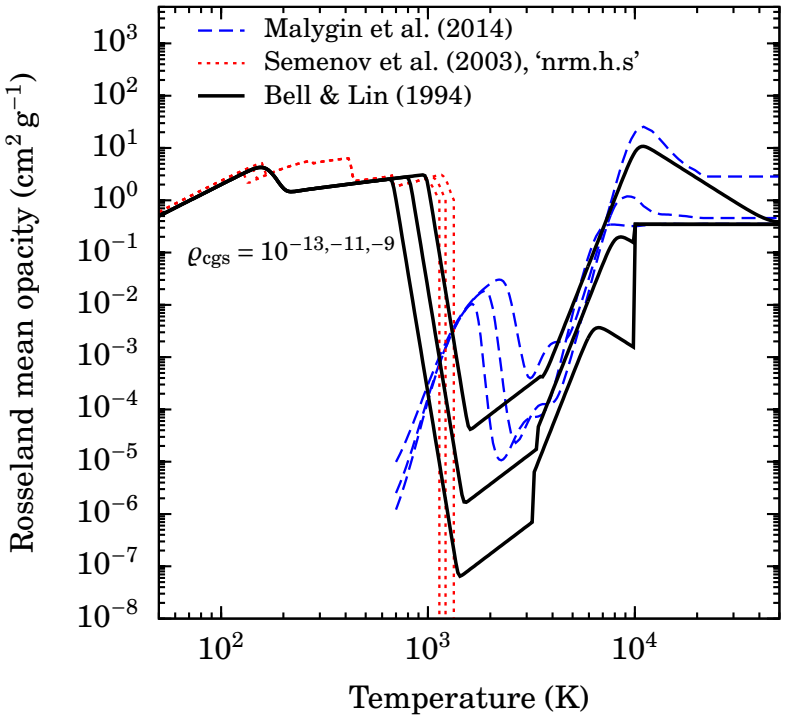

Fig. 2.2.: Gas, dust, and total Rosseland mean opacities from Malygin et al. (2014), BL94, and Semenov et al. (2003). Three densities are shown: $\varrho = 10^{-13,-11,-9}$ g cm^{-3}. For the Semenov et al. (2003) opacities, we use their 'nrm.h.s' model, with dust grains made of 'normal silicates' ([Fe/(Fe+Mg)] = 0.4) as homegeneous spheres. The Malygin et al. (2014) opacities are kept constant above the table limit of $T = 2 \times 10^4$ K.

2.3. Quantities of interest

The goal of these simulations is to determine the appropriate boundary conditions for an accreting protoplanet by measuring the temperature and pressure downstream of the shock, as well as the amount of kinetic energy not converted to radiation at the shock. Through the equation of state, knowledge of (T, P) can be recast as of (T, ϱ) and *vice versa*, and also provides the entropy $S(T, P)$. To make a prediction about the post-formation entropy of a planet, however, requires coupling to formation calculations, which can follow the thermal response of the entire planet over the complete formation phase (Mordasini et al., 2012). Since we model only the upper layers of the atmosphere and thus do not include the bulk of the mass of the planet, we focus on the luminosity, and defer the coupling to subsequent work.

We will find that the shock Mach number is always $\mathcal{M} \gtrsim 2$, implying efficiencies close to 100 per cent. Since the relevant quantity for the planet is $1 - \eta^{\rm kin}$, this would require a very high precision (better than parts in a hundred) in the measurement of $\eta^{\rm kin}$. This is however not possible due to the presence of (small) temporal oscillations in the temperature profile and inaccuracies in determining the shock location (spread over a few cells).

Therefore, we adopt a different approach. Since we find isothermal shocks, with $T_- = T_1$, we will determine the precise value of the efficiency by measuring the shock temperature, calculating the upstream Mach number, and using Equation (1.11). Explicitly,

$$1 - \eta^{\rm kin} = \frac{1}{\gamma^2 \mathcal{M}^4} = \left(\frac{k_{\rm B} T^+}{{v_{\rm shock}}^2 \mu m_{\rm H}} \right)^2 , \tag{2.12}$$

which provides the shock heating as $Q^+_{\rm shock} = (1 - \eta^{\rm kin}) L_{\rm acc,\,max}$. The fractional uncertainty in $1 - \eta^{\rm kin}$ is only twice that on T. Even though this is an exact equation directly following from

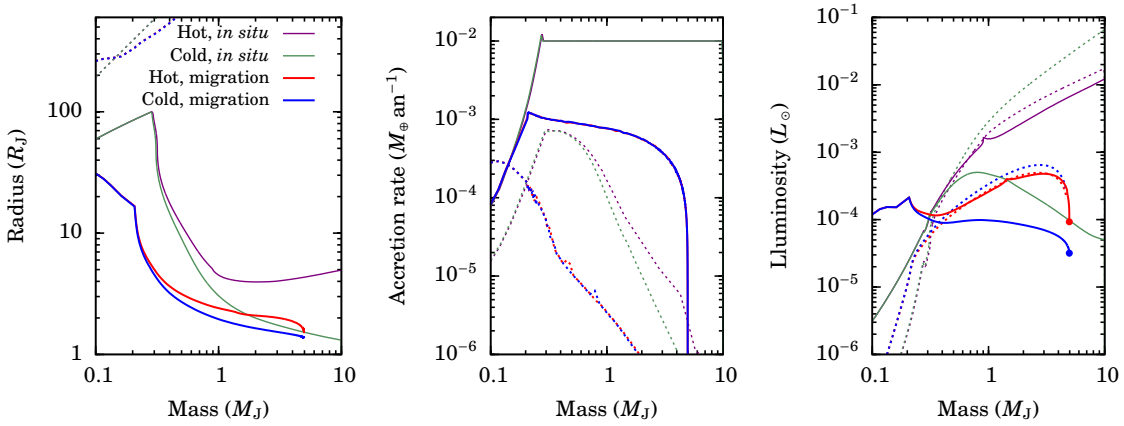

Fig. 2.3.: Radius (*left panel*), accretion rate (*middle*), and internal luminosity (*right*) against mass (growing with time) of a 10-M_J planet (final mass) forming *in situ* at 5.2 au with a constant accretion rate during the detached phase assuming hot or cold accretion (*violet and green curves, respectively*), and for a 5 M_J planet with a more realistic accretion rate history due to migration in the disc, assuming hot or cold accretion (*red and blue curves, respectively*). (Cold and hot *starts* refer to the post-formation condition and are used synonymously.) Dotted lines in the three panels show, respectively, the accretion radius from which the gas falls (same for cold and hot starts), the solids accretion rate, and the maximal accretion luminosity due to kinetic energy $L_{\text{acc, max}} = GM_p\dot{M}(1/R_p - 1/R_{\text{acc}})$. The post-formation luminosity of the migrating planets is highlighted (*filled circle*).

conservation of mass, momentum, and energy, it will be explicitly verified, within errorbars, by comparing the jump in L at the shock, ΔL, to the incoming $L_{\text{acc, max}}$.

The effect of using 1-T radiation transport will be assessed in Chapter 3 and found to be negligible in most cases.

2.4. Relevant parameter space

Before addressing the shock problem itself, we show the values of the 'formation parameters' (defined below) which occur in formation calculations during the detached phase, when the accretion shock can play a significant role. While coupling of our shock results to these formation calculations will be needed, considering hot and cold starts (i.e., hot and cold accretion; the terms are used interchangeably) should provide a bracketing of the expected range of results. Secondly, based on these, we estimate the shock temperature and density to assess what values for the 'microphysical parameters' μ, γ, and κ are likely to be relevant.

2.4.1. Formation parameters

The key shock parameters are M_p, R_p, $\dot{M}$, and L_p, i.e., mass, radius, accretion rate, and internal luminosity. Their range is shown in Figure 2.3 for the *in situ* formation at 5.2 au of a planet with a final mass of 10 M_J (Mordasini et al., 2012) with a fixed accretion rate in the detached phase, as in Pollack et al. (1996). (Because of this fixed accretion rate, tracks for planets with smaller final masses simply cut off earlier.) For comparison, planets with a final mass of 5 M_J accreting with $\eta^{\text{kin}} = 0$ or $\eta^{\text{kin}} = 1$ and with an accretion rate set by their migration in the disc are also displayed. When the planet detaches from the nebula, its radius very quickly decreases from $\approx$ 100 R_J for the *in situ* case or $\approx$ 20 R_J for the more realistic migrating one to several R_J over a small mass range, from $\approx$ 0.2 to 1 M_J. The radii are smaller (around 1–2 R_J) in the case with a lower accretion rate and show a smaller difference between hot and cold accretion than for the fixed-$\dot{M}$ cases. The luminosities also, especially the post-formation values, are very different. The fixed-$\dot{M}$ provide a more conservative upper bound.

We now turn to full population synthesis calculations Mordasini et al. (2012), which display a similar but larger diversity, as shown in Figures 2.4 and 2.5 for cold and hot accretion, respectively. This will help us define the relevant region of parameter space. For $M_\mathrm{p} \geqslant 1.3\ M_\mathrm{J}$, the radii range from 1 to $\approx 4\ R_\mathrm{J}$ ($6\ R_\mathrm{J}$) for cold (hot) starts, and, in general, the lower the accretion rate, the lower the radii are at a given mass. In the cold-accretion case, for most points at $\dot{M} > 10^{-3}\ M_\oplus\,\mathrm{an}^{-1}$, $L_\mathrm{acc,\,max}$ dominates by a factor of at least 3, with a significant number where $L_\mathrm{acc,\,max} \geqslant 10 L_\mathrm{p}$, up to a few orders of magnitude. In the case of hot accretion, however, $L_\mathrm{acc,\,max}$ is always comparable (with ±0.5 dex) to L_p, and for many planets 3–10 times smaller for $\dot{M} \leqslant 10^{-5}\ M_\oplus\,\mathrm{an}^{-1}$.

Although there are clear correlations between M_p, R_p, $\dot{M}$, and L_p, Figures 2.4 and 2.5 show that they there is a certain scatter, i.e., a significant portion of the four-dimensional formation parameter space, which spans several orders of magnitude in each dimension, needs to be covered. As a first step, we will focus on those cases where L_p is negligible compared to $L_\mathrm{acc,\,max}$. Since the luminosity right of the shock is $L_\mathrm{p} + \eta^\mathrm{kin} L_\mathrm{acc,\,max}$ and we find $\eta^\mathrm{kin} \approx 1$, this means that we have to choose for the simulations only the desired $(M_\mathrm{p}, R_\mathrm{p}, \dot{M})$ and do not have to worry about obtaining a particular L_downstr, which would be the effective L_p. To evaluate the effects of boundary conditions and other simulation details, however, we will make use of the full grids of simulations, whether the resulting L_downstr match or not the L_p found in the current population syntheses.

2.4.2. Microphysics parameters

Figure 2.6 shows the estimated shock temperature from Equation (1.18), using the free-fall velocity (Equation 2.7), and the pre-shock density, given by Equation 2.8, for the migrating forming planet of Figure 2.3 and for planets from the cold-start population synthesis, shown in Figure 2.4. We focus on the formation phase when the shock could be important. Comparing to the contours of constant γ and the rough ϱ–T region were dust is destroyed and the opacity drops from ~ 1 to $\sim 10^{-2}\ \mathrm{cm}^2\,\mathrm{g}^{-1}$, one can expect for $\dot{M} \lesssim 10^{-5}\ M_\oplus\,\mathrm{an}^{-1}$ the hydrogen to remain molecular and dust to be only partially destroyed, but for higher accretion rates (i.e., for most of the parameter space of interest here) great importance of both dissociation and dust destruction. For hot-start population synthesis, the highest temperature reached is, for increasing $\dot{M}$, ≈ 700–2000 K instead of 1000–5000 K, due to the radii being larger and thus the shock velocity lower.

From the temperature and densities covered, both hydrogen and helium ionisation should be entirely negligible at the shock. While these estimates will have to be compared with a full, self-consistent calculation, they do indicate that reasonable values include

$$\begin{aligned}\gamma &\approx 1.1\text{–}1.44,\\ \mu &= 1.23\text{–}2.353,\\ \kappa &\sim 10^{-4}\text{–}1\ \mathrm{cm}^2\,\mathrm{g}.\end{aligned}$$

In other words, the gas giant formation shock problem occupies an interesting region of the micro-physical parameter space, including phase transitions and clearly non-constant opacities. We wish to address all these effects simultaneously in future work but begin here with calculations performed using a constant equation of state, nevertheless with either constant or tabulated opacities.

2.5. Results: Efficiencies and downstream quantities

The key output quantities which will serve to couple to formation calculations are the luminosity going into the planet (and thus not radiated away at the shock) as well as the temperature and pressure left of the shock. We begin (Section 2.5.1) by looking at shock structures and efficiencies as a function of the optical depth to r_max by varying the value of the constant opacity. We also confirm that Equation (1.11), which is a local relation, holds independently of the optical depth to r_max. This will allow us to avoid the large numerical noise in $1 - \eta^\mathrm{kin}$, given that $\eta^\mathrm{kin} \approx 1$ almost always, by focussing on determining the temperature upstream of the shock to obtain the

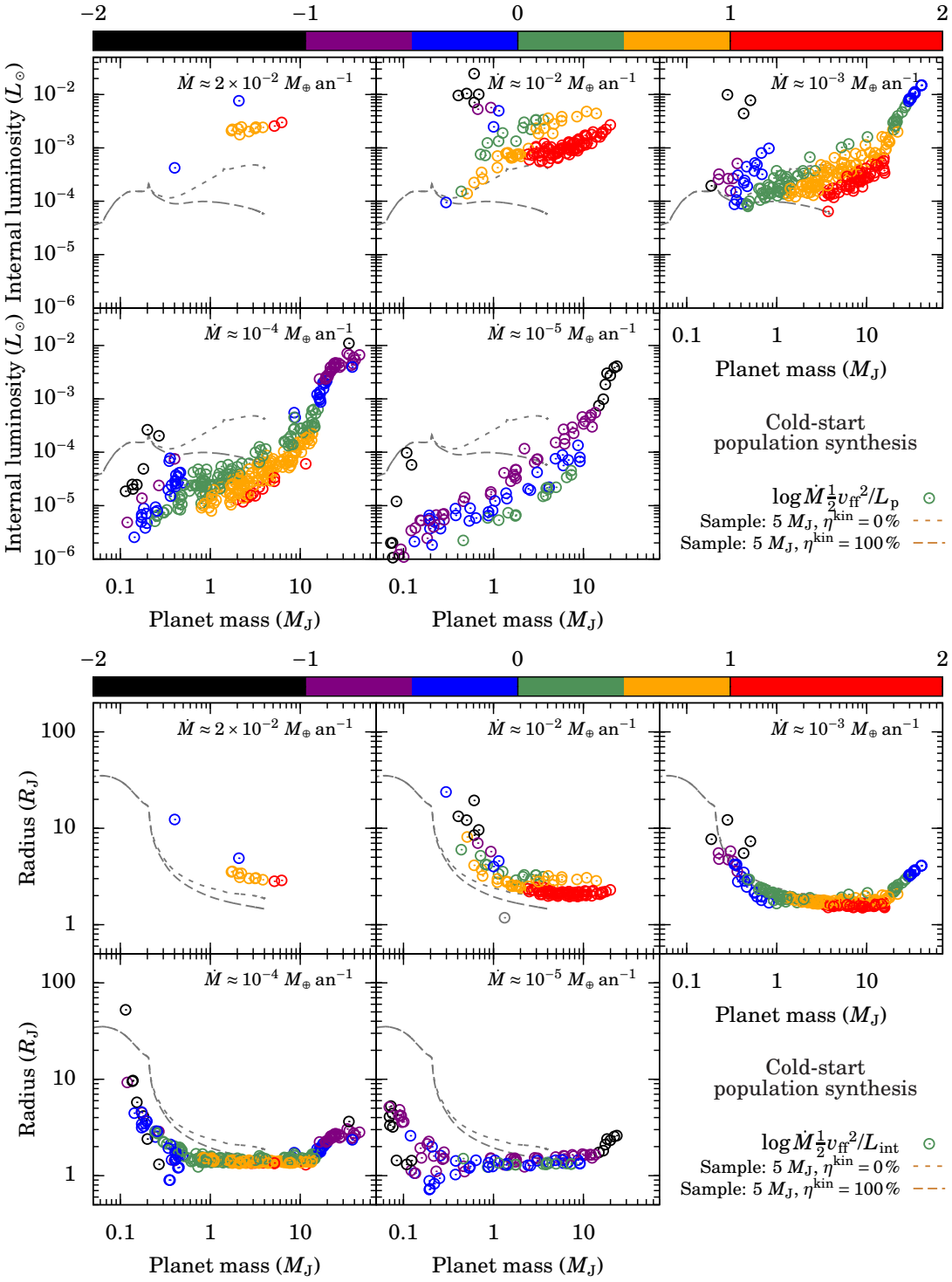

Fig. 2.4.: Parameter space covered by a standard cold-accretion population synthesis: Ratio of the maximal kinetic energy influx to the internal luminosity (*colour*) as a function of luminosity (*top group of panels*) or radius (*bottom group*) and mass for different gas accretion rates (*subpanels*). The points selected are within 0.05 dex of the accretion rate indicated. The grey curves (identical in all panels) reproduce the hot- and cold-start 5-M_J formation tracks shown in Figure 2.3.

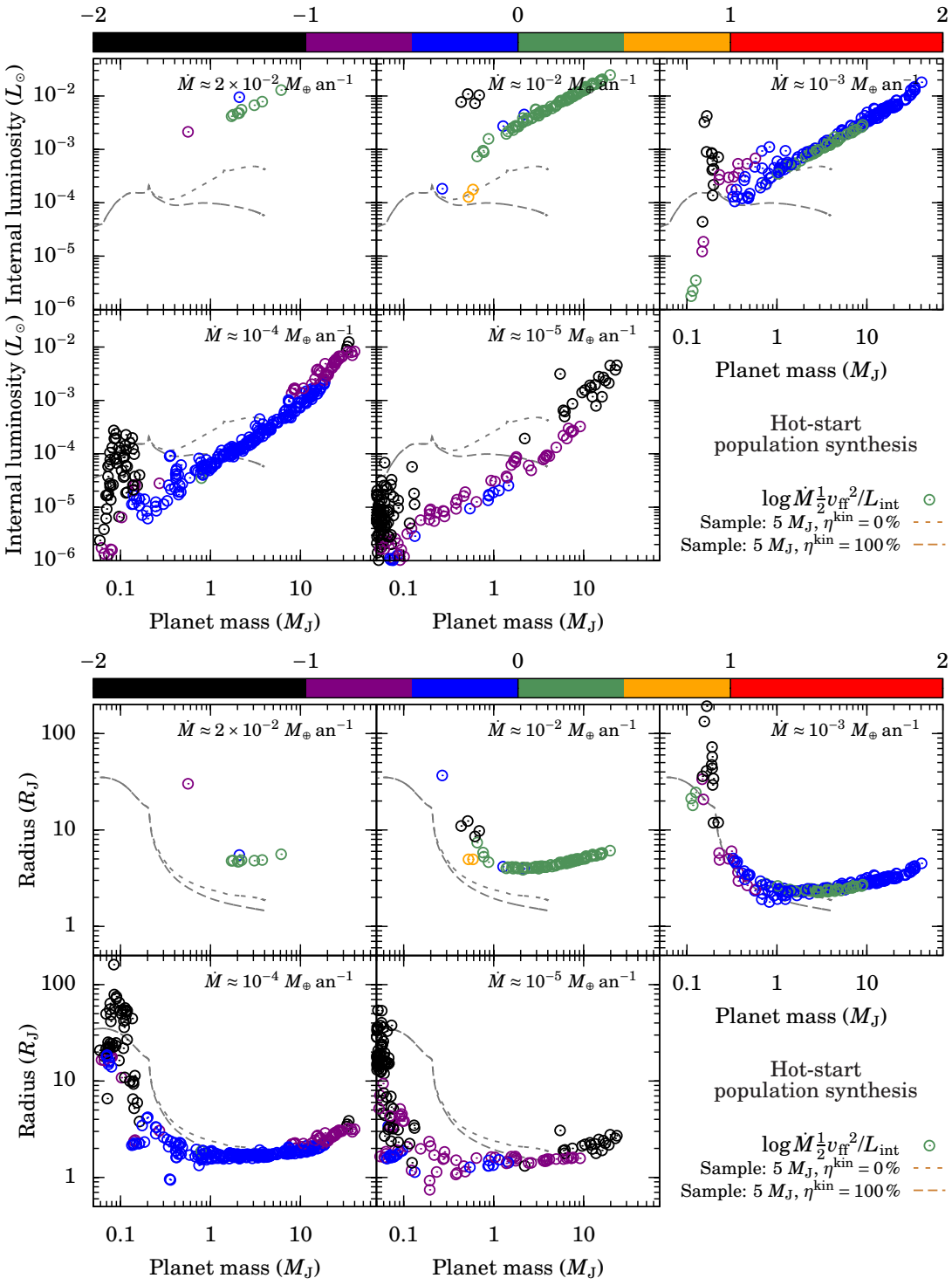

Fig. 2.5.: As in Figure 2.4 but for hot starts, i.e., always assuming that $\eta^\mathrm{kin} = 0$.

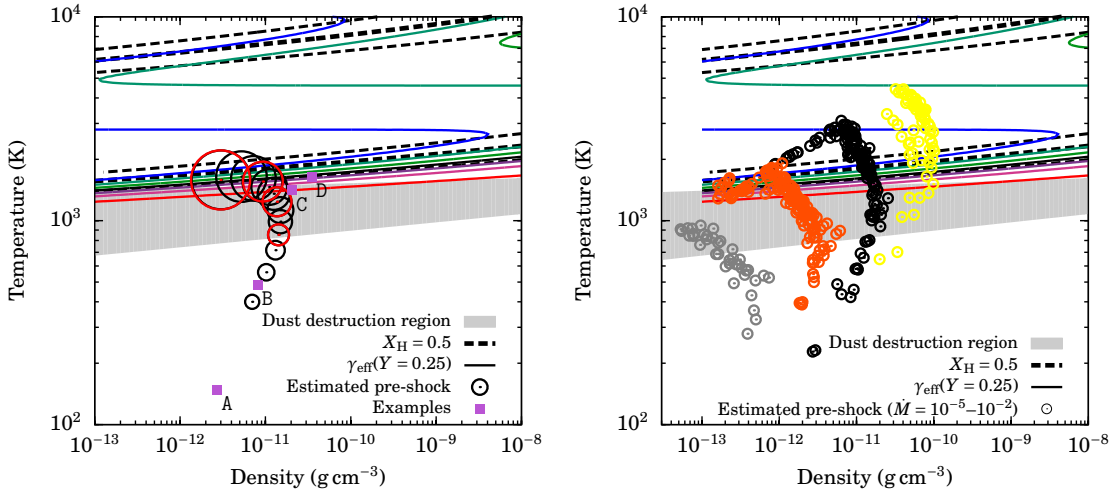

Fig. 2.6.: *Left panel: A posteriori* estimate of the shock temperature and density upstream for for the migrating case of Figure 2.3, made by assuming $\eta^{\rm kin} = 1$, $f_{\rm red} = 1$ upstream, and $L(r_{\rm shock}{}^-) \ll L(r_{\rm shock}{}^+)$, which leads to $4\pi {R_{\rm p}}^2 caT^4_{\rm shock} \approx GM_{\rm p}\dot{M}/R_{\rm p}$, with ϱ given by the free-fall density. The symbol size is proportional to the Mach number using the estimated temperature, with the size in the legend corresponding to $\mathcal{M} = 10$. Points are shown in steps of 0.1 dex in $M_{\rm p}/M_{\rm J}$, starting at $M_{\rm p} = 0.2$ at the bottom, with 0.5, 1, 2, and 4 $M_{\rm J}$ highlighted in red. No point is shown at 5 $M_{\rm J}$. Shown are contours of $\gamma = 1.1$–1.65 in steps of 0.05 (from ≈ 100 to 1000 K is $\gamma \approx 1.4$), as in Figure 2.1 (*coloured solid lines*), contours of $X_{\rm H} = 0.1$, 0.5, and 0.9 (*black dashed lines*), and the region of dust destruction in BL94 (*grey band*), with κ of order 1 cm^2 g^{-1} at lower T (cf. Figure 2.2). The fuchsia squares are examples from Section 2.5.2 and will be discussed there. *Right panel:* Same but for the population synthesis planets of Figure 2.4, however showing all times and not displaying the Mach number. The groups of points are, from left to right, for $\log \dot{M}/(M_\oplus\,{\rm an}^{-1}) = -5$, -4, -3, and -2.

Mach number. Results will then be presented for a few representative cases for a forming planet (Section 2.5.2) and then for large grids in parameter space (Section 2.5.3).

2.5.1. Dependence of the structure and efficiency on optical depth

We first explore how the shock profiles depend on the optical depth between the shock and the outer edge. For this purpose, unrealistically high opacity values are also considered to help span a large range of optical depths ($\Delta\tau = 10^{-2}$–100), but plausible values are chosen for the other parameters. As an example, in Figure 2.7 are shown results for a low-mass ($M_{\rm p} = 0.316\ M_{\rm J}$), large ($r_{\rm min} = 15.85\ R_{\rm J}$) planet with $Q^+_{\rm atm} = 0$ and with an accretion rate of $\dot{M} = 10^{-2}\ M_\oplus\,{\rm an}^{-1}$. The grid extends out to 0.9 $R_{\rm acc}$ with as outer boundary conditions ${\rm d}P/{\rm d}r = 0$ for the hydrodynamics and ${\rm d}r^2 E_{\rm rad}/{\rm d}r = 0$ for the radiation transport.

Overall, the radial structures are as expected and show a number of typical features, discussed next.

Density and velocity The density reveals a nearly hydrostatic atmosphere abruptly cut off at the shock, followed upstream by accelerating gas falling almost at free fall from $R_{\rm acc}$ due to the planet's gravity and a lack of pressure support[2]. The density jumps are in part much larger than for a hydrodynamical shock. As it falls deeper in the potential well of the planet, the gas slows down to sub-free-fall speeds due to the pressure gradient caused by the increasing temperature (and density). Even in the case with the hottest accretion envelope, this causes only a decrease of some ten per cent in the pre-shock $|v|$ at the time shown. For the case with the highest opacity, the precursor (discussed below) is contained within the simulation,

[2] The radial re-increase of density at $r > \frac{3}{4}R_{\rm acc}$ is due the decrease in velocity there (see Equation 2.7), with the velocity at $R_{\rm acc}$ zero and thus formally the density infinite; all grids end at $r_{\rm max} \leqslant 0.9\ R_{\rm acc}$.

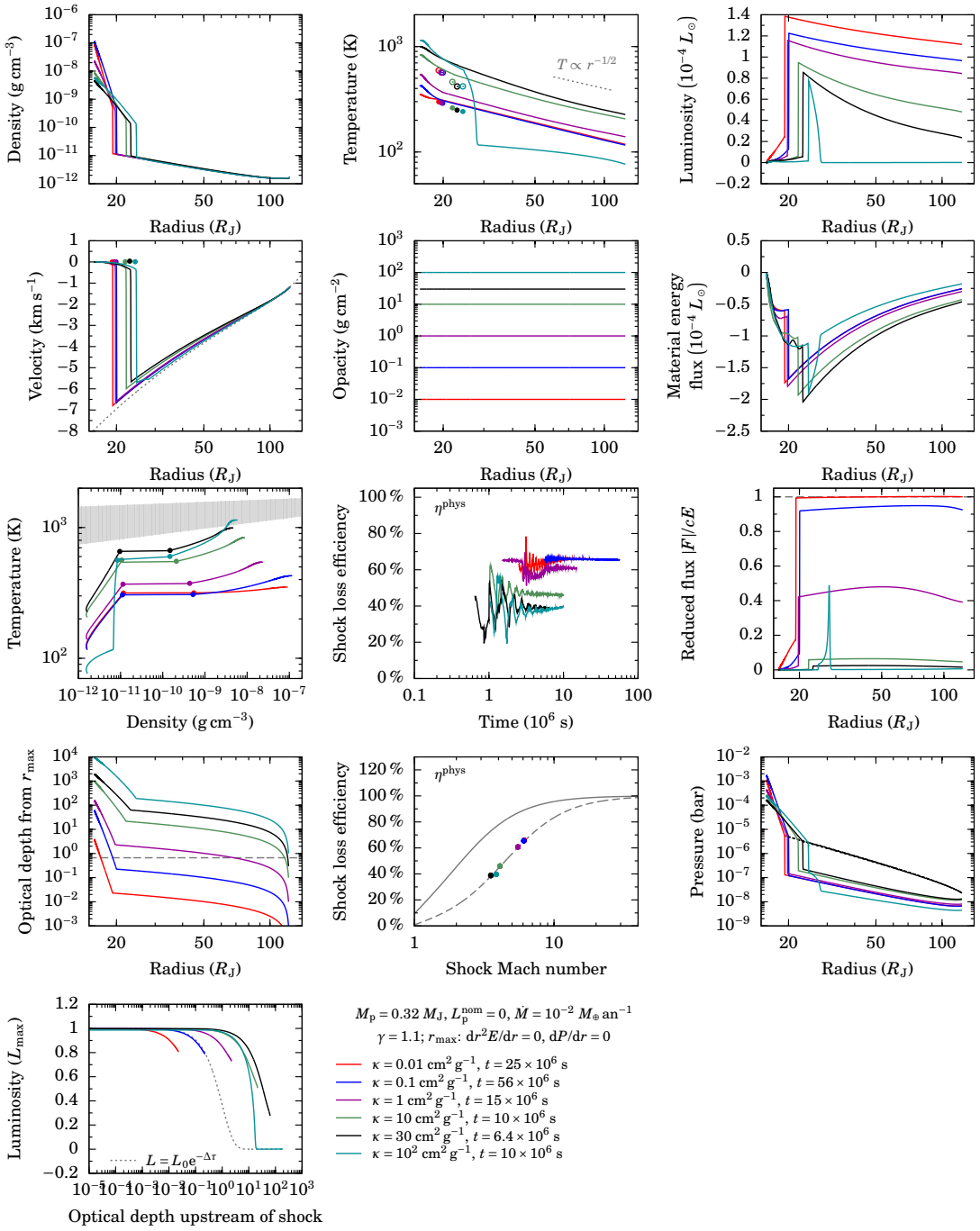

Fig. 2.7.: Profiles for runs with different optical depths between the shock and $r_{\rm max}$ for a constant EOS. See the legend for the parameter values and the axis labels for a description of the quantities shown. Only a few comments are needed: The *temperature* panel also shows the strong-shock, non-radiating post-shock value (Equation 1.19; *open dots*), the free-streaming lower bound (Equation 1.18; *filled dots*), as well as $T \propto r^{-1/2}$ (*grey dashed line segment*); the *velocity* and *energy fluxes* are evaluated in the laboratory frame, with the shock expansion velocity (usually positive) shown in the velocity panel (*filled dots*); the *material energy flux* refers to $\dot{M}(e_{\rm kin} + e_{\rm int} + P/\varrho)$ (i.e., a 'material luminosity'); the *velocity* panel displays also the free-fall velocity from $R_{\rm acc}$ (the same for all simulations; *grey dashed line*); the solid dots in the *temperature–density phase diagram* mark the up- and downstream conditions of the hydrodynamical shock; the *shock loss efficiency* shown is the physical one (Equation 1.13) directly across the shock; the *reduced-flux* panel shows the relativity ratio v/c as dotted lines; the *shock loss efficiency* as a function of the Mach number of the gas immediately upstream of the shock is compared to grey lines showing the analytical optically-thin, isothermal result (Equation 1.13) for $\gamma = 1.44$ (*solid curve*) and 1.1 (*dashed grey*); the *luminosity*, against the optical depth measured upstreamward from the shock, is normalised to the maximum value in the profile, which is compared to steady-state exponential absorption (*dashed grey curve*); and the *pressure* panel also displays the ram pressure (*dashed curves*). Note that 1 bar = 10^6 erg cm^{-3}, and that the first two simulations have the same Mach number and efficiency.

and this feature can be seen as a slight additional slow-down. Due to our simulating only the upper layers of the atmosphere, the shocked matter can settle down only over a limited radial extent, so that the shock moves out over time as mass accumulates below[3]. This is subsonic (e.g., $\sim 0.3\ \mathrm{km\,s^{-1}}$) and thus usually, for higher Mach numbers, negligible compared to the free-fall velocity. At small Mach numbers, unless otherwise stated, we take into account the shock velocity and evaluate all relevant quantities in the frame in which the shock is at rest.

Note that during runaway gas accretion, the planet contracts at first at a rate $\mathrm{d}R_\mathrm{p}/\mathrm{d}t \sim 1\ \mathrm{m\,s^{-1}}$, decreasing quickly to $\sim 1\ \mathrm{cm\,s^{-1}}$. Thus the velocities are usually decoupled by several orders of magnitude. All the same, to test whether this changes the shock structure, after an adjustment phase mass was removed from the innermost cell of a simulation at the same rate as the accretion rate, thus keeping the total mass constant. The shock remained stationary and the structure did not change.

Temperature profile In the examples in Figure 2.7, the temperature always decreases radially. Only for the lowest-opacity case ($\kappa = 10^{-2}\ \mathrm{cm^{-2}\,g^{-1}}$) is the reduced flux $f_\mathrm{red} \equiv F_\mathrm{rad}/cE_\mathrm{rad} = 1$ (with $f_\mathrm{red} \approx 0.9$ for $\kappa = 0.1$), i.e., the accretion envelope is in the free-streaming regime. At higher opacities, the effective speed of light is less than c, nevertheless remaining several orders of magnitude larger than the gas flow speed. Interestingly, since f_red is rather constant radially for all simulations, $T \propto r^{-1/2}$ at least approximately, even when $f_\mathrm{red} \ll 1$. Finally, note that if the temperature increased solely due to adiabatic compression, i.e., at constant entropy (for which there would need to be no radiation transport), we would have $T \propto \varrho^{\gamma-1} \propto r^{-1.5(\gamma-1)}$, i.e., $T \propto r^{-0.15}$ or $T \propto r^{-0.66}$ for $\gamma = 1.1$ or 1.44, respectively. Thus, when $T \propto r^{-1/2}$, entropy decreases inward if $\gamma > 4/3 \approx 1.33$.

Shock temperature The temperatures immediately up- and downstream of the hydrodynamics shocks are equal to within roughly one per cent or much less, depending on the opacity. An approximate lower bound to this temperature was obtained in Equation (1.18),

$$\sigma T^4 \geqslant \frac{\varrho v^3}{8}.$$

The simulations whose pre-shock region is almost in the free-streaming regime indeed have a temperature given by Equation (1.18), whereas in the other cases a higher temperature is needed to carry a similar luminosity. One way of thinking about this is that the effective speed of light is lower than c, so that E_rad must increase in order to have the same $F_\mathrm{rad} = c_\mathrm{eff}E_\mathrm{rad}$. (See the filled circles in Figure 2.7.)

Pressure The radial profile of the pressure reveals clearly the precursor as an increase in the pre-shock region. Also, the post-shock pressure is given very accurately by the ram pressure of the incoming gas,

$$P_\mathrm{post} = P_\mathrm{ram} = \varrho v^2. \tag{2.13}$$

This differs slightly from the strong-shock, non-radiating case where $P_\mathrm{post} = 2/(\gamma+1)\varrho v^2$ (see equation 4.18 of Drake, 2006), as we verified with a simulation using $\gamma = 5/3$ to increase the potential difference.

Optical depth and regime According to the classical definition of the optical depth as the number of photon mean free paths between two points r_1 and r_2, $\Delta\tau(r_1, r_2) = \int_{r_1}^{r_2} \kappa\varrho\,\mathrm{d}r$, the simulations of Figure 2.7 have $\Delta\tau(r_\mathrm{shock}, r_\mathrm{max}) \approx 10^{-2}$–$10^2$ at the times shown, while the region below the shock and down to r_min has $\Delta\tau(r_\mathrm{min}, r_\mathrm{shock}) \approx 4$–$10^4$. The effective speed of light $F_\mathrm{rad}/E_\mathrm{rad}$, which is the diffusion velocity, ranges from $\approx c$ for the least optically deep

[3] For some (but not all) of the simulations with $\mathcal{M} \gtrsim 15$, the shock position actually moves inward while the layers between r_min and the shock cool over time, the density increasing close to r_min but decreasing closer to the shock. However, this velocity too is small compared to the shock velocity and does not affect our results.

cases to $\approx 10^{-3}\ c$ for the thickest, however always remaining much larger—at least by a factor 100—than the gas speed. This is termed 'static diffusion' by Mihalas & Mihalas (1984). (For $\kappa = 10^4\ \mathrm{cm^2\ g^{-1}}$ (not shown), the diffusion velocity becomes equal to the gas velocity, yet there is no qualitative change in the profiles.)

The reduced flux directly upstream of the shock is compared to the optical depth to $r_{\max}$ in Figure 2.8. The tight correlation can be understood thus: First, for an opacity which depends on radius as $\kappa \propto r^{-\alpha}$, the optical depth through an arbitrary density profile $\varrho \propto r^{-\beta}$ is given by

$$\Delta\tau_\infty \equiv \Delta\tau(r_{\mathrm{shock}}, \infty) = \int_{r_{\mathrm{shock}}}^{\infty} \kappa\varrho\, \mathrm{d}r \tag{2.14a}$$

$$= \frac{1}{\alpha+\beta-1}\kappa\varrho(r_{\mathrm{shock}})r_{\mathrm{shock}}, \tag{2.14b}$$

where for a free-fall profile $\beta = 3/2$ exactly when $R_{\mathrm{acc}} \gg r_{\mathrm{shock}}$, and assuming that $\alpha+\beta-1 > 0$; for a sufficiently constant opacity ($\alpha \ll \beta - 1 = 0.5$), this implies

$$\Delta\tau_\infty = \frac{1}{0.5+\alpha}\kappa\varrho_{\mathrm{ff}} r_{\mathrm{shock}} \approx 2\kappa\varrho_{\mathrm{ff}} r_{\mathrm{shock}}. \tag{2.15}$$

We note in passing that this justifies (within a factor of a few) the estimate[4] of Stahler et al. (1980) of the optical depth upstream of the second-core accretion shock as $\kappa\varrho r_{\mathrm{shock}}$. A similar estimate is used by Mordasini et al. (2012) for their boundary conditions.

Secondly, as discussed above (Equation 1.26), the radiation quantity R is given as a function of radius by $R_{\text{free stream}} = 2/\varrho\kappa r$ when $f_{\mathrm{red}} = \lambda(R)R$ is not too much smaller than 1 (the criterion will be discussed below), i.e., in the free-streaming regime, and with a radially constant luminosity. Therefore, $R(r_{\mathrm{shock}}) = 4/\Delta\tau$ for a free-fall, constant-L profile in the free-streaming regime with a constant opacity, which yields

$$f_{\mathrm{red}} = \lambda\left(\frac{4}{\Delta\tau}\right) \times \frac{4}{\Delta\tau} \tag{2.16a}$$

$$\approx \left(\frac{3}{4}\Delta\tau + 1\right)^{-1}, \tag{2.16b}$$

where the last expression uses the simple flux limiter $\lambda(R) = 1/(3+R)$ taken in Ensman (1994). Equation (2.16a) is compared to the data of Figure 2.7 in Figure 2.8 and matches very well, especially taking the non-constancy of the luminosity profiles into account.

Luminosity The luminosity increases approximately linearly from $r_{\min}$ to the shock where it jumps by a finite amount, then decreasing with radius. The value of L downstream of the shock reflects in part the cooling of the layers below it, which will probably have a different thermal history than if the layers were allowed to sink further down into the planet instead of stopping at most at $r_{\min}$. Since we are interested only in the jump at the shock and the radial behaviour of L has no bearing upon the efficiency, we do not investigate it further.

Efficiency We find that for this small subset of parameter space, the kinetic efficiency measured directly across the shock is $\eta^{\mathrm{kin}} \approx 100$ per cent, i.e., all the incoming kinetic energy is converted into radiation. The nominal values range from 100.6 to 101.9 per cent but this is due to small oscillations in the temperature profile, which lead to changes in the luminosity, as well as to simulation- and resolution-dependent ringing downstream of the shock and the details of a robust but simple analysis algorithm.

[4] This had puzzled Vaytet et al. (2013), who took $\kappa\varrho r_{\mathrm{shock}}$ to be at best an estimate of the *downstream* optical depth. The estimate is certainly rough for a non-constant opacity but at least it does estimate the optical depth in the correct (upstream) direction.

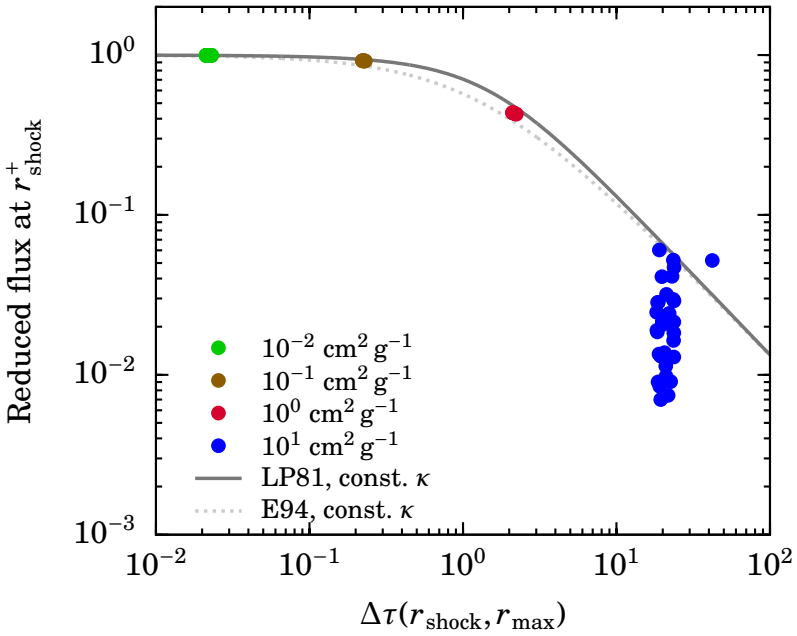

Fig. 2.8.: Reduced flux $f_{\rm red}$ directly upstream of the shock compared to the optical depth between the shock and $r_{\rm max}$ for simulations from Figure 2.7. The highest-opacity cases were left out. Several times are included for simulation, which is visible as 'noise' only in the $\kappa = 10$ cm^2 g^{-1} case. In all cases, the gas velocity is near $v/c = 10^{-5}$, which is much smaller than $F_{\rm rad}/E_{\rm rad}$, the radiation diffusion velocity. Equation (2.16a) is shown for the Levermore & Pomraning (1981) (*solid grey line*) and Ensman (1994) ($\lambda = 1/(3 + R)$; *dashed grey*) flux limiters.

Given that the Mach numbers are all $\mathcal{M} \gtrsim 3$, the efficiency values thus match convincingly Equation (1.11), as expected. See Figure 2.7. (The small deviation at the highest opacity is due to a slight inaccurary in determining the shock front velocity, which affects both the denominator of the efficiency and the Mach number.)

For our actual profiles with a finite $R_{\rm acc}$, we can compute $\Delta\tau$ to $r_{\rm max}$, either analytically or numerically. The estimate $\Delta\tau_\infty \approx 2/\kappa\varrho_{\rm ff} r_{\rm shock}$ is 1.4–1.8 times larger than the integrated $\Delta\tau$ from $r_{\rm shock}$ to $r_{\rm max}$. This is, of course, in part a function of time as the shock moves out. Moreover, since $\kappa\varrho r$ re-increases for $r \gtrsim 0.5$, the integral to $r_{\rm max}$ does depend somewhat sensitively on the value of $r_{\rm max}$. Thus the estimate is approximate only.

In summary, we have shown that the profiles we obtain are sensible and have confirmed, up to small, essentially numerical fluctuations, the validity of Equation (1.11), independently of the optical depth regime upstream of the shock.

2.5.2. Results for selected cases with tabulated opacities

We now turn to parameter combinations likely to be directly relevant to formation calculations. From Figures 2.3 and 2.4, we select four combinations of formation parameters given in Table 2.1 and provide estimates of the shock quantities in Table 2.2. The pre-shock density $\varrho_{\rm pre}$ is the free-fall density at the chosen radius (Equation 2.8), and the shock temperature $T_{\rm shock}$ is estimated from Equation (1.18). By placing these values in the ϱ–T diagram, one can easily estimate the mean molecular weight, effective heat capacity ratio, and opacity. This is done in Figure 2.6a and the results are displayed in Table 2.2.

The pre-shock densities are around 10^{-11} g cm^{-3}, and for Cases `A` and `B`, $T_{\rm shock} \approx 150$–$500$ K. At those densities, dissociation starts becoming important near 1300 K, so that even though $T_{\rm shock}$ is a lower limit, we should indeed find that the hydrogen remains molecular, assuming $f_{\rm red}({r_{\rm shock}}^{+})$

Table 2.1.: Selected points in parameter space for forming planets as shown in Figures 2.4–2.5. The values are chosen approximately. The column 'Origin' refers to (1c) *in situ* formation with cold accretion (Figure 2.3); (1h) *idem*, hot accretion; (2) cold accretion with migration (Figure 2.3); (3c) cold accretion population synthesis (Figure 2.4); and (3h) hot accretion population synthesis (Figure 2.5). In the notation $a(b)$, a is the mantissa and b is the base-10 exponent. Entropy values are provided for reference; S_{cent} refers to the central entropy of the planet and S_{surf} to the value at the photosphere.

Name, Origin	M_{p} (M_{J})	R_{p} (R_{J})	$\dot{M}$ ($M_{\oplus}\,\mathrm{an}^{-1}$)	S_{cent} (k_{B}/baryon)	S_{surf} (k_{B}/baryon)	L_{p} ($L_{\odot}$)	$L_{\mathrm{acc,\,max}}$ ($L_{\odot}$)
A: (1c/h)	0.3	70/81	10^{-2}	10.7	11.27/11.31	1(−4)	4/3(−5)
B: (3c)	0.3	5–6	10^{-3}	11.0	11–12.5	1–3(−4)	5–4(−5)
C: (2)	1.3	1.8	10^{-3}	10.2	10.4	9(−5)	6(−4)
D: (3h)	2.5	4	10^{-2}	12.0	12.1	4(−3)	5(−3)

Table 2.2.: For the cases of Table 2.1, estimated (*left of the vertical bar*) and measured (*right thereof*) shock quantities. The pre-shock density ϱ_{pre} is the free-fall density at the chosen radius. $T^{+} = T(r_{\mathrm{shock}}{}^{+})$ and $\mathcal{M}^{+}$ are the actual pre-shock temperature and Mach number in the shock frame. Note that the simulations actually used all have $\mu = 2.353$ and $\gamma = 1.44$ but that this does not make a significant difference (and does not change the estimate of ϱ and T_{shock}). The measured Mach number and Equation (1.18) serve to compute η^{kin}. See text for details.

Name, Origin	ϱ_{pre} ($\mathrm{g\,cm}^{-3}$)	T_{shock} (K)	μ	γ	κ ($\mathrm{cm}^2\,\mathrm{g}^{-1}$)	T^{+} (K)	$\mathcal{M}^{+}$	$(1-\eta^{\mathrm{kin}})L_{\mathrm{acc,\,max}}$ ($L_{\odot}$)
A: (1c/h)	3(−12)	150	2.353	1.44	5	210	3.5	2(−7)
B: (3c)	8(−12)	480	2.353	1.44	2	550	8.5	5(−9)
C: (2)	2(−11)	1400	2.353	1.44	10^{-6}	1630	17	3(−9)
D: (3h)	4(−11)	1600	1.5	1.3	10^{-2}	1670	16	4(−8)

is not orders of magnitude smaller than 1. For the standard $Y = 0.3$ H–He mixture, this means that $\mu = 2.353$ and $\gamma = 1.44$. For Case C, the estimate implies also molecular hydrogen, although less securely so, whereas Case D is clearly in the phase transition from molecular to atomic hydrogen. We quote for Case D $\mu = 1.5$ but this is highly uncertain due to the steep slope of $\mu(T)$ there. Likewise, $\gamma \approx 1.4$ for Case C but $\gamma = 1.3$ for Case D, here again with high uncertainty; it could be as low as $\gamma \approx 1.1$ if at a slightly (~ 0.1 dex) higher temperature.

For the opacities, Cases A and B are clearly in the dust-dominated region, with $\kappa \approx 5$ and $2\ \mathrm{cm}^2\,\mathrm{g}^{-1}$, respectively (see Figure 2.2). The estimate of κ for Case C is very approximate since it is in the dust destruction region, where κ decreases by several orders of magnitude over a small temperature range of a few 100 K Semenov et al. (2003). For Case D we quote an approximate value for the region dominated by gas opacities. Note that these estimates of κ serve only as reference and will not be used any further.

Figure 2.9 shows structures for the examples of Table 2.1 with the BL94 opacities. They are qualitatively similar to all but the optically thickest of Figure 2.7; the optical depth from the shock to r_{max} is $\Delta\tau \approx 0.4$–2 but in no case does the luminosity upstream of the shock decrease markedly towards r_{max}. The reduced flux is $f_{\mathrm{red}} \gtrsim 0.2 \gg v/c$ for all simulations.

Consider first the opacity profiles. In the accretion envelope (i.e., upstream of the shock) of Case B, temperatures remain below approximately 500 K, so that the dust grains contribute to the opacity, with $\kappa \sim 3\ \mathrm{cm}^2\,\mathrm{g}^{-1}$ out to $r_{\mathrm{max}} \approx 100\ R_{\mathrm{J}}$. Cases C and D are different: there, the dust is destroyed ahead of the shock, letting the opacity drop some six orders of magnitude (see shaded region in the ϱ–T panel; the opacity remains low up to ~ 3000 K). Thus there is a 'dust destruction front' (DDF) as is the case for protostellar collapse (Stahler et al., 1980; see, e.g., also

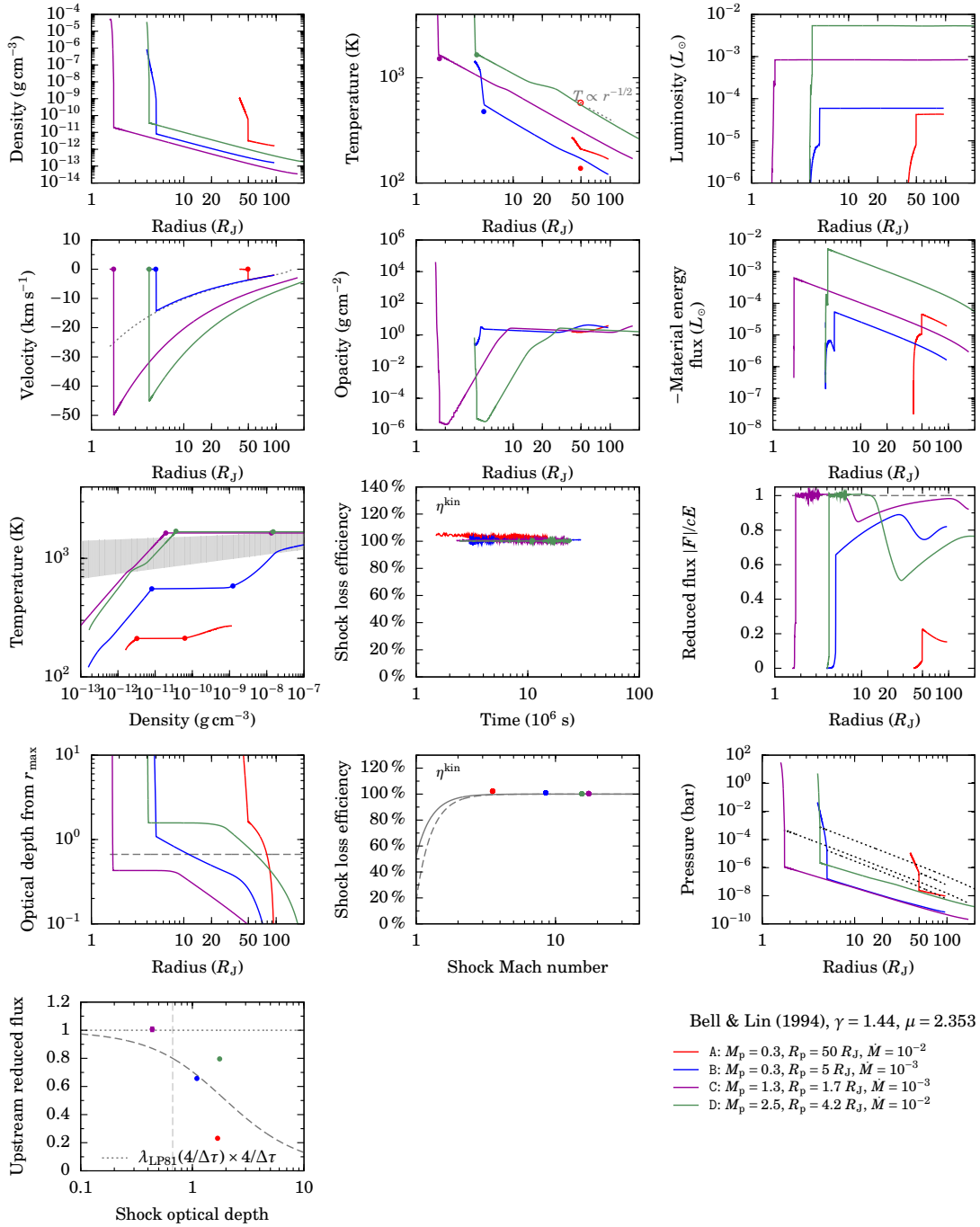

Fig. 2.9.: As in Figure 2.7 but for the four cases of Table 2.1, using the BL94 opacities. The grey band in the ϱ–T plane shows the zone of dust destruction region in BL94. The outer boundary conditions are $\mathrm{d}P/\mathrm{d}r = 0$ and $\mathrm{d}r^2 E_{\rm rad}/\mathrm{d}r = 0$.

figure 8 of Vaytet et al. (2013)). Since BL94 are missing opacity sources in that temperature region, as discussed in Section 2.2.2, more realistic opacities (e.g., Ferguson et al., 2005; Malygin et al., 2014) should lead to a less pronounced 'opacity gap' (Stahler et al., 1980) but the qualitative feature should remain.

Because of the steeply changing opacity as a function of temperature in BL94, the flux limiter is somewhat noisy, leading to jumps between adjacent grid cells in the reduced flux ($f_{\rm red} = \lambda \times R(\lambda)$) and the temperature profile. In effect, this assumes that the dust evaporates instantaneously compared to the flow timescale. One way of mitigating the jumps would be to introduce a computational time lag between the computation of the opacities and the temperature or to use explicitly time-dependent dust destruction. Using other opacities with a smaller gradient might also prove to be sufficient.

Despite the noise in the `C` case, as we verified with other simulations (shown in Section B.2), the respective shock temperatures are similar whether using the constant or BL94 opacities. Since all $L_{\rm downstr}$ are negligible compared to the luminosity right of the shock, the small differences in temperature are due only to the change in $f_{\rm red}$. The largest difference is in Case `D`, where $T_{\rm shock}$ is higher in the constant-opacity case by about 18 per cent, which is consistent with $f_{\rm red}$ being lower by 50 per cent ($0.5^{-1/4} \approx 1.19$). The respective Mach numbers change only slightly and the shock heating $Q^+_{\rm shock}$ (discussed below) remains around $10^{-5}\ L_{\rm acc,\ max}$ (see Figure 1.2b).

The last panel of Figure 2.9 shows the reduced flux at the shock compared to the optical depth to $r_{\rm max}$. For a constant opacity, we were able to write down a unique analytical relation between the two (Equation 2.16a) and found that the simulations matched very well. Ignoring Case `A`, we see that this relation is in fact a lower bound to $f_{\rm red}$; if upstream of the shock the opacity is much lower, photons have a longer mean free path, i.e., their effective diffusion velocity is closer to c, and $f_{\rm red} = c_{\rm eff}/c$ is closer to one. This is a local effect; the optical depth, a path-integral quantity, can still remain similar, as is the case in these examples.

For Case `A`, it appears that the shock is too close to $r_{\rm max}$ for Equation (2.15) to apply, as we formally integrated out to infinity, taking also $R_{\rm acc} \gg R_{\rm p}$ to avoid a diverging density at $R_{\rm acc}$, where $v_{\rm ff} = 0$ (this is a limitation of this simple one-dimensional picture).

Note that the presence of a DDF does not necessarily imply that the accretion envelope is optically thin; Cases `C` and `D` both have a DDF but $\Delta\tau = 0.5$ for Case `C` and $\Delta\tau \approx 1.5$ for Case `D`.

To assess the importance of the residual kinetic energy on the structure of the planet one can compare $(1 - \eta^{\rm kin})L_{\rm acc,\ max}$ to the respective internal luminosity. Looking at the respective columns of Tables 2.1 and 2.2, it is clear that the fraction of the energy that is not lost radiation is entirely negligible, being at most 0.2 per cent of the internal luminosity (Case `A`). As discussed in Section 2.3, the luminosity is not very sensitive to possible errors in the temperature determination (choice of grid cell, etc.), so that, given the orders-of-magnitude difference, our conclusion is a robust one for these four cases.

We defer a discussion of the post-shock pressure and temperature to the next section, in which we look at a much larger parameter space.

2.5.3. Results for a large parameter space and constant opacity

In this section, we consider a large grid of parameters as appropriate for the phase of detached runaway accretion where the accretion shock might have a significant effect on the planet's growh. We cover

$$0.1\ M_{\rm J} < M_{\rm p} < 10\ M_{\rm J}$$
$$1\ R_{\rm J} \lesssim R_{\rm p} \lesssim 20\ M_{\rm J}$$
$$10^{-5}\ M_\oplus\,{\rm an}^{-1} < \dot{M} < 10^{-2}\ M_\oplus\,{\rm an}^{-1},$$

using $\gamma = 1.1$ and a constant opacity $\kappa = 1\ {\rm cm}^2\,{\rm g}^{-1}$. The grid extends out to $0.7\ R_{\rm acc}$ (to have $|v|$ monotonically increasing inward) and has the outer boundary conditions ${\rm d}P/{\rm d}r = 0$ for the hydrodynamics and ${\rm d}r^2 E_{\rm rad}/{\rm d}r = 0$ for the radiation transport.

Figures 2.10–2.12 display key results of this study: the shock temperature $T_{\rm shock}$, the resulting upstream Mach number $\mathcal{M}$, the effective heating from the shock $Q^+_{\rm shock} = (1-\eta^{\rm kin})L_{\rm acc}$, and the post-shock pressure, as well as the upstream reduced flux and optical depth, and the luminosity jump across the shock compared to the Mach number. Each point represents one simulation, with starting radii $r_{\rm min}$ = 1, 1.6, 2.5, 3.9, 6.3, 10, and 16 $R_{\rm J}$. Only a subset of the masses is shown. For each simulation, we choose one snapshot when the actual accretion rate $4\pi {r_{\rm shock}}^2 \varrho(v - v_{\rm front})$ is within one per cent of the desired value, after an early adjustment phase. (Usually the actual rate deviates by much less than this.) The radius, which usually decreases over time during the detached accretion stage, is the shock position at that time and we use $r_{\rm shock}$ and $R_{\rm p}$ interchangeably.

As expected, the shock temperature is equal to or greater than the estimate (Equation 1.18), and it agrees overall with it, although there are some deviations. Almost all temperatures for $\dot{M} = 10^{-2}\ M_\oplus\,{\rm an}^{-2}$ are slightly higher ($\approx$ 0.1–0.2 dex) than predicted, especially at low masses, while the match is very good for $\dot{M} = 10^{-3}\ M_\oplus\,{\rm an}^{-2}$. At $\dot{M} = 10^{-4}\ M_\oplus\,{\rm an}^{-2}$ there is a slight deviation for temperatures around 1000 K, with however a strong departure from the trend by the points with the smallest radius for the two highest masses. Perhaps surprisingly, despite their high Mach numbers ($\mathcal{M} \approx$ 30–50), their $L_{\rm acc,\ max}$ is much smaller than the luminosity left of the shock $L_{\rm downstr}$, so that the actual temperature greatly exceeds the lower bound (Equation 1.18). The situation is similar for the $\dot{M} = 10^{-5}\ M_\oplus\,{\rm an}^{-2}$ cases[5]. We also verified that the temperatures left and right are indeed equal, to less than 4 per cent (not shown).

The post-shock pressure range roughly from $P = 10^{-8}$ to 10^{-2} bar and matches quite well the ram pressure $P_{\rm ram} = \varrho {v_{\rm shock}}^2$. The very small simulation-dependent but always positive offset is simply due to resolution effects (the choice of the 'post-shock cell'), while the more noticeable deviations at very low accretion rates ($\dot{M} = 10^{-5}\ M_\oplus\,{\rm an}^{-1}$) are associated with simulations in which the shock position oscillates.

The top panel of Figure 2.11 displays the reduced flux $f_{\rm red} = F_{\rm rad}/cE_{\rm rad}$ against the optical depth upstream of the shock. The higher the accretion rate, the lower the reduced flux, i.e., the less the upstream position is in the free-streaming regime. Nevertheless, the lowest value is $f_{\rm red} \approx 0.1$, which is greater than the transition near $f_{\rm red} \approx 0.01$ seen in Figure 2.8. We can also see that the optical depth ahead of the shock is at most $\Delta\tau(r_{\rm shock}, r_{\rm max}) \sim 10$, and closer to $\Delta\tau \sim$ 0.01–0.1 for the lower accretion rates. (Note that material between $r_{\rm max}$ and infinity, ignoring the accretion radius, would essentially not contribute at all to the $\Delta\tau$ integral.) At face value, this means that for some simulations, the shock is located below the photosphere ($\Delta\tau \approx 2/3$). However, the opacity ($\kappa = 1\ {\rm cm^2\,g^{-1}}$) is typical of the dust-dominated regime; comparing to the temperature panel of Figure 2.10 shows that those simulations with the highest optical depths also have the highest shock temperatures, so that with realistic opacities the dust might be destroyed, lowering the optical depth by a few to several orders of magnitude. This is discussed in the next section.

Figure 2.11 also presents the post-shock luminosity $L_{\rm downstr}$. The post-shock luminosity is, in some sense, the effective internal luminosity of the planet, but it is has proven difficult to control since it reflects the thermal history of the accreted gas below the shock; for a given shock radius, this depends on the choice of $r_{\rm min}$. The values we obtain differ in part by several orders of magnitude from the actual $L_{\rm p}$ of population-synthesis planets (see Figures 2.4 and 2.5). For instance, at $\dot{M} = 10^{-3}\ M_\oplus\,{\rm an}^{-1}$, $L_{\rm p} \approx 10^{-4}$–$10^{-3}\ L_\odot$ for $0.6 \lesssim M_{\rm p} \lesssim 13\ M_{\rm J}$ in the cold-accretion case, whereas from our simulations $L_{\rm downstr} \approx 10^{-5}$–$10^{-4}\ L_\odot$ for those masses and the corresponding radius range ($1.3 \lesssim R_{\rm p} 3\ R_{\rm J}$). However, for cold accretion, Figure 2.4 reveals that for a large portion of the parameter space $L_{\rm p}$ is much smaller than the maximum accretion luminosity. Since we find that $\eta^{\rm kin} \approx$ 100 per cent as discussed below, this means that the interior luminosity (here, $L_{\rm downstr}$) is mostly irrelevant in determining the shock structure. Work is planned to extend the parameter space to cover those cases with $L_{\rm p} \sim L_{\rm acc,\ max}$.

We compare in Figure 2.12 $\eta^{\rm kin}$ as measured from ΔL and the gas properties directly upstream

[5] Note that some points are missing because they were still in the adjustment phase and the time of analysis; the numerical timestep being independent of the accretion rate (since $v_{\rm ff}$ does not depend on $\dot{M}$), the wall-clock time to adjustment is larger at lower $\dot{M}$.

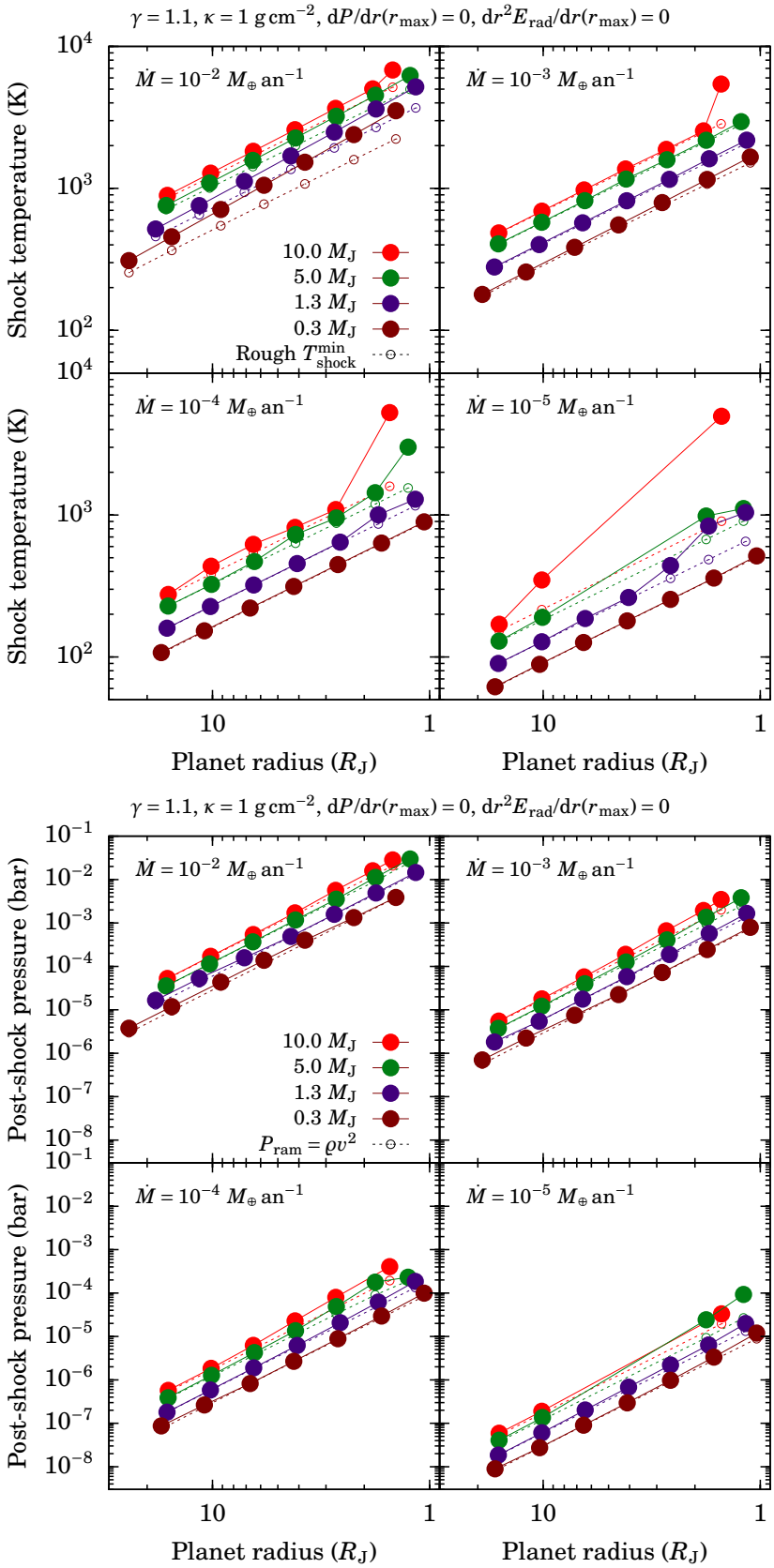

Fig. 2.10.: Shock results for a constant equation of state and opacity ($\gamma = 1.1, \mu = 2.353, \kappa = 1\,\mathrm{cm^2\,g^{-1}}$). *Top panel:* Temperature at the shock (*filled circles*), compared to the estimated lower bound of Equation (1.18; *open circles*). *Bottom panel:* Downstream pressure (*filled circles*), compared to the ram pressure (*open circles*). Each panel group shows the quantities as a function of accretion rate (*subpanels*), planet mass, and shock position (i.e., planet radius). The boundary conditions at r_{max} are indicated in the titles, with ϱ and v as always given by their free-fall values from R_{acc}.

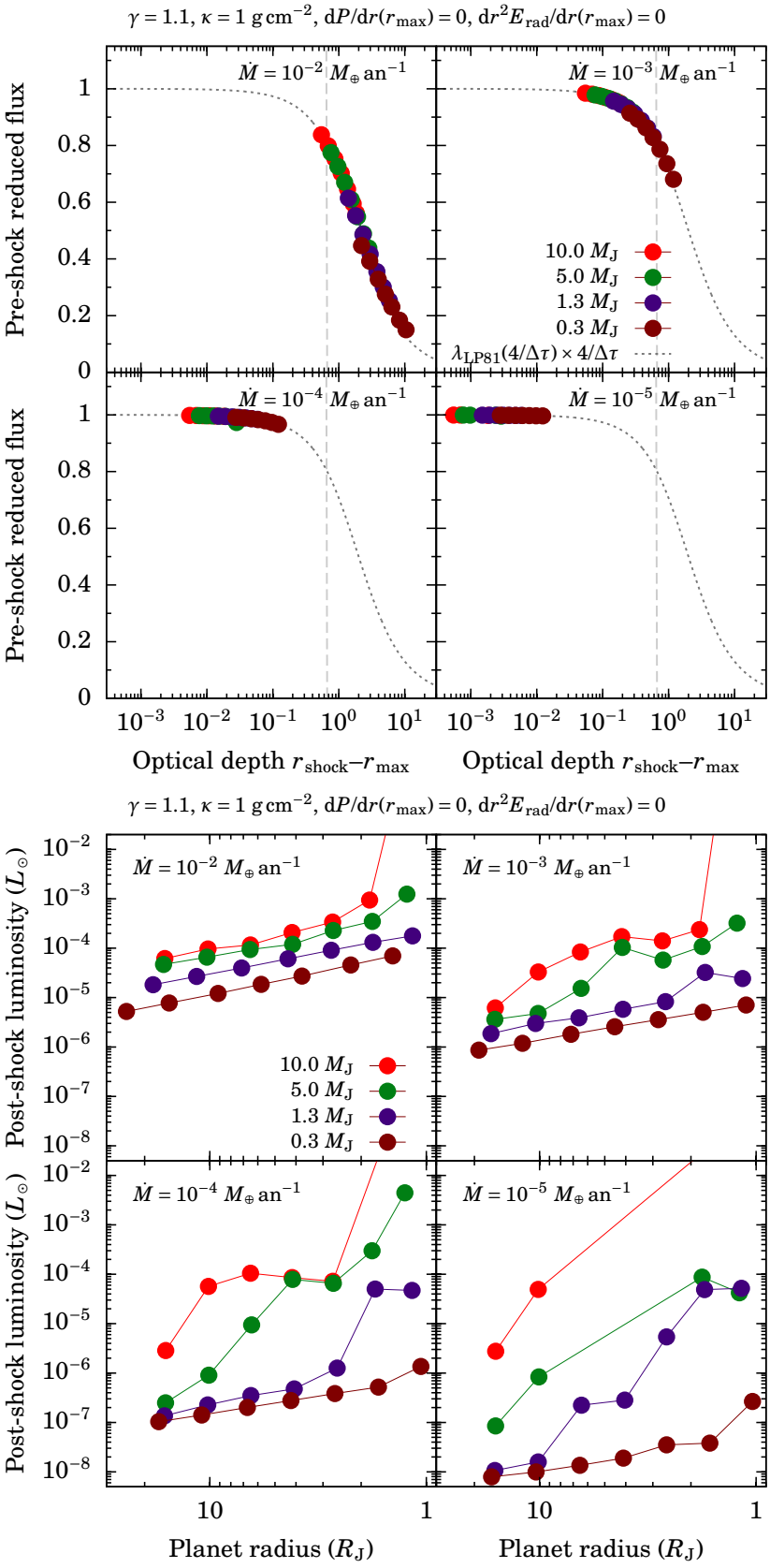

Fig. 2.11.: *(Continued from Figure 2.10.) Top panel:* Reduced flux upstream of the shock against the optical depth to $r_{\max}$, compared to Equation (2.16a) with the flux limiter used in this work (*dashed line*). The $\Delta\tau = 2/3$ location marking the photosphere is highlighted (*vertical dashed line*). *Bottom panel:* Post-shock (i.e., downstream) luminosity.

of the shock to Equation (1.11). Since most upstream regions are in the free-streaming regime, small temperature fluctuations are amplified into larger flux variations. For this reason, we average the efficiency over several measurements and display the standard deviation as an errorbar. Some simulations were quite unstable and have large root-mean square values (around ten percentage points), which is possibly due to resolution effects. Since this affects only a small number of cases, it was not studied further. Most simulations, however, are quite stable and show fluctuations of order three percentage points, with several much smaller than one percentage point, with a trend to more stability at lower $\dot{M}$. All simulations agree within their errorbars with the theoretical prediction.

The Mach numbers range from $\mathcal{M} \approx 5$ to 50, with the lowest values at the highest accretion rates as expected from the temperature scaling and $c_s \propto \sqrt{T}$. This means that, overall, 99.9 per cent or more of the kinetic energy is radiated away, with only a small part kept as internal heat by the gas.

This heating by the shock, $Q^+_{\text{shock}} = (1 - \eta^{\text{kin}})L_{\text{acc}}$, is shown in the bottom panel. It is an insignificant $Q^+_{\text{shock}} \approx 10^{-13}\ L_\odot$, going up to only $10^{-6}\ L_\odot$ at the highest accretion rate $\dot{M} = 10^{-2}\ M_\oplus\,\text{an}^{-1}$, with approximately $Q^+_{\text{shock}} \propto \dot{M}^{3/2}$ as expected. (Note that Q^+_{shock} was again derived from the measured Mach number and the expression for energy conservation in Equation (1.11) because the deviation of η^{kin} from 100 per cent is extremely small.) Thus the gas only brings its internal energy through the shock and into the planet.

2.5.4. Results for a large parameter space and tabulated opacities

Figure 2.13 displays the shock temperature for the same points from the grid as above. The shock temperature increases with increasing mass, increasing accretion rate, and decreasing radius, and is again close to its expected minimum value (Equation 1.18). There are more deviations from the theory, especially at low accretion rates. These seem to be due for some simulations to the extremely steep temperature derivative of the opacity in the dust destruction region in BL94, which leads to orders-of-magnitude jumps in temperature over a few grid cells, or also to the relatively large contrast in opacity from up- to downstream, even when the transition is resolved numerically. Usually, at low accretion rates, the pre-shock luminosity is a large fraction of the downstream luminosity since the shock contribution is small.

The upstream reduced flux (shown in Figure B.3 for completeness) is always greater than v/c, so that we are in the same physical regime as in the previous sections, static diffusion (Mihalas & Mihalas, 1984).

The post-shock pressure is equal to the ram pressure, augmented by a small amount which reflects the numerical thickness of the shock and the choice of the post-shock cell as discussed above, leading to an offset of a few grid cells, which represents 0.001–0.1 R_J depending on r_{min}, M_p, and the shock location. Those simulations which show a large deviation from the trend are those with non-converged structures.

The lowest Mach numbers reached are for the largest planets with the smallest mass accreting at the largest rate. Out to a radius of $\approx 20\ R_J$, this is $\mathcal{M} \approx 4$, so that again approximately the whole $L_{\text{acc, max}}$ is radiated away at the shock. The effective shock heating, as in the constant-opacity case, is therefore negligible. It thus appears to be a robust conclusion that over the range of formation parameters we considered and which covers a large part of the relevant parameter space, the shock is efficient in converting kinetic energy to radiation.

2.6. Estimate of the coupling

Self-consistent and exact coupling of our results with formation calculations will require the use of η^{kin}, P_{downstr}, and T_{shock} as provided by our simulations. Before doing so, however, one can simply compare these values to the ones from formation tracks to assess how much of an influence this could have. Since we find that, over the range of parameters considered (valid, roughly, for

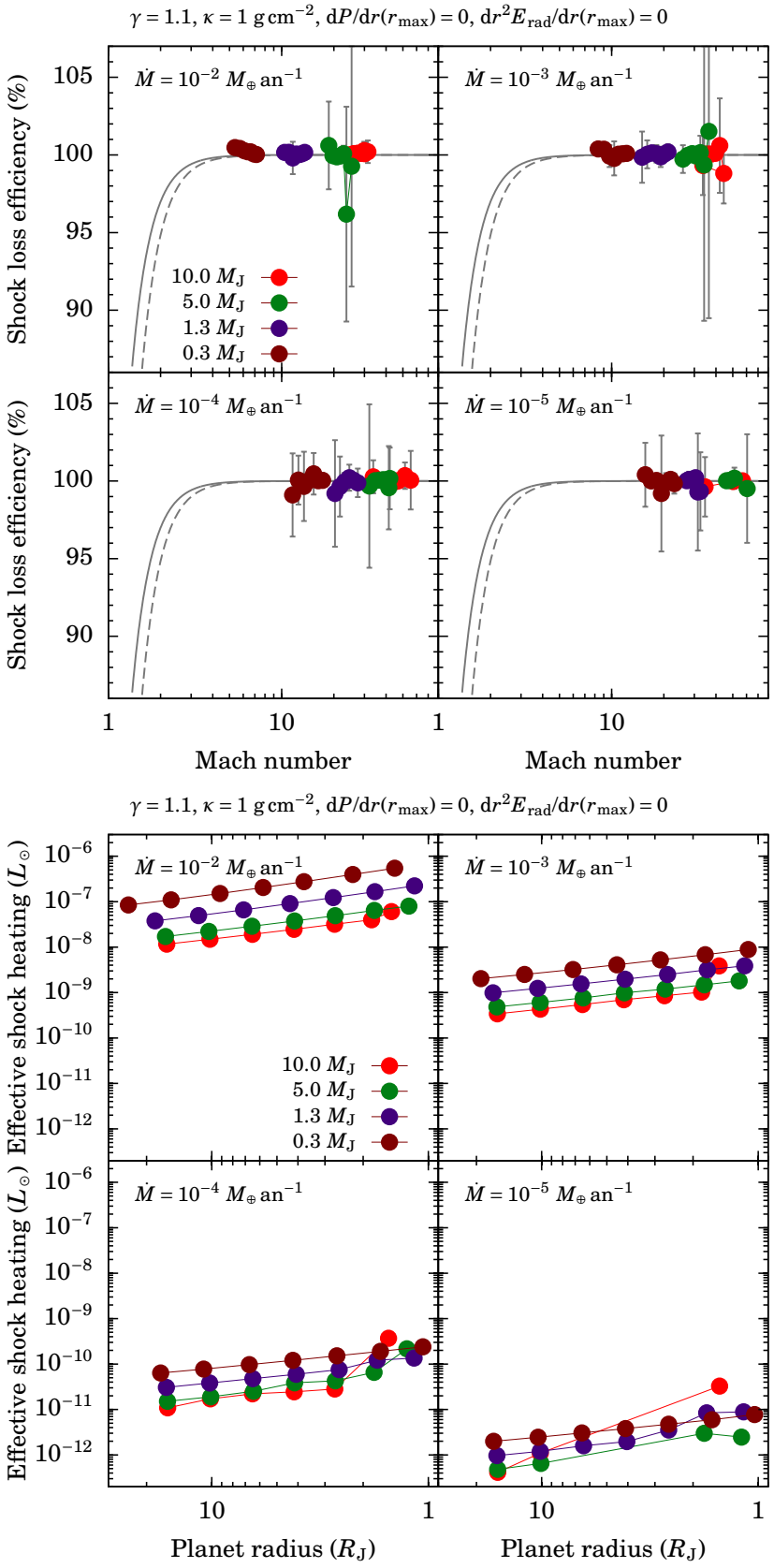

Fig. 2.12.: *(Continued from Figure 2.11.) Top panel:* Kinetic loss efficiency η^{kin} against Mach number. Each point is a time average, with a standard deviation given by the errorbars. Notice the small range of the vertical axis. *Bottom panel:* Effective heating from the shock $Q^+_{\mathrm{shock}} = (1 - \eta^{\mathrm{kin}})L_{\mathrm{acc}}$, i.e., what is not lost as radiation, using the measured $\mathcal{M}$ and Equation (1.11).

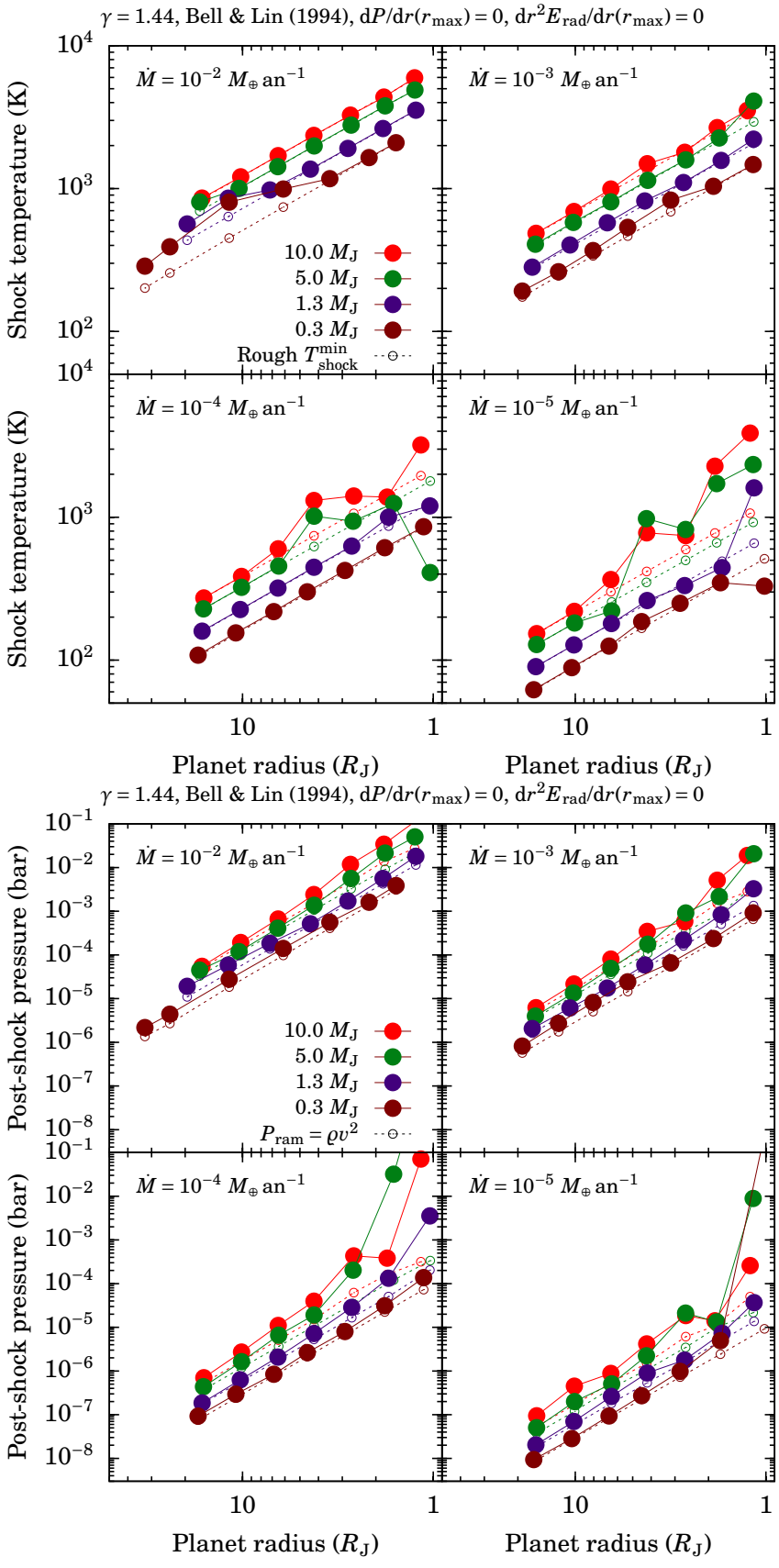

Fig. 2.13.: As in Figure 2.10 but for the BL94 opacities and with $\gamma = 1.44$.

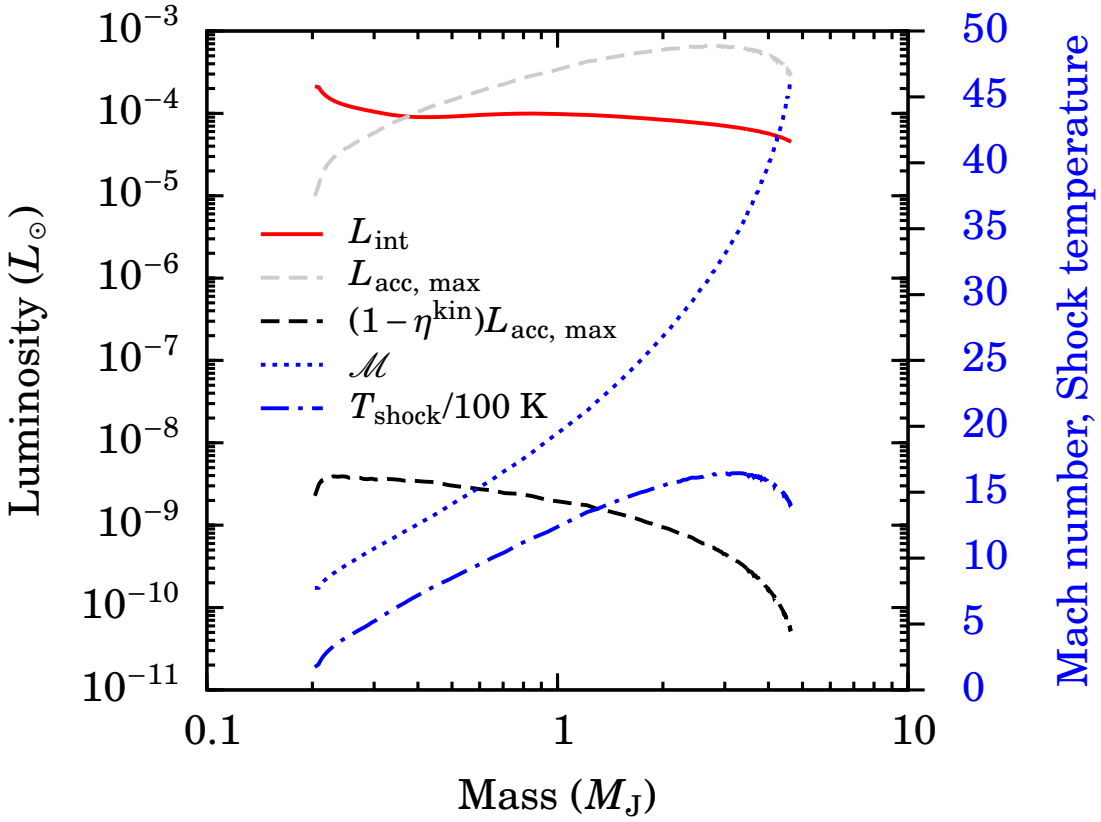

Fig. 2.14.: Approximate comparison of the luminosity brought into the planet through the shock with the interior one for a planet with a final mass of 5 M_J migrating. The luminosity does not depend on γ but does on μ. The raw tracks (mass, radius, accretion rate, intrinsic luminosity as a function of time) were provided by Ch. Mordasini. For the temperature and Mach number, $\gamma = 1.1$, and $\mu = 2.353$.

$R_p \lesssim 20\ R_J$), the shock efficiency $\eta^{kin} \approx 100$ per cent, we use the cold-accretion (cold-start) formation tracks as the basis for our estimates.

First we look at a single planet taken from a population synthesis. Figure 2.14 compares the shock heating $Q^+_{shock} = (1-\eta^{kin})L_{acc}$ with the interior luminosity of the cold-accretion, 5-M_J planet whose evolution is shown in Figure 2.3. The tracks are displayed starting from the detached phase, when the local disc cannot provide gas anymore at the rate at which the planet is contracting and the radius shrinks significantly below the Hill sphere radius, and ending once the complete mass is assembled. The planet migrates in the disc and experiences a time-varying accretion rate but, from 0.2 M_J onward, $\dot{M}$ is slowly decreasing from $\dot{M} = 10^{-3}$ to $10^{-4}\ M_\oplus\,\mathrm{an}^{-1}$. Estimating the shock temperature with Equation (1.18), we find that it is a few 100 K at small masses (early times), increases with time to 1700 K when the planet has reached $\approx 3\ M_J$, and decreases slightly afterward.

The estimated Mach number reaches almost 50 and does not drop below $\mathcal{M} \approx 7$, and taking the effective temperature of the planet into account only lowers the mininum Mach number to 5. Therefore, over the whole accretion history, the interior luminosity is at least four orders of magnitude larger than the part of the kinetic energy which was not lost as radiation. Thus, this is very securely cold accretion and the assumption $\eta^{kin} = 1$ turns out to be very well justified.

Figure 2.15 shows the same luminosity comparison as in Figure 2.14 for the whole population synthesis. (Explicit temperatures and Mach numbers are displayed in Figure B.7.) We find similar results as for the single-planet example, namely that for no planet is $1-\eta^{kin}$ important, so that we do not expect the shock heating Q^+_{shock} to play a direct role, at least for planets where L_p is negligible compared to $L_{acc,\ max}$ (see also the discussion of this point in the next section). As Figure B.7 shows, This conclusion is not sensitive to the value of μ used to estimate the shock temperature.

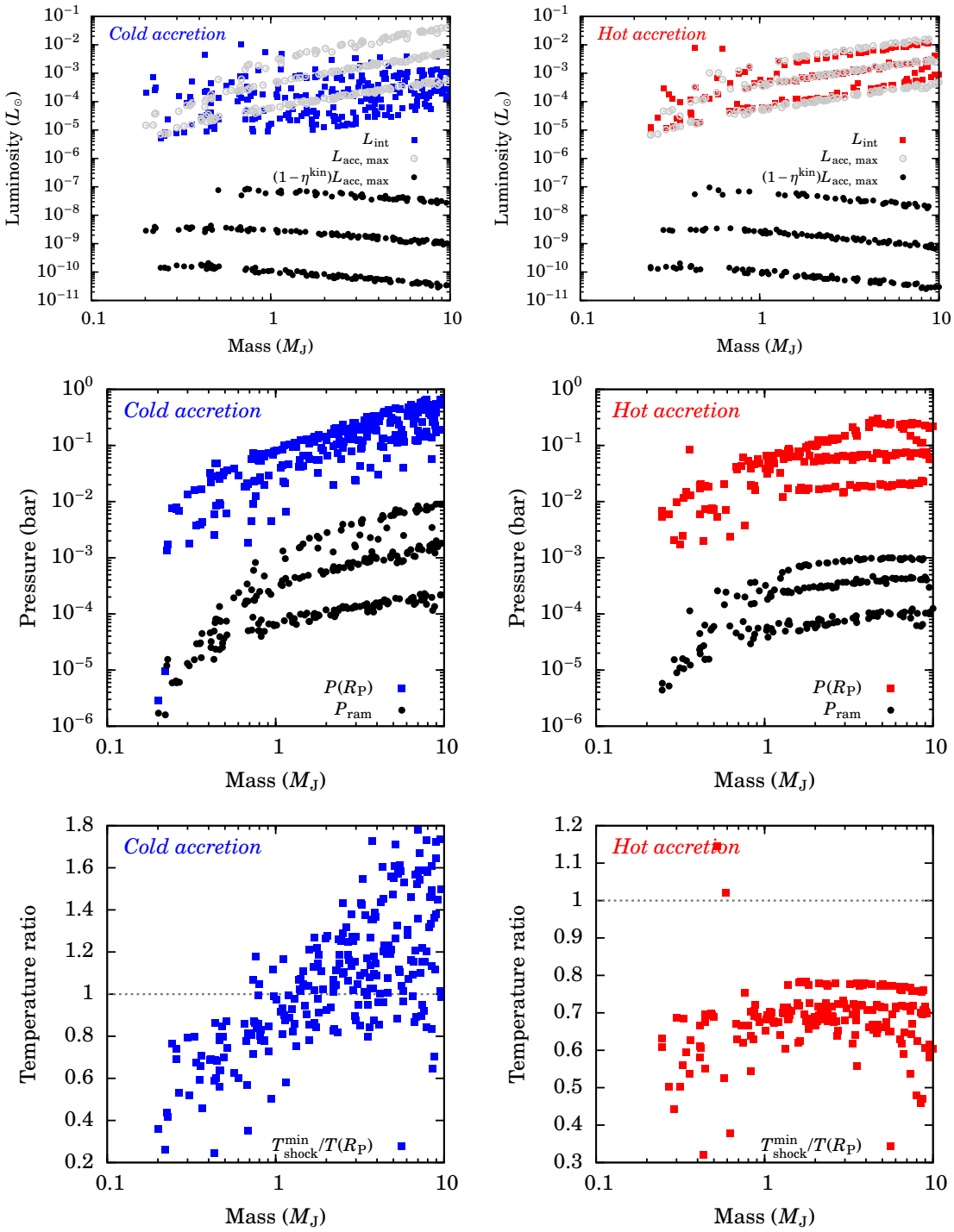

Fig. 2.15.: Approximate comparison of the shock effects on cold-accretion (*left column*) and hot-accretion (*right column*) population synthesis planets (data as in Mordasini et al., 2012; provided by Ch. Mordasini). Three accretion rates ($\dot{M} \approx 10^{-4}$ to $\approx 10^{-2}$ $M_\oplus\,{\rm an}^{-1}$; *clusters of points from bottom to top*) are selected as in Figures 2.4 and 2.5. Here also, for the temperature and Mach number estimates, $\gamma = 1.1$, and $\mu = 2.353$. *Top row*: Luminosity brought into the planet through the shock compared to the interior one. For cold accretion, there is a larger range of interior luminosities at a given $\dot{M}$, whereas $L_{\rm acc,\,max}$ dominates for the hot accretion. *Middle row*: Ram pressure and actual pressure in cold-start (*left*) and hot-start (*right*) population synthesis for $\dot{M} \approx 10^{-4}$ to 10^{-2} $M_\oplus\,{\rm an}^{-1}$ (*groups of points from bottom to top*). *Bottom row*: Ratio of the estimated pre-shock temperature (Equation 1.18) to the actual temperature in the same formation calculations. For the mininum shock-temperature estimate, $\gamma = 1.1$.

We next turn to the post-shock pressure and temperature. The pressure is estimated with the ram pressure $P_{\mathrm{ram}} = \varrho v^2$, where v is the pre-shock velocity, and the shock temperature as usual by Equation (1.18), which actually provides only a lower bound. We find that P_{ram} is always much smaller than the photospheric pressure, as mentioned in Mordasini et al. (2012). If the temperature structure and thus opacity at the photosphere were to remain the same, this would mean that the shock happens well above the photosphere.

The bottom row of Figure 2.15 compares the obtained shock temperatures to the effective temperatures of the population synthesis planets. For most cold-start planets, the shock temperature is larger than T_{eff}, but only up to a factor of two, with also a significant group for which $T_{\mathrm{shock}} < T_{\mathrm{eff}}$, down to a factor near 0.2. In the hot-start case, as expected, the shock temperature is very similar to the effective temperatures, with $T_{\mathrm{shock}} \approx 0.3$–$0.8 T_{\mathrm{eff}}$. This will have to be studied further but our results seem to indicate that the shock is heating the atmosphere not through an inward radiative flux (Q^+_{shock}) but by making the pre-shock gas hot: the shock being isothermal, this internal energy is brought into the planet, effectively heating it.

2.7. Discussion

As shown in Section 2.4.1, the parameter space of planet formation is large and practical considerations (runtime of the simulations) have forced us to restrict ourselves to a subset. We offer a few comments on these restrictions:

Neglect of the interior luminosity We have explicitly focussed on cases where the luminosity coming from the deep interior of the planet L_{p} is negligible compared to the luminosity coming from the shock, $L_{\mathrm{acc}} = \eta^{\mathrm{kin}} L_{\mathrm{acc,\,max}} \approx L_{\mathrm{acc,\,max}} = GM_{\mathrm{p}}\dot{M}/R_{\mathrm{p}}$. As shown in Figure 2.4, this approximation is appropriate for the highest accretion rates and towards higher masses, and less so for the early phases of detached runaway accretion.

In cases where L_{downstr} (an effective L_{p}) was not negligible, the shock temperature was higher than given by the simple estimate (Equation 1.18). Thus taking L_{p} into account should raise the temperature, thereby lowering the Mach number and leading to a lower η^{kin} value. We can try to estimate how important this effect can be: The smallest Mach number we found for realistic opacities was around $\mathcal{M} \approx 5$ (see Figure 2.12 and also Figure B.7) with temperatures around 500 K. To have a significant shock heating with, e.g., $1 - \eta^{\mathrm{kin}} = 99$ per cent, the Mach number would need to be around 2.7–3.0 (for $\gamma = 1.44$–1.1), i.e., a factor of two smaller. Keeping v_{ff} constant, this would require a temperature at the shock approximately four times higher, or around 2000 K, which seems plausible given the hot- and cold-start T_{eff} in the currently available (non-coupled) population syntheses.

A priori, the reduction in the Mach number could be weaker because of two effects: (i) The higher temperature could lead to a more pronounced upstream pressure gradient and therefore to a slow-down of the gas, thereby diminishing $\mathcal{M}$. (ii) Secondly, the shock expansion speed v_{front} is related to the compression ratio, which itself is a function of the Mach number, and thus could become more important at lower Mach numbers. However, both effects are probably small.

Note that should the efficiencies at early times turn out to be much smaller than 100 per cent, one could imagine a self-amplifying mechanism very similar to that discussed by Mordasini (2013): a low efficiency would lead to hotter material being added to the planet, which would make it larger, thereby reducing the free-fall speed of the material accreted next and thus lowering further the efficiency. Whether this amplication, if it takes place, stops with transition into the '$L_{\mathrm{acc,\,max}}$-dominated regime' will also have to be investigated.

Choice of r_{min} It was realised that, at least in principle, the choice of r_{min} for a given $R_{\mathrm{p}} = r_{\mathrm{shock}}$ can have a certain influence on the temperature at the shock. This occurs through the luminosity structure, determined in part by the amount of mass that has been accreted below

$r_{\rm shock}$, which is greater for lower $r_{\rm min}$. We look at the size of this effect in Section B.4 for one example and find that it is modest; however, it will be necessary to explore this more systematically to assess the influence of $r_{\rm min}$ on the shock temperature and thus efficiency.

We now discuss some of the simplifications made both in our approach but also in the underlying model.

Choice for the radiation transport We have made three main simplifications concerning the radiation transport (RT):

(i) We have used flux-limited diffusion (FLD), for which a flux limiter λ is neeed to solve approximately the RT equation. The flux limiter is essentially a mathematical trick designed to recover the free-streaming and diffusion limits, with no guarantee that the transition behaviour is correctly modeled. How important this is in our work would need to be assessed for instance by using a different functional form for λ.

Because of its diffusion *ansatz*, FLD leads in 3D to unphysical behaviour, in which the radiation field diffuses around an opaque obstacle instead of casting a hard shadow (e.g., Klassen et al., 2014). However, in 1D, the work of Ensman (1994) and Commerçon et al. (2011) show that it yields results comparable to more sophisticated RT schemes.

(ii) Secondly, we have used 1-T RT, which assumes that the radiation field and the gas are always in equilibrium. We study this assumption by considering the 2-T case in the next chapter.

(iii) Finally, we computed frequency-averaged, i.e., grey RT. While Vaytet et al. (2013) show that the detailed shock structure, including the extent of the precursor, depends on the number of frequency groups (i.e., bins), these differences are on lengthscales which are not relevant in the astrophysical context. Indeed, studying the collapse of a cloud core with M1 radiation transfer, a scheme more accurate than FLD, Vaytet et al. (2013) found no significant difference between grey and frequency-dependent RT.

Neglect of convection The assumption of spherical symmetry prevents the development of convective instabilities, which in a 3D situation could transport a significant portion of the energy flux in the downstream region. As a result, the actual temperature gradient we obtain can be larger than the adiabatic one, which leads in some cases to density inversions (see Section B.6). Clearly, this is not realistic and, while it does not influence directly the energy conversion at the shock, this density structure could lead to a different shock temperature, in particular when using temperature- and density-dependent opacities.

However, short of performing computationally expensive 3D simulations, it should be possible to simulate the effects of convection by adding a flux term $\nabla F_{\rm conv}$ to the right-hand side of energy equation (Equation 1.3c), where $F_{\rm conv} \propto (\nabla_{\rm act} - \nabla_{\rm ad})^{3/2}$ when $\nabla_{\rm act} > \nabla_{\rm ad}$ and $F_{\rm conv} = 0$ otherwise (e.g., Hansen & Kawaler, 1994). For numerical stability, it would probably be best to write this flux implicitly by increasing the diffusion coefficient

$$\mathbf{F}_{\rm rad} = -\left(D_{\rm F} + D_{\rm conv}\right) \nabla {E_{\rm rad}}^{n+1}, \tag{2.17a}$$

$${D_{\rm conv}}^{n} \equiv \frac{F_{\rm conv}}{\nabla {E_{\rm rad}}^{n}}. \tag{2.17b}$$

That this is approximate should not matter as convection is very efficienct at cancelling superadiabatic temperature gradients (e.g., Mihalas & Mihalas, 1984).

Equation of state In star formation, the endothermic transition from molecular to atomic hydrogen in a collapsing core is a key process which leads to the formation of the 'second core' (Larson, 1969; Commerçon et al., 2011; Tomida et al., 2013). Here, we assumed a constant equation of state (EOS), and preliminary studies such as displayed in Figure B.6 seem to show that the dependence of the efficiency on γ and μ is weak. Nevertheless, considering

a non-constant EOS (i.e., $\mu = \mu(\varrho, T)$, $\gamma = \gamma(\varrho, T)$) could lead to interesting effects at the shock. We have begun investigating this and will present the results in a dedicated study.

Geometry Finally, the most important simplification is that of a spherically symmetric accretion geometry as in the models of Stevenson (1982); Pollack et al. (1996); Bodenheimer et al. (2000). As for low-mass star formation (Hartmann et al., 1997; Zhou et al., 2014), accretion onto a forming gas giant can be expected to be highly non-spherically symmetric but rather along magnetic field lines ('magnetospheric accretion'), due to interactions with the local disc which are hydrodynamical and magnetic in nature (Lovelace et al., 2011; Ormel et al., 2015; Uribe et al., 2013; Keith & Wardle, 2015). Thus the accretion shock is probably relevant only for a small fraction of the planetary surface, where the accretion column hits the stellar surface.

In the low-mass star case, this fraction f ranges from 0.1 to 10 per cent (Calvet & Gullbring, 1998), and in our 1D model, we would need to increase the accretion rate by a factor $1/f$ = 1000–10 to obtain the corresponding pre-shock densities. This would significantly raise the optical depth $\Delta\tau$ upstream of the shock, which could possibly lead to a non-isothermal shock and, in general, to a different (i.e., lower) shock efficiency.

Moreover, since only a small fraction of the planetary surface is affected by the shock, the rest is free to radiate into space with usual photospheric boundary conditions. Hartmann et al. (1997) found that this consideration made a significant difference on the observational appearance of protostars at the end of formation compared to spherically-symmetric accretion. On the planetary side, Eisner (2015) and Zhu (2015) discuss possible signatures of this accretion (and of the circumplanetary discuss) *during* formation. Given recent first (possible) observations of accretion onto planets (Zhou et al., 2014; Sallum et al., 2015), it would be particularly interesting to look at the influence of the different efficiency on the accretion luminosity, especially in the H α band.

2.8. Summary

We have studied spherically symmetric gas accretion onto a gas giant planet during the detached runaway phase, when the gas falls in free-fall from the accretion radius (of order of the Hill or Bondi radius). We set out primarily to determine the radiative efficiency of the shock defining the planet's surface, i.e., what fraction of the incoming kinetic energy flux, the maximal accretion luminosity $L_{\rm acc,\,max} \approx GM_{\rm p}\dot{M}/R_{\rm p}$, is lost at the shock, being however interested in the complementary fraction as this gets added to the planet. Further quantities of interest are the post-shock temperature and pressure of the gas as these set the boundary conditions for the calculation of the interior structure. To the best of our knowledge the energetics of the shock have not yet been studied in detail as we have, yet are thought to be key in determining the post-formation thermal state of gas giants, with several orders of magnitude of difference in luminosity betwee the two extreme cases.

We have focussed on planets whose accretion luminosity dominates over their internal luminosities and used a constant equation of state. Both constant and tabulated opacities (Bell & Lin, 1994) were considered. Summarising, we find the following:

- Our radiation hydrodynamics simulations confirm, over a large range of Mach numbers, the theoretical expression for the efficiency given by Commerçon et al. (2011, our Equation 1.11).

- Unrealistically high opacity values ($\kappa \sim 10^2$ cm^2 g^{-1}) were needed to cause the luminosity generated at the shock to be completely absorbed in the precursor, ahead of the shock region. For realistic constant or tabulated opacities, all luminosity profiles are qualitatively similar, decreasing by some amount with increasing radius or staying rather constant.

- The effective speed of light of the escaping photons, even for the smallest $f_{\rm red}$ values, is always much larger than the gas flow speed, so that the upstream region is in the 'static diffusion' regime (Mihalas & Mihalas, 1984).
- We found a relation between the reduced flux directly upstream of the shock and the optical depth out to $r_{\rm max}$ (Equation 2.16a). For constant opacities, this is an exact correspondence, as can be shown analytically, whereas in the case of tabulated opacities it provides a lower limit on $f_{\rm red}$ given $\Delta\tau$ or vice versa.
- The shock was observed to always be isothermal, which corresponds in the classical terminology to a supercritical shock (Stahler et al., 1980; Mihalas & Mihalas, 1984).
- This shock temperature at the shock was found to be well approximated by Equation (1.18) since $f_{\rm red}$ is usually not much smaller than 1. This estimate is less accurate for planets whose internal luminosity $L_{\rm p}$ is a significant fraction of their accretion luminosity.
- Most importantly, we find that for most of the formation parameter space, the Mach number at the shock is sufficiently high that very nearly all of the kinetic energy is radiated away at the shock, i.e., $\eta^{\rm kin} \approx 100$ per cent. This shock luminosity, which can be quite large, should be observable, and may even have already been detected for a few objects (Quanz et al., 2015; Sallum et al., 2015).
- The associated shock heating of the planet $Q^{+}_{\rm shock} = (1 - \eta^{\rm kin} L_{\rm acc,\,max})$ was compared to the range of internal luminosities seen in formation calculations. The shock contribution was found to be several orders of magnitude smaller than $L_{\rm p}$, at least for planets up to a moderately large size. Thus the planetary accretion shock appears to lead to cold accretion.
- We also compared the shock temperatures and pressures to the effective temperature and photospheric pressure of modeled planet formation and found that $T_{\rm shock}$ was between a factor 0.2 and 2 of $T_{\rm eff}$, while the post-shock pressure $P_{\rm post}$, quite accurately given by the ram pressure $P_{\rm ram} = \varrho v_{\rm ff}{}^2$, was orders of magnitude smaller than the photospheric pressure.

The next step will be to use these results self-consistently in planet formation calculations by using tabulated values of $\eta^{\rm kin}$, $T_{\rm shock}$, and $P_{\rm post}$ at every step. Interestingly, Mordasini (2013) show the results of formation calculations in which, as a test, the dominant photospheric pressure was dropped, leaving only $P_{\rm ram}$. The resulting planets were a factor of a few brighter than planets calculated with the usual boundary conditions. We expect that this corresponds approximately to our situation, although the difference in temperature at the planet surface—i.e., at the shock—may have a non-negligible effect.

In parallel, we will address the effects of a non-constant equation of state, which may be important if the shock is isothermal, since a jump in density at constant temperature will lead in general to a change in internal energy. We will also extend our analysis to cases where the internal luminosity is not negligible compared to $L_{\rm acc,\,max}$. This should increase the temperature at the shock and thus, at a constant $M_{\rm p}/R_{\rm p} \propto v_{\rm ff}$, lead to lower Mach numbers and thus possibly higher shock heating. Whether this has an influence on the early evolution of gas giants will also be addressed in future work.

'Epsilon' in Greek means small;
that's why we call our children 'my little epsilons'.

— A McGill physics professor

3

Shock calculations with two-temperature radiation transport

3.1. Introduction

The description of radiative shocks as presented in Section 1.1 showed that, in the precursor as well as immediately behind the shock, the radiation temperature $T_{\rm rad} = (E_{\rm rad}/a)^{0.25}$ can be different from the gas temperature $T_{\rm gas}$. To capture this, it is necessary to have non-equilibrium radiation transport by evolving the gas and the radiation temperatures separately. For flux-limited diffusion (FLD), the energy equation (Equation 1.3c) becomes (Mihalas & Mihalas, 1984; Turner & Stone, 2001)

$$\frac{\partial(E_{\rm kin}+E_{\rm int})}{\partial t} + \nabla\left([E_{\rm int}+E_{\rm kin}+P]\,v\right) = -c\kappa_{\rm P}4\pi B + c\kappa_{\rm E}E_{\rm rad} - \varrho v g, \tag{3.1a}$$

$$\frac{\partial E_{\rm rad}}{\partial t} + \nabla F_{\rm rad} = +c\kappa_{\rm P}4\pi B - c\kappa_{\rm E}E_{\rm rad}, \tag{3.1b}$$

where the radiation pressure was omitted since it is negligible here and where $\kappa_{\rm P}$ and $\kappa_{\rm E}$ are, respectively, the Planck and energy mean opacities. They will be assumed to be equal. (See also the derivation in Appendix A.) B is the Planck function and thus assumes the radiation to be thermal. Equations (3.1a) and (3.1b) state that the material (gas or dust) is losing energy at the rate $\kappa_{\rm P}\varrho 4\pi B$ but absorbing photons at the rate $c\kappa_{\rm E}\varrho E_{\rm rad}$, and conversely for the radiation.

In this chapter, we perform shock calculations in the planetary formation context discussed in Chapter 2 but using 2-T radiation transport as this is more accurate. We wish to assess the consequences this has on the pre-shock temperature, which sets the efficiency, and use for this the module, `Belt`, which was written and coupled to `PLUTO` v.4.1 by R. Kuiper and is as presented in Klassen et al. (2014). Since `Belt` has a number differences from `Makemake` beyond the energy equation (e.g., in the choice of the stencil for the flux), these can be considered to be two semi-independent codes. Note also that is uses a slightly updated version of `PLUTO` (4.1 instead of 3.0), although the changes to the hydrodynamics module are small.

Additionally, we look at a slightly different approach to the accretion shock calculation. Instead of focussing only on the top layers of the atmosphere, we simulate the planetary structure down to the rocky core and accrete as much of the envelope as possible. We can then compare the resulting downstream luminosities to the ones from formation calculations.

3.2. Selected cases with tabulated opacities

We consider the same examples as in Section 2.5.2, as listed in Table 2.1 and shown in Figure 2.9. The resulting structures are shown in Figures 3.1–3.3 for both the 1-T code of Chapter 2, `Makemake`, and for `Belt` with 1-T and 2-T radiation transport. The simulations are set up exactly in the same way, with three exceptions: (i) we start only with a free-fall density profile reaching down to $r_{\rm min}$ instead of adding a hydrostatic atmosphere; (ii) it was necessary to halve the CFL number to CFL = 0.4 for the 1-T `C` and `D` cases to avoid code crashes in the early adjustment phase; and (iii) because Bell & Lin (1994) does not provide Planck mean opacities, it was necessary to turn to an alternative data set. The dust contribution to the opacity is provided by Weingartner & Draine (2001) and is modeled to vanish sharply over 200 K around an evaporation temperature given by Pollack et al. (1994). Since the opacities of Malygin et al. (2014) were not available for `Belt` yet, we took the gas opacity of Helling et al. (2000). As pointed out by Malygin et al. (2014), note however that the Helling et al. (2000) Planck opacities are underestimated by up to four orders of magnitude between 3300 K and 10000 K. We take again $\gamma = 1.44$ and $\mu = 2.353$ for all cases.

In all cases, the qualitative features of the results are similar:

- The gas and radiation temperatures are everywhere equal except for a sharp peak in $T_{\rm gas}$ at the shock location, whereas $T_{\rm rad}$ remains smooth. This peak can be very dramatic and represent up to a factor-ten increase in temperature. However, it does not affect the rest of the profile. We note in passing that, as in Vaytet et al. (2013), this is clearly not the real Zel'dovich spike as its physical size should be orders of magnitude smaller, on order of the gas mean free path.

- The velocity and pressure profiles are almost identical between all three models.

- The opacities (and thus resulting optical depths) are within a factor of a few of each other for the different table. The only exception is for Case `C`, where the solution goes through the dust destruction region, and in particular, the minimum of the Bell & Lin (1994) opacities is reached. As discussed above, however, these extremely low values are not realistic.

- The Mach numbers and thus efficiencies are very similar between the 1-T and 2-T runs. Note however that the `Belt` 1-T efficiency was left out for Case `B` because the luminosity profile was actually not converged at the time the desired radius was reached.

Thus both `Makemake` and the newer code `Belt` yield very similar results, despite further differences (in opacity and initial set-up). Most importantly, the 1-T and 2-T shock upstream temperatures (and thus efficiencies) are found to be essentially the same.

3.2.1. Gas–radiation equilibrium

To address the accuracy of the one-temperature approximation is extreme cases, we look at Mach numbers $\mathcal{M} \approx 3$–4 (correcting to the shock frame, which can be important at lower $\mathcal{M}$) with a high constant opacity in Figure 3.4 and with a lower opacity in Figure 3.5. All other parameters (see legend) are the same and standard. We will compare the flow timescale from $r_{\rm max} = 0.9\, R_{\rm acc} \approx 300\, R_{\rm J}$ down to the shock, which is roughly

$$\tau_{\rm flow} = \Delta r / v \sim 200\, R_{\rm J} / 2\ {\rm km\,s^{-1}} \approx 10^7\ {\rm s}, \tag{3.2}$$

to the radiation–gas equilibration time. If the latter is much shorter than the flow time, 1-T and 2-T computations should give the same results, while in the other case the gas and radiation will not be able to come into equilibrium before the gas reaches the downstream region.

To derive the time needed by the gas to equilibrate with the radiation, one assumes that the gas is initially at $T \ll T_{\rm rad0}$, where $T_{\rm rad0}$ is the initial and constant radiation temperature, and that the density does not change temporally, which, in our case, is equivalent to assuming that $\tau_{\rm st.\,st.} \ll \tau_{\rm flow}$

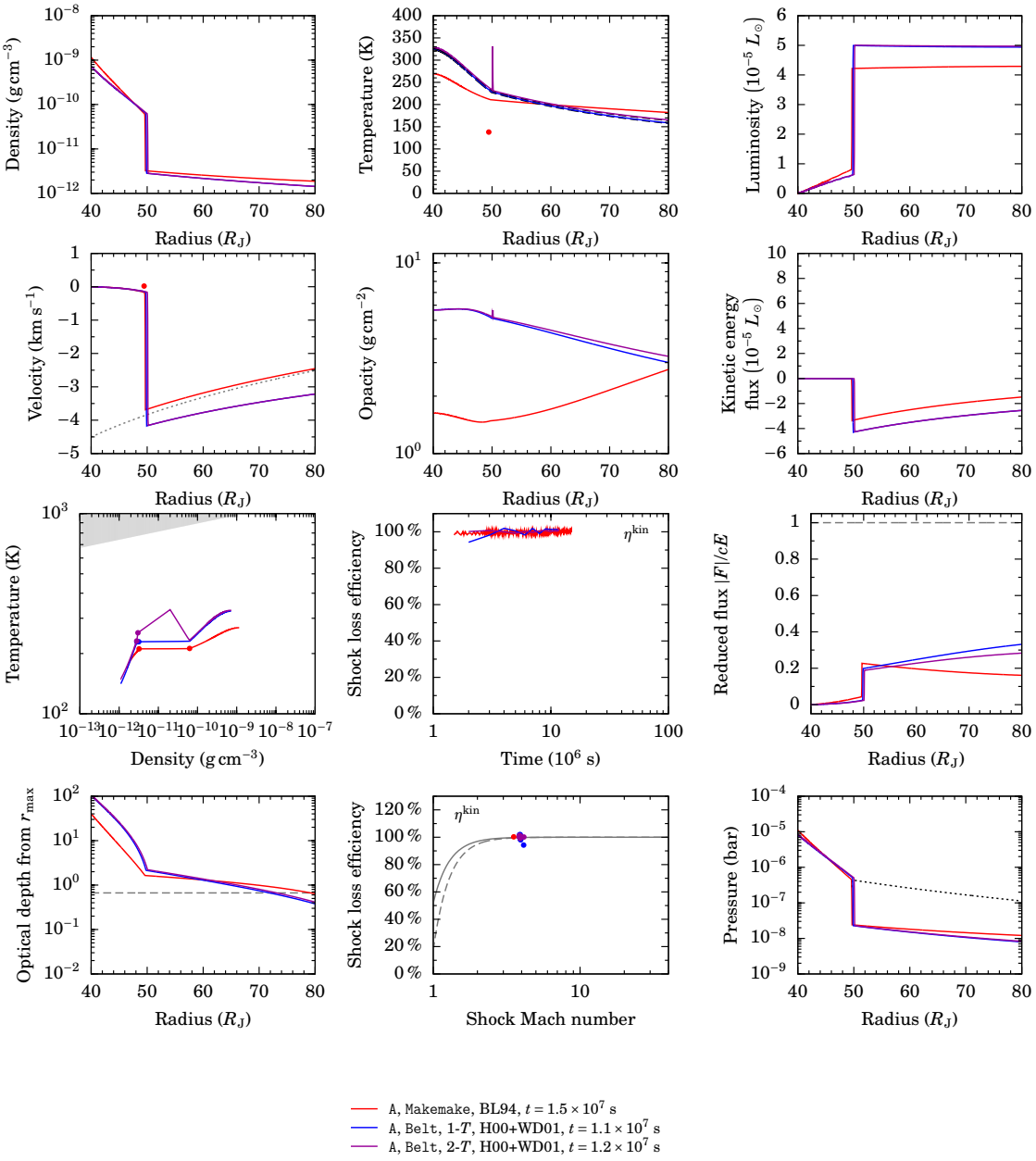

Fig. 3.1.: Comparison between 1-T and 2-T for Case A of Table 2.1, as in Figure 2.9. The curve labeled '`Makemake`' is from that figure (see legend). The shock temperature estimate (Equation 1.18) was left out for the `Belt` results. In the panel of efficiency against Mach number, the different points for a single simulation correspond to different times.

(which is to be checked *a posteriori*). Thus, one writes the energy equation as (see the matter–radiation coupling test of Ramsey & Dullemond, 2015 or equation 7.108 of Drake, 2006)

$$\frac{\mathrm{d}\varrho c_\mathrm{v} T}{\mathrm{d}t} = c\kappa\varrho(E_\mathrm{rad} - aT^4) \overset{!}{\approx} \frac{E_\mathrm{int}(T_\mathrm{eff}) - 0}{\tau_\mathrm{st.\,st.}}, \tag{3.3}$$

uses that $E_\mathrm{rad} \gg aT^4$, and obtains what Drake (2006) calls the steady-state timescale, the time

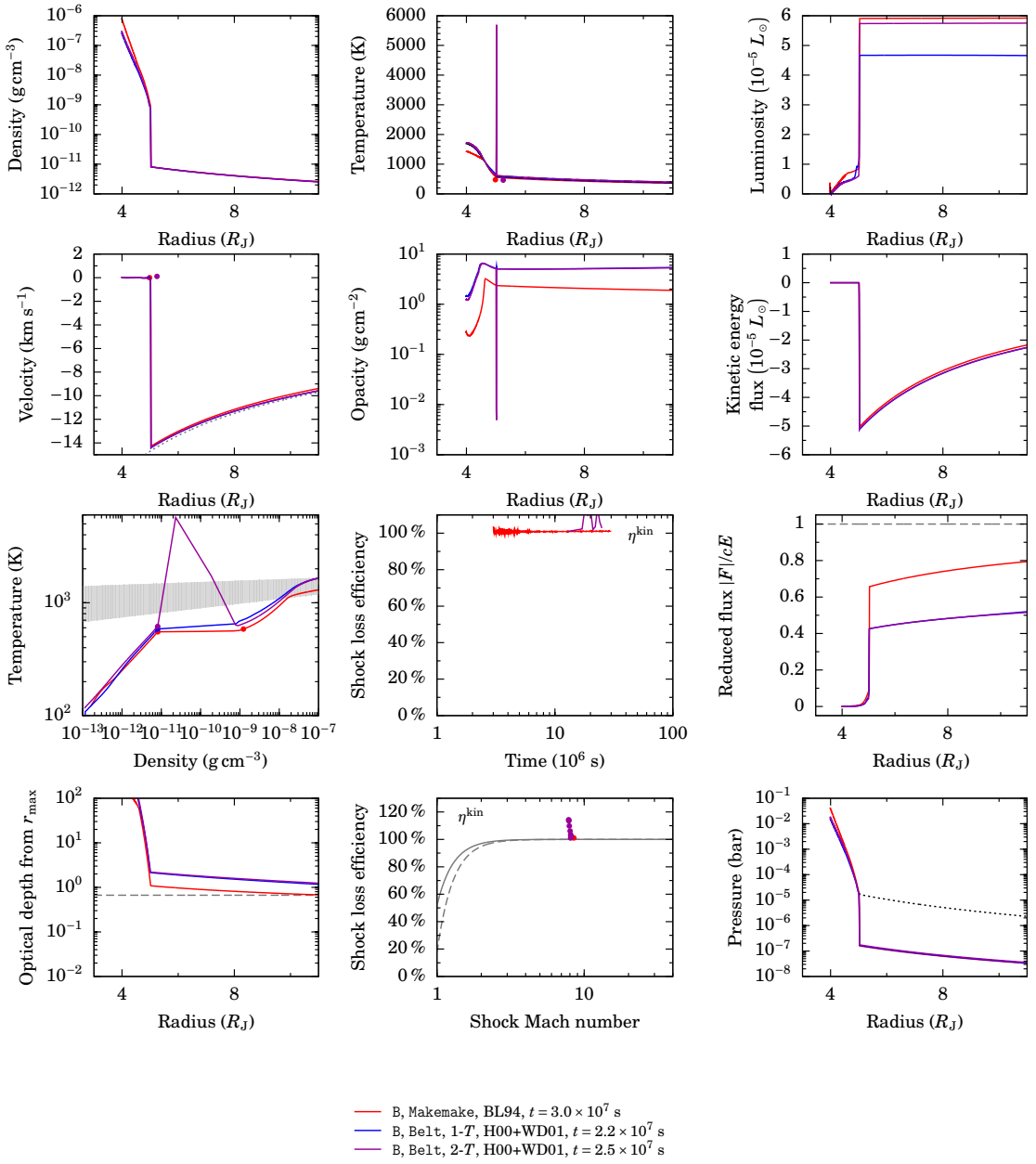

Fig. 3.2.: As in Figure 3.1 but for Case B of Table 2.1.

required for the gas to reach $T = T_{\rm rad0} = T_{\rm eff}$, as

$$\tau_{\rm st.\,st.} = \frac{1}{\kappa\varrho c}\frac{E_{\rm int}(T_{\rm eff})}{E_{\rm rad}(T_{\rm eff})} = \frac{c_{\rm v}}{\kappa c a {T_{\rm eff}}^3}. \tag{3.4}$$

Equation 3.4 differs by a factor $E_{\rm int}/E_{\rm rad} \approx 10^3$ from $1/\kappa\varrho c$, the expression given by Kuiper et al. (2010) for the energy exchange time, based on the *radiation* energy equation.

In Figure 3.4, one thus finds $\tau_{\rm st.\,st.} = c_{\rm v}/(\kappa\sigma {T_{\rm eff}}^3) \sim 0.3 \times 10^6\,(1\ {\rm cm^2\,g^{-1}}/\kappa)$ s for $\gamma = 1.44$, $\mu = 2.353$, and $T_{\rm eff} = 160$ K. Since, for $\kappa = 1\ {\rm cm^2\,g^{-1}}$, we have that $\tau_{\rm st.\,st.} \approx 0.03\tau_{\rm flow}$, the gas should be in equilibrium with the radiation, whereas for lower values of κ (at the same post-shock temperature $T_{\rm eff}$) this is not so certain.

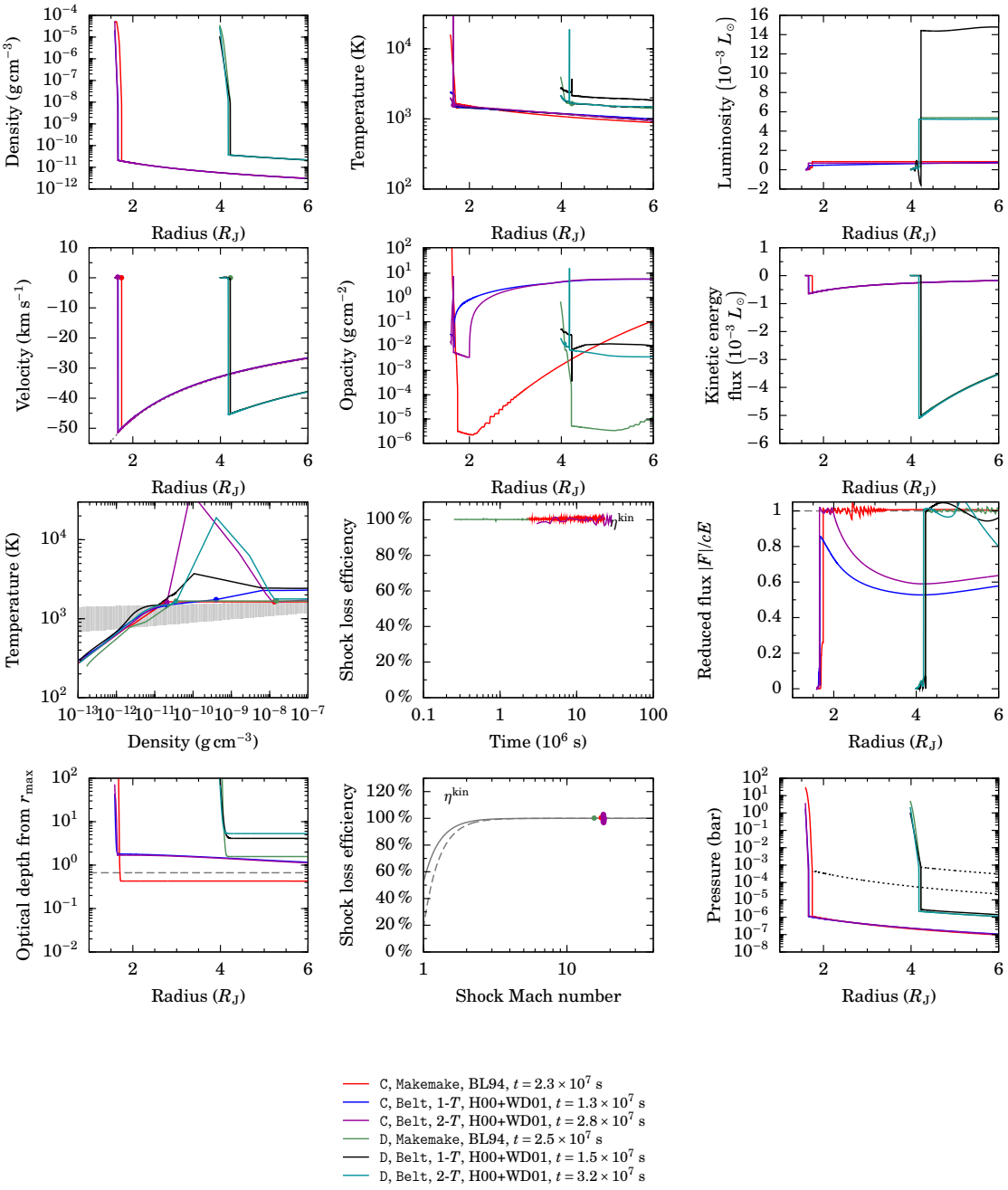

Fig. 3.3.: As in Figure 3.1 but for Cases C and D of Table 2.1. Note that Case C has not quite reached the desired radius yet.

Indeed, in Figure 3.5 we have $\kappa = 10^{-2}$ cm^2 g^{-1} and again $T_{\rm eff} = 150$ K (which actually reflects the radiation Dirichlet boundary condition) with the same flow timescale of $\sim 10^7$ s but a timescale for equilibrium of $10^{7.5}$ s. Thus, gas and radiation should not be in equilibrium, and they are not, which means that the 1-T approach in this case would not be valid. The 1-T (gas) temperature can be seen to match the radiation temperature upstream of the shock and in the downstream cooling region.

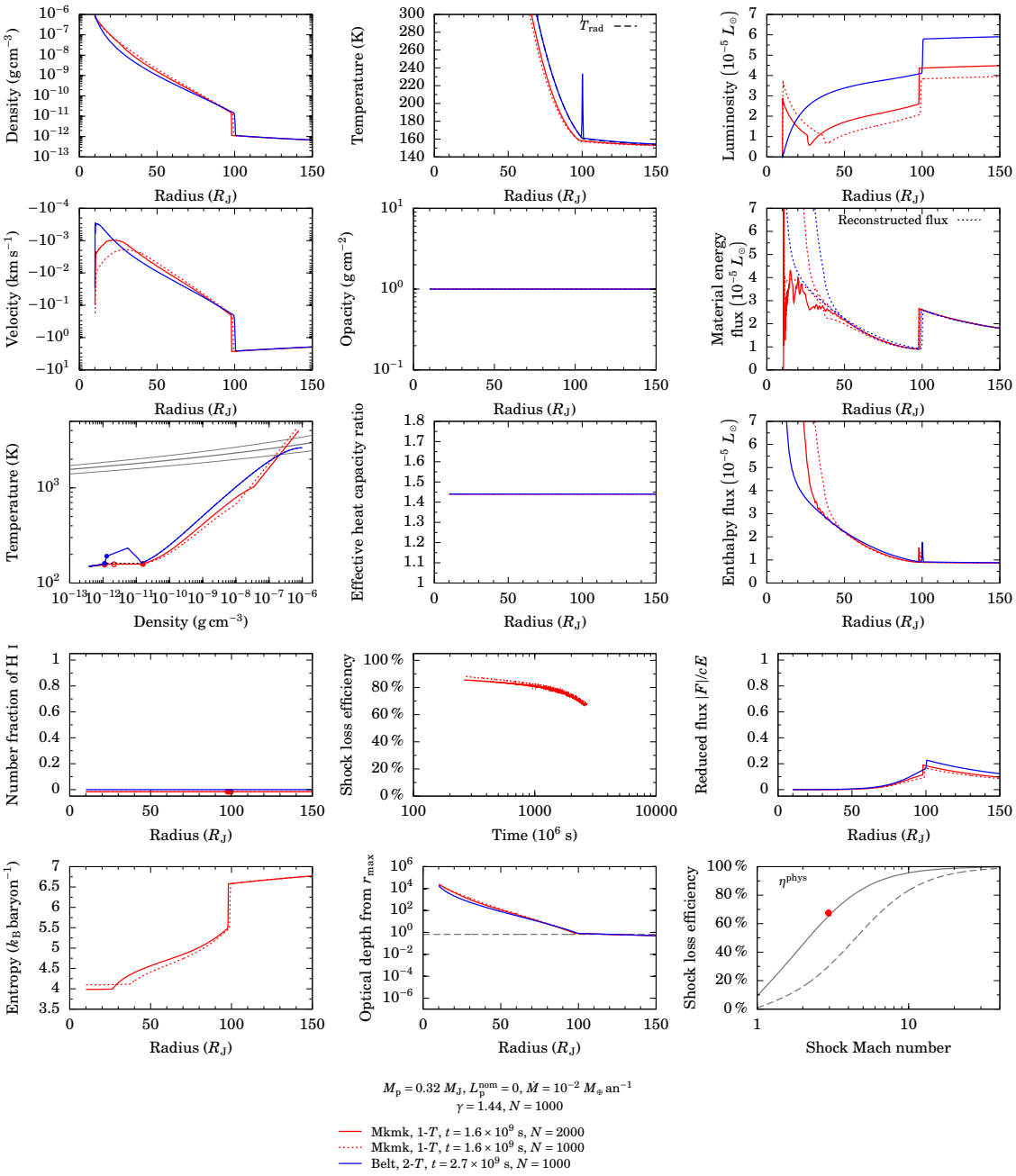

Fig. 3.4.: Comparison between 1-T and 2-T for a high opacity. The shock was not identified in the 2-T case. The Mach numbers and efficiencies are clearly the same (same ΔL), even though the luminosity left of the shock is different for 2-T. Note that the long-dashed curve in the ϱ–T phase diagram shows the radiation temperature and thus belongs to the `Belt` curve.

3.3. Accreting a whole planet

One of the issues we have seen in the previous chapter is that we cannot easily control the luminosity left of the shock. In this section, we try to see what luminosity structure arises if the whole atmosphere is accreted. Specifically, we start with a small-mass, solid core and accrete as much atmosphere as possible, taking values typical for protoplanets at the onset of runaway accretion: $r_{min} = 2\,R_\oplus$ and $M_p = 10\,M_\oplus$, which is thus the core mass. For simplicity, we let the gas fall from

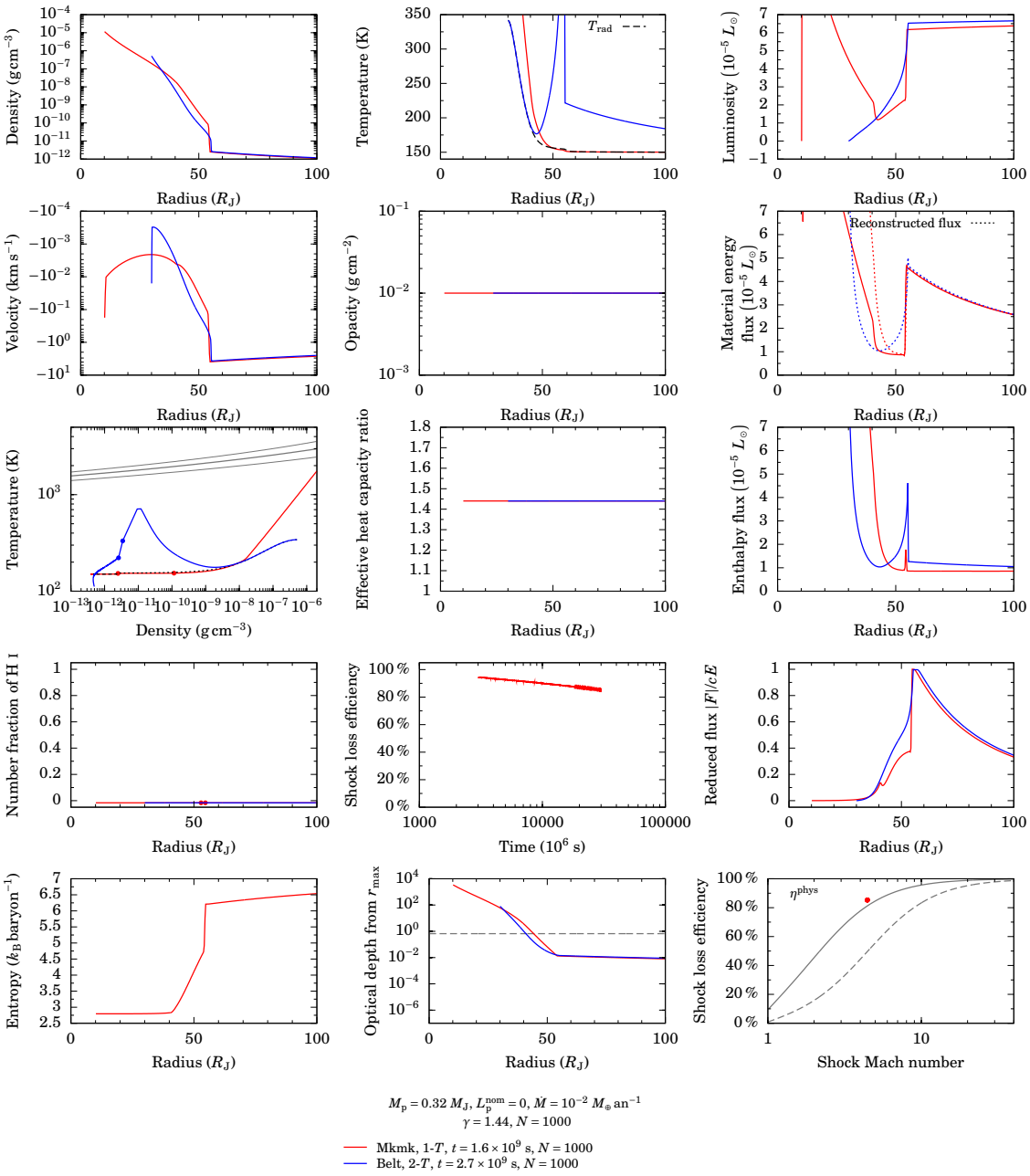

Fig. 3.5.: Same as Figure 3.4 but for $\kappa = 10^{-2}$ cm^2 s^{-1}. Notice in the phase diagram the very clear cooling zone downstream of the shock The 1-T shock moves out at a higher velocity than the 2-T case ($\sim 90\,R_J$ in 1.6×10^9 s vs. in 2.7×10^9 s). in the 2-T case.

120 R_J, which is much larger than actual Hill radius (the planet is still attached in the early runaway phase) but avoids moving the outer edge as a function of time as the Hill radius grows. In the spirit of these simplifications, we take a constant accretion rate $\dot{M} = 10^{-3}$ or even $10^{-2}\,M_\oplus\,an^{-1}$ to speed up the process in wall-clock time.

Since the mass of the atmosphere will eventually dominate, we take into account spherically

symmetric self-gravity[1] by including a potential $\Phi(r)$ given by

$$\Phi(r) = -\int_{r_{\rm min}}^{r_{\rm max}} \frac{G\varrho}{\max(r', r)}\,{\rm d}V', \tag{3.5}$$

where the volume element ${\rm d}V = 4\pi r^2{\rm d}r$, to yield an acceleration $g(r) = -\nabla\Phi(r)$. The effect of the fixed core mass is added as a body force as in the main work.

Two important elements are missing: convection and a stiffer (less compressible) equation of state. Convection would provide an upper limit to the temperature gradient to transport a given amount of energy, thus leading to lower central temperatures if the current gradient were higher. Given that the pressure at a given mass coordinate is set by the mass of the layers above, lowering the temperature would cause the density to be higher and thus the planet more compact.

We compare 1-T and 2-T radiation transport and, to speed up the computation, try cases without self-gravity and cases where Φ is calculated only every 100th step, which is much shorter than the flow time across a cell. We take $N = 500$ and 1000 cells to asses the effect of resolution. It was noticed that the choice of γ does not strongly influence the shock radius although, perhaps surprisingly, lower γ values lead to slightly more compact structures. We consider $\gamma = 1.05$ and 1.44. The dust and gas opacities are from Weingartner & Draine (2001) and Helling et al. (2000), respectively, since Malygin et al. (2014) is not currently available for `Belt` and BL94 do not provide Planck opacities, needed for 2-T radiation transport. As pointed out by Malygin et al. (2014), note however that the Helling et al. (2000) Planck opacities are underestimated by up to four orders of magnitude between 3300 K and 10000 K.

The boundary conditions are as in Chapter 2: at $r_{\rm min}$, reflective in the hydrodynamics and the radiation transport ($P' = \varrho' = v' = E_{\rm rad}{}' = 0$, where $X' = {\rm d}X/{\rm d}r$), and at $r_{\rm max}$, $\varrho = \varrho_{\rm ff}$, $v = v_{\rm ff}$, $P' = 0$, and ${\rm d}r^2E_{\rm rad}/{\rm d}r = 0$. We initialise the domain with $v = 0$ everywhere, a constant gas and radiation temperature $T_{\rm rad} = T_{\rm gas} = T_{\rm neb}$, and a free-fall density profile from infinity. The total mass above the core is negligible. For simplicity, the core mass is kept constant, with the 30-$M_\oplus$ cases providing an estimate of the effects of a core mass increasing in time. The cases are listed in Table 3.1 and the simulations are currently running.

3.3.1. First results

Figure 3.6 shows preliminary results for some cases from Table 3.1. Only the innermost parts of the grid are shown. We can observe the following:

- The temperature spike at the shock in the 2-T cases is resolved and is relatively small ($\Delta T \sim 100$ K at 1500 K) for $\dot{M} = 10^{-2}\ M_\oplus\,{\rm an}^{-1}$ but very pronounced ($\Delta T \sim 4000$ K at 1500 K) for $\dot{M} = 10^{-3}\ M_\oplus\,{\rm an}^{-1}$.
- The velocities follows a free-fall profile, as expected, and show some ringing downstream of the shock.
- All simulations pass through the dust destruction region.
- The reduced fluxes at the shock front are $f_{\rm red} \sim 0.2$, which means that radiation is flowing almost in free streaming. Nevertheless, the optical depths to $r_{\rm max}$ are gigantic, with $\Delta\tau \sim 10^{20}$.
- The luminosity profiles increase somewhat radially and are non-monotonic with radius downstream of the shock. It is not yet clear whether this is a numerical or a physical effect since doubling the resolution changed the flux by 20 per cent upstream (leaving however the gas temperature, velocity, and density unchanged) but did not change the qualitative appearance of the solution.

[1] Included in R. Kuiper's `Belt`.

Name	Core mass	γ	Opacity	$\dot{M}$	Self-gravity	N	RT
`10ME.1T`	10 $M_\oplus$	1.44	Std	10^{-2}	1	500	1-T
`10ME.2T`	10 $M_\oplus$	1.44	Std	10^{-2}	1	500	2-T
`10ME.2T.1k`	10 $M_\oplus$	1.44	Std	10^{-2}	1	1000	2-T
`10ME.2T.gam`	10 $M_\oplus$	1.05	Std	10^{-2}	1	500	2-T
`10ME.2T.SG10`	10 $M_\oplus$	1.44	Std	10^{-2}	10	500	2-T
`10ME.1T.noSG`	10 $M_\oplus$	1.44	Std	10^{-2}	0	1000*	1-T
`10ME.2T.Mdot`	10 $M_\oplus$	1.44	Std	10^{-3}	1	1000	2-T
`30ME.1T`	30 $M_\oplus$	1.44	Std	10^{-2}	1	500	1-T
`30ME.2T`	30 $M_\oplus$	1.44	Std	10^{-2}	1	500	2-T
`30ME.2T.2k`	30 $M_\oplus$	1.44	Std	10^{-2}	1	2000	2-T
`30ME.1T.noSG`	30 $M_\oplus$	1.44	Std	10^{-2}	0	1000*	1-T
`30ME.2T.Mdot`	30 $M_\oplus$	1.44	Std	10^{-3}	1	1000	2-T

Table 3.1.: Small parameter study. The opacity is Weingartner & Draine (2001) with smoothed dust destruction and Helling et al. (2000). The number in the 'Self-gravity' column refers to the how often the potential is computed (see discussion below), in numbers of steps (1: every step). The column 'RT' refers to radiation transport. Number of cells with a star indicate that the simulation is run in parallel. All core radii are 1.9 $R_\oplus$. Recall that $R_\oplus = 0.089 R_\mathrm{J} = 6.38\times^8$ cm and $M_\oplus = 0.0031 M_\mathrm{J} = 5.97 \times 10^{27}$ g.

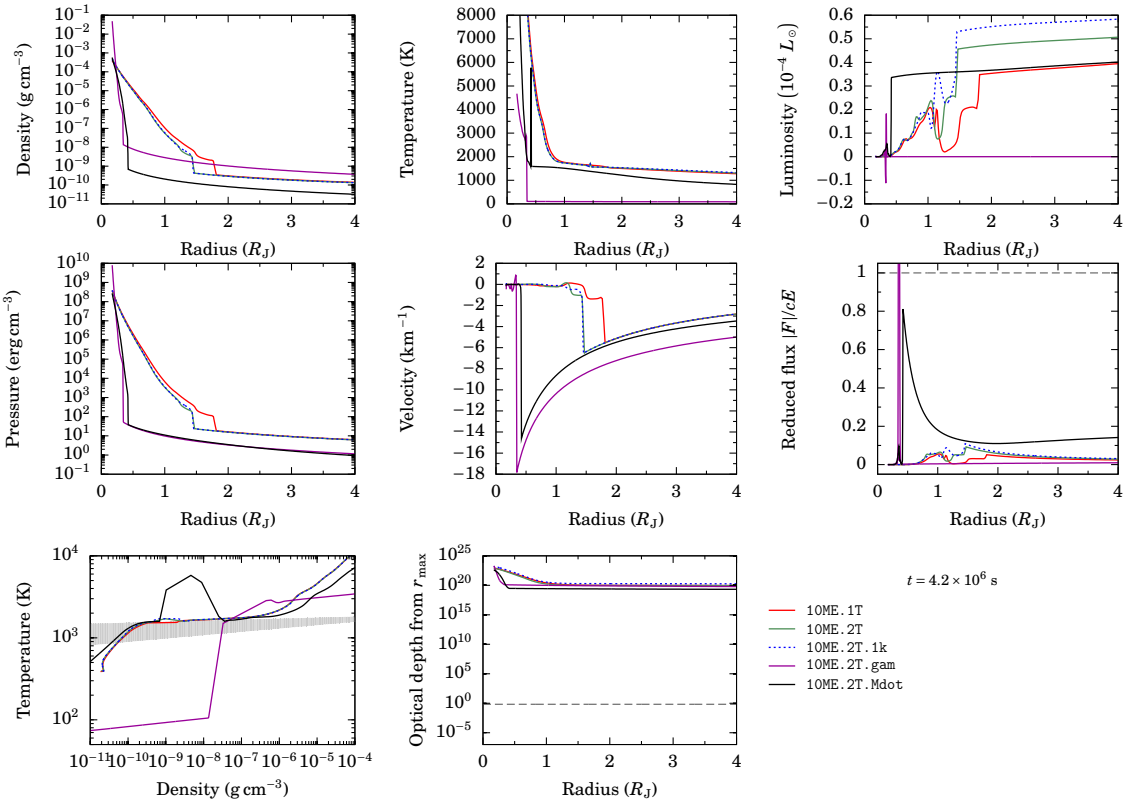

Fig. 3.6.: Same as Figure 3.4 but for five selected cases from Table 3.1. To ease the comparison, they are all measured at 4.2×10^6 s. Notice in the phase diagram the very clear cooling zone downstream of the shock (shock region indicated by points) in the 2-T case.

In 48h of wallclock time, simulation `10ME.2T.SG10` has reached 5×10^8 s and thus accreted a mass of 0.2 $M_\oplus$. Therefore, it seems possible to reach on a reasonable timescale a mass where the

self-gravity could have an effect (compared to the mass of the core if 20 $M_\oplus$), albeit perhaps only at the ten-per cent level.

3.4. Conclusion

To assess how good our approximation that the gas and radiation are perfectly coupled (1-T radiation transport), we have compared for selected representative cases the shock structures and efficiencies obtained with 1-T and 2-T transport. At the same time, we recomputed the 1-T cases from Chapter 2 using a new, semi-independent version of the radiation-hydrodynamics code.

Our main and most important finding is that the 2-T results agree extremely well with the 1-T results and thus that the equilibrium approximation seems justified in the context of the planetary accretion shock. While we found a sharp peak in the gas temperature at the shock for the 2-T case, while the radiation temperature remains smooth, this feature (akin to but not to be identified with the Zel'dovich peak) is of no consequence for the gas temperature down- or upstream of the shock. In particular, we find in that sense isothermal shocks also in 2-T, again justifying our use of Equation (1.11). The small differences seen in the profiles can be confidently mainly attributed to the use of different opacity tables. Thus the shock heating $Q^+_{\rm shock}$, the post-shock temperature, and the post-shock pressure are expected to be independent of the approximation of 1-T radiation transport.

As an exercise, we looked at the valididy of the 1-T approach for a low and for a high constant opacity. The results were as expected theoretically from the comparison of the gas–radiation equilibration timescale and the flow timescale, with the gas and radiation temperatures being equal at high opacity and not otherwise. However, it is important to emphasise that this situation of non-equilibrium was obtained for a contrived example with a low constant opacity which we did not see with realistic opacities.

We observed that in the low-opacity case, there is no clear jump in the radiative flux at the shock when using non-equilibrium (2-T) radiation transport. This contrasts with the 1-T case, and the precise cause would need to be investigated. Incidentally, the absence of a clear jump in the flux means that the shock loss efficiency could not be measured as $\eta^{\rm kin} = \Delta L / L_{\rm acc,\,max}$; rather, use would have to be made of Equation (1.11), which is valid independently of the radiation transport. However, this remains presently a question purely of academic interest.

Two concluding remarks concerning the main part of this chapter are in order. We caution that we have not yet attempted to cover the full extent of the relevant formation parameter space, so that definitive conclusions about the appropriateness of 1-T radiation transport will have to await a more detailed study. Secondly, using a variable equation of state in the 2-T approach might lead to interesting behaviour; dissociation or, more likely given the temperatures attained, ionisation could change markedly the energy budget at the shock since the peak temperature is currently very large. This additional microphysics could possibly lead to efficiencies very different from the constant-EOS value at high Mach numbers, $\eta^{\rm kin} \approx 100$ per cent.

Finally, we also presented first results from accreting a large amount of the atmosphere, starting with a solid core. We found that the resolution may not be high enough to determine the absolute value of the luminosity but that the other quantities (gas temperature, density, velocity) did not depend on the resolution. Once the simulations have had more time to run, it will be interesting to see what luminosity structures develop.

This is the most difficult part of the calculation;
the rest is pure routine and could be entrusted
to even an unskilled computer.

— Kassel, J. Chem. Phys. **1**, 576–585 (1933)

4

Cooling tracks for gas giants using BT-Settl atmospheres

4.1. Introduction

The atmosphere of a gas giant (planet or brown dwarf) is the bottleneck through which the energy flux coming from the deep interior must pass to allow the object to cool. Moreover, the spectral appearance of sub-stellar mass objects is clearly sculpted by the molecular lines and bands, for $T_{\rm eff} \lesssim 4000$ K (Baraffe, 2014), and condensates for $T_{\rm eff} \lesssim 2000$ K, in the photospheric layers of the atmosphere (i.e., where the optical depth to infinity τ at a given wavelength λ is $\tau_\lambda \sim 1$). Therefore, realistic atmospheres are necessary both to compute accurately the cooling of gas giants and to predict their spectra.

Work in this field has a long history, starting with studies of the Solar System gas giants (e.g., Hubbard, 1977; Lunine et al., 1989). Observations of extrasolar and brown dwarfs, starting twenty years ago (e.g., Rebolo et al., 1995; Oppenheimer et al., 1995), revealed chemically complex atmospheres and motivated the development of models with increasing numbers of species (and in particular molecular lines) and an increasing level of detail of the modeled physical processes (amongst others, dust formation, (patchy) cloud formation, vertical mixing leading to non-equilibrium chemistry, and even lightning; e.g., Tsuji et al., 1996; Allard et al., 2001; Ackerman & Marley, 2001; Barman et al., 2011b; Helling et al., 2011; Morley et al., 2014). This in turn has spurned progress in fundamental-physics calculations of atomic and molecular line lists and continua (see Mollière et al., 2015 for an up-to-date compilation). The interested reader is referred to a number of detailed reviews (Allard et al., 1997, 2012; Helling & Casewell, 2014; Baraffe, 2014; Marley & Robinson, 2015) as well as a thorough comparison of the different cloud models in Helling et al. (2008).

There exists a number of sets of cooling tracks, which provide the bolometric luminosity $L_{\rm bol}$, $T_{\rm eff}$, and magnitudes as a function of time for a gas giant of a given mass and assuming a certain state at the beginning of the cooling. The classical works by Burrows et al. (1997), Chabrier et al. (2000b), Baraffe et al. (2003), and Saumon & Marley (2008), which all use detailed atmospheres, are appropriate for the planetary and brown-dwarf regime and publicly available. More recently, Spiegel & Burrows (2012) computed cooling curves which begin with an explicitly-specified entropy available in a range covering the extreme outcomes of planetary formation; it was the first work to do so.

Nevertheless, several reasons motivate us to perform our own coupling between detailed atmospheres and a cooling code:

- First, current population synthesis calculations (e.g., Mordasini et al., 2012) make use of simple boundary conditions (detailed below) to compute the evolution of gas giants of masses

up to $\sim 50\ M_J$. Luminosity predictions (Mordasini et al., in prep.) of population synthesis would therefore gain from coupling to realistic atmospheres, especially in the light of direct-detection surveys (e.g., Beuzit et al., 2006; Vigan et al., 2012; Brandt et al., 2014).

- The widely-used models of Burrows et al. (1997) and Baraffe et al. (2003) assume 'hot starts', i.e., a high initial entropy (see Chapters 2 and 5), and there have been significant developments in atmospheric modeling since these works. The recently-published cooling curves of Baraffe et al. (2015) represent the latest instalment from the Lyon group (Baraffe et al., 2003) but focus explicitly on the stellar and high-mass brown-dwarf regime, since models at lower effective temperature are not ready yet.

- While we use `BT-Settl` because it is a state-of-the-art set of atmospheres, which fare well when used to interpret observations (Bonnefoy et al., 2014; Baraffe, 2014), performing our own coupling also allows us to use any other atmosphere.

We note that a common approach in the literature consists of taking published tracks such as Baraffe et al. (2003) and interpolating the $(\log g, T_{\rm eff})$ pairs as a function of time in the $X = X(\log g, T_{\rm eff})$ mapping provided by another (in particular, more recent) atmospheric model, where $\log g$ is the surface gravity ($g = GM_{\rm p}/{R_{\rm p}}^2$, always using cgs units and base ten) and X here stands for an arbitrary observable (magnitude in some band, luminosity, effective temperature). However, this is not *self-consistent*, in the sense that the same atmosphere model is not used to regulate the cooling and predict the brightness. Moreover, while this *a posteriori* approach does provide a useful estimate, it is possible and conceptually simple to perform an exact coupling.

The remainder of this chapter is structured as follows: Section 4.2 presents the existing code which calculates the cooling, the coupling approach. and an overview of the `BT-Settl` atmospheres. The extracted `BT-Settl`-2010 grid is shown in Section 4.3.1, with the resulting cooling tracks in Section 4.3.2. A brief summary (Section 4.4) closes this chapter.

4.2. Background

4.2.1. Overview of the cooling code

The planetary structure and evolution code, `Rapax 21`, is the $\dot{M} = 0$ limit of the code described in Alibert et al. (2005), Mordasini et al. (2012), and Mollière & Mordasini (2012) and is sketched here. At each timestep t, the radial structure $[T(r),\ P(r),\ m(r),\ L(r)]$ is determined by inward integration of the usual equations of hydrostatic equilibrium (Equations 2.3). The idea is to find by bisection the outer radius, from which the integration begins, which yields the desired total mass, i.e., such that $m = 0$ at $r = 0$. Integrating the $\mathrm{d}T/\mathrm{d}r$ equation requires the luminosity $L_{\rm p}$, assumed spatially constant in the planet (which was verified to be an excellent approximation as discussed in section 3.4 of Mordasini et al., 2012). It is provided in one of two ways: (i) for the first time step, $L_{\rm p}$ is simply the desired initial value, chosen by the user; (ii) for all subsequent steps, $L_{\rm p}$ is determined at each trial radius ${R_{\rm p}}'$ in the root-finding iterations by the corresponding difference in the total energy, the contraction luminosity: $L_{\rm p}({R_{\rm p}}', t) = -[E_{\rm tot}({R_{\rm p}}', t + \Delta t) - E_{\rm tot}(t)]/\Delta t$, where Δt is the size of the timestep between t and the new time, and the total energy $E_{\rm tot}$ is the sum of the gravitational and internal energies: $E_{\rm tot} = E_{\rm grav} + E_{\rm int} = \int \left(e_{\rm int} - \frac{Gm_r}{r}\right) \mathrm{d}m$. Since $E_{\rm tot}$ is not available for the new step since the structure has not yet been determined, it needs to be estimated. The presence of deuterium burning does not change this basic picture and the details are given in Mollière & Mordasini (2012).

The mass outer boundary condition for any trial ${R_{\rm p}}'$ is trivially $M({R_{\rm p}}') = M_{\rm p}$, and the atmosphere model provides the remaining conditions $T({R_{\rm p}}')$ and $P({R_{\rm p}}')$. `Rapax 21` currently uses the simple classical relations provided by the Eddington approximation[1], which yields a photosphere

[1] This assumes, to solve the radiative transfer equation in a plane-parallel atmosphere, that the radiation pressure everywhere is related to the radiation energy density by $P_{\rm rad} = \frac{1}{3}E_{\rm rad}$, which is appropriate both in the diffusion limit and the two-stream approximation; see e.g., Mihalas & Mihalas (1984).

at $T = T_{\rm eff}$ with the photospheric pressure $P_{\rm phot} = 2g/3\kappa$. These simple boundary conditions yield reasonably good results when compared to detailed atmospheres (see Section 5.2.6) and will serve as a comparison to the coupling with the BT-Settl atmospheres.

4.2.2. Description of the coupling

The idea behind the coupling of interior calculations to model atmospheres is simple and consists of matching the adiabatic convective layers of the atmosphere to the convective zone of the planet, as described, e.g., in Chabrier & Baraffe (1997). This connection can be made at a fixed pressure of 10 bar (Saumon et al., 1996), although there is the possibility that the atmosphere not be adiabatic there (Burrows et al., 1997). A safer choice is to take a layer at a high optical depth, $\tau = 30$ or 100 where structures are always convective (Chabrier & Baraffe, 1997). In both cases, the distance to the photospheric radius $R_{\rm p}$ (at $\tau = 2/3$) is less than 1 percent and thus negligible (Chabrier & Baraffe, 1997), and so is the amount of mass contained in the upper layers, as can be easily shown[2].

When information about the interface is shown by atmospheric modelers, it is usually in the form of T_{10}, the temperature at 10 bar on the adiabat, whether the atmosphere is convective there or not (e.g., Saumon et al., 1996; Burrows et al., 1997; Saumon & Marley, 2008; Fortney et al., 2011). The entropy can also directly be shown (Saumon et al., 1994). Ultimately, however, for a given (trial) $g = GM_{\rm p}/{R_{\rm p}}'^2$ and $T_{\rm eff} \propto (L_{\rm p}/{R_{\rm p}}'^2)^{1/4}$, one needs a pressure and temperature point (P, T), which is what we will extract from the BT-Settl structures. Ideally, the atmosphere and the interior model would need to be computed with exactly the same equation of state, in particular, with the same helium mass fraction Y and metals distribution. However, in practice, the latter is usually neglected in the interior equation of state, and small changes in Y are of not consequence; for instance, Baraffe et al. (2015) report that a mismatch in Y of 0.01 yields less than 1 per cent differences in $T_{\rm eff}$ and 0.01 mag for all colours.

4.2.3. Overview of BT-Settl atmospheres

As summarised by Bonnefoy et al. (2013) and Baraffe (2014), the BT-Settl models (Allard et al., 2003, 2012, 2013) use a cloud description which solves for the formation and gravitational settling of dust model and solve frequency-dependent radiative transfer self-consistently in spherical geometry. The cloud model, based on Rossow (1978, see also Mordasini, 2014), compares the timescales for mixing, sedimentation, condensation, coalescence, and coagulation of the dust particles to find the cloud structure, using for the mixing the results of dedicated 2D radiation hydrodynamics simulations (Freytag et al., 2010). The radiative transfer is computed with PHOENIX (Allard et al., 2001, 2003), and iterations are performed on the structure, cloud model, and radiative transport modules until convergence. Different releases of BT-Settl use different elemental abundances: unless noted otherwise, we use the BT-Settl-2010 grid, which took elemental abundances from Asplund et al. (2009), but also compare to the CIFIST grid, which uses the Caffau et al. (2011) abundances.

Atmospheric structures were not directly available and had to be extracted from the log files as available at http://phoenix.ens-lyon.fr/fallard/. (The awk script written for this is reproduced in Section B.7.) A few examples are shown in Figure 4.1a and reveal a complex atmospheric structure where zones dominated by radiative transport alternate with convective layers. Figure 4.1b compares structures from different versions of BT-Settl and shows that, while the upper atmospheric layers differ noticeably (by a few hundred kelvins for $P \lesssim 1$ bar), these differences mostly at levels above the photosphere do not affect significantly the deep adiabat.

[2] Combining Equations (2.3) yields $\mathrm{d}m/\mathrm{d}P = 4\pi r^4/Gm_r$, and using the one-zone estimate of the central pressure $P_{\rm c} \sim {M_{\rm p}}^2/{R_{\rm p}}^4$, this implies that the mass Δm above a (small) pressure ΔP is $\Delta m/M_{\rm p} \sim \Delta P/P_{\rm c}$. Given typical central pressures (see Figure 5.1), this is entirely negligible.

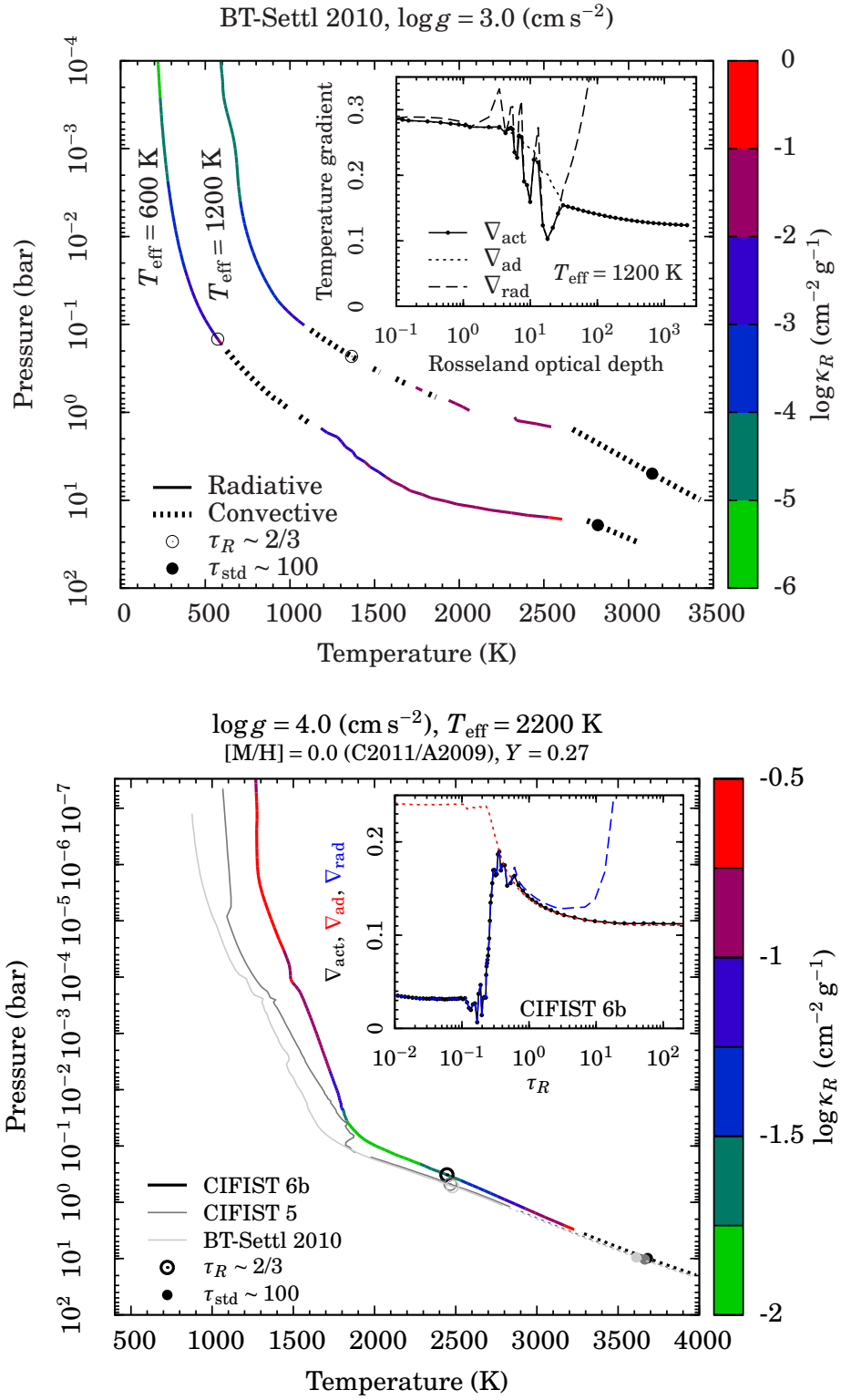

Fig. 4.1.: *Top panel:* Pressure–temperature profiles of `BT-Settl`-2010 (i.e., with Asplund et al. (2009) abundances) for $\log g = 3$ and $T_{\rm eff} = 600$ K and 1200 K. Radiative parts of the structures are shown by full lines and convective parts, in the sense that $F_{\rm conv}/F_{\rm tot} > 0.5$, by dotted segments. Apparent gaps in the profiles are due to a change in the dominant flux transport mode over a single cell. The Rosseland mean opacity in each radiative layer is indicated by the colour of the curve. Indicated are the photosphere $\tau_{\rm R} \sim 2/3$ (where $\tau_{\rm R}$ is the Rosseland optical depth) and the deep layer at $\tau_{\rm std} \sim 100$ used for the coupling (the index stands for 'standard' and refers to 2.15 µm; F. Allard, priv. comm.) (*open and filled circle, respectively*). Compare to figures 2ff of Burrows et al. (1997). Note that the pressure increases downward as is usual when showing atmospheric structures as it corresponds to the physical situation. *Inset:* Actual, adiabatic, and radiative gradients as a function of the Rosseland optical depth for the $T_{\rm eff} = 2000$ K case. *Bottom panel:* Similar but comparing the structure of a $\log g = 4.0$, $T_{\rm eff} = 2200$ K atmosphere for two versions of `BT-Settl`-CIFIST and for `BT-Settl`-2010 (see legend).

4.3. Results

4.3.1. Input from the BT-Settl atmospheres

Figure 4.2a shows the pressure and temperature in the convective zone of the BT-Settl-2010 atmospheres as a function of $\log g$ and $T_{\rm eff}$. The lowest available $T_{\rm eff}$ is 600 K and we show only up to 3000 K since this is the domain relevant for $M_{\rm p} \lesssim 50\ M_{\rm J}$ (see e.g., figure 9 of Burrows et al., 1997). (As it cools, the $T_{\rm eff}$ of a planet drops, while the surface gravity stays roughly constant, increasing (typically by less than 1 dex) slightly as it contracts.) The curves are smooth and mostly monotonic for decreasing $T_{\rm eff}$, and the rough $P \propto g$ scaling (especially around 3000 K) reflects the atmospheric opacities (e.g., Chabrier & Baraffe, 1997). A closer inspection of the figure reveals, however, that the pressure and temperature reincrease with decreasing $T_{\rm eff}$ around 1500 K. This behaviour is more clearly seen in the entropy, shown in the bottom panel. This will have a noticeable effect on the cooling curves and contrasts with the result from simple Eddington boundary conditions.

Figure 4.2b shows the corresponding entropies. As a planet cools, its entropy decreases over time (see e.g., Section 5.2.1), which is why the entropy is shown as the independent variable. As expected, the curves are smooth for $T_{\rm eff} \gtrsim 2000$ K and also for $T \lesssim 1000$ K, but in the intermediate region, especially around $T_{\rm eff} = 1400$–1500 K, the $T_{\rm eff}$ in atmospheric models does not decrease monotonically with entropy but rather is multiple-valued.

This behaviour seems to be due to a cycle of dust condensation (D. Homeier and F. Allard, priv. comm.). If in the course of the iterations the temperature in the atmosphere drops sufficiently, solids start condensing out of the gas phase and thus increase the opacity; this rise in opacity causes the temperature in the atmosphere to reincrease to carry the same flux $\sigma T_{\rm eff}{}^4$, which in turn causes the dust to evaporate. Due to the different mixing and formation timescales, there is a certain amount of hysteresis, and the resulting non-monotonicity may be compounded by the fact that each atmospheric model (i.e., each point in Figure 4.2) is calculated independently.

This feature, which indicates non-perfect convergence of the models, was not noticed before because the atmospheres had not been analysed in this way. Moreover, the common *a posteriori* interpolation of colours using the $(\log g, T_{\rm eff})$ provided by a simpler cooling track (e.g., Baraffe et al., 2003) will not exhibit unusual features if the underlying track is monotonic in $T_{\rm eff}$.

Before proceeding to showing coupled cooling curves, we note that the latest BT-Settl-CIFIST atmospheres, as used for Baraffe et al. (2015) and from D. Homeier (priv. comm., 2015 June 26), have a monotonic $T_{\rm eff}(S)$ but there are steep regions where $T_{\rm eff}$ decreases very quickly for a small S decrement. This behaviour should be, qualitatively, physical, but whether the slope is as steep as predicted remains to be seen. In any case, since this new grid does not cover temperatures lower than ≈ 1500 K, we refrain from using it in its current version.

4.3.2. Cooling tracks with BT-Settl

Figure 4.3 shows hot-start cooling tracks for $M_{\rm p} = 3$, 5, 10, and 15 $M_{\rm J}$. We compare our self-consistent coupling with the results from an Eddington boundary condition as well as to Baraffe et al. (2003), Burrows et al. (1997), and Spiegel & Burrows (2012). Of relevance to direct detections (e.g., Bonnefoy et al., 2014), both the (bolometric) luminosity and the absolute K_s-band magnitude are shown. (The effective temperature as a fuction of time is shown in Figure B.8.) The zero-point for the time is the begin of the cooling, i.e., the end time of the formation, which, in principle, should not be identified directly with the age of an observed system (Fortney et al., 2005).

There are noticeable differences between the BT-Settl-2010 (hereafter simply BT-Settl) and the Eddington (grey) luminosities but these are not systematic and are relatively small. However, the effects of the non-converged atmospheres around $T_{\rm eff} \approx 1300$–1700 K are clearly visible as up-and-down jumps, as the high- or the low-$T_{\rm eff}$ solutions at given neighbouring entropies are chosen by the cooling algorithm. These jumps affect most clearly the 10-$M_{\rm J}$ planet at 3–10 Myr, as well as the 15-$M_{\rm J}$ track at 70–100 Myr after its deuterium-burning 'shoulder'. The effect is also slightly

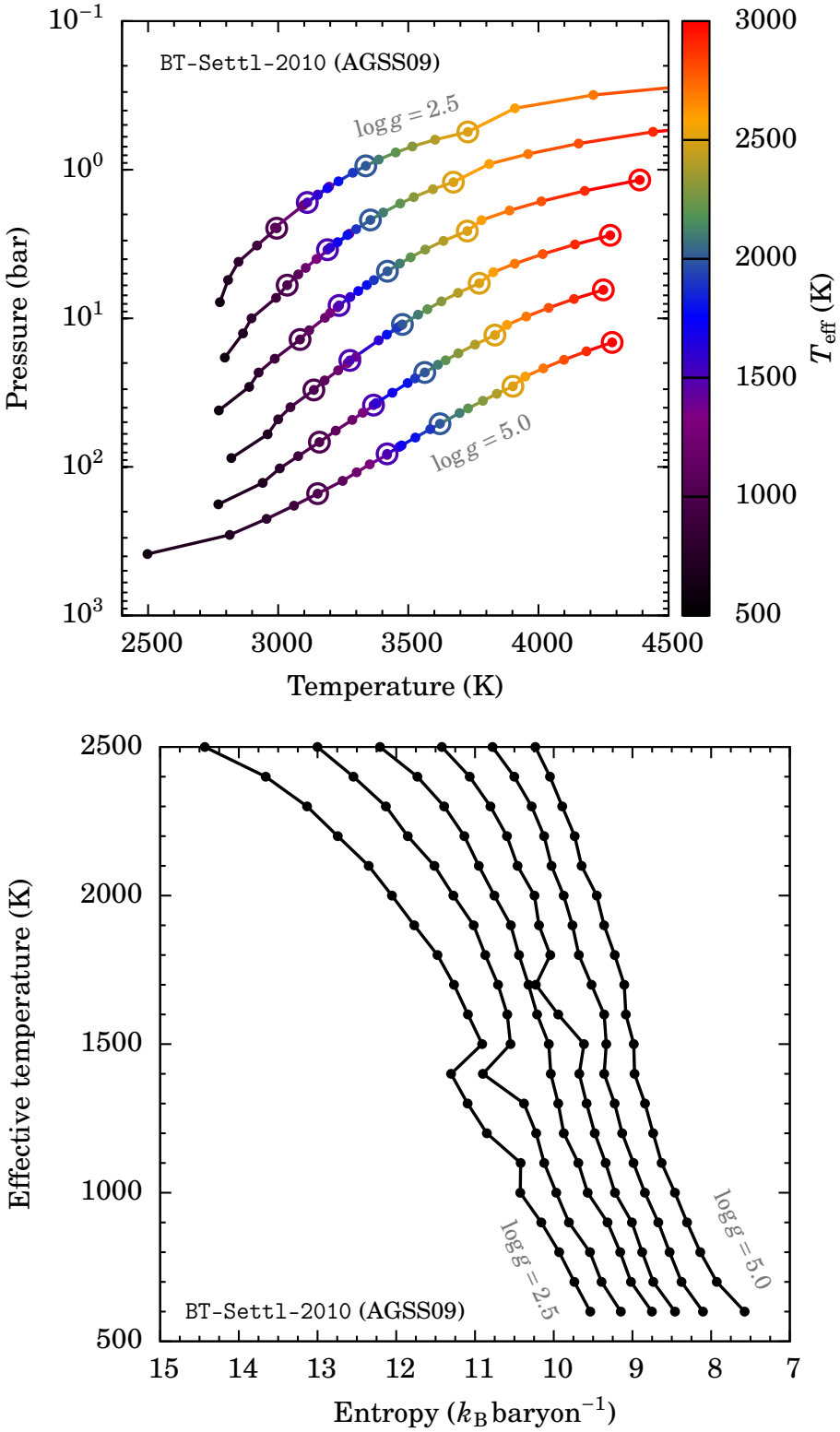

Fig. 4.2.: *Top panel:* Pressure and temperature at $\tau \sim 139$, as used for the coupling, for the `BT-Settl-2010` grid as a function of $\log g$ and $T_{\rm eff}$. Each curve is for models with the same surface gravity, from $\log g = 2.5$ to 5.0 (cm^2 s^{-1}) (*bottom to top*), and each point is a different effective temperature (*colour*), with $T_{\rm eff} = 600$ to 3000 K from left to right but the last points not shown for the smaller $\log g$. Multiples of 500 K are highlighted (*open circles*). Notice the non-monotonicity around 1500 K for low surface gravities. *Bottom panel:* Corresponding $T_{\rm eff}$ as function of the entropy S at the point shown in the left panel, with S decreasing to the right to represent a time evolution. (For reference, the proton spin term (see Section 5.8) is not included.) The curves are, from left to right, for $\log g = 2.5$ to 5.0 in steps of 0.5 dex.

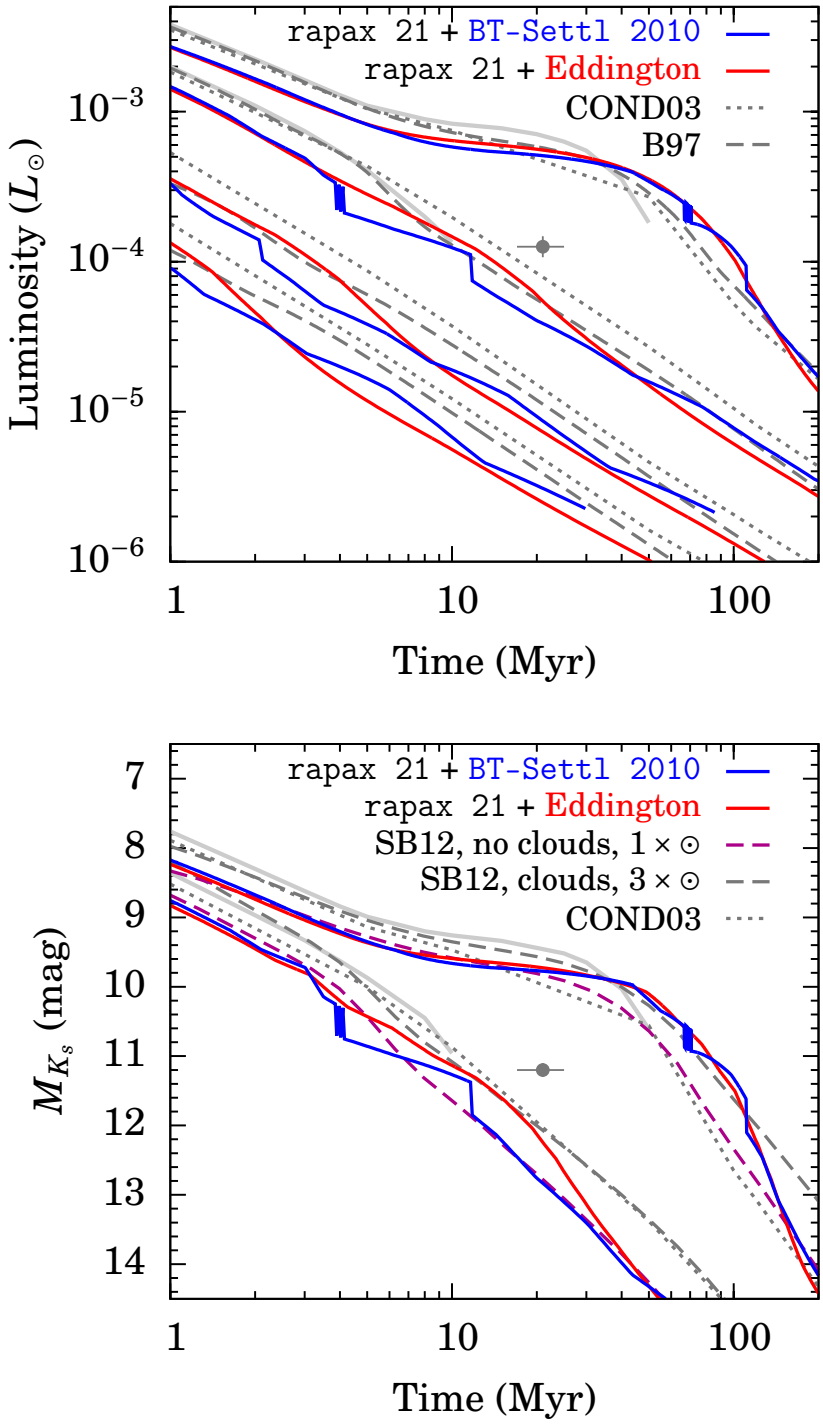

Fig. 4.3.: Hot-start cooling curves in luminosity (*top panel*) and K_s band absolute magnitude (*bottom panel*) for M_p = 3, 5, 10, and 15 M_J. Results for the self-consistent use of the `BT-Settl`-2010 atmospheres (*solid blue curves*; shown only down to the grid edge of T_{eff} = 600 K) are compared to tracks using the Eddington boundary condition (*solid red*), Baraffe et al. (2003) ('COND03'; *dotted grey*), Burrows et al. (1997) (*dashed grey*), and Spiegel & Burrows (2012) (*dashed fuchsia and grey* for, respectively, their cloud-free solar-metallicity and cloudy 3 × solar-metallicity models). The non-labeled, pale grey curves are from `http://perso.ens-lyon.fr/isabelle.baraffe/BHAC15dir/` and are available as cooling tracks only for the highest masses and down to $T_{eff} \approx$ 1600 K (which is more restrictive than what is shown in Baraffe et al., 2015). As an example, β Pic b is shown (*dot with errorbars*; Bonnefoy et al., 2014b).

visible for 3 M_J, though only at a very early time ($\approx$ 2 Myr).

Overall, and despite the unphysical features, our `BT-Settl` tracks agree relatively well with those of Burrows et al. (1997) and Baraffe et al. (2003). Nevertheless, there is both in luminosity and magnitude the non-constant but systematic trend that we predict fainter objects at a given time. In particular, at early times for the highest masses (where all other tracks agree), is lower by roughly 40 per cent. However, at later times, there is a larger spread between the different models, and our systematic offset is comparable to this spread. For instance, at 10 Myr for 5 M_J, our `BT-Settl` curve is a factor of two (0.3 dex) smaller in luminosity compared to Baraffe et al. (2003).

In Figure 4.3, we focus on the tracks of absolute K_s magnitude for 10 and 15 M_J as interpolated as a function of $(\log g, T_{\rm eff})$ in the `BT-Settl`-2010 grid (Ch. Mordasini and M. Bonnefoy, priv. comm.). Interestingly, the difference between Eddington and the `BT-Settl` tracks is negligible at early times even though the effective temperatures and surface gravities differ. We verified that the situation is similar in the J and H bands. Moreover, both 10-M_J tracks join onto the Spiegel & Burrows (2012) cloud-free, solar-metallicity curve at later times, namely $t > 10$ and $\approx$ 40 Myr for the `BT-Settl` and Eddington models, respectively. Given the numerous differences between the atmospheric models (especially the absence of clouds), it is difficult to determine whether this agreement is fortuitous or has a deeper cause.

In any case, we note that the curves for various models differ by up to a magnitude at a given age, which is much larger than typical errorbars. Thus it is useful to work with bolometric magnitudes, especially when they can be constrained empirically as done recently for β Pic b by Morzinski et al. (2015).

4.4. Summary

The choice of outer boundary conditions for the calculation of gas giant cooling curves, which is set by the atmosphere, has measurable consequences on both the cooling rate and the observable spectra and magnitudes. For this reason, and with in mind the on-going direct-detection surveys, the attempted to couple our in-house cooling track code (`Rapax 21`) with the detailed `BT-Settl`-2010 atmospheres. This produced cooling tracks in reasonable agreement with previously published work using both very simple or detailed atmospheres, but revealed unphysical jumps in the cooling tracks that occur at ages relevant to direct observations. This is due to non-converged atmosphere models because of dust condensation for $T_{\rm eff} \approx 1500$ K, leading to a multi-valued relation between $T_{\rm eff}$ and the internal entropy S. Given these issues with the input data, we focussed on hot starts, especially since cold starts only differ by a time offset in the cooling tracks.

The `BT-Settl` models are continuously being updated but the other grids (e.g., `BT-Settl-CIFIST_2011`) have several 'holes' in $(\log g, T_{\rm eff})$ which made it impossible to perform the coupling. Therefore, the production of useful and accurate, self-consistent cooling tracks will have to await the completion of the `BT-Settl` grid with fully converged models.

Wait here for further instructions.

— Sticker on a wall in Berlin

5

Constraining the initial entropy of gas giants

This chapter includes work published in ***Marleau*** *& Cumming, MNRAS* ***437****, 1378–1399 (2014), "Constraining the initial entropy of directly detected exoplanets" (Marleau & Cumming, 2014). Some figure have therefore already been presented in author's Master's thesis (Marleau, 2012), but several results and figures go beyond that. More specifically:*

- *A small part of the text (roughly 20 per cent by page number) containing the key ideas was written originally by A. Cumming but this was thoroughly rewritten and very significantly extended (in terms of content) by the author.*
- *All figures except for Figures 5.4b, 5.6, 5.7, and 5.12 were present in the author's Master's thesis. They have been slightly updated, however, with a handful of data points added to Figure 5.8 and the MCMC simulations (see Sections 5.5.2ff) added to Figures 5.9ff.*
- *A small part of the literature review on the 2M 1207, HR 8799 and β Pic systems was included in the author's Master's thesis, but it was considerably extended (by roughly more than a factor of two by page count) and updated.*

Many sections, representing a sizeable effort, are entirely original work by the author and not present in his Master's thesis: Sections 5.2.3, 5.2.4, 5.2.5, 5.3, 5.4, as well as 5.7 and 5.8.

The second, minor part of this chapter consists of a reevaluation of the companion to β Pic (Section 5.10) as work published subsequently, in Bonnefoy et al. (2014b), and of a similar analysis performed on κ Andromeda b (Section 5.11), published in Bonnefoy et al. (2014a). In both cases, only the author's contribution is included, with the strictly necessary information from the rest of the publications summarised.

Abstract

The post-formation, initial entropy S_i of a gas giant planet is a key witness to its mass-assembly history and a crucial quantity for its early evolution. However, formation models are not yet able to predict reliably S_i, making unjustified the use solely of traditional, 'hot-start' cooling tracks to interpret direct imaging results and calling for an observational determination of initial entropies to guide formation scenarios. Using a grid of models in mass and entropy, we show how to place joint constraints on the mass and initial entropy of an object from its observed luminosity and age. This generalises the usual estimate of only a lower bound on the real mass through hot-start tracks. Moreover, we demonstrate that with mass information, e.g. from dynamical stability analyses or radial velocity, tighter bounds can be set on the initial entropy. We apply this procedure

to 2M1207 b and find that its initial entropy is at least 9.2 k_B/baryon, assuming that it does not burn deuterium. For the planets of the HR 8799 system, we infer that they must have formed with $S_i >$ 9.2 k_B/baryon, independent of uncertainties about the age of the star. Finally, a similar analysis for β Pic b reveals that it must have formed with $S_i > 10.5\ k_B$/baryon, using the radial-velocity mass upper limit. These initial entropy values are respectively ca. 0.7, 0.5, and 1.5 k_B/baryon higher than the ones obtained from core accretion models by Marley et al., thereby *quantitatively* ruling out the coldest starts for these objects and constraining warm starts, especially for β Pic b.

5.1. Introduction

While only a handful of directly-detected exoplanets is currently known, the near future should bring a statistically significant sample of directly-imaged exoplanets, thanks to a number of surveys underway or coming online soon. Examples include VLT/SPHERE, Gemini/GPI, Subaru/HiCIAO, Hale/P1640 (Vigan et al., 2010; Chauvin et al., 2010; McBride et al., 2011; McElwain et al., 2012; Yamamoto et al., 2013; Hinkley et al., 2011). An important input for predicting the yields of such surveys and for interpreting their results is the cooling history of gas giant planets. In the traditional approach (Stevenson, 1982; Burrows et al., 1997; Baraffe et al., 2003), objects begin their cooling, fully formed, with an arbitrarily high specific entropy[1] and hence radius and luminosity. In the past, the precise choice of initial conditions for the cooling has been of no practical consequence because only the 4.5-Gyr-old Solar System's gas giants were known, while high initial entropies are forgotten on the short Kelvin–Helmholtz time-scale GM^2/RL (Stevenson, 1982; Marley et al., 2007). However, direct-detection surveys are aiming specifically at young ($\leqslant$ 500 Myr) systems, and the traditional models, as their authors explicitly recognised, are not reliable at early ages.

Using the standard core-accretion formation model (Pollack et al., 1996; Bodenheimer et al., 2000; Hubickyj et al., 2005), Marley et al. (2007, hereafter M07) found that newly-formed gas giants produced by core accretion should be substantially colder than what the usual cooling tracks that begin with arbitrarily hot initial conditions assume. These outcomes are known as 'cold start' and 'hot start', respectively. M07 however noted that there are a number of assumptions and approximations that go into the core accretion models that make the predicted entropy uncertain. In particular, the accretion shock at the surface of the planet is suspected to play a key role as most of the mass is processed through it (M07; Baraffe, Chabrier & Barman, 2010) but there does not yet exist a satisfactory treatment of it. Furthermore, there may also be an accretion shock in the other main formation scenario, gravitational instability, such that it too could yield planets cooler than usually expected (see section 8 of Mordasini et al., 2012). Conversely, Mordasini (2013) recently found that the initial entropy varies strongly with the mass of the core, leading nearly to warm starts for reasonable values of core masses in the framework of core accretion.

The most reasonable viewpoint for now is therefore to consider that the initial entropy is highly uncertain and may lie almost anywhere between the cold values of M07 and the hot starts. In fact, M07 calculated 'warm start' models that were intermediate between the cold and hot starts, and recently, Spiegel & Burrows (2012) calculated cooling tracks and spectra of giant planets beginning with a range of initial entropies. This uncertainty in the initial entropy means that observations are in a privileged position to inform models of planet formation, for which the entropy (or luminosity) at the end of the accretion phase is an easily accessible output. Its determination both on an individual basis as well as for a statistically meaningful sample of planets would be very valuable, with the latter allowing quantitative comparisons to planet population synthesis (Ida & Lin, 2004; Mordasini et al., 2012). Moreover, upcoming and ongoing surveys should bring, in a near future, both qualitative and quantitative changes to the collection of observed planets to reveal a number of light objects at moderate separations from their parent star (i.e. Jupiter-like planets), which contrasts with the few currently known direct detections. *With this in mind, we stress the importance of interpreting direct observations in a model-independent fashion* and of thinking about

[1] The 'initial' entropy refers to the entropy at the beginning of the pure cooling phase, once the planet's mass is assembled.

the information that these yield about the initial (i.e. post-formation) conditions of gas giants.

In this paper, we investigate the constraints on the mass M and initial, post-formation entropy S_i that come from a luminosity and age determination for a directly-detected object, focusing on exoplanets. Since the current luminosity increases monotonically both with mass and initial entropy, these constraints take the form of a 'trade-off curve' between M and S_i. We show that, in the planetary regime, the allowed values of M and S_i can be divided into two regions. The first is a hot-start region where the initial entropy can be arbitrarily high but where the mass is essentially unique. This corresponds to the usual mass determination by fitting hot-start cooling curves. The second corresponds to solutions with a lower entropy in a narrow range and for which the planet mass has to be larger than the hot-start mass. (A priori, this may even reach into the mass regime where deuterium burning is important, which is discussed in a forthcoming paper.) The degeneracy between mass and initial entropy means that in general the mass and entropy cannot be constrained independently from a measurement of luminosity alone. When additional mass information is available, for example for multiple-planet systems or systems with radial velocity, it is possible to constrain the formation entropy more tightly.

We start in Section 5.2 by describing our gas-giant cooling models, discussing the luminosity scalings with mass and entropy, and comparing to previous calculations in the literature. In Section 5.3, we show in general how to derive constraints on the mass and initial entropy of a directly-detected exoplanet by comparing its measured luminosity and age to cooling curves with a range of initial entropies. We briefly consider in Section 5.4 similar constraints based on a (spectral) determination of the effective temperature and surface gravity. After a brief discussion of the luminosity–age diagram of directly-detected objects, we apply the procedure based on bolometric luminosities in Section 5.5 to three particularly interesting systems – 2M1207, HR 8799, and β Pictoris – and derive lower bounds on the initial entropies of the companions. For HR 8799 and β Pic, we use the available information on the masses to constrain the initial entropies more tightly. Finally, we offer a summary and concluding remarks in Section 5.6.

5.2. Cooling models with arbitrary initial entropy

Given its importance in the initial stages of a planet's cooling, we focus in this paper on the internal entropy of a gas giant as a fundamental parameter which, along with its mass, determines its structure and controls its evolution. Very few authors have explicitly considered entropy as the second fundamental quantity even though this approach is more transparent than the usual, more intuitive use of time as the second independent variable. In this section, before comparing our models to standard ones, we discuss interior temperature–pressure profiles and semi-analytically explain the different scalings of luminosity on mass and entropy which appear in the models.

5.2.1. Calculation of time evolution

We calculate the evolution of cooling gas giants by a 'following the adiabats' approach (Hubbard, 1977; Fortney & Hubbard, 2004; Arras & Bildsten, 2006). We generate a large grid of planet models with ranges of interior specific entropy S and mass M and determine for each model the luminosity $L = L(M, S)$ at the top of the convection zone. We then use it to calculate the rate of change of the convective zone's entropy $\mathrm{d}S/\mathrm{d}t$, which is defined by writing the entropy equation $\partial L/\partial m = -T\partial S/\partial t$ as

$$L = -\frac{\mathrm{d}S}{\mathrm{d}t}\int T\,\mathrm{d}m + L_\mathrm{D}, \tag{5.1}$$

with L_D the luminosity due to deuterium burning in the convection zone. With the current S and $\mathrm{d}S/\mathrm{d}t$ in hand, calculating a cooling curve becomes a simple matter of stepping through the grid of models at a fixed mass. This is computationally expeditious and gives results nearly identical to the usual procedure based on the energy equation (Henyey et al., 1964; Kippenhahn & Weigert, 1990), as discussed in Section 5.2.6.

The assumptions in the 'following the adiabats' approach are that $\partial S/\partial t$ is constant throughout the convective zone and that no luminosity is generated in the atmosphere. For these to hold, we require both the thermal time-scale $t_{\rm therm}(r) = Pc_P T/gF$ (Arras & Bildsten, 2006) – where c_P is the specific heat capacity, g the gravity, and F the local flux – in the radiative zone overlying the convective core and the convective turnover[2] time-scale to be much shorter than the time-scale on which the entropy is changing, $\tau_S = -S/({\rm d}S/{\rm d}t) = M\overline{T}S/L$, with $\overline{T}$ the mass-weighted mean temperature in the convection zone. A similar approach was used to study the evolution of ohmically-heated irradiated gas giants by Huang & Cumming (2012).

We do not include deuterium burning directly in the planet models since it always occurs inside the convection zone. Instead, we calculate the deuterium burning luminosity per unit deuterium mass fraction for each model in the grid and use it in equation (5.1) to follow the cooling of the planet and the time evolution of the deuterium mass fraction averaged over the convective region. However, we focus in this work on masses below the (parameter-dependent) deuterium-burning limit near 12–14 $M_{\rm J}$ (Spiegel, Burrows & Milsom, 2011; Mollière & Mordasini, 2012; Bodenheimer et al., 2013), such that deuterium burning does not play a role in the objects' evolution. We defer a detailed exploration of deuterium burning in our models to an ulterior publication but already mention the interesting result that cooling curves starting at low entropy can exhibit an initial increase in their luminosity due to deuterium burning. We subsequently noticed that the colder starts in fig. 8 of Mollière & Mordasini (2012) show a similar behaviour, and that Bodenheimer et al. (2013) also find in their formation simulations the possibility of deuterium 'flashes'.

5.2.2. Calculation of gas giant models

To construct a model with a given mass M and internal entropy S, we integrate inwards from the photosphere and outwards from the centre, adjusting the central pressure, the cooling time τ_S, and the luminosity L and the radius R at the top of the inner zone until the two integrations match at a pressure of 30 kbar. We use the Eddington approximation at the photosphere, setting $T = T_{\rm eff}$ at $P_{\rm phot} = 2g/3\kappa$, and take the solar-metallicity (based on Lodders, 2003) radiative opacity from Freedman, Marley & Lodders (2008). In the deep interior, the contribution from the electron conductive opacity of Cassisi et al. (2007) is also included. The equation of state for the hydrogen–helium mixture is that of Saumon, Chabrier & van Horn (1995, hereafter SCvH) with a helium mass fraction $Y = 0.25$. Since we focus on gas giants, we do not include a rocky core, which was found in a test grid to increase the luminosities by at most a few per cent at the lower masses, as in Saumon et al. (1996).

The grid has a lower entropy limit of $S \simeq 7$–$7.5\ k_{\rm B}$/baryon[3]. The upper S limit in the grid is set by the requirement that $R \lesssim 7\ R_{\rm J}$, a value found to make numerical convergence straightforward. The upper limits are $S_{\rm max} \simeq 12$ near 1 $M_{\rm J}$ and $S_{\rm max} \simeq 14$ for the higher masses.

Fig. 5.1 shows interior profiles in the T–P plane for a range of entropies and masses. Schematically, since hydrostatic balance dictates $P_{\rm c} \sim M^2/R^4$, increasing the mass at a fixed entropy extends the centre to a higher pressure along the adiabat. This is exacerbated at high entropies, where the planet substantially shrinks with increasing mass, while low-entropy objects have a roughly constant radius. (Radii as a function of M and S are presented in Appendix 5.7.) At fixed mass, increasing the entropy mostly shifts the centre to higher T or to lower P. The first case obtains for low-entropy objects, which are essentially at zero temperature in the sense that $k_{\rm B}T_{\rm c} \ll E_{\rm F}$, where $T_{\rm c}$ is the central temperature and $E_{\rm F}$ is the Fermi energy level at the centre, taken to approximate the electron chemical potential. Increasing the entropy partially lifts the degeneracy since the degeneracy parameter $y \approx k_{\rm B}T_{\rm c}/E_{\rm F} \propto T_{\rm c}/\varrho_{\rm c}{}^{2/3}$ is a monotonic function of S, and $P_{\rm c}$ remains constant

[2] We do make the standard assumption that the interior is fully convective, even though stabilising compositional gradients have been suggested to possibly shut off large-scale convective motions (Stevenson, 1979; Leconte & Chabrier, 2012, 2013).

[3] Entropy values in this work are given in the usual units, written explicitly or not, of multiples of Boltzmann's constant $k_{\rm B}$ per baryon (i.e. per mass of hydrogen atom). For comparison, 4.5-Gyr-old Jupiter has a current entropy of 7 $k_{\rm B}$/baryon (Marley et al., 2007, but see Appendix 5.8).

because of the constant radius. At entropies higher than a turn-over value of $\simeq 10.4\,k_\mathrm{B}$/baryon, the central temperature does not increase (and even decreases) with entropy. As pointed out in Paxton et al. (2013), this entropy value is given by $k_\mathrm{B}T_\mathrm{c} \sim E_\mathrm{F}$ – we find that $y \simeq 0.15$ for $S = 10.4$ – and is thus independent of mass. As for P_c, it decreases because the radius increases. These behaviours also hold at higher masses not shown in the figure.

As for the 1-M_J planet with $S = 9$ shown in Fig. 5.1, some models with entropy $S \simeq 8$–9.5 show a second, 'detached' convective zone at lower pressures, which follows from a re-increase of the Rosseland mean opacity (see section 3.1 of Burrows et al., 1997). This second convection zone, which is at most at an entropy $0.2\,k_\mathrm{B}$/baryon higher than the convective core, will not affect the evolution of the object since the radiative thermal time-scale is much shorter than the cooling time τ_S throughout the atmosphere. This holds in particular at the inner radiative-convective boundary (RCB); for example, the 1-M_J, $S = 10$ model has $\tau_S = 14$ Myr and $t_\mathrm{therm} = 0.2$ Myr at its RCB. Planets with a second convective zone can equivalently be thought of as having a radiative shell interrupting their convective zone, as originally predicted for Jupiter's adiabat by Guillot et al. (1994) and based on too low opacities (see e.g. the brief review in Freedman et al., 2008).

Finally, we note that the higher-entropy objects ($S \gtrsim 11.5$, with some dependence on mass) are convective from the centre all the way to the photosphere.

5.2.3. Luminosity as a function of mass and entropy

To provide a model-independent way of thinking about an object's brightness and thus to facilitate comparison with other models, we show in Fig. 5.2 the luminosity of the planet as a function of its internal entropy. We focus on objects without significant deuterium burning. Two main regimes are apparent: at lower entropies, the scaling with mass is roughly $L \sim M$, while at high entropies, the luminosity becomes almost insensitive to mass. Looking more closely, the high-luminosity regime is described by $L \propto M^{0.3}$ (for $M \gtrsim 1\ M_\mathrm{J}$), and the brief steepening of the luminosity slope with respect to entropy between $L \simeq 10^{-6}$ and $10^{-4}\ L_\odot$ (at $S \sim 8.2$–9, depending on mass) marks a transition from $L \propto M^1$ to $L \propto M^{0.7}$ at fixed intermediate and low entropy respectively.

To try to understand these luminosity scalings, we firstly note that the radiative luminosity at the radiative-convective boundary, which is equal to the total luminosity, can always be written as (Arras & Bildsten, 2006)

$$L = \left(4\pi r^2 \frac{4acT^3}{3\kappa\rho}\frac{\mathrm{d}T}{\mathrm{d}r}\right)_\mathrm{RCB} = \frac{16\pi Gac}{3}\frac{MT_\mathrm{RCB}^4\nabla_\mathrm{adRCB}}{\kappa_\mathrm{RCB}P_\mathrm{RCB}}, \tag{5.2}$$

approximating the convection zone to contain the whole mass (cf. the 99-per-cent mass labels in Fig. 5.1) and radius. Thus, one way of obtaining $L(M,S)$ is to express the four quantities P_RCB, T_RCB, ∇_adRCB and κ_RCB in terms of M and S. This will now be done for the three regimes in turn, starting with low entropies.

Low-entropy regime: $L \propto M^{0.7} f_\mathrm{low}(S)$

To begin, consider the entropy dependence of luminosity at a fixed mass when $S \lesssim 9$–8 (at 1–10 M_J respectively). Fig. 5.1 reveals that the opacity at the radiative-convective boundary κ_RCB remains constant at a given mass, which provides a first relation. Secondly, over the temperature and pressure range of interest in this regime, the hydrogen and helium remain respectively molecular and neutral. This implies that ∇_adRCB is constant and that the entropy has a simple functional form in the ideal-gas approximation, given by the Sackur–Tetrode expression (e.g. Callen, 1985). For an H_2–He I mixture with $Y = \frac{1}{4}$, this is

$$S = 9.6 + \frac{45}{32}\ln(T/1600\ \mathrm{K}) - \frac{7}{16}\ln(P/3\ \mathrm{bar}) \tag{5.3}$$

(hence $\nabla_\mathrm{ad} = 0.31$), where S is the entropy per baryon in multiples of k_B, $\ln 10 = 2.3$, and the reference T and P values were chosen for Section 5.2.3. Finally, T_RCB is approximately fitted by

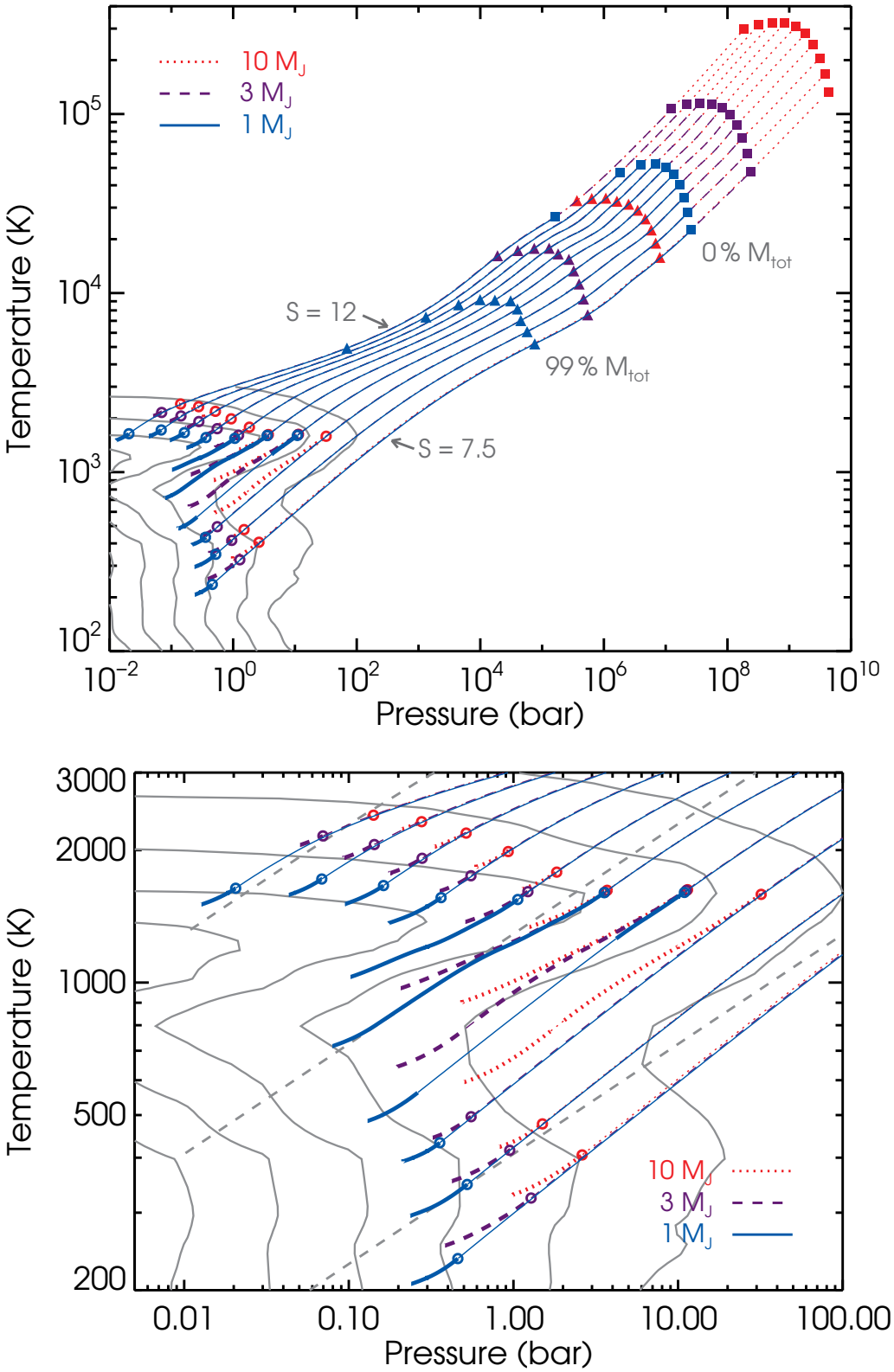

Fig. 5.1.: *Top panel:* Temperature–pressure profiles of core-less planets with entropy $S = 7.5$–$12\ k_B$/baryon (bottom to top), in steps of $0.5\ k_B$/baryon, and $M = 1$, 3, and 10 M_J (full, dashed, and dotted lines, respectively). Squares indicate the centre and triangles mark where the enclosed mass is 99 per cent of the total mass for each model. Curves end at the photosphere in the Eddington approximation, and the thick part(s) of each curve show the radiative zone(s), while the thin part(s) of the curve are convective; the radiative-convective boundary relevant for the thermal evolution is highlighted by a ring. Thin grey lines at low P and T indicate contours of constant Rosseland mean opacity (Freedman et al., 2008), with $\log \kappa = -3.5$ to -1.0 (cm^2 g^{-1}) in steps of 0.5 dex, increasing with P. See text for a mention of the dominant sources of opacity in some parts of the diagram. *Bottom panel:* Same as top panel but focussing on the atmospheres. The three diagonal dashed lines mark $\log R \equiv \log \varrho / {T_6}^3 = 2$, 4, and 6 (g cm^{-3} K^{-3}), from top to bottom.

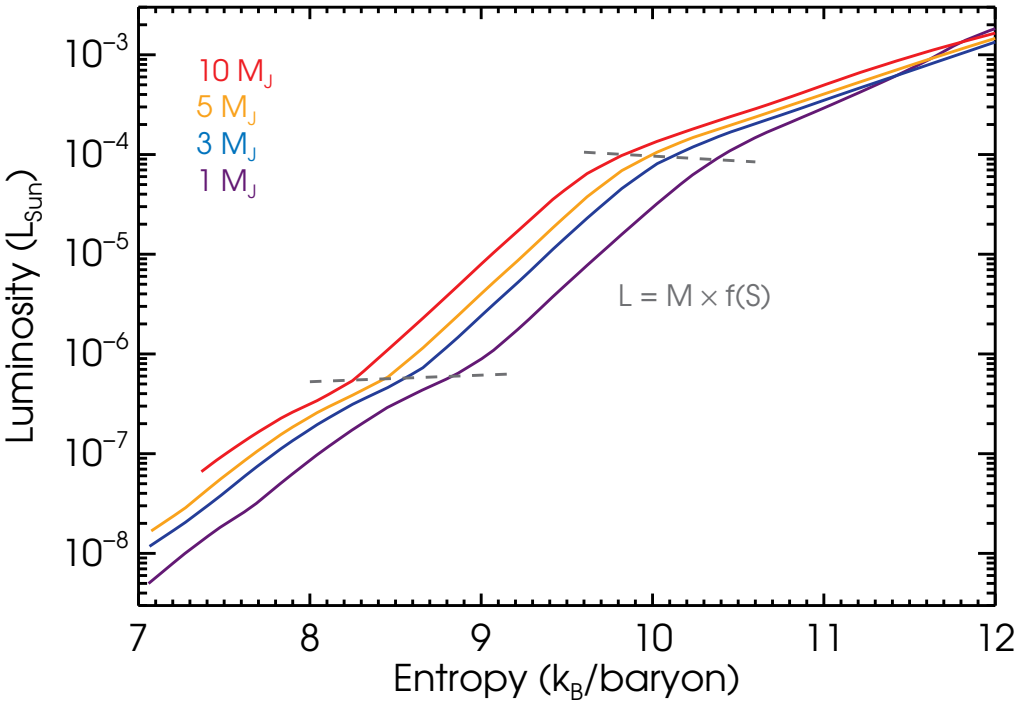

Fig. 5.2.: Luminosity as a function of entropy for our planet models. The masses shown are (bottom to top) $M = 1, 3, 5$, and 10 M_J.The two dashed lines approximately indicate the mass-dependent entropy boundaries between the low-, intermediate- and high-entropy regimes of the luminosity $L = L(M, S)$. At intermediate entropies, the atmosphere reaching the radiative-zero solution leads to the simple result that L/M depends only on S (see text for details). Here as throughout, $L_{\rm Sun} = 3.86 \times 10^{33}$ erg s^{-1}.

$T_{\rm RCB} \propto 10^{0.19S}$. Combining the four relations (constant $\nabla_{\rm adRCB}$ and the three non-trivial ones) with equation (5.2) yields $L \propto 10^{1.04S}$. This is quite close to a power-law fit of Fig. 5.2, which gives $L \propto 10^{1.3S}$.

Next, consider the position of the RCB at fixed low entropy for different masses. Fixed entropy immediately implies $T \propto P^{\nabla_{\rm ad}}$, and the constant $\nabla_{\rm ad} = 0.31$ gives the second relation. The profiles of Fig. 5.1 indicate that in this low-entropy regime (for $T \simeq 200$–400 K, $P \simeq 0.01$–10 bar), the opacity depends approximately only on the pressure, with $\kappa \propto P^{0.9}$. Finally, we find that $P_{\rm RCB} \propto M^{0.5}$, thus providing the fourth relation. Combining these and using equation (5.2) gives $L \propto M^{0.8}$, in good agreement with a direct fit, which gives $L \propto M^{0.7}$.

Thus, a constant adiabatic gradient, an RCB opacity dependent only on the mass, and a few power laws suffice to show that in the low-entropy regime

$$L_{\rm low} = 10^{-7.7}\, L_\odot \left(\frac{M}{M_J}\right)^{0.7} 10^{1.3(S-7.5)}, \tag{5.4}$$

which defines $f_{\rm low}(S)$ up to a constant. For Jupiter's adiabat with $T = 165$–170 K at 1 bar (Saumon & Guillot, 2004) and thus an entropy of 6.71–6.75 k_B/baryon, this predicts $\simeq 1.9 \times 10^{-9}\, L_\odot$, in good agreement with the current value $L_J = 8.7 \times 10^{-10}\, L_\odot$.

Intermediate-entropy regime: $L \propto M f_{\rm rz}(S)$

We now look at intermediate entropies, which are in the range 9–10.2 at 1 M_J to 8.2–9.6 k_B/baryon at 10 M_J. (More concisely, this corresponds to planets with $L \sim 10^{-6}$–$10^{-4}\, L_\odot$.) As explained by Arras & Bildsten (2006), equation (5.2) is of the form $L = Mf(S)$, where $f(S)$ is a function of the entropy in the convection zone, only if the quantity $T^4\nabla_{\rm ad}/\kappa P$ at the RCB is a function of a unique variable, S. The intermediate-S behaviour can then be understood by noticing in Fig. 5.1 that

objects at those entropies have a $T_{\rm RCB}$ independent of internal entropy *and* an extended atmosphere (interrupted or not by a second convection zone, i.e. including the deeper radiative window when present). For these planets, the photosphere is sufficiently far from the RCB ($P_{\rm RCB} \gtrsim 10\,P_{\rm phot}$, ${T_{\rm RCB}}^4 \gtrsim 5\,{T_{\rm eff}}^4$) that the atmosphere merges on to the radiative-zero profile, which solves (Cox & Giuli, 1968)

$$\frac{{\rm d}T}{{\rm d}P} = \frac{3}{16acG}\frac{L}{M}\frac{\kappa}{T^3}, \tag{5.5}$$

where the boundary condition is by definition of no consequence. The solution is a $T(P)$ relation, which yields the radiative gradient $\nabla_{\rm rad} = {\rm d}\ln T/{\rm d}\ln P$ along it. The important point is that both the atmosphere profile and its gradient depend only on the quantity L/M. Now, choosing an internal entropy fixes the adiabat, i.e. sets a second $T(P)$ relation. We require that at the intersection of the atmosphere and the adiabat $\nabla_{\rm rad}$ be equal to $\nabla_{\rm ad}$, which is the slope of the chosen adiabat. This thus pins down $\nabla_{\rm rad}$ in the atmosphere and hence L/M (and the atmosphere profile itself). Therefore, there is a unique L/M associated with an S, which means that L must be of the form[4] $L/M = f(S)$.

Since we determine convective instability through the Schwarzschild criterion $\nabla_{\rm ad} < \nabla_{\rm rad}$, where $\nabla_{\rm ad}$ is relatively constant and the radiative gradient is given by

$$\nabla_{\rm rad} = \frac{3LP}{16\pi acGMT^4}\kappa \tag{5.6}$$

near the surface, a slow inward increase of κ will ensure a deep RCB. Consequently, the $L \propto Mf(S)$ scaling will hold for those M and S such that, starting at the photosphere with $P_{\rm phot} \simeq f(M)$ and $T_{\rm eff} \simeq f(P_{\rm phot}, S)$, the opacity increases only slowly along the adiabats. (For a power-law opacity $\kappa = \kappa_0 P^n T^{-n-s}$, this means $n/(n+s) \simeq \nabla_{\rm ad}$.) This is indeed the case for intermediate-S models in Fig. 5.1, where the $T(P)$ profiles are nearly aligned with contour lines of constant opacity. For this argument to hold, the radius must be rather independent of the mass (cf. Zapolsky & Salpeter, 1969) and of the entropy. Also, one needs to approximate the entropy at the photosphere to be that of the interior, which is reasonable: even in the extended atmospheres, the entropy increases by at most $\simeq 0.5\ k_{\rm B}$/baryon over our grid of models.

The functional form of $f(S)$ can be obtained by fixing $T_{\rm RCB}$ and using equation (5.3) for the entropy of an ideal gas. The reference temperature of 1600 K was chosen based on the radiative-convective boundaries of Fig. 5.1. For convenience, S(3 bar, 1600 K) was computed using the interpolated SCvH tables. These include the contribution from the ideal entropy of mixing[5], a remarkably constant $S_{\rm mix} = 0.18\ k_{\rm B}$/baryon in a large region away from H_2 dissociation. Combining this $S(P,T)$ with equation (5.2), fixing $T = 1600$ K, and taking $\kappa(P, 1600\ {\rm K}) \simeq 0.0104(P/3\ {\rm bar})^{0.2}\ {\rm cm^2\ g^{-1}}$ from the interpolated table yields

$$\log_{10}\frac{L_{\rm rz}/L_\odot}{M/M_{\rm J}} = -5.05 + 1.51(S - 9.6), \tag{5.7}$$

i.e. $L = Mf_{\rm rz}(S)$ with $f_{\rm rz}(S) = 3.4{\times}10^{28}\ {\rm erg\ s^{-1}}{M_{\rm J}}^{-1}\ 10^{1.51(S-9.6)}$. (Thus, if $\kappa \propto P^n$ and ${\rm d}S/{\rm d}\ln P = -b$, $\log_{10} f_{\rm rz}(S) \propto (n+1)/b\ln 10$.) The subscript 'rz' highlights that the solution applies when the radiative-zero solution is reached. This fits excellently (being mainly only 0.1 dex too high in $\log L$) the L/M–S relationship found in our grid of models at intermediate entropies.

High-entropy regime: $L \propto M^{0.3} f_{\rm high}(S)$

For $S \gtrsim 10$–9 (at 3–10 $M_{\rm J}$, respectively), the luminosity becomes almost independent of mass at a given entropy. This indicates that the radiative solution does not hold anymore, and indeed Fig. 5.1 shows that planets with high entropy have atmospheres extending only over a small pressure range, with the more massive objects fully convective from the centre to the photosphere. The shortness

[4] This regime was obtained by Arras & Bildsten (2006) when looking at irradiated planets. This can be roughly thought to fix $T_{\rm RCB}$ to the irradiation temperature, so that $T^4\nabla_{\rm ad}/\kappa P$ at the RCB is automatically a function of only one thermodynamic variable, for instance S, for all entropies.

[5] We use the corrected version of the equations in SCvH; see the appendix of Saumon & Marley (2008).

of the atmosphere is due to the opacity's rapid increase inward, as constant-κ contours are almost perpendicular to $T(P)$ profiles in that region. As in Section 5.2.3, we look at the behaviour of T, P, κ, and $\nabla_{\rm ad}$ at the RCB as a function of M and S.

Fig. 5.1 shows that at a fixed mass, $T_{\rm RCB}$ is almost independent of the (high) entropy, with the actual scaling closer to ${T_{\rm RCB}}^4 \propto 10^{0.2S}$. Also, $\kappa_{\rm RCB}$ is again mostly independent of S, as for the low entropies. At high entropies, $\nabla_{\rm ad RCB}$ drops continuously with increasing S (decreasing $P_{\rm RCB}$), with a very rough $\nabla_{\rm ad} \propto 10^{-0.13S}$. For the fourth relation, we can fit $P_{\rm RCB} \propto 10^{-0.6S}$. Combining all this with equation (5.2) then gives $L \propto 10^{0.7S}$, which is quite close to a fit $L \propto 10^{0.6S}$.

At fixed high entropy, $\nabla_{\rm ad}$ is somewhat constant at 0.25–0.13 for $S = 10.5$–12. Also, above $\simeq 1500$ K and at $P < 1$ bar, the opacity is approximately independent of pressure, scaling only with temperature as $\kappa \sim T^4$. Finally, as in the low-entropy regime, $P_{\rm RCB} \propto M^{0.5}$; combining the four relations, we should have $L \propto M^a$ with $a \simeq 0.5$–0.4. This is not far from the direct fit $L \propto M^{0.3}$.

Therefore, the luminosity in the high-entropy regime is

$$L_{\rm high} = 10^{-3.88}\, L_\odot \left(\frac{M}{M_{\rm J}}\right)^{0.3} 10^{0.6(S-10.5)}, \tag{5.8}$$

which defines $f_{\rm high}(S)$ up to a multiplicative constant. Fig. 5.2 indicates that the luminosity at the lower masses ($M \lesssim 2\ M_{\rm J}$) depends more steeply on S ($\simeq 10^{0.85\,S}$ at 1 $M_{\rm J}$), but this was ignored when obtaining equation (5.8).

Before summarising, let us briefly digress about the $P_{\rm RCB} \propto M^{0.5}$ scaling seen both at fixed low entropy and at fixed high entropy. In both cases, the model grid shows that, as a reasonable approximation, $P_{\rm RCB} \propto P_{\rm phot}$. At low entropies, R is constant, such that $P_{\rm RCB} \propto P_{\rm phot} = 2g/3\kappa \propto M/\kappa$. Then, the opacity's scaling of $\kappa \sim P$ (see Section 5.2.3; the exponent is actually closer to $\simeq 0.95$) immediately implies roughly $P_{\rm RCB} \propto M^{0.5}$. At high entropies, planetary radii are significantly larger and vary, such that the radius dependence of the photospheric pressure should not be neglected; thus $P_{\rm phot} \propto M/R^2\kappa$. Fitting the $R(M, \text{fixed high } S)$ relation in our models, we find $R \sim M^{-1.1}$ or $R \sim M^{-1.2}$, depending on the entropy. Then, $\nabla_{\rm ad} \simeq 0.2$ and $\kappa \sim T^4$ yield $\kappa \sim P^{0.8}$ at fixed S, and thus, isolating, $P_{\rm RCB} \sim M^{0.6}$ or $P_{\rm RCB} \sim M^{0.7}$. This is a slightly stronger dependence on mass than what is found in the grid, but the argument shows how the rough scaling can be derived.

Summary of luminosity scalings

In summary, we found from fitting the $L(M, S)$ relation across our planet models that $L \propto M^a\, 10^{\lambda S}$, with $a = (0.7, 1, 0.3)$ and $\lambda = (1.3, 1.5, 0.6)$ at low ($S \lesssim 9$–8, for 1–10 $M_{\rm J}$ respectively), intermediate ($S \lesssim 10.2$–9.6), or high entropy, respectively, from considering the behaviour of the different factors in equation (5.2). Fitting directly the relations in the grid gives very similarly

$$L_{\rm low} = 1.5 \times 10^{-7}\, L_\odot\, \tilde{M}^{0.72} 10^{1.3\,(S-8.2)}, \tag{5.9a}$$

$$L_{\rm rz} = 7.2 \times 10^{-6}\, L_\odot\, \tilde{M}^{0.98} 10^{1.58\,(S-9.6)}, \tag{5.9b}$$

$$L_{\rm high} = 8.7 \times 10^{-5}\, L_\odot\, \tilde{M}^{0.29} 10^{0.58\,(S-10.2)}, \tag{5.9c}$$

with $\tilde{M} \equiv M/M_{\rm J}$, to $\simeq 0.01$ dex in $\log L$ except for $M \lesssim 2\ M_{\rm J}$ at high entropies.

Our approximate understanding of the different regimes is the following. For the conditions found in the atmospheres of intermediate-entropy planets, contours of constant opacity are almost parallel to adiabats, which is equivalent to saying that κ is almost constant along lines of constant R (see Fig. 5.1), where $\log R \equiv \log \varrho/{T_6}^3$ and $T_6 = T/10^6$ K. Since $\nabla_{\rm rad} \propto \kappa$ by equation (5.6) and, for a constant $\nabla_{\rm ad}$, only $\nabla_{\rm rad}$ determines when the atmosphere becomes convective, a slow inward increase of the opacity causes the radiative zone to extend over a large pressure range. This in turn means that the atmosphere can reach the radiative-zero solution, which we have shown necessarily implies $L = Mf(S)$. For the conditions found in the atmospheres of planets with high and low entropy, however, opacity increases relatively quickly along an adiabat. Since the $T(P)$ slope in the

atmosphere is not too different from that of the convective zone's adiabat, this means that opacity increases rapidly in the atmosphere, which therefore cannot join on to the radiative-zero solution before becoming convective. It is interesting to note that the transition from low to intermediate entropies is accompanied by a 'second-order' (i.e. relatively small) change in a and λ, while the physical explanation changes to 'zeroth order'.

The different $L(M, S)$ scalings then reflect in part the approximate temperature- and pressure-*in*dependence of the opacity at low and high S, respectively, and the fact that opacity increases relatively little along adiabats at intermediate S. While developing even a rough analytical understanding of the various opacity scalings would be interesting but outside the scope of this work, we briefly indicate the major contributors in the high- and intermediate-S regimes. (The following temperatures should all be understood as somewhat approximate; cf. Fig. 5.1). Moving from 2800 K (or 3000 K at higher P), above which continuum sources dominate, down to 1300 K, the decrease in opacity is due to the settling of the rovibrational levels of H_2O. Similarly, the settling of the rovibrational levels of CH_4 dominates from 800 K down to 480 K, with H_2O also contributing. Around 2000 K, where opacity is nearly independent of pressure across a wide pressure range, H_2O dominates the opacity, with its abundance remaining rather constant. In the intermediate-entropy range, from 1300 or 1600 K to 800 K, H_2 dominates the composition but it is the appearance of CH_4 which is crucial for the opacity. The same qualitative behaviours can be found in the data of Ferguson et al. (2005) (J. Ferguson 2013, priv. comm., who also provided the information just presented). Ferguson et al. (2005) do not include the powerful alkali Na, K, Cs, Rd, and Li as Freedman et al. (2008) do, which can raise the opacity by some 0.2 dex near the RCB of intermediate-entropy planets.

5.2.4. Luminosity as a function of helium fraction

The standard grid used for analyses in this work uses a helium mass fraction $Y = 0.25$ but results can be easily scaled to a different Y. Following a suggestion by D. Saumon (2013, priv. comm.), one can write

$$\left(\frac{\mathrm{d}L}{\mathrm{d}Y}\right)_{M,S} \approx \left(\frac{\partial L}{\partial \ln S}\right)_{M,Y} \times \left.\frac{\mathrm{d}\ln S}{\mathrm{d}Y}\right|_{(P_0,T_0)}, \tag{5.10}$$

where (P_0, T_0) is some appropriate location, and compute $\gamma S \equiv \mathrm{d}S/\mathrm{d}Y = (S_\mathrm{H} - S_\mathrm{He}) + \mathrm{d}S_\mathrm{mix}/\mathrm{d}Y$, where $S = (1-Y)S_\mathrm{H} + YS_\mathrm{He} + S_\mathrm{mix}$, S_H, S_He, S_mix are respectively the total, hydrogen, helium, and mixing entropies per baryon (SCvH). Given equation (5.2), one might heuristically expect (P_0, T_0) to be near the radiative–convective boundary (RCB), at least when determining $\mathrm{d}S/\mathrm{d}Y$ at constant L. Indeed, we find this to be the case, with $\gamma \simeq -0.63$ at the RCB of the $Y = 0.25$ or 0.30 models for intermediate to high entropies. Thus, for Y' sufficiently close to 0.25,

$$X(M, S', Y') = X(M, S, Y) \tag{5.11}$$

if

$$S' = S \times [1 - 0.63\,(Y' - 0.25)], \tag{5.12}$$

where X is a planet property such as L or τ_S. For $Y = 0.27$, this is at worse accurate only to 0.05 dex in luminosity towards high entropies for masses below $\simeq 12\ M_\mathrm{J}$ when $S \lesssim 8$. This rescaling is also adequate (in the same domain) for $X = R$, to 15 per cent towards *high* entropies, but a more accurate fit can be obtained with $\gamma \simeq -0.3 \pm 0.1$. Interestingly, nowhere within a planet structure in the grid does $|\gamma|$ drop below 0.55; the explanation in this case (in analogy to γ being evaluated at the RCB for L) is not clear.

Since at the RCBs in the grid the hydrogen is molecular, one might try to obtain γ analytically with the Sackur–Tetrode formula. Neglecting the subdominant contribution from the rotational degrees of freedom of H_2 yields $S_\mathrm{H}/S_\mathrm{He} \approx \mu_\mathrm{He}/\mu_{H_2} = 2$, where μ_X is the molecular mass of X. This leads to $\gamma = -0.57$, which is not far from the accurate result -0.63 yet shows that the $\mathrm{d}S_\mathrm{mix}/\mathrm{d}Y$ term cannot be neglected.

Equation (5.12) makes it simple to convert e.g. constraints on the initial entropy based on cooling curves with a particular Y to another set with a different Y, regardless of the approach used for the cooling. The typically small change in the entropy ($\simeq 3$ per cent) is nevertheless significant because of the strong dependence of L on S.

5.2.5. Cooling

One can also derive the functional form of the cooling tracks with a few simple arguments. With $L \propto M^a\, 10^{\lambda S}$, equation (5.1) implies $\mathrm{d}S/\mathrm{d}t = -M^{a-1} f(S)/\overline{T}$. Since hydrostatic balance yields $P_\mathrm{c} \sim GM^2/R^4$ and the convective core is adiabatic, we expect $\overline{T} \simeq T_\mathrm{c} \propto (M^2/R^4)^{\nabla_\mathrm{ad}}$. (Across the whole grid, $\overline{T}/T_\mathrm{c} = 0.55$–$0.63$.) Therefore, ignoring the radius dependence (since $4\nabla_\mathrm{ad}$ is not large and R is rather constant at lower entropies), $-\mathrm{d}S/f(S) \propto M^{-2\nabla_\mathrm{ad}-1+a}\,\mathrm{d}t$. This means that the entropy of a cooling planet should be approximately a function of $t/M^{2\nabla_\mathrm{ad}+1-a}$, and that more massive planets cool more slowly since a is always smaller than $2\nabla_\mathrm{ad} + 1 \simeq 5/3$. In fact, using that $f(S) = 10^{\lambda S}$, one can compute the integral to obtain an analytic expression for the cooling tracks:

$$\frac{1}{L(t)} = \frac{1}{L_\mathrm{i}} + \frac{1}{L_\mathrm{hs}(t)}, \quad L_\mathrm{hs}(t) = \frac{M^{2\nabla_\mathrm{ad}+1}}{\beta\, t}, \tag{5.13}$$

where L_i and L_hs are the initial and hot-start luminosities, respectively, and $\beta = C\lambda \ln 10$ with C a dimensional constant grouping prefactors. We have assumed that a, λ, and ∇_ad do not change as the planet cools. Thus, $L \propto M^a$ at fixed entropy, with $a = 0.3$–1, but at a fixed time the luminosity has a steeper dependence on M, $L \propto M^{2\nabla_\mathrm{ad}+1} \simeq L \propto M^2$ for intermediate entropies. A more detailed analytic understanding of the cooling curves for irradiated planets along these lines was developed by Arras & Bildsten (2006), and a careful, approximate but surprisingly accurate analysis for brown dwarfs may be found in Burrows & Liebert (1993).

Equation (5.13) approximately describes cooling tracks with arbitrary initial entropy, with our cooling curves well fitted (to roughly 0.1 dex) below $10^{-5}\ L_\odot$ by $C = 3 \times 10^{-2}$ cgs when $\lambda = 1.5$ and $\nabla_\mathrm{ad} = 1/3$. At higher luminosities, in particular for hot starts, a better fit (with the restriction of $L \gtrsim 10^{-6}\ L_\odot$ if $M \lesssim 2.5\ M_\mathrm{J}$) which captures the average shape and spacing of the cooling curves is provided directly by the classical result of Burrows & Liebert (1993), who find

$$L_\mathrm{hs} = 7.85 \times 10^{-6}\ L_\odot\, \frac{(M/3\ M_\mathrm{J})^{2.641}}{(t/10\ \mathrm{Myr})^{1.297}} \tag{5.14}$$

(for $\kappa = 0.01\ \mathrm{cm^2\ g^{-1}}$), i.e. a somewhat different mass and time dependence.

5.2.6. Comparison with classical hot starts and other work

We now compare our cooling curves to classical hot starts. Fig. 5.3 shows cooling curves for large initial entropy compared to the hot-start models of Marley et al. (2007), the COND03 models (Baraffe et al., 2003) and those of Burrows et al. (1997), all of which use non-grey atmospheres with detailed opacities. The agreement is excellent, with our luminosities within the first 3 Gyr approximately within −30 and 20 per cent and −30 and 60 per cent above those of Baraffe et al. and Burrows et al.. (Of interest for the example of Section 5.4, our radii along the cooling sequence are at most approximately two to five per cent greater at a given time. This difference is comparable to the effect of neglecting heavy elements in the equation of state (EOS) or not including a solid core (Saumon et al., 1996) and not significant for our purposes. See also Appendix 5.7.) Our deuterium-burning phase at 20 M_J ends slightly earlier than in Burrows et al. (1997) but this might be due to our simplified treatment of the screening factor.

Fig. 5.4 shows cooling curves for lower initial entropies than in Fig. 5.3. The cooling curves show the behaviour found by M07 and Spiegel & Burrows (2012) in which the luminosity initially varies very slowly, with the cooling time at the initial entropy much larger than the age of the planet. Eventually, the cooling curve joins the hot start cooling curve once the cooling time becomes comparable to the age.

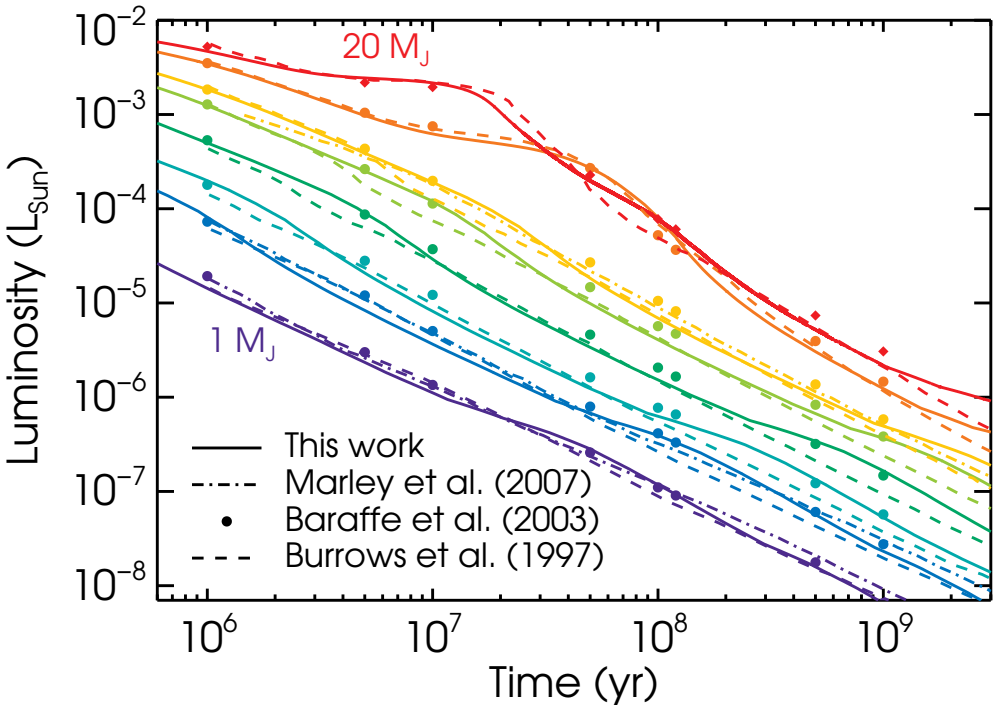

Fig. 5.3.: Cooling curves for (bottom to top) $M = 1, 2, 3, 5, 8, 10, 15$, and 20 M_J (solid curves) compared with the Marley et al. (2007) hot starts (for $M = 1, 2$, and 10 M_J only; dash-dotted curves), the COND03 tracks (dots) and the Burrows et al. (1997) models (dashed curves). The COND03 data is shown as dots because of insufficient sampling of the cooling tracks at higher masses.

Comparing to the cold starts in fig. 4 of M07, our models are a factor of $\simeq$ 3.5–3.9 lower in luminosity for the same initial entropies, as given in their fig. 2. Increasing our initial entropies by 0.38 k_B/baryon brings our cooling curves into agreement with theirs when the planet has not yet started cooling. (For this comparison, we do not correct the time offset for the higher masses (see figs. 2 and 4 of M07), which are already on hot-start cooling curves at the earliest times shown.) As mentioned in Appendix 5.8, this implies a real difference between our $L(S)$ of only 0.14 k_B/baryon.

Spiegel & Burrows (2012) computed the evolution of gas giants starting with a wide range of initial entropies. To compute the bolometric luminosity of their models, we take the published spectra and integrate the flux in the wavelength range given, 0.8–15 μm. The bottom panel of Fig. 5.4 shows the comparison to all four model types, with or without clouds and at solar or three times solar metallicity. Increasing our entropy by 0.45 k_B/baryon – e.g. comparing the Spiegel & Burrows (2012) model with $S = 9.0$ to ours with $S = 9.45$ – yields very good agreement, with our luminosities overlying their curves or within the spread due to the different atmospheres. As discussed in Appendix 5.8, this is mainly due to a constant entropy offset of 0.52 k_B/baryon between the tables used by the Burrows et al. group and the published SCvH tables used in the present work, leaving a net offset of merely 0.07 k_B/baryon.

The apparent disagreement with Spiegel & Burrows (2012) at late times comes from the increasing fraction of the flux in the Rayleigh–Jeans tail of the spectrum beyond 15 μm. For comparison, the implied required bolometric correction is equal to 10 to 50 per cent of the flux in 0.8–15 μm for a blackbody with $T_{\rm eff} \simeq$ 700–300 K. From this and the hot-start $T_{\rm eff}$ tracks shown in Spiegel & Burrows (2012), we estimate that integrating the spectrum should give a reasonable estimate (to ca. 30 per cent) of the bolometric luminosity only up to $\simeq$ 50, 200, and 1000 Myr for objects with $M = 1$, 3, and 10 M_J respectively. This is indeed seen in Fig. 5.4. Bolometric luminosities kindly provided by the authors (D. Spiegel 2013, priv. comm.), which are rather insensitive to the atmosphere type, are also shown for a more direct comparison and confirm the reasonable match of our cooling curves with those of Spiegel & Burrows (2012).

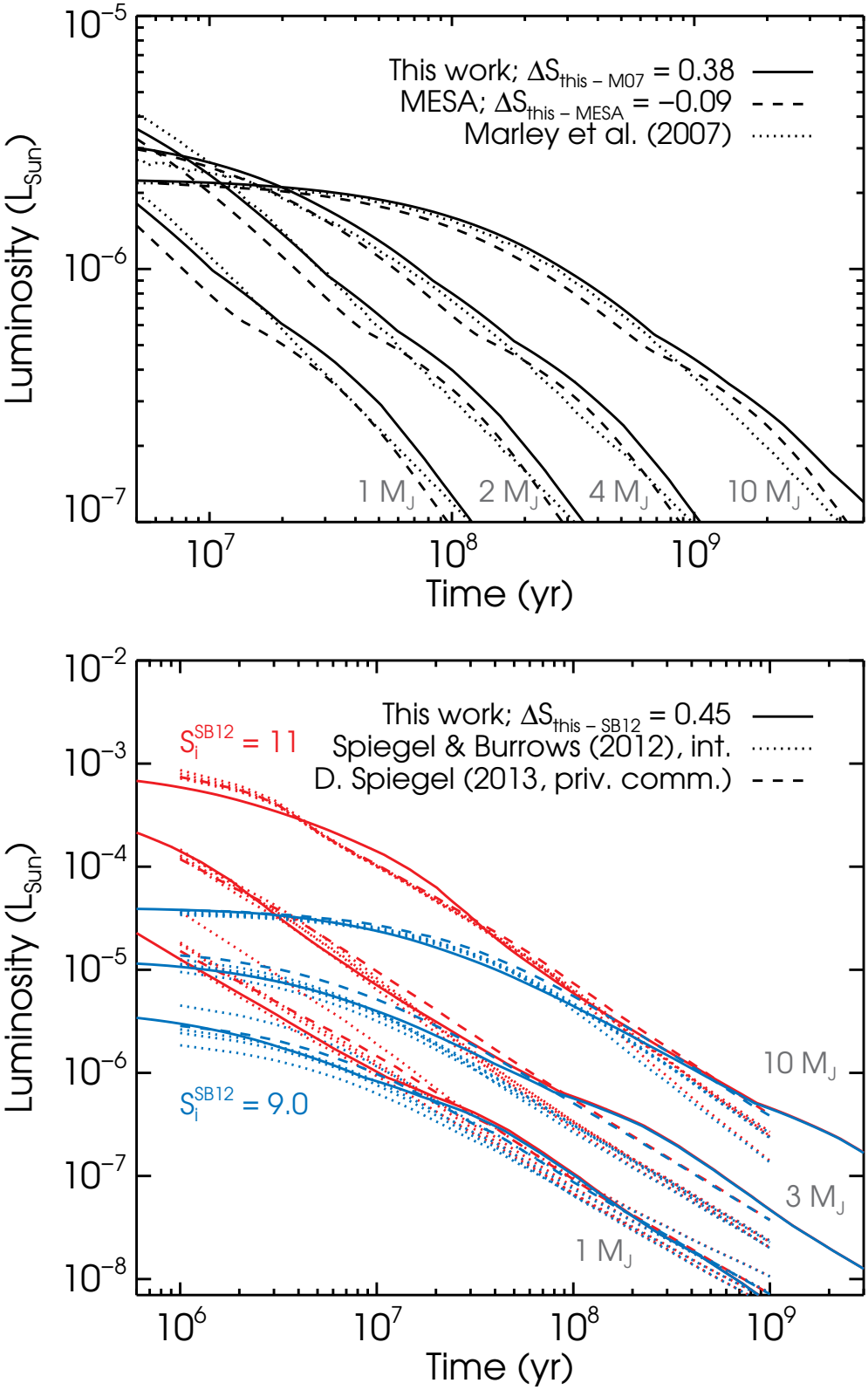

Fig. 5.4.: *Top panel:* Cooling curves for $M = 1, 2, 4, 10\ M_J$ and initial entropies equal to the Marley et al. (2007, M07) 'tuning-fork diagram' (their fig. 2) values $S_i = 9.23, 9.00, 8.60, 8.23$. The initial entropies for our cooling tracks were increased by 0.38 k_B/baryon to compare with Marley et al. (2007), with those of MESA further increased by 0.09 k_B/baryon. *Bottom panel:* Cooling curves for $M = 1, 3, 10\ M_J$ (bottom to top) with initial entropies $S_i = 9.0$ and $S_i = 11$ increased by 0.45 k_B/baryon mainly for 'thermodynamic reasons' (see text; solid lines), compared to those of Spiegel & Burrows (2012, SB12) with $S_i = 9.0$ and $S_i = 11$ (dashed and dotted lines). For each mass and initial entropy, the four dotted lines (some overlap) correspond to the integrated spectra for the four atmosphere types in no particular order, serving only to indicate a range. The red-side truncation of the Spiegel & Burrows (2012) spectra causes an underestimation of the bolometric luminosity at late times (see text). The dashed line at each mass and initial entropy shows the bolometric luminosity directly from the models.

We have also computed cooling curves with the MESA stellar evolution code (Paxton et al., 2011, 2013, revision 4723), and they are in excellent agreement with our results. We compared our $L(S)$ relation to ones obtained from MESA, (also with $Y = 0.25$) at different masses and found that they are very nearly the same, with an entropy offset $\Delta S \lesssim 0.1$. Moreover, Fig. 5.4 shows that the agreement of the time evolution is quite good, with in particular the late-time 'bumps' due to opacity when the cooling curves enter the intermediate-entropy regime (cf. Figs. 5.1, 5.2, and 5.6). We also produced grids with other opacities, using the MESA tables with the default $Y = 0.28$ and $Z = 0.02$ (for the opacity calculation only), and the Freedman et al. (2008) tables with [M/H] = ±0.3 dex, and found that this changed the luminosity by at most $\simeq 10$ per cent at a given mass and internal entropy. Similarly, small differences were found to result from a changed helium mass fraction in the bulk of the planet at a given mass and entropy per *nucleus*.

The upshot of these comparisons to classical, non-grey-atmosphere hot and cold starts is that cooling tracks computed with the simple and numerically swift cooling approach described above can reproduce models which explicitly calculate the time dependence of the luminosity. When comparing models from different groups, one should keep in mind that there can be a systematic offset in the entropy values of $\Delta S_{\rm syst} = 0.52$ (at $Y = 0.25$) due to different versions of the SCvH EOS, which however has no physical consequence for the cooling. Moreover, the remaining difference $|\Delta S| \lesssim 0.15$ is small compared to the entropy range between hot and cold starts.

5.3. General constraints from luminosity measurements

Masses of directly-detected exoplanets are usually inferred by fitting hot-start cooling curves (e.g. Burrows et al., 1997; Baraffe et al., 2003) to the measured luminosity of the planet, using the stellar age as the cooling time. Since the hot-start luminosity at a given age is a function only of the planet mass, the measured luminosity determines the planet mass. Equation (5.14) provides a quick estimate of this 'hot-start mass':

$$M_{\rm hs} = 3\ M_{\rm J} \left(\frac{L}{7.85\times10^{-6}\ L_\odot}\right)^{0.379} \left(\frac{t}{10\ {\rm Myr}}\right)^{0.491} . \tag{5.15}$$

Moreover, a planet's luminosity, at a given time and for a given mass, can never exceed that of the hot starts, since a larger initial entropy would have merely cooled on to the hot-start cooling track at an earlier age.

However, we have seen above that the luminosity at a given mass can be lowered by considering a sufficiently smaller initial entropy, which might be the outcome of more realistic formation scenarios (Marley et al., 2007; Spiegel & Burrows, 2012). With the fact that luminosity increases with planet mass at a given entropy, this simple statement has important consequences for the interpretation of direct-detection measurements, namely that *there is not a unique mass which has a given luminosity at a given age*. Cold-start solutions correspond to planets not having forgotten their initial conditions, specifically their initial entropy $S_{\rm i}$, and every different initial entropy is associated to a different mass. In other words, a point in (t, L) space – a single brightness measurement – is mapped to a curve in $(M, S_{\rm i})$ space. Since Marley et al. (2007) (but see also Baraffe et al., 2002; Fortney et al., 2005), it is generally recognised that direct detections should not be interpreted to yield a unique mass solution, but, with the exception of Bonnefoy et al. (2013), who used infrared photometry, this is the first time that this degeneracy is calculated explicitly.

5.3.1. Shape of the M–$S_{\rm i}$ constraints

The top panel of Fig. 5.5 shows the allowed masses and initial entropies for different values of luminosity $L_{\rm bol}/L_\odot = 10^{-7}$, 10^{-6} and 10^{-5}, at ages of 10, 30, and 100 Myr. Below the deuterium-burning mass, constant-luminosity curves in the M–$S_{\rm i}$ plane have two regimes. At high initial entropies, the derived mass is the hot-start mass independent of $S_{\rm i}$ since all $S_{\rm i}$ greater than a certain value have cooling times shorter than the age of the system. There, uncertainty in the stellar

age translates directly into uncertainty in the planet mass: since $L \propto 1/t$ and $L \sim M^2$, the mass uncertainty is $\Delta M/M \simeq \frac{1}{2}\Delta t/t$. At lower entropies, the luminosity measurement occurs during the early, almost constant-luminosity evolution phase. Given a luminosity match in this region, one can obtain another by assuming a lower (higher) initial entropy and compensating by increasing (decreasing) the mass. As seen in Section 5.2, L is a very sensitive function of S at low and intermediate entropies, so that a small decrease in initial entropy must be compensated by a large increase in mass to yield the same luminosity at a given time; this yields the approximately flat portion of the curves. As long as the cooling time for a range of masses and entropies remains shorter than the age, *the entropy constraints do not significantly depend on the age*. The uncertainty in the initial entropy is $\Delta S_\mathrm{i} \simeq 1/\lambda\, \Delta \log_{10} L_\mathrm{bol}$, where $1/\lambda \simeq 0.7$ or 1.7 at low or high entropy (see Section 5.2.3).

The circles in the top panel of Fig. 5.5 show the initial entropies for cold- and hot-start models from M07, the 'tuning-fork diagram of exoplanets'. The entropies were increased by 0.38 k_B/baryon as in the top panel of Fig. 5.4 to match our models. Since the cooling time increases with mass (see Section 5.2.5), heavier planets of the hot-start (upper) branch, i.e. with arbitrarily high initial luminosity, have cooled less and are therefore at higher S. For their part, the cold-start entropies, which are still the post-formation ones, lie close to a curve of constant luminosity $L \simeq 2 \times 10^{-6}\ L_\odot$. This reflects the fact that the post-formation luminosities in M07, as seen in their fig. 3, have similar values for all masses. The cause of this 'coincidence' is presently not clear; it might be a physical process or an artefact of the procedure used to form planets of different masses. Putting uncertainties in the precise values aside, the two prongs of the tuning fork in Fig. 5.5 give an approximate bracket within which just-formed planets might be found.

Mass information for a directly-detected planet can put useful constraints on its initial entropy and also potentially on its age and luminosity simultaneously. For instance, dynamical-stability analyses and radial-velocity observations (see Section 5.5 and Appendix 5.9) typically provide upper bounds on the masses. Since S_i decreases monotonically with M at a fixed luminosity, this translates into a *lower limit* on the initial entropy. This has the potential of excluding the coldest-start formation scenarios. Conversely, a lower limit on the planet's mass implies an *upper* bound on S_i. If it is greater than the hot-start mass, this lower limit on the mass of a planet would be very powerful, due to the verticalness of the hot-star branch. Combined with the flatness of the 'cold branch' of the $M(S_\mathrm{i})$ curve, this could easily restrict the initial entropy to a dramatically small $\Delta S_\mathrm{i} \simeq 0.5 \sim \Delta S_\mathrm{syst}$. Also, the top panel of Fig. 5.5 shows that not all age and luminosity combinations are consistent with a given mass upper limit. Given the often important uncertainties in the age and the bolometric luminosity, this may represent a valuable input.

5.3.2. Solutions on the hot- vs. cold-start branch

The bottom panel of Fig. 5.5 shows lightcurves illustrating the two regimes of the $M(S_\mathrm{i})$ curves discussed above. The hot-start mass is 1.85 M_J, whereas the selected cold-start case ($S_\mathrm{i} = 8.33$) has $M = 12\ M_\mathrm{J}$ – i.e. *a six times larger mass* – and both reach $\log L_\mathrm{bol}/L_\odot = -6$ at $t = 30$ Myr, with the cold-start values essentially independent of age. The hatched region around the 1.85-M_J curve comes from hot-start solutions between 1.35 and 2.35 M_J and is within a factor of two of the target luminosity, showing the moderate sensitivity of the cooling curves to the mass. However, in the cold-start phase, a variation by a factor of two can also be obtained by varying at a fixed mass the initial entropy from 8.23 to 8.43 k_B/baryon. This great sensitivity implies that combining a luminosity measurement with information on the mass would yield, if some of the hot-start masses can be excluded, tight constraints on the initial entropy.

5.3.3. Definition of 'hot-start mass'

By showing the entropy of hot starts as a function of time, Fig. 5.6 provides another way of looking at Fig. 5.5. Given a mass obtained from hot-start cooling tracks, the entropy value at that time read off from the curves indicates what 'hot' is, i.e. provides a lower bound on the initial entropy if the

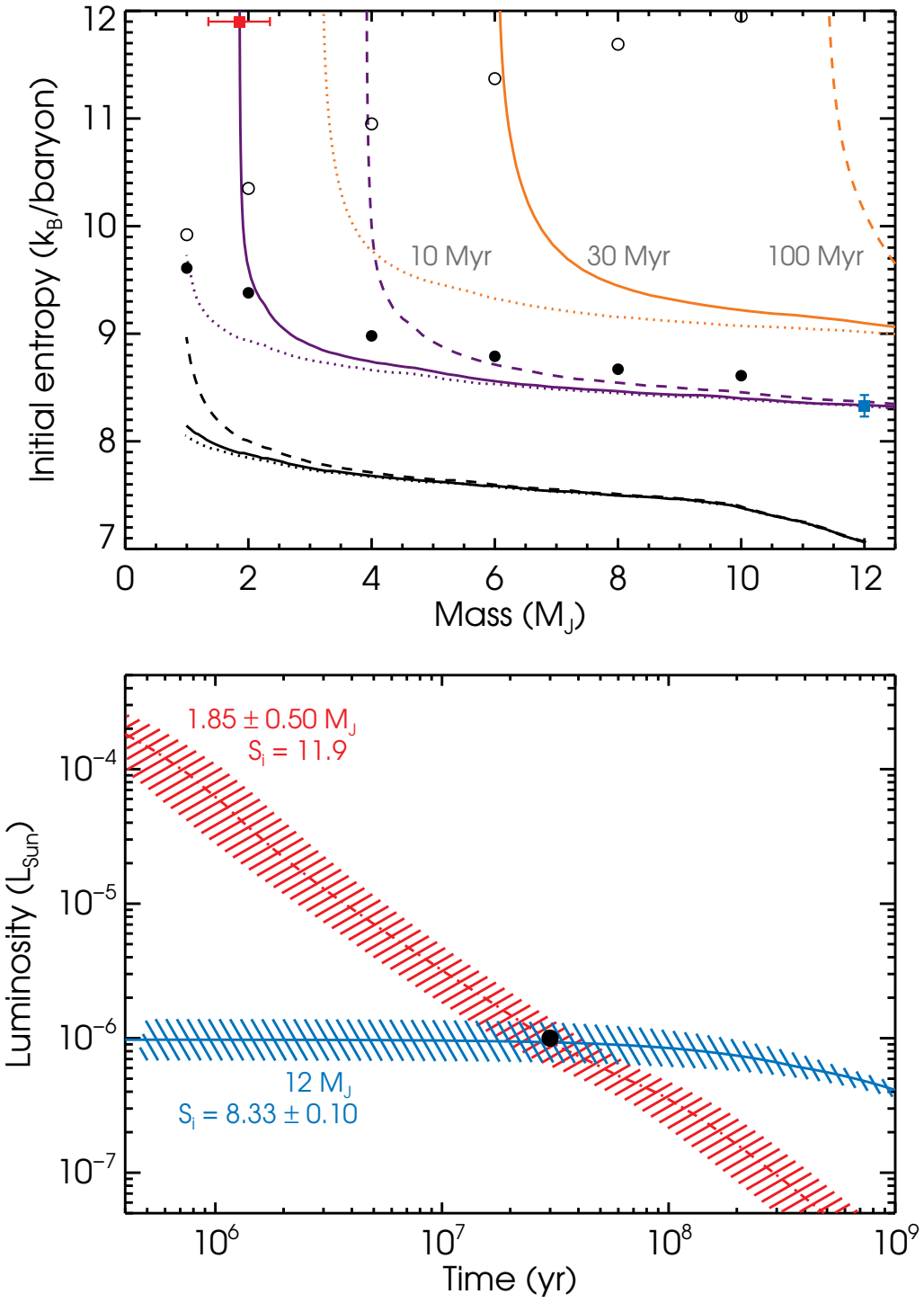

Fig. 5.5.: *Top panel:* Allowed values of planet mass M and initial entropy S_i corresponding to $L_{bol} = 10^{-7}$, 10^{-6}, and 10^{-5} $L_\odot$ (bottom to top sets of curves) and ages t = 10, 30, and 100 Myr (left to right or dotted, full and dashed lines). The circles show the results from Marley et al. (2007), increased by 0.38 k_B/baryon (cf. Fig. 5.4), for cold starts (filled circles) and hot starts (open circles), where the entropy is 1 Myr after the onset of cooling. Red and blue squares indicate the illustrative M and S_i used for the lightcurves in the bottom panel, with errorbars corresponding to the hatched regions there. *Bottom panel:* Two examples of cooling curves that have $L = 10^{-6}$ $L_\odot$ at 30 Myr. The dot-dashed (red) line has M = 1.85 M_J and S_i = 11.9 (hot start), while the full (blue) one has M = 12 M_J and S_i = 8.33 (cold start). Hashed regions indicate a spread of 0.5 M_J (0.1 k_B/baryon) for the hot- (cold-)start curve. The respective relative uncertainties are $\Delta M/M \simeq \frac{1}{2}\Delta t/t$ and $\Delta S_i \simeq 0.7\Delta \log_{10} L_{bol}$ for the cold- and hot-start cases, respectively (see text).

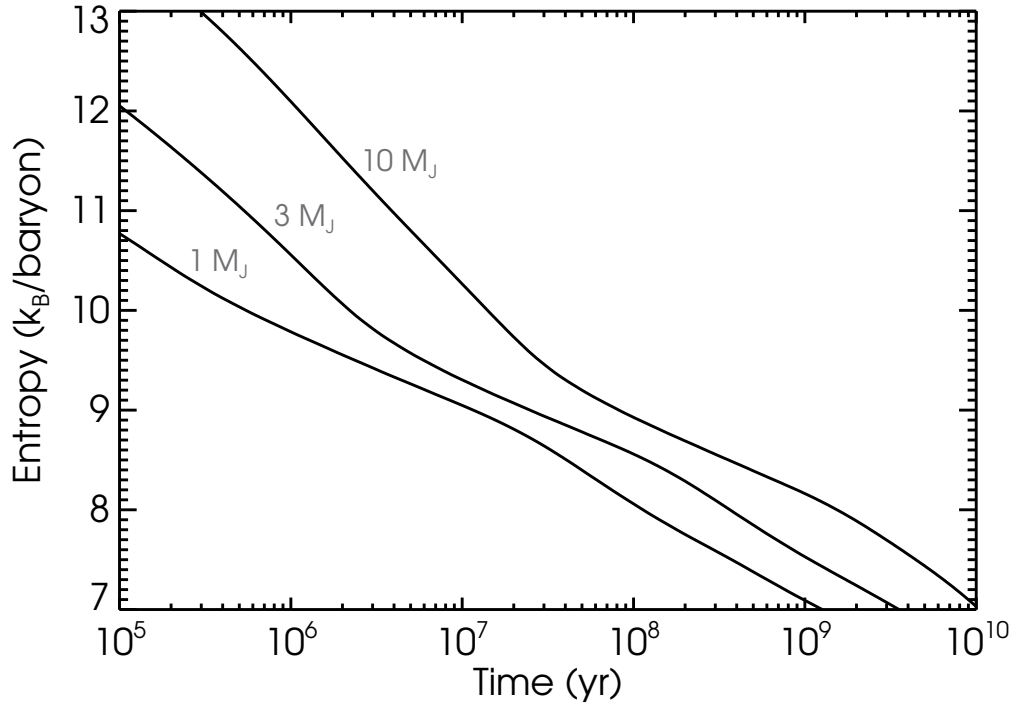

Fig. 5.6.: Entropy of hot starts as a function of time for planet masses of 1, 3, and 10 M_J (bottom to top). At a given age, the curve indicates the value of initial entropy above which the 'hot-start mass' applies. For a planet mass larger than the hot-start value, the initial entropy must be lower than the hot-start entropy at the current age.

hot-start mass is the true mass. If however the planet is more massive, this entropy value is instead an upper bound on the post-formation entropy. As a rule of thumb, the entropy slope is $\simeq -2$ or -1 k_B/baryon per time decade at early or late times, approximately, with the break coming from the change in the entropy regime (cf. Fig. 5.2).

5.4. General constraints from gravity and effective-temperature measurements

Before applying the analysis described in the previous section to observed systems, it is worth discussing a second way by which constraints on the mass and initial entropy can be obtained. The idea is to firstly derive an object's effective temperature and surface gravity by fitting its photometry and spectra with atmosphere models. Integrating the best-fitting model spectrum gives the luminosity, and this can be combined with $T_{\rm eff}$ and $\log g$ to yield the radius and the mass. This procedure was described and carefully applied by Mohanty et al. (2004) and Mohanty, Jayawardhana & Basri (2004). However, one can go further: considering models coupling detailed atmospheres with interiors at an arbitrary entropy, the mass and radius translate into a mass and current entropy. Then, using cooling tracks beginning with a range of initial conditions, the initial state of the object can be deduced given the age. Thus, in contrast to the case when only luminosity is used, M and $S_{\rm i}$ can both be determined without any degeneracy between the two.

In practice, however, there seems to be too much uncertainty in atmosphere models for this method to be currently reliable, as the work of Mohanty et al. shows. Their sample comprised a dozen young ($\sim$ 5 Myr) objects with $T_{\rm eff} \simeq$ 2600–2900 K[6] with high-resolution optical spectra.

[6]The spectral types are $\simeq$ M–M7.5, but Mohanty, Jayawardhana & Basri (2004) stress that the correspondence between the spectral type and effective temperature of young objects has not yet been empirically established and thus that calibration work (in continuation of theirs) remains to be done.

The combined presence of a gravity-sensitive Na I doublet and effective-temperature-sensitive TiO band near 0.8 μm allowed a relatively precise determination of $\log g$ and $T_{\rm eff}$ for most objects, with uncertainties of 0.25 dex and 150 K (Mohanty et al., 2004). However, there were significant offsets in the gravity ($\simeq$ 0.5 dex) of the two coldest objects with respect to model predictions of Baraffe et al. (1998) and Chabrier et al. (2000a). Mohanty et al. (2004) came to the conclusion that the models' treatment of deuterium burning, convection[7] or accretion – i.e. the assumed initial conditions – are most likely responsible for this disagreement at lower $T_{\rm eff}$. Moreover, the more recent work of Barman et al. (2011b) (see Section 5.9.1 below) indicates that 'unexpected' cloud thickness and non-equilibrium chemistry may compromise a straightforward intepretation of spectra in terms of gravity and temperature for young, low-mass objects. (See also Moses (2014) for a review of photochemistry and transport-induced quenching in cool exoplanet atmospheres.) Nevertheless, with the hope that future observations will allow a reliable calibration of atmosphere models, we illustrate with an example how M and $S_{\rm i}$ can be determined for an object from its measured $T_{\rm eff}$ and $\log g$.

Fig. 5.7 shows the constraints on the current mass and entropy of a planet with $\log g = 4.00 \pm 0.25$ (cm s^{-2}) and $T_{\rm eff} = 900 \pm 50$ K, where the uncertainties in the gravity and effective temperature are the possible accuracy reported by Mohanty et al. (2004) and thus correspond to an optimistic scenario. The constraints are obtained by simultaneously solving for M, S, R, and L given $T_{\rm eff}$ and $\log g$, with the $L(M,S)$ and $R(M,S)$ relations given by our model grid. The required mass and current entropy are $M = 6.5\ M_{\rm J}$ and $S = 9.2$, with the 1-σ ellipse within 4.0–10.1 $M_{\rm J}$ and 9.0–9.3 $k_{\rm B}$/baryon. The large uncertainty in the mass (the width of the ellipse) is dominated by the uncertainty in the gravity, since radius is roughly constant at these entropies. We note that non-Gaußian errorbars are trivial to propagate through when determining the mass and entropy in this way since it is only a matter of mapping each $(\log g, T_{\rm eff})$ pair to an (M,S) point.

Since this M–S determination concerns only the current state, it is independent of the cooling sequence, in particular of the 'hot vs. cold start' issue. Nevertheless, with this approach, it is immediately apparent what constraints the age imposes on the initial conditions. Indeed, not all (M,S) are consistent with an age since no planet of a given mass can be at a higher entropy than the hot-start model at that time (see Fig. 5.6). The entropy of hot starts is shown in Fig. 5.7 after 10, 30, and 50 Myr. The 30-Myr age excludes objects with $M \lesssim 6\ M_{\rm J}$, which is the hot-start mass of this example. Considering only hot-start evolution sequences would have been equivalent to requiring the solution to be on one of the hot-start (grey) curves. This is however a restriction which currently could not be justified, given our ignorance about the outcome of the formation processes.

The solid line in Fig. 5.7 indicate the derived constraints on the initial entropy, assuming an age of 30 Myr. These constraints are similar to ones based on luminosity (see Fig. 5.5) but are somewhat tighter since an upper mass limit is provided by the measurement of $\log g$. Even within a set of models, i.e. putting aside possible systematic issues with the atmospheres of young objects, it is however often the case that the surface gravity is rather ill determined (as for the objects discussed below in Section 5.5). In this case, provided a sufficiently large portion of the spectrum is covered, we expect the approach based on the bolometric luminosity presented in this work to be more robust than the derivation of constraints from effectively only the surface temperature. Indeed, the former avoids compounding uncertainties in $T_{\rm eff}$ with those in the radius in an evolutionary sequence, which can be further affected by the presence of a core (of unknown mass). With both sustained modelling efforts and the detailed characterisation of an increasing number of detections, one may hope that reliable atmosphere models for young objects will become available in a near future, allowing accurate determinations of the mass, radius, and initial entropy of directly-detected exoplanets.

[7] Qualitatively, their finding that theoretical tracks predict too quick cooling at low masses might be evidence for the argument of Leconte & Chabrier (2012) that convection in the interior of these objects could be less efficient than usually assumed.

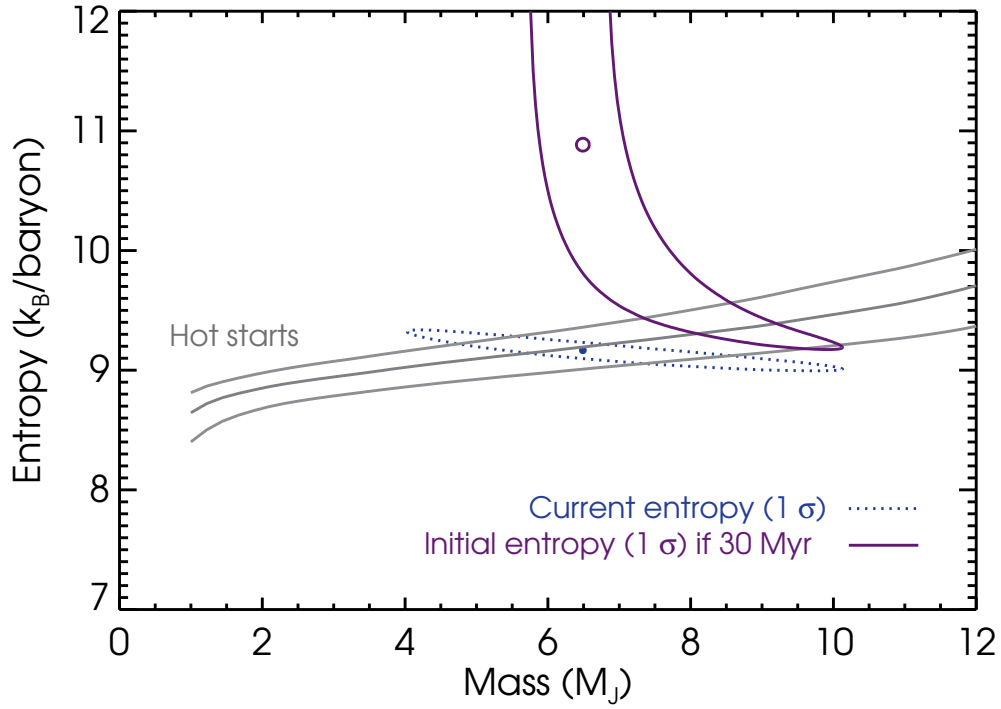

Fig. 5.7.: Constraints on the mass and entropy of an example planet from its gravity and effective temperature, with $\log g = 4.00 \pm 0.25$ (cm s^{-2}) and $T_{\rm eff} = 900 \pm 50$ K (and thus optimistic errorbars; see text). The mass and current entropy corresponding to $\log g = 4.00$ and $T_{\rm eff} = 900$ K are shown by a filled circle. The narrow ellipse (dotted line) shows the 1-σ confidence region in the mass and current entropy, whereas the deformed ellipse (solid line) shows the constraints on the initial entropy assuming an age of 30 Myr. The open circle corresponds to the 'measured' central value. The three solid grey lines indicate the entropy of hot starts at 20, 30, and 50 Myr (top to bottom). Higher masses can be seen to cool more slowly (see Section 5.2.5).

5.5. Comparison with observed objects

5.5.1. Directly-detected objects

Neuhäuser & Schmidt (2012) recently compiled and homogenously analysed photometric and spectral data for directly-imaged objects and candidates, selecting only those for which a mass below $\simeq 25\ M_{\rm J}$ is possible[8]. They report luminosities and effective temperatures, which they either take from the discovery articles or calculate, usually from bolometric corrections when a spectral type or colour index is available or brightness difference with the primary when not. Neuhäuser & Schmidt then use a number of hot-start cooling models to derive (hot-start) mass values along with errorbars, while recognising that hot starts suffer from uncertainties at early ages.

In this section, we determine joint constraints on the masses and initial entropies of directly-detected objects, focusing on the ones for which (tentative) additional mass information is available. A proper statistical analysis of the set of $M(S_{\rm i})$ curves would be challenging at this point due to the inhomogeneity of the observational campaign designs. However, upcoming surveys should produce sets of observations with well-understood and homogenous biases, convenient for a statistical treatment.

Before turning to specific objects, we display in Fig. 5.8 the data collected and computed by Neuhäuser & Schmidt (2012), as well as more recent detections, along with hot- and cold-start cooling tracks for different masses. This is an update of the analogous figures of Marley et al.

[8] This value was chosen by Schneider et al. (2011) as an approximation to the 'brown-dwarf desert', which is a gap in the mass spectrum between $\simeq$ 25–90 $M_{\rm J}$ (Marcy & Butler, 2000; Grether & Lineweaver, 2006; Luhman et al., 2007; Dieterich et al., 2012).

(2007) and Janson et al. (2011), which had only a handful of data points. Given doubts about its nature (e.g. Janson et al., 2012; Currie et al., 2012; Kalas et al., 2013; Kenworthy et al., 2013; Galicher et al., 2013; Currie et al., 2013), we do not include the reported upper limit for Fomalhaut b in this plot. Since their uncertainties are large, the central age values are taken as the geometric mean of the upper and lower bounds reported if no value is given. For RXJ1609 B/b, we use instead 11 ± 2 Myr (Pecaut, Mamajek & Bubar, 2012). The errorbars for the HR 8799 planets go up to 160 Myr and do not include the controversial Moya et al. (2010) asteroseismology[9] measurement of 1.1–1.6 Gyr since it is not used in our analysis (see discussion in Section 5.9.2). Finally, since no luminosity was given for WD 0806-661 B/b, we crudely estimate from the hot-start mass of 6–9 $M_{\rm J}$ from Luhman et al. (2012) and the Spiegel & Burrows (2012) models a luminosity of $\log L/L_{\odot} = -7.0 \pm 0.3$ at 1.5–2.5 Gyr.

Fig. 5.8 also includes four recent objects discovered since the analysis of Neuhäuser & Schmidt (2012): 2M0122 b (Bowler et al., 2013), GJ 504 b (Kuzuhara et al., 2013), 2M0103 ABb (Delorme et al., 2013), and κ And b (Carson et al., 2013; Bonnefoy et al., 2014a). For 2M0103 ABb, we estimate a bolometric luminosity of $\log L/L_{\odot} = -4.87 \pm 0.12$ as done in Appendix 5.9.3 for β Pic b. The same approach with κ And b yields $\log L/L_{\odot} = -3.83 \pm 0.15$, which is entirely consistent with the published value of -3.76 ± 0.06 dex (Bonnefoy et al., 2014a). We show the conservative age range of 30^{+120}_{-10} Myr for κ And b.

A recent detection which is not included in Fig. 5.8 is a candidate companion to HD 95086 with a hot-start mass near 4 $M_{\rm J}$ (Rameau et al., 2013; Meshkat et al., 2013), since only an L'-band measurement is available. Nevertheless, we report a prediction for its luminosity of $\log L_{\rm bol}/L_{\odot} \simeq -4.8 \pm 0.4$ from the estimated $T_{\rm eff} = 1000 \pm 200$ K and $\log g = 3.9 \pm 0.5$ (cm s^{-2}), with the $L_{\rm bol}$ errorbars entirely dominated by those on $T_{\rm eff}$ and ignoring that the atmospheric parameters were in fact estimated from hot-start models.

Fig. 5.8 shows that there are already many data points which – at least based solely on their luminosity – could be explained by cold, warm, or hot starts, highlighting the importance of being open-minded about the initial entropy when interpreting these observations. Indeed, as Mordasini et al. (2012) carefully argue, it is presently not warranted to assume a unique mapping between core accretion (CA) and cold starts on the one hand, and gravitational instability and hot starts on the other hand. (Even in the case of a weak correlation, planets found beyond $\simeq$ 50 AU, the farthest location where CA should be possible (Rafikov, 2011), could still in principle have formed by core accretion and then migrated outward (e.g. Ida et al., 2013).) As an extreme example of a cold start, we also display a cooling curve for a deuterium-burning object with a low $S_{\rm i}$ which undergoes a 'flash' at late times, somewhat arbitrarily chosen to pass near the data point of Ross 458 C (Burgasser et al., 2010); this contrasts with a monotonic hot-start cooling track at $\simeq$ 12 $M_{\rm J}$ which would also match the data point. Such solutions will be explored in a forthcoming work but we already note that, very recently, Bodenheimer et al. (2013) independently found lightcurves with flashes to be a possible outcome of a realistic formation process.

There are two features of the data distribution in Fig. 5.8 which immediately stand out. The first is that the faintest young objects are brighter than the faintest oldest objects, i.e. that the minimum detected luminosity decreases with the age of the companion. Moreover, this minimum, with the exception of data points (7), (31), and (30) (2M1207 b and WD 0806-661 B/b, which are particular for different reasons, and GJ 504 b) approximately follows the cooling track of a hot-start planet of $\simeq$ 10 $M_{\rm J}$. The interpretation of this fact is not obvious given that the data points forming the lower envelope come from multiple surveys and that different observational biases apply at different ages (e.g. due to the relatively low number of young objects in the solar neighbourhood).

The second feature is the absence of detections between the hot-start 10- and 15-$M_{\rm J}$ cooling curves, roughly between 20 and 100 Myr. More accurately, there is, in a given age bin in that range, a lower density of data points with luminosities around 10^{-4} $L_{\odot}$ than at higher or lower luminosities. A proper assesment of the statistical significance of this 'gap' in the data points

[9] The linguistically inclined reader will delight in the communication of Gough (1996) about the term's prefix 'ast(e)ro-'.

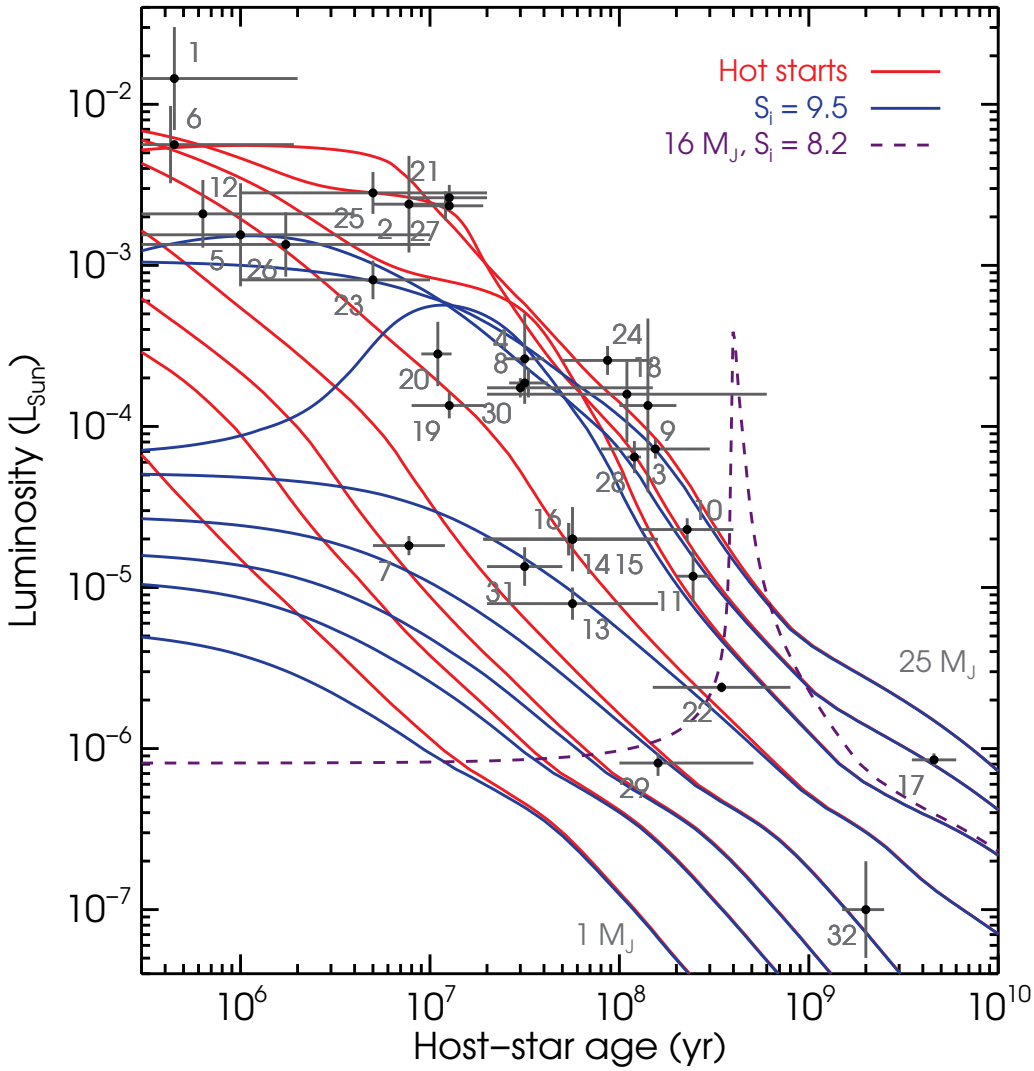

Fig. 5.8.: Directly-observed objects with a hot-start mass below ~ 25 M_J compared with cooling curves for $M = 1, 2, 3, 5, 10, 15, 20$, and 25 M_J (bottom to top), for $S_i = 9.5$ (dashed) and hot starts (dash-dotted); the 25-M_J curve is from Burrows et al. (1997) and has no cold-start equivalent. A lightcurve with a late-time deuterium 'flash' (at 400 Myr for $M = 16$ M_J, $S_i = 8.2$) is also shown to draw attention that some of these objects could, in principle, be undergoing rapid deuterium burning (Marleau & Cumming, in prep., but see Bodenheimer et al., 2013, who independently found such flashes). The data points are based on Neuhäuser & Schmidt, 2012 (see text for details) and are, with in boldface those investigated more closely below: (1) GG Tau Bb, (2) TWA 5 B, (3) GJ 417 BC, (4) GSC 8047 B/b, (5) DH Tau B/b, (6) GQ Lup b, **(7) 2M1207 b**, (8) AB Pic B/b, (9) LP 261-75 B/b, (10) HD 203030 B/b, (11) HN Peg B/b, (12) CT Cha b, **(13, 14, 15, 16) HR 8799 bcde**, (17) Wolf 940 B/b, (18) G 196-3 B/b, **(19) β Pic b**, (20) RXJ1609 B/b, (21) PZ Tel B/b, (22) Ross 458 C, (23) GSC 06214 B/b, (24) CD-35 2722 B/b, (25) HIP 78530 B/b, (26) SR 12 C, (27) HR 7329 B/b, (28) 2M0122 b, (29) GJ 504 b, (30) κ And b, (31) 2M0103 ABb, (32) WD 0806-661 B/b. Note that some luminosity errorbars were shifted for clarity and that those of Ross 458 C (0.03 dex) are smaller than its symbol.

would require taking both the smallness of the number of detections around 40 Myr and the biases and non-detections of the various surveys into account. However, it would not be surprising if the underdensity in the luminosity function $\mathrm{d}N/\mathrm{d}L$ of the data points, at a fixed age, proved to be real, since there is also a suggestive underdensity in the cooling curves. Indeed, the onset of deuterium burning near 13.6 M_J slows down the cooling, which breaks the hot-start scaling $L \propto t^{-1}$ (see Section 5.2.5) and leads to a greater distance between the hot-start cooling curves for 10 and 15 M_J than for 5 and 10 M_J. (This is clearly visible in fig. 1 of Burrows et al. (2001), which also shows that there is a similar gap for low-mass stars at 10^{-4} $L_\odot$ and 1–10 Gyr, due to the hydrogen main sequence.) In particular, cooling tracks for objects of 15, 20, and 25 M_J nearly overlap at $\sim$ 100 Myr around 10^{-4} $L_\odot$, where data points and their errorbars collect too. This tentative indication of an agreement between the detections and the cooling tracks suggests that the latter might be consistent with the data[10]. It will therefore be interesting to see how significant the 'gap' is and how it evolves as data points are added to this diagram.

In Fig. 5.8, the best-fitting age is calculated as the geometric mean of the reported upper and lower bounds since, in most cases, no best-fitting value is provided, and the bounds are typically estimates from different methods, which cannot be easily combined. In fact, the ages of young ($\lesssim$ 500 Myr) stars are in general a challenge to determine, as Soderblom (2010) reviews, and represent the main uncertainty in direct observations. Moreover, as Fortney et al. (2005) point out, assuming co-evality of the companion and its primary may be problematic for the youngest objects. Indeed, a formation time-scale of $\simeq$ 1–10 Myr in the core-accretion scenario would mean that some data points of Fig. 5.8 below $\sim$ 10 Myr may need to be shifted to significantly lower ages, by an unknown amount. This consideration is thus particularly relevant for GG Tau Bb, DH Tau B/b, GQ Lup b, and CT Cha b (data points 1, 5, 6, and 12), which are all possibly younger than 1 Myr, and would require a closer investigation.

We now provide detailed constraints for three planetary systems, chosen for the low hot-start mass of the companion (2M1207) or because additional mass information is available (HR 8799 and β Pic).

5.5.2. 2M1207

The companion to the brown dwarf 2MASSWJ 1207334–393254 (2M1207 A, also known as TWA 27 A; Gizis, 2002) is the first directly-imaged object with a hot-start planetary mass (Chauvin et al., 2004, 2005). Since the age and luminosity of 2M107 b are the inputs for our analysis, they are discussed in some detail in Section 5.9.1, along with tentative information on the mass. We adopt an age of 8^{+4}_{-3} Myr (Chauvin et al., 2004; Song et al., 2006) and a luminosity of $\log L/L_\odot = -4.68 \pm 0.05$ (Barman et al., 2011b), and assume that deuterium-burning masses above $\simeq$ 13 M_J (Spiegel et al., 2011) are excluded.

Fig. 5.9 shows the joint constraints on the mass and initial entropy of 2M1207 b based on its luminosity and age. We recover the hot-start mass of 3–5 M_J (Barman et al., 2011b), with equation (5.15) predicting $\simeq$ 3.9 M_J, but also find solutions at higher masses. If deuterium-burning masses can be excluded, the formation of 2M1207 b must have led to an initial entropy of $S_\mathrm{i} \geqslant 9.2$, with an approximate formal uncertainty on this lower bound of 0.04 k_B/baryon (see Section 5.3.1) due solely to the luminosity's statistical error, independent of the age's. This initial entropy implies that the M07 cold starts are too cold by 0.7 k_B/baryon, roughly independently of the mass, to explain the formation of this planet. This is consistent with the time-scale-based conclusion of Lodato, Delgado-Donate & Clarke (2005) that core accretion cannot be responsible for the formation of this system *if* one also accepts the received wisdom that core accretion necessarily leads to the coldest

[10] Cold-start curves too show this gap, to the extent that the luminosity rise due to deuterium burning is very sensitive to the initial entropy (see Fig. 5.8), which would need to be set accordingly finely to have the lightcurves pass through the data gap. The implicit assumptions here are that the observed distribution of masses is uniform in the approximate range 5–25 M_J (as are the mass values chosen for Fig. 5.8), and that the same applies to the initial entropy. The former cannot currently be validated but the latter seems reasonable, as the entropy interval over which cooling curves change from going above to below the gap is very narrow.

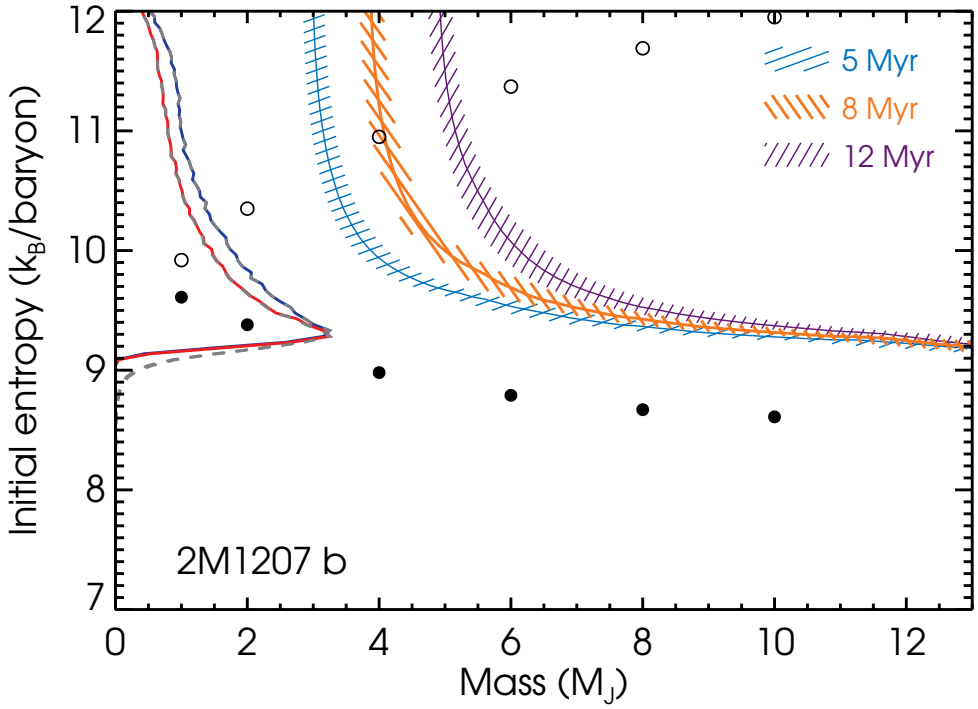

Fig. 5.9.: Allowed values of planet mass M and initial entropy S_i for 2M1207 b for assumed ages of 8^{+4}_{-3} Myr. The luminosity is that of Barman et al. (2011b), $\log L_{bol}/L_\odot = -4.68 \pm 0.05$, with the hatched regions corresponding to curves within $\pm 1\,\sigma$ of the luminosity values and the thick lines to the central value. The curves along the vertical axis show posterior distributions from MCMCs with different mass priors and assumed luminosity distributions. The solid curves only have an upper mass limit of 13 M_J, while the dashed curves include solutions in the deuterium-burning region, up to 20 M_J. For the blue curve (further from the left axis) and the corresponding dashed grey posterior (practically identical), a lognormal error distribution in time centred at $\sqrt{5 \times 12} \simeq 7.7$ Myr and of width 0.19 dex was used, while the red curve and corresponding dashed line are for a flat distribution in time between 5 and 12 Myr (and zero otherwise). The circles show the results from Marley et al. (2007), increased by 0.38 k_B/baryon (cf. Fig. 5.4), for cold starts (filled circles) and hot starts (open circles), where the entropy is 1 Myr after the onset of cooling.

starts. However, our robust quantitative finding is more general, in that it provides constraints on the result of the formation process which are *model-independent*.

To show how these $M(S_i)$ constraints can easily be made even more quantitative and thus suitable for statistical analyses, we ran a Metropolis–Hastings Markov-chain Monte Carlo (MCMC; e.g. Gregory, 2005) in mass and entropy with constant priors on these quantities. Uncertainties in the luminosity L and age t were included in the calculation of the χ^2 by randomly choosing an 'observed' L_{obs} and a stopping time for the cooling curve t_{stop} at every step in the chain. The quantity $\log L_{obs}$ was drawn from a Gaußian defined by the reported best value and its errorbars, and t_{stop} from a distribution which is either constant in t between the adopted upper and lower limits $t_1 = 5$ Myr and $t_2 = 12$ Myr and zero otherwise, or lognormal in t, centred at $t_0 = \sqrt{t_1 t_2} = 7.7$ Myr and with $\sigma_{\log t} = \log t_2/t_1 = 0.19$ dex. The results are shown along the vertical axis of Fig. 5.9 for four different assumptions. To obtain the two solid lines, we applied an upper mass cut at 13 M_J and took a lognormal (less peaked curve) or a top-hat (more peaked) distribution in time. The dashed curves come from the same MCMC chains but with a mass cut-off of 20 M_J, i.e. including deuterium-burning objects. Because of the delayed cooling due to deuterium burning, the required initial entropy drops down faster with mass than in the cold-start branch, such that lower S_i values are possible. At 20 M_J, the required S_i is 8.2, but it is still only 9 k_B/baryon at 15 M_J. However, the phase space for high masses is very small since the initial entropy needs to be extremely finely tuned; hence the smallness of the effect on the posteriors. As Fig. 5.9 shows, different assumptions on the luminosity, age, and mass priors all lead to similar results for the initial entropy, namely that

$S_\mathrm{i} \geqslant 9.2$ and that there are more solutions near this lower limit.

5.5.3. HR 8799

We now turn to the only directly-imaged system with multiple objects for which planetary masses are possible, HR 8799. The age of the system and the luminosities of the companions are discussed in Section 5.9.2, along with information on the mass. We consider ages of 20 to 160 Myr, close to the values of Marois et al. (2008), and use the standard luminosities of $\log L_\mathrm{bol}/L_\odot = -5.1 \pm 0.1$ (HR 8799 b), -4.7 ± 0.1 (cd) and -4.7 ± 0.2 (e) from Marois et al. (2008, 2010). It also seems reasonable to assume that deuterium-burning masses can be excluded for all objects, thanks to the (preliminary) results from simulations of the system's dynamical stability.

Fig. 5.10 shows the joint constraints on the masses and initial entropies of HR 8799 b, d, and e. Uncertainties in the age are taken into account by considering the two extremes of 20 Myr and 160 Myr separately, while the 1-σ errors in the luminosities are reflected by the width of the hatched regions. We find hot-start masses for 20 Myr of $4.4^{+0.4}_{-0.5}$ (b), 6.3 ± 0.6 (cd), and 6 ± 1 M_J (e), where the errorbars here come only from those on the luminosity, fully consistent with the prediction by equation (5.15) of $\simeq 4.2$ or 6 M_J. These values are in good agreement with Neuhäuser & Schmidt (2012) and are similar to the usually-cited 30-Myr values of $(5, 7, 7, 7)$ M_J (Marois et al., 2010). The hot-start masses for 160 Myr are above 12 (HR 8799 b) and 13 M_J (cde), and the $M(S_\mathrm{i})$ constraints for the latter three are not shown since they are within the deuterium-burning regime.

Excluding deuterium-burning masses for all objects and using only the luminosity measurements, Fig. 5.10 shows that all planets of the HR 8799 system must have formed with an initial entropy greater than 9 k_B/baryon, with $S_\mathrm{i} \gtrsim 8.9$ for b, $S_\mathrm{i} \gtrsim 9.2$ for c and d, and $S_\mathrm{i} \gtrsim 9.1$ for e (using as throughout this work the published SCvH entropy table; see Appendix 5.8). Using tentative upper mass limits of 7 and 10 M_J, respectively, the lower bounds on the initial entropies can be raised to 9.2 (b) and 9.3 k_B/baryon (cde) if one takes the conservative scenario of the 1-σ lower luminosities value at 20 Myr. These lower bounds on the entropy are however mostly independent of the age because they are set by cold-start solutions, where the age is much smaller than the cooling time at that entropy. Formal uncertainties on the lower bounds due to those in the luminosities are (see Section 5.3.1) approximately 0.07 (bcd) or 0.14 k_B/baryon (e) and thus negligible.

Here too we ran an MCMC to derive quantitative constraints on the initial entropy of each planet. The quantity $\log L_\mathrm{obs}$ was drawn from a Gaußian defined by the reported best value and its errorbars, and t_stop from a distribution which is either constant in t between the adopted upper and lower limits $t_1 = 20$ Myr and $t_2 = 160$ Myr and zero otherwise, or lognormal in t, centred at $t_0 = \sqrt{t_1 t_2} = 57$ Myr and with $\sigma_{\log t} = \log t_2/t_1 = 0.9$ dex. Posteriors on the initial entropy for each of the HR 8799 planets are shown along the vertical axis in Fig. 5.10, using a flat prior in S_i and a mass prior constant up to an M_max and zero afterward. The cases 'without mass constraints' ($M_\mathrm{max} = 13$ M_J) are nearly constant in S_i, especially for planet b, but show a peak near cold-branch values of 9 and 9.5 k_B/baryon for HR 8799 b and cde. Adding mass information from dynamical-stability simulations by taking $M_\mathrm{max} = (7, 10, 10, 10)$ M_J flattens the S_i posterior and shifts the minimum bounds at half-maximum from $(8.9, 9.2, 9.2, 9.2)$ to $(9.3, 9.5, 9.5, 9.4)$ k_B/baryon, respectively. We note that these results are insensitive to both the form of the uncertainty in t and the use of a non-flat prior in mass (as shown below for β Pic b in Section 5.5.4).

Comparing to the 'tuning fork' entropy values reproduced in Fig. 5.10, we find that the coldest-start models of M07 cannot explain the luminosity measurements for the HR 8799 planets. Spiegel & Burrows (2012) and Marley et al. (2012) also came to this conclusion, with the latter noting that 'warm starts' match the luminosity constraints. It is now possible to say specifically that *the Marley et al. (2007) cold starts would need to be made* $\Delta S \simeq 0.5$ k_B*/baryon hotter to explain the formation of the HR 8799 planets*. Given that the precise outcomes of the core accretion and gravitational instability scenarios are uncertain and that this system represents a challenge for both (as Marois et al., 2010 and Currie et al., 2011 review), quantitative comparisons such as our procedure allows should be welcome to help evaluate the plausibility of the one or the other.

We note in passing that one needs to take care also when interpreting the measurements of Hink-

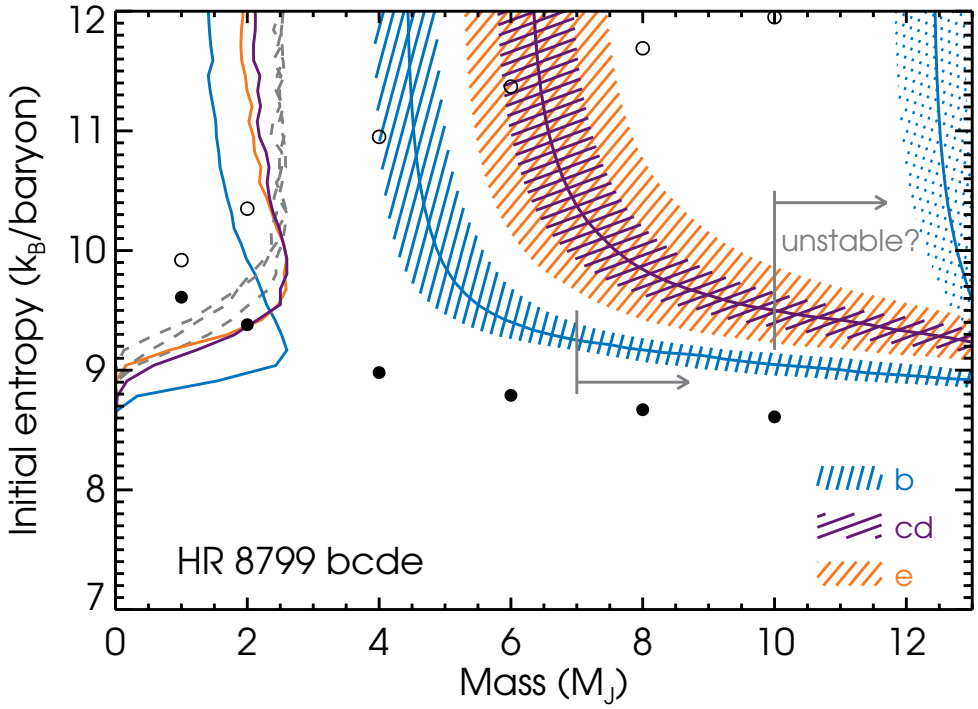

Fig. 5.10.: Allowed values of planet mass M and initial entropy S_i for HR 8799 b ($\log L_{bol}/L_\odot = -5.1 \pm 0.1$; blue bands), HR 8799 cd (-4.7 ± 0.1; purple), and HR 8799e (-4.7 ± 0.2; orange) for assumed ages of 20 (lower-mass group) and 160 Myr (higher-mass band; planets cde are outside the plotting range). Luminosities are from Marois et al. (2008, 2010), and nearly in agreement with Marley et al. (2012). The lines correspond to the best-fitting luminosity values, while the hatched regions use the 1-σ errorbars. Along the left axis are shown the posterior distributions in S_i (colours as for the M–S_i hashed bands), with no particular relative normalisation. These were obtained from an MCMC, taking luminosity and age uncertainties into account based on lognormal distributions (see text), and using flat priors in S_i and M. The mass upper cut-off is $M_{max} = 13\ M_J$ (full lines) or $M_{max} = (7, 10, 10, 10)\ M_J$ (for planets bcde, respectively; dashed lines), since analyses of the system's dynamical stability seem to indicate that higher masses are unstable. This is indicated by the vertical line segments with arrows in the direction of the excluded masses. The circles show the results from M07, increased by 0.38 k_B/baryon (cf. Fig. 5.4), for cold starts (filled circles) and hot starts (open circles), where the entropy is 1 Myr after the onset of cooling.

ley et al. (2011) and Close & Males (2010). These authors measured upper limits on the brightness of companions within 10 AU and between 200 and 600 AU from the star, respectively. However, both groups then used the hot-start models of Baraffe et al. (2003) to translate the brightness limits into masses (11 M_J at 3–10 AU and 3 M_J within 600 AU, respectively). Therefore, since colder-start companions would need to be more massive to have the same luminosity, what they provide are really "*lower* upper limits" on the mass of possible companions. How much higher the masses could realistically be in this case is difficult to estimate without a bolometric luminosity, but there is an important general point: without the restriction of considering only hot-start evolutionary tracks, *luminosity upper limits do not provide unambiguous mass constraints*. Incidentally, this more general view of the results of Hinkley et al. (2011) means that the unseen companion evoked by Su et al. (2009) as the possible cause of the inner hole (at $\lesssim 6$ AU) does not have to be of small mass. However, this inner object would nevertheless have to be consistent with the results of dynamical stability simulations, with those of Goździewski & Migaszewski (2014) indicating a mass less than $\simeq$ 1–8 M_J.

5.5.4. β Pic

A companion to the well-studied star β Pic was first observed in 2009 (Lagrange et al., 2009; Bonnefoy et al., 2011) and, very recently, it became the first directly-detected object with a planetary

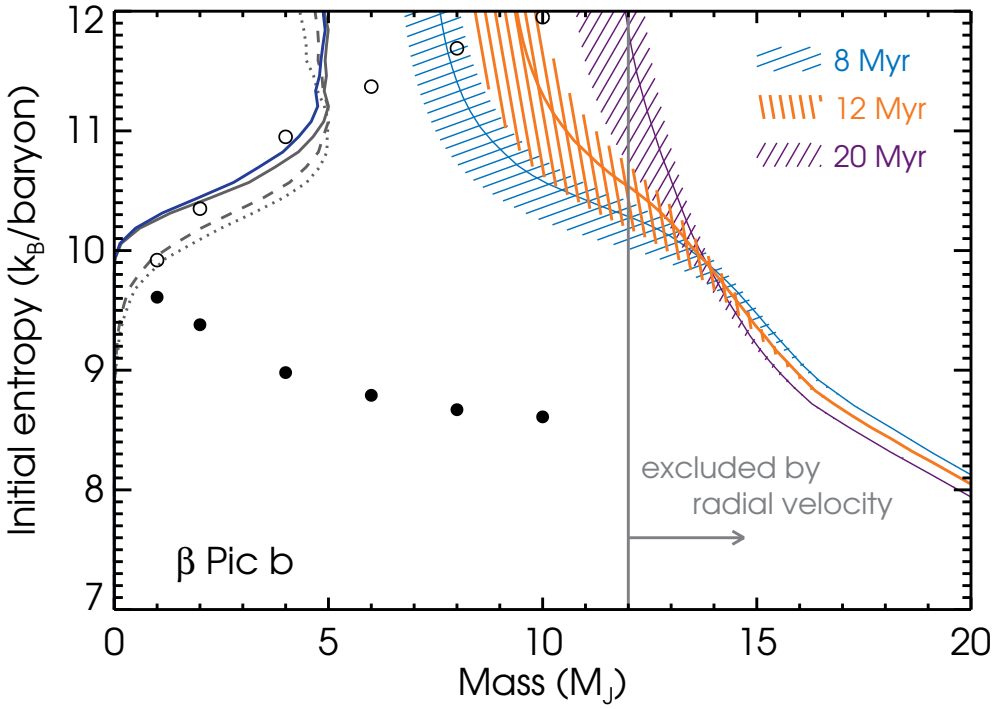

Fig. 5.11.: Allowed values of planet mass M and initial entropy S_i for β Pic b using our estimated $\log L_\mathrm{bol}/L_\odot = -3.90^{+0.05}_{-0.12}$ and an age of 12^{+8}_{-4} Myr. The hatched regions correspond to luminosity values within the (asymmetrical) 1-σ interval, with the central values marked by thick lines. The curves along the vertical show the marginalised posterior distribution on S_i from an MCMC simulation using the luminosity and age values and their uncertainties. These were taken to be lognormal but asymmetric for the luminosity, and lognormal in time, centred at $t_0 = \sqrt{8 \times 20} = 12.7$ Myr with a standard deviation of 0.35 dex. The full blue line (closer to the vertical axis) results from the (M, S_i) distribution being multiplied by a $\mathrm{d}N/\mathrm{d}M \propto M^\alpha$ prior, with $\alpha = -1.3$ (Cumming et al., 2008; Nielsen & Close, 2010), and zero for $M > 12\ M_\mathrm{J}$, while the full grey posterior has only a mass cut at 12 M_J, from the Lagrange et al. (2012) radial-velocity constraint. The dashed and dotted curves both have an upper mass cut of 20 M_J, with and without the $\mathrm{d}N/\mathrm{d}M$ prior applied, respectively. The circles show the results from Marley et al. (2007), increased by 0.38 k_B/baryon (cf. Fig. 5.4), for cold starts (filled circles) and hot starts (open circles), where the entropy is 1 Myr after the onset of cooling.

mass for which radial-velocity data are also available. The age of the system is taken as 12^{+8}_{-4} Myr (Zuckerman et al., 2001), and we discuss in detail in Section 5.9.3 how we derive a bolometric luminosity[11] of $\log L_\mathrm{bol}/L_\odot = -3.90^{+0.05}_{-0.12}$.

Fig. 5.11 shows the $M(S_\mathrm{i})$ constraints available for β Pic b from our luminosity estimate and the radial-velocity (RV) constraint. We recover a hot-start mass $\simeq 9.5 \pm 2.5\ M_\mathrm{J}$ (cf. $\simeq 9.4\ M_\mathrm{J}$ from equation 5.15), in agreement with Quanz et al. (2010) and Neuhäuser & Schmidt (2012), but additionally find that higher masses are consistent with the luminosity measurement. Excluding solutions where deuterium burning plays an important role in the evolution of the object (recognisable by the extreme thinness of the constant-luminosity $M(S_\mathrm{i})$ curve) implies that $S_\mathrm{i} \geqslant 9.8$. Using the RV mass upper limit, these constraints on the initial entropy can be made tighter: with an age of 12 Myr, it must be that $S_\mathrm{i} \geqslant 10.5$. Since this corresponds to a warm start, both uncertainties on the age and on the luminosity contribute to that on the minimum S_i, of order 0.5 k_B/baryon.

[11] As this manuscript was being prepared, we became aware of the first robust estimate of the bolometric luminosity, by Bonnefoy et al. (2013). They find $\log L_\mathrm{bol}/L_\odot = -3.87 \pm 0.08$, which excellently agrees with our value and thus does not change our conclusions. In particular, they find similar constraints on the initial entropy of β Pic b, although this depends on which band they use (cf. their fig. 11 with our Fig. 5.11). We also note the more recent estimate by Currie et al. (2013) of $\log L_\mathrm{bol}/L_\odot = -3.80 \pm 0.02$ (very near our approximate 1-σ upper limit), from which they estimate a (hot-start) mass in the 3–11-M_J range. Importantly, they obtain the lower masses by considering an age of 7 Myr for β Pic b, i.e. by relaxing the assumption that it is co-eval with its star (see Section 5.5.1).

This lower limit on S_i implies that coldest-start objects of any mass are too cold by a significant 1.5–2.0 k_B/baryon. Various authors (e.g. Quanz et al., 2010; Bonnefoy et al., 2011) recognised that the classical cold starts (M07; Fortney et al., 2008) cannot explain the observations, but it is now possible to quantify this. These results are mostly insensitive to the uncertainty on the age range; using instead 12–22 Myr as summarised by Fernández et al. (2008) would not change the conclusions.

As for the objects in the 2M1207 and HR 8799 systems, we ran an MCMC to obtain a posterior distribution on the initial entropy. This is shown along the vertical axis of Fig. 5.11 for four different assumptions. In all cases, we assumed lognormal uncertainties on the age and the luminosity, with asymmetric upper and lower errorbars for the latter. For the full curve closer to the vertical axis (in blue), we applied an upper mass cut at 12 M_J and took into account that the underlying (real) mass distribution is possibly biased towards lower masses, as radial velocity measurements indicate (Cumming et al., 2008; Nielsen & Close, 2010). Out of simplicity, this was done by taking the (M, S_i) distribution obtained with a flat prior in mass and using importance sampling to put in a posteriori a $dN/dM \propto M^\alpha$ prior, with $\alpha = -1.3$, thus weighing lower masses more[12]. Of course, the value of α might depend on the formation mechanism relevant to the object but this serves to illustrate the effects of a non-constant prior on mass. The other three posterior distributions on S_i of Fig. 5.11 (in grey) correspond to the remaining combinations of 'with mass cut or not' and 'with power-law mass prior or not'. These curves are all similar, with the radial-velocity measurement increasing the minimum bound at half maximum from 10.2 to 10.5 k_B/baryon, quite insensitively to the use of the dN/dM prior.

At the distance from its primary where β Pic b is currently located ($\simeq$ 9 AU), core accretion is expected to be efficient and thus a likely mechanism for its formation (Lagrange et al., 2011; Bonnefoy et al., 2013). Thus, the question posed to formation models is whether core accretion can be made hotter (by 1.5–2 k_B/baryon) than what traditional cold starts predict. Very recently, Bodenheimer et al. (2013) and Mordasini (2013) showed that in the framework of formation models (which seek to predict S_i), different rocky core masses are associated with a significantly different initial entropies at a fixed total mass; for instance, Bodenheimer et al. (2013) found $S_i = 7.5$ for a 12 M_J object with a core of 5 $M_\oplus$ but $S_i = 9.1$ when a different choice of parameters lead to a core mass of 31 $M_\oplus$. Since these coldest starts assume that all the accretion energy is radiated away at the shock, the constraints on the initial entropy stress the need to investigate the physics of the shock (and its dependence on physical quantities such as the accretion rate), when the initial energy content of the planet is claimed to be set.

5.6. Summary

The entropy of a gas giant planet immediately following its formation is a key parameter that can be used to help distinguish planet formation models (Marley et al., 2007). In this paper, we have explored the constraints on the initial entropy that can be obtained for directly-detected exoplanets with a measured bolometric luminosity and age. When the initial entropy is assumed to be very large, a 'hot start' evolution, the measured luminosity and age translate into a constraint on the planet mass. In contrast, when a range of initial entropies are considered ('cold starts' or 'warm starts'), the hot-start mass is in fact only a lower limit on the planet mass: larger-mass planets with lower initial entropies can also reproduce a given observed luminosity and age. Fig. 5.5 shows the

[12] Wahhaj et al. (2013) derive in a recent analysis of the NICI campaign results for debris-disc stars a similar slope: if the linear semi-major axis power-law index $\beta_a = -0.61$ as Cumming et al. (2008) found for radial-velocity planets within 3 AU, the 66 non-detections combined with the Vigan et al. (2012) survey imply $\alpha < -1.7$ to 2 σ, with the most likely values at $0.3\alpha + \beta_a \ll -1$. When however β Pic b and HR 8799 bcd are included in the analysis, $\alpha > 2.2$ for $\beta_a = -0.61$, with more solutions at $\beta_a = -2.1$, $\alpha \geqslant 2.2$. (Too few detected objects prevent Biller et al. (2013) from inferring constraints on α and β in a similar analysis of young moving-group stars.) Note finally that hot-start models were used to convert magnitudes to masses and that most targets are less than 100 Myr old, with a significant fraction near 10 Myr; ignoring cold starts at these ages can skew the inferred (limits on the) mass distribution. Also considering colder starts should yield more negative constraints on α given the same luminosity constraints.

allowed values of mass and entropy for different ages and luminosities, and can be used to quickly obtain estimates of mass and initial entropy for any given system.

To derive these constraints, we constructed a grid of gas giant models as a function of mass and internal entropy which can then be stepped through to calculate the time evolution of a given planet. In a hot-start evolution, the structure and luminosity of cooling gas giant planets are usually thought of as being a function of mass and time only; this leads to a 'hot-start mass' as given by equation (5.15). Once the assumption of hot initial conditions is removed, however, a more convenient variable is the entropy of the planet. One way to think of this is that gas giants obey a Vogt–Russell theorem in which the internal structure, luminosity, and radius of a planet depend only on its mass and entropy (as well as its composition, as for stars). Fig. 5.2 shows the luminosity as a function of entropy for different masses, and a general fitting formula for $L(M, S)$ is given by equation (5.9). (Similarly, cooling tracks with arbitrary initial entropy are well described analytically by equations (5.13–5.14).) A noteworthy result is that in the intermediate-entropy regime ($S \simeq 8.5$–$10\ k_\mathrm{B}$/baryon), where the outer radiative zone is thick and follows a radiative-zero solution, the luminosity obeys $L = Mf(S)$ as found for irradiated gas giants by Arras & Bildsten (2006), with $f(S)$ a steeply increasing function of the entropy. We also note that constraints obtained for models with a particular helium mass fraction Y can be easily translated to another Y with equation (5.12) as it provides an approximate value for $\mathrm{d}S/\mathrm{d}Y$ at constant L. This is general and independent of the approach used to compute the cooling.

We find that our models are in good agreement (within tens of per cent) with the hot-start models of Burrows et al. (1997) and Baraffe et al. (2003), as well as the cold-start models of Marley et al. (2007), and cooling models calculated with the MESA stellar evolution code (Paxton et al., 2011, 2013). We caution that the Spiegel & Burrows (2012) and Mollière & Mordasini (2012) models, for example, use a version of the Saumon et al. (1995) equation of state whose entropy is offset by a constant $0.52\ k_\mathrm{B}$/baryon from the published tables (which the present work uses); this difference is not significant physically but needs to be taken into account when comparing results of various groups. Details and (Y, P, T, ϱ, S) points for a quick comparison are provided in Appendix 5.8. The remaining intrinsic difference in entropy between our models and those just cited is then approximately $|\Delta S| \simeq 0.15$ at worse. This is more important than differences in opacities or composition; for example, we estimate from Saumon et al. (1996) that the uncertainty in the helium (Y) and metal (Z) mass fractions introduces variations of at most 10 per cent in the luminosity at a given age.

We stress again that when the initial entropy is allowed to take a range of values, the hot-start mass (equation (5.15)) is only a lower limit on the companion mass. The larger range of allowed masses means that the hot-start mass could actually lead to the mischaracterization of an object, with a hot-start mass in the planetary regime actually corresponding to an object with a mass above the deuterium-burning limit for low enough entropies. One way to break the degeneracy between mass and entropy is an accurate determination of the radius from spectral fitting (or actually a determination of $\log g$ and T_eff from the spectrum), which would yield the mass and (current) entropy of the object without any degeneracy (see e.g. Fig. 5.7). As discussed in Section 5.4, however, current atmosphere models have significant uncertainties that make this approach difficult. Another possibility is to obtain independent constraints on the mass of a companion, for example from dynamical considerations.

In Section 5.5, we applied our models to three directly-imaged objects which have hot-start masses in the planetary-mass regime and for some of which there are additional constraints on the planet mass. We find that the initial entropy of 2M1207 b is at least $9.2\ k_\mathrm{B}$/baryon, assuming that it does not burn deuterium. For the planets of the HR 8799 system, we infer that they must have formed with $S_\mathrm{i} > 9.2\ k_\mathrm{B}$/baryon, independent of the age uncertainties for the star. Finally, a similar analysis for β Pic b reveals that it must have formed with $S_\mathrm{i} > 10.5\ k_\mathrm{B}$/baryon, using the radial-velocity mass upper limit of $12\ M_\mathrm{J}$. These initial entropy values are respectively ca. 0.7, 0.5, and $1.5\ k_\mathrm{B}$/baryon higher than the ones obtained from core accretion models by Marley et al. (2007). This quantitatively rules out the coldest starts for these objects and constrains warm starts,

especially for β Pic b.

An important point is that the uncertainties in age and luminosity impact the derived hot-start mass and the lower bound on initial entropy in different ways. The major uncertainty in direct detections is the age of the star and, relevant for very young systems, all the more that of the planet. This age uncertainty translates into errorbars for the hot-start mass which are $\Delta M/M \simeq \frac{1}{2}\Delta t/t$. However, the uncertainty on the initial entropy on the mass-independent branch of the $M(S_\mathrm{i})$ curve is due only to that in the bolometric luminosity, with $\Delta S_\mathrm{i} \simeq 1/\lambda \Delta \log L_\mathrm{bol}$ where $\lambda \simeq 0.7$ when $S_\mathrm{i} \lesssim 9.6$ (or, less accurately, when $L \sim 10^{-6}$–$10^{-4}\ L_\odot$). This uncertainty ΔS_i is typically very small, which means that, up to systematic errors, the initial entropy can be determined quite accurately.

It has been pointed out before that current direct-imaging detections are all inconsistent with the cold-start predictions from core-accretion models. It is important to stress however that the cold starts are in some sense an extreme case, as they assume complete radiation efficiency at the shock during runaway accretion, which is argued to set the low initial entropy of planet. By varying the nebula temperature or the accretion rate, Marley et al. (2007) were able to change the entropy by barely $\Delta S \simeq 0.1$; however, Mordasini (2013) and Bodenheimer et al. (2013) report that it is possible within the core-accretion scenario to obtain considerably higher entropies, increased by as much as 1–2 k_B/baryon, when considering different masses for the solid core (through a self-amplifying process explained in Mordasini, 2013). With β Pic b a likely candidate for formation by core accretion, this indicates that it is essential to gain a deeper understanding about what sets the initial entropy, for instance by looking in more detail at the properties of the shock during runaway accretion.

The derived bounds on S_i for the HR 8799 objects and β Pic b made use of information on the mass, which comes from dynamical stability analyses and radial velocity, respectively. Radial-velocity data of directly-detected planets are currently available only for β Pic b, but this should change in a near future as close-in planets start being detected directly. In the absence of dynamical information, an upper limit to the mass (and thus a lower limit on the initial entropy) should be obtainable from $\log g$, even if its errorbars are large; thus, in practice, the $M(S_\mathrm{i})$ constraint curve does not extend to arbitrarily high masses as a pure luminosity measurement would imply.

Finally, we ran Markov-chain Monte Carlo simulations to derive more detailed quantitative constraints on the mass and entropy of directly-detected objects. When taking the uncertainties in the age and luminosity into account, we considered normal, lognormal, and flat distributions and found the chosen form to make little difference. The advantage of this approach is that it allows one to derive posterior distributions on the initial entropy, which are suitable for statistical comparisons. Given the small semi-major axis of β Pic b (9 AU), we also tried a prior $\mathrm{d}N/\mathrm{d}M \propto M^{-1.3}$ (which describes the population of radial-velocity planets) in addition to a flat prior on M. The latter case yielded posterior distributions on S_i with a more pronounced peak.

The benefits that the expected large increase in the number of directly-detected exoplanets in the near future should bring are at least twofold. Firstly, each new detection will yield a new constraint on the initial entropy and therefore formation mechanism. Particularly with the ability to detect lower mass gas giants at small semi-major axes ($\lesssim$ 20 AU), which should be possible with instruments such as GPI or SPHERE, there will be an opportunity to constrain the state of the gas giant immediately following core accretion. Secondly, with a larger sample of objects comes a chance for a statistical comparison with formation models. For example, as noted in Section 5.5.1, the onset of deuterium burning leads to a relative underdensity of planets with luminosities $\sim 10^{-4}\ L_\odot$ and ages of tens of Myr (assuming that the masses of substellar objects are smoothly distributed near the deuterium-burning limit). Indeed, it is interesting that there appears to be such an underdensity in the current data sample (see Fig. 8), although the small number of detections so far means that this could be due to a statistical fluctuation. The best constraints on initial conditions for planet cooling will come from improved spectral models that can give reliable determinations of $\log g$ and T_eff.

Acknowledgments

We thank P. Bodenheimer, D. Saumon, J. Ferguson, K. Goździewski, A. Burrows, J. Fortney, A. Showman, M. Marley, X. Huang, C. Mordasini, D. Spiegel, T. Guillot, T. Schmidt, M. Bonnefoy, B. Biller, and J. Carson for useful and often detailed discussions, helpful and rapid answers to inquiries, and generosity with data. This work was supported by the National Sciences and Engineering Research Council of Canada (NSERC) and the Canadian Institute for Advanced Research (CIFAR), and by a scholarship from the Fonds de recherche du Québec – Nature et technologies (FRQNT). GDM warmly thanks the MPIA for support during the last stages of this work.

5.7. Appendix A: Radii

For completeness, we present and compare the radii R in our models as a function of mass M and entropy S. This comparison thus separates out possible differences in the treatment of deuterium burning since the planetary structure at a given (M, S) is independent of the nuclear energy generation, which only affects the time evolution.

Fig. 5.12a shows $R(S)$ for different masses, using the standard grid with a helium mass fraction $Y = 0.25$ and without a solid core. At low entropies, objects of a given mass have a roughly constant radius asymptotically tending to the zero-temperature value (Zapolsky & Salpeter, 1969; Hubbard, 1977; Arras & Bildsten, 2006), while the radius increases at high entropies. This increase is less pronounced for higher masses, with more massive objects being smaller at any given entropy. Finally, there is at a given mass a maximum entropy for which a finite radius is possible, as the upturn of the curves suggests. In fact, each curve turns over on to a hot branch (not calculated) where the ion thermal pressure dominates, leading to distended objects; see for instance the analytic one-zone model of Deloye & Bildsten (2003).

The inset of Fig. 5.12a shows the relative difference $\Delta R/R_{\rm ref} = (R - R_{\rm ref})/R_{\rm ref}$ between our radius at a given mass and entropy and that from more detailed calculations, either Burrows et al. (1997) or MESA (revision 4723; Paxton et al., 2011, 2013), over the range where data are available. There are larger deviation at higher entropies but the overall agreement for masses between 1 and 20 $M_{\rm J}$ is excellent, with our models systematically a few per cent smaller.

In Fig. 5.12b are displayed radii as a function of mass for entropies from 14 down to 7 $k_{\rm B}$/baryon. Objects with $S < 10$ have $R < 2\ R_{\rm J}$ for all masses, with radii rapidly increasing at higher entropies. Low-entropy planets approach the zero-temperature limit (Zapolsky & Salpeter, 1969), with a maximum[13] radius of 1.08 $R_{\rm J}$ at 2.1 $M_{\rm J}$ for $S = 7$ (cf. the $T = 0$ result of $R_{\rm max} = 0.98\ R_{\rm J}$ at 2.77 $M_{\rm J}$). At higher entropies, there are no solutions below a certain mass, preventing the existence of a finite maximum to $R(M)$ (cf. Deloye & Bildsten, 2003).

Fig. 5.12b also shows $R(M)$ curves at fixed S in a grid with a 20-$M_\oplus$ core at a constant density of 8 g cm^{-3} and in a grid with a helium mass fraction $Y = 0.30$ (and no core). Differences are small when including a solid core but larger when varying the helium fraction, with differences of the order of tens of per cent at smaller entropies. Note that a realistic equation of state for the core, such as a half-half rock–ice mixture from ANEOS (Marley et al., 2007) as formation by core accretion may produce, would yield average core densities closer to $\simeq$ 10–100 g cm^{-3}. The effect on the radius should however still be within tens of per cent.

5.8. Appendix B: A systematic entropy offset in different versions of the SCvH EOS

Investigating the entropy offset between the models of Spiegel & Burrows (2012) and our work (see Section 5.2.6), we noticed that there is a nearly constant entropy offset of 0.51–0.52 $k_{\rm B}$/baryon

[13] The presence of a turnover in the mass–radius relationship is due to the balance between the attractive Coulomb forces in the ion-electron plasma and the repulsive Fermi forces between the degenerate electrons.

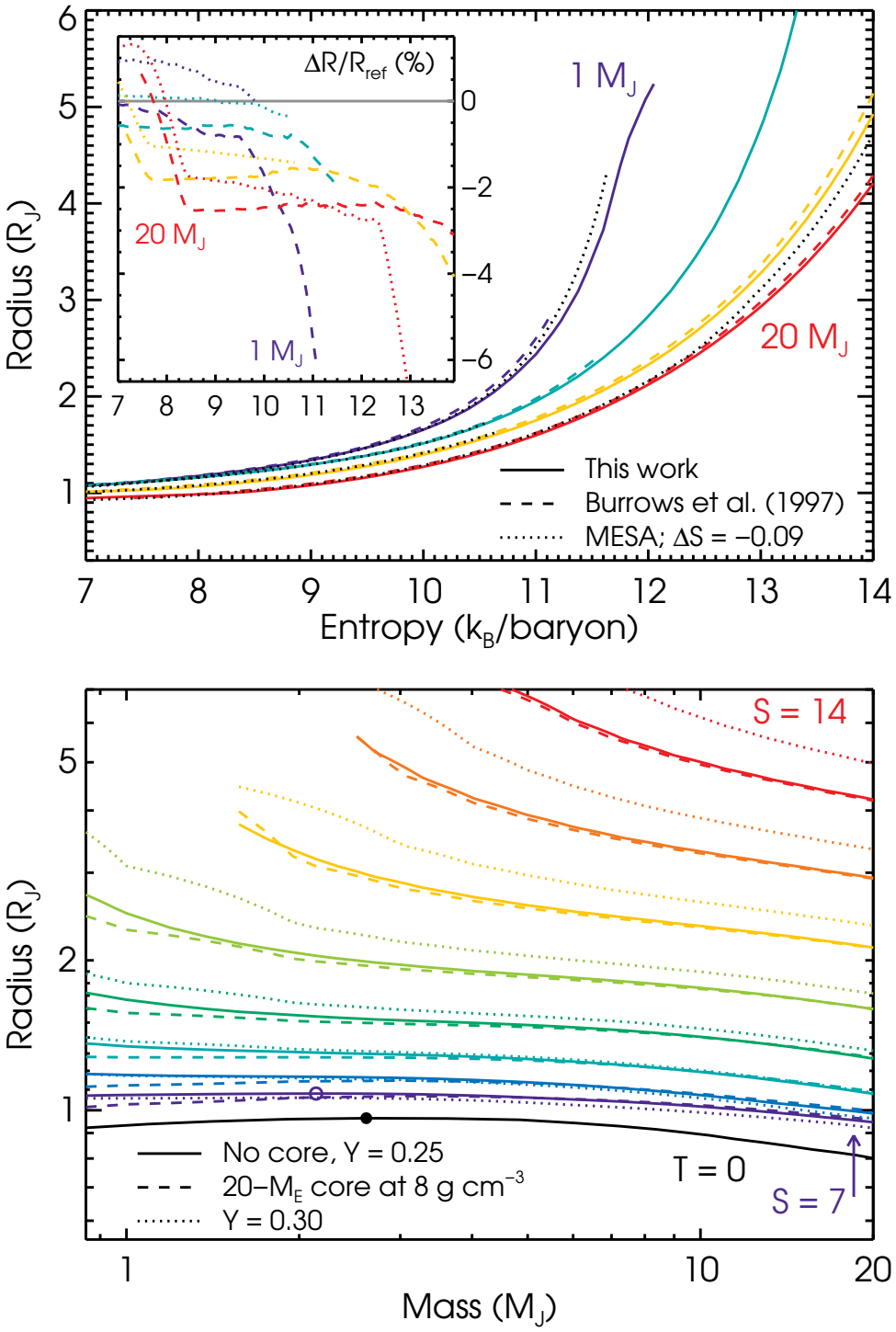

Fig. 5.12.: *Top panel:* Radii as a function of entropy for $M = 1$, 3, 10, and 20 M_J from top to bottom in our models (solid lines) compared to those of Burrows et al. (1997) (dashed) and MESA (revision 4723; dotted). The entropy values of Burrows et al. (1997) were shifted by $(1-Y)\ln 2 = 0.52\ k_B$/baryon for 'thermodynamic reasons' as discussed in Appendix 5.8, while those of MESA were shifted by the $-0.09\ k_B$/baryon offset needed to match $L(S)$ (see Fig. 5.4). The inset shows the percentage difference with Burrows et al. (1997) (dashed lines) and MESA (dotted lines) against entropy. We use for Jupiter's radius $R_J = 7.15 \times 10^9$ cm. *Bottom panel:* Radii as a function of mass for $S = 7$–14 in steps of 1 k_B/baryon from top to bottom in the standard grid (without a core and with a helium mass fraction $Y = 0.25$; solid lines). Note the logarithmic vertical scale. The lowest curve is the $T = 0$ result of Zapolsky & Salpeter (1969) for $Y = 0.25$, with the peak of $R_{max} = 0.96\ R_J$ at 2.6 R_J indicated by a filled circle (note that their table 1 indicates instead 0.98 R_J at 2.77 M_J). A ring symbol indicates the peak for $S = 7$ in the standard grid. For comparison, radii in grids with a 20-$M_\oplus$ core and $Y = 0.25$ (dashed) or without a core but with $Y = 0.30$ (dotted) are also shown.

over a large portion of the ϱ–T plane between the entropy of Burrows et al. (1997)[14] and that of our SCvH data[15]. As pointed out by D. Saumon (2013, priv. comm.), this is very probably due to the absence, in some versions of the EOS, of the statistical weight due to the spin states of the proton in the hydrogen partition function. The term omitted in the entropy (to facilitate comparisons with other equations of state, which usually do not include it; D. Saumon 2013, priv. comm.) is of $k_B \ln 2$ per proton, which implies an offset of $(1 - Y) \ln 2 = 0.52\ k_B$/baryon for $Y = 0.25$. This is almost what we find from the direct comparison, leaving only a small residual difference $\Delta S \simeq 0.07$ from the luminosity comparison ($\Delta S \simeq 0.14$ when comparing with Marley et al., 2007). Thus Burrows et al. (1997), Spiegel & Burrows (2012), and Mollière & Mordasini (2012) all use a version which does not include the contribution, while the published tables include it.

We emphasize however that an additive constant in the entropy is not important physically, nor for the evolution of the planet, since only differences in the entropy are meaningful. The relevance here is only when comparing (initial) entropies as determined using different models, with the entropy being a convenient label for the adiabat of the interior. In this spirit, we provide a few values to allow a quick determination of whether a given EOS includes the term or not: for $Y = 0.25$ at $P = 5.5{\times}10^{12}$ erg cm^{-3} and $T = 5{\times}10^4$ K (hence $\varrho = 1.001$ erg cm^{-3}), $S = 10.557\ k_B$/baryon according to the interpolated published SCvH tables. For $Y = 0.243$ (0.30), $\varrho = 0.9954$ (1.044) erg cm^{-3} and $S = 10.617$ (10.128) at the same (P, T). To avoid confusion, we encourage publications using the Saumon et al. (1995) equation of state to quote entropy values as given in the published tables, and to make clear that this is the case.

5.9. Appendix C: Age, luminosity, and mass constraints

5.9.1. 2M1207

Age and luminosity

The first directly-imaged object with a hot-start planetary mass (Chauvin et al., 2004, 2005) is located 0.8″ from its M8 brown-dwarf primary, a well-studied (see Gizis, 2002 for the report of the discovery and Skemer et al., 2011 for a summary) member of the young (8^{+4}_{-3} Myr) TW Hydræ association (Chauvin et al., 2004; Song et al., 2006) at a distance of 53±1 pc (as averaged by Skemer et al., 2011 from Gizis, 2002; Gizis et al., 2007; Biller & Close, 2007; Mamajek, 2005; Mamajek & Meyer, 2007; Ducourant et al., 2008), implying a projected orbital separation of 41 ± 1 AU.

Determining the luminosity of 2M1207 b is not straightforward. Photometry is available in the J Mohanty et al. (2007), H, K_s, and L' bands from NaCo observations at the VLT (Chauvin et al., 2004; Mohanty et al., 2007), at 0.8–1.0, 1.0–1.2, 1.35–1.55, and 1.4–1.8 μm (similar to H) from the *Hubble Space Telescope* (Song et al., 2006), and in the *Herschel* SPIRE bands of 250 and 350 μm Riaz et al. (2012b,a). Skemer et al. (2011) also obtained an upper limit at 8.3–9.1 μm. Spectroscopy is available at 1.1–1.35 μm, 1.4–1.8 μm (Chauvin et al., 2004; Mohanty et al., 2007; Patience et al., 2010), and 1.95–2.5 μm (Patience et al., 2010) and 2.0–2.4 μm (Mohanty et al., 2007), i.e. in JHK_s and slightly redwards. Summing up the fluxes in J, H, K_s, and L' listed in Mohanty et al. (2007) and using the known distance gives a luminosity of 2.1×10^{28} erg s^{-1}, or 27–30 per cent of a bolometric luminosity $\log L_{bol}/L_\odot = -4.68$ to -4.74 (see below). A 'direct luminosity determination' is thus not possible.

As summarised by Barman et al. (2011b), there are inconsistencies between the luminosity of 2M1207 b and its spectral type, determined by Chauvin et al. (2004) to be L5–L9.5. With the corresponding bolometric correction BC_K of Golimowski et al. (2004), the K_s-band magnitude implies a luminosity of $\log L/L_\odot = -4.7 \pm 0.1$ (Barman et al., 2011b). The hot-start, equilibrium models of Baraffe et al. (2003) then yield from the age and luminosity an effective temperature of 1010 ± 80 K (Barman et al., 2011b) in disagreement with $T_{eff} \simeq 1600$ K implied by the spectral type (Mohanty et al., 2007; Patience et al., 2010, 2012). However, this second value is questionable.

[14] From the data available at http://www.astro.princeton.edu/~burrows/dat-html/data/.
[15] As available at http://aas.org/archives/cdrom/volume5/doc/files5.htm.

Indeed, the high effective temperature and low luminosity would require an improbably small radius of $\simeq 0.6\,R_{\rm J}$.

There are two distinct approaches to the solution. Mohanty et al. (2007) argue that the actual luminosity has been underestimated due to grey extinction by an almost edge-on disc (the $\simeq 25$-$M_{\rm J}$ brown-dwarf primary is accreting; e.g. Stelzer, Scholz & Jayawardhana, 2007). The correspondingly higher luminosity is reported by Ducourant et al. (2008) as $\log L_{\rm bol}/L_\odot = -3.8 \pm 0.1$. In contrast, Skemer et al. (2011) argue against the disc explanation and suggest that thicker clouds than what might be naïvely expected[16] are needed. Barman et al. (2011a,b) go further and explicitly claim that the problem is with the derived $T_{\rm eff}$. They show that an atmosphere model with $T_{\rm eff} = 1000$ K can fit very well the photometry and spectroscopy if clouds of typical thickness and also, crucially, non-equilibrium chemisty are included. The latter leads to a heavily reduced methane abundance (by ca. two orders of magnitude at photospheric depths) compared to the chemical-equilibrium clouds and thus to redder colours than expected. From their best-fitting models, Barman et al. (2011b) estimate a luminosity of $\log L/L_\odot = -4.68 \pm 0.05$, in agreement with the luminosity derived from BC_K. As Luhman (2012) notes, differing bolometric corrections for old (field) and young brown dwarfs are thus not the sole explanation.

We adopt the luminosity of Barman et al. (2011b), in agreement with Neuhäuser & Schmidt (2012) who report $\log L/L_\odot = -4.74 \pm 0.06$ (with however $T_{\rm eff} = 1590 \pm 280$ K). Using the age of 5–12 Myr and the Baraffe et al. (2003) cooling tracks, this luminosity yields a hot-start mass of 2–5 $M_{\rm J}$ as Barman et al. (2011b) state. Skemer et al. (2011) give a slightly higher hot-start mass between 5 and 7 $M_{\rm J}$ based on $T_{\rm eff} = 1000$ K and the Burrows et al. (1997) models. We note that these errorbars match the estimate $\Delta M/M \simeq \frac{1}{2}\Delta t/t \simeq 0.5$ from Section 5.3.1.

Mass information

Mass information of dynamical origin for this two-body system is not available. Indeed, since the separation implies a period of at least (depending on the eccentricity) 1700 yr, detectable orbital evolution or change of the velocity amplitude are not expected in the near future (Mamajek, 2005), precluding both astrometry and radial-velocity measurements.

However, the surface gravity is somewhat constrained, which can be used to set an approximate mass upper limit. Barman et al. (2011b) state that their best-fitting model has $g = 10^4$ cm s^{-2} but do not provide any sense of how large the uncertainty on this value might be. However, typical errorbars (as in their similar analysis for HR 8799 b; Barman et al., 2011a) are at least of 0.5 dex. Mohanty et al. (2007) found that the fit to both the photometric and spectroscopic data is rather insensitive to $\log g$ within 3.5–4.5 (cm s^{-2}), in agreement with the indications of low gravity from the triangular H-band spectral shape and relatively weak Na I absorption (e.g. Allers et al., 2007; Mohanty et al., 2007). Also, Patience et al. (2012) fit J, H, and K spectra with five grids of atmosphere models, including BT-*Settl* (Allard, Homeier & Freytag, 2011), *Drift*-PHOENIX (Helling et al., 2008), and those of Marley et al. (Ackerman & Marley, 2001). The Marley et al. models yielded a gravity on the edge of their grid ($g = 10^{5.0}$ cm s^{-2}), but the others gave $\log g \simeq 3.5$, 3.5, 4.3, and 5.0 (cm s^{-2}), respectively. (With the best-fitting $T_{\rm eff} = 1500$–1650 K, the implied radii are of 0.4–0.7 $R_{\rm J}$, well below any theoretical cooling track.) Even though systematic issues with atmosphere models of young, low-mass brown dwarfs are expected, we will take these results to suggest tentatively that 2M 1207 b has a low gravity. As discussed below, the initial entropy on the cold-start branch is $S_{\rm i} = 9.2$, which is thus an *upper* limit to the current entropy. With $S < 9.2$ and a reasonable upper limit $\log g < 4.0$ (cm s^{-2}), the upper bound on the mass is $\simeq 7\,M_{\rm J}$, and for $\log g = 4.35$ (cm s^{-2}) it is 12.7 $M_{\rm J}$. Therefore, we shall assume that the estimates of the surface gravity imply a mass below the deuterium-burning limit, near 13 $M_{\rm J}$ (Spiegel et al., 2011; Mollière & Mordasini, 2012; Bodenheimer et al., 2013; Marleau & Cumming, in prep.).

[16] See comment in section 1.2.2 of Marley et al. (2012).

5.9.2. HR 8799

Age and luminosities

Several properties of HR 8799 let its age be estimated: variability from non-radial oscillations, low abundance of iron-peak elements, and far-IR excess due to circumstellar dust (Marois et al., 2008). Along with its Galactic space motion and position in a Hertzsprung–Russell diagram, these lead Marois et al. (2008) to estimate an age range of 30–160 Myr with a preferred value of 60 Myr, consistent with the 20–150 Myr range of Moór et al. (2006) based on membership in the Local Association. Recently, Baines et al. (2012) used interferometric measurements of HR 8799's radius to derive a stellar mass and age. They found best-fitting ages of 33 or 90 Myr, depending on whether the star is approaching or moving away from the main sequence. However, the statistical errorbars, which do not take uncertainties in the stellar models into account, are considerable in the second case (the 1-σ ranges are 20–40 and 40–471 Myr, respectively). Nevertheless, if Baines et al.'s measurement of the stellar radius and the deduced metallicity are correct, the age range of 1.1–1.6 Gyr from the asteroseismological analysis of Moya et al. (2010) would be compromised, as Baines et al. (2012) point out. Indeed, they estimate a near-solar metallicity, which contrasts with the [M/H] $\simeq -0.3$ or -0.1 result of Moya et al. (2010), while metallicity is an important input of asteroseismological analyses. Moreover, there is the statistical argument put forth by Marois et al. (2008) that massive discs (such as HR 8799's of 0.1 $M_\oplus$; Su et al., 2009) are unlikely to be found around older stars. In our analysis, we shall therefore ignore the 1.1 Gyr result and instead use 20 and 160 Myr as lower and upper limits, which brackets the ranges reviewed in Moya et al. (2010) and Baines et al. (2012).

Marois et al. (2008, 2010) estimated luminosities of $\log L_{\rm bol}/L_\odot = -5.1 \pm 0.1$ (HR 8799 b), -4.7 ± 0.1 (cd) and -4.7 ± 0.2 (e) from the known distance of 39.4 ± 0.1 pc and six infrared magnitudes, covering $\simeq$ 40 per cent of the bolometric luminosity, and also from bolometric corrections for brown dwarfs. For their part, Marley et al. (2012) recently derived luminosities of $\log L_{\rm bol}/L_\odot = -4.95 \pm 0.06$, -4.90 ± 0.10, and -4.80 ± 0.09 for planets b, c[17], and d, respectively, by self-consistently obtaining the radius from evolutionary models. This contrasts with the usual procedure of optimising $(R/d)^2$ along with $T_{\rm eff}$ and $\log g$ to fit the photometry, which yields unphysically small radii of $\simeq 0.8\ R_{\rm J}$ (Barman et al., 2011a; Marley et al., 2012). Similarly, in a recent study[18] using "atmospheric retrieval" (non-parametric determination of the P–T and composition structure) including a simple cloud model, Lee, Heng & Irwin (2013) also find for HR 8799 b a small radius of $0.66^{+0.07}_{-0.04}\ R_{\rm J}$, which implies with their $T_{\rm eff} = 900^{+30}_{-90}$ K and $\log g = 5.0^{+0.1}_{-0.2}$ (cm s^{-2}) a bolometric luminosity $\log L/L_\odot = -5.57$. Since Marley et al. considered only hot starts, i.e. fixed $S_{\rm i}$ = high, the cooling tracks are $L_{\rm bol}(M,t)$ and $R(M,t)$ relations, which let R and t be uniquely determined from $\log g$ and $T_{\rm eff}$. This gives an age of 360 Myr for HR 8799 b and age ranges of 40–100 Myr and 30–100 Myr for c and d, consistent with other literature estimates. Given the difficulties in obtaining a reasonable fit, Marley et al. (2012) warn that the first result should not be taken seriously, and note that the tension in the age would be reduced by considering colder initial conditions. In our analysis, the luminosity values of Marois et al. (2008, 2010) will be used since they are standard and almost or marginally consistent with those of Marley et al. (2012).

Finally, an age of 30 or 60 Myr for the system leads Marois et al. (2010) to derive from the luminosity and the cooling tracks of Baraffe et al. (2003) masses of $(5, 7, 7, 7)$ or $(7, 10, 10, 10)\ M_{\rm J}$. The uncertainty in the age implies (see Section 5.3) $\Delta M \simeq 1$–$1.3\ M_{\rm J}$ for the hot-start values.

Dynamical stability

Since it is to date the only directly-imaged multiple-planet system, HR 8799 has received a considerable amount of attention with regard to its dynamical stability (e.g. Marois et al., 2008; Reidemeister et al., 2009; Fabrycky & Murray-Clay, 2010; Moro-Martín et al., 2010; Marois et al., 2010;

[17] In fact, the errorbars on the luminosity of HR 8799 c are clearly non-Gaußian, but this will not be taken into account out of simplicity.

[18] Note also their careful and detailed review of atmospheric modelling efforts for HR 8799 b and their problems.

Bergfors et al., 2011; Currie et al., 2011; Sudol & Haghighipour, 2012; Esposito et al., 2013; Currie et al., 2012; see reviews in Sudol & Haghighipour, 2012 and Goździewski & Migaszewski, 2014). However, only the most recent studies were able to consider all four planets. Crucial questions include whether there are two- or three-planet mean-motion resonances (MMRs; as Goździewski & Migaszewski, 2009 and Fabrycky & Murray-Clay, 2010 suggest), what the inclination and eccentricities of the orbits are (for instance, Lafrenière et al., 2009 estimated 13–23° for the inclination of HR 8799 b with respect to the plane of the sky) and whether they are co-planar (against which Currie et al., 2012 recently provided evidence, while Kennedy et al. (2013) argues in favour), and, naturally, what the masses (including that of the star) are and how long the system should be required to survive. Solutions are very sensitive to these parameters and even to the numerical integrator used, as Esposito et al. (2013) note. The parameter space's high dimensionality makes a proper exploration – i.e. without artificially-imposed restrictions as all authors had to assume – , computationally prohibitive, and trying to include information about the disc would only make matters worse.

Stability is estimated by using astrometric constraints and numerically evolving the system over time, requiring that it be stable (without collisions nor ejections) for a period equal to its age. However, Goździewski & Migaszewski (2009) and Fabrycky & Murray-Clay (2010) point out that if it is young with respect to its main-sequence lifetime, HR 8799 could indeed be a transient system undergoing dynamical relaxation. Therefore, it may not be possible to draw firm conclusions even from the results of a complete analysis.

Nevertheless, if the direction in which these studies point is correct, the planets should have as low masses as allowed, with however somewhat higher masses permitted if some orbits are resonant. For this reason, we shall consider as approximate upper limits from stability analyses[19] masses of 7, 10, 10, and 10 $M_{\rm J}$ (bcde). In particular, as Goździewski & Migaszewski (2014) also find, it seems very likely that none is a deuterium-burning object.

5.9.3. β Pic

Age and luminosity

The namesake A5 dwarf of the nearby (9–73 pc; Malo et al., 2013) β Pictoris moving group has an age of 12^{+8}_{-4} Myr (Zuckerman et al., 2001) and asymmetric outer and warped inner discs, which have been observed for more than two decades (Lagrange et al., 2009, 2012, see review in Lagrange et al., 2011). A companion was first detected in L' (Lagrange et al., 2009) and subsequently confirmed at 4 µm (Quanz et al., 2010) and in K_s (Bonnefoy et al., 2011). Very recently, Bonnefoy et al. (2013) added to these observations photometry in J, H, and M'. The distance of 19.44 ± 0.05 pc[20] to β Pic b implies an orbital separation of 8–9 AU (Chauvin et al., 2012; Bonnefoy et al., 2013), which is the smallest of all low-mass directly-detected objects. An object at this position had been predicted from the disc morphology by Freistetter, Krivov & Löhne (2007).

Until recently (Bonnefoy et al., 2013; Currie et al., 2013), the only bolometric luminosity estimate for β Pic b was due to Neuhäuser & Schmidt (2012), who report $\log L_{\rm bol}/L_\odot = -3.90^{+0.07}_{-0.40}$. They firstly derived, from the $T_{\rm eff}$ = 1700 ± 300 K of Bonnefoy et al. (2011), a spectral type SpT ≃ L2–T4 using the $T_{\rm eff}$–SpT relation of Golimowski et al. (2004, hereafter G04). They then estimated from their SpT–BC$_K$ curve a bolometric correction BC$_K$ = $3.3^{+0.15}_{-1.00}$ (T. Schmidt 2012, priv. comm.). Thus, the large, asymmetric lower errorbar on the luminosity comes from the large, asymmetric lower errorbar on the bolometric correction, which itself is due to the flat $T_{\rm eff}$–SpT relation between L7 and T4 in G04. A more direct approach to the bolometric luminosity consists of converting the colour to a spectral type and obtaining from this a bolometric correction. Also

[19] Note that in a very recent study, Goździewski & Migaszewski (2014) find, using a novel approach which assumes multiple MMRs but yields masses independently, that broad mass rangeswhich include the hot-start values (though not perfectly for HR 8799 c and d) are possible: 4–8, 8–12, 8–12, and 7–10.5 $M_{\rm J}$ (bcde). Using these values instead would barely change our derived minimum bounds on $S_{\rm i}$, lowering some by ≃ 0.1 $k_{\rm B}$/baryon.

[20] This is the value obtained from a re-reduction of *Hipparcos* data by van Leeuwen (2007). However, a number of recent studies still use the value of 19.3 ± 0.2 pc (Crifo et al., 1997).

using the fits[21] of G04, this gives the same luminosity as found by Neuhäuser & Schmidt (2012) but with a smaller lower errorbar of 0.12 dex. One should however note that BC_K(SpT) is not a monotonic function (see fig. 6a of G04), so that the errorbars are strongly non-Gaußian. With a maximum BC_K of 3.3 mag near L3.5, $\log L_{bol}/L_\odot$ cannot formally be above −3.9 dex. However, the BC_K–SpT relation of G04 was derived for field dwarfs (see also Stephens et al., 2009), and the spectral classification of young objects is not yet well understood nor, in fact, well defined (see e.g. Liu et al., 2011; Faherty et al., 2012). Keeping in mind these uncertainties in interpreting the photometry, we shall use for the analysis $\log L_{bol}/L_\odot = -3.90^{+0.05}_{-0.12}$, where the upper errorbar reflects the residuals of the G04 fit. This is at some variance with the value of $\log L/L_\odot = -3.80 \pm 0.02$ of Currie et al. (2013) but compares favourably with $\log L/L_\odot = -3.87 \pm 0.08$ from Bonnefoy et al. (2013).

Mass information

The object β Pic b is particularly interesting because it is the first directly-imaged companion for which radial-velocity data are also available (Lagrange et al., 2012). Using new and archival data spanning eight years and thanks to the high inclination of the system (88 ± 2°; Chauvin et al., 2012), Lagrange et al. (2012) were able to place tentative lower mass limits of 1–2 M_J, which is fully consistent with all reasonable age and luminosity combinations, even allowing for very large lower errorbars on the latter. However, Lagrange et al.'s upper limit of 10–25 M_J, with 12 M_J for the most probable orbit of 9 AU (Lagrange et al., 2009; Chauvin et al., 2012) is an important result which excludes high-mass solutions and puts the object quite likely in the planetary (non-deuterium burning) range.

We conclude with a brief digression. To the rarity of objects observable simultaneously in radial velocity (RV) and in direct imaging contribute both intrinsic detection biases – direct imaging favours planets further out from their star, resulting in a small RV signal – as well as selection biases – target stars are usually chosen based on the presence of a disc, which implies that the systems are preferentially seen face-on. A further hindrance is that young stars – young systems being of greater interest because of a smaller brightness contrast – are usually active and thus less amenable to radial-velocity measurements. See also Lagrange et al. (2013) for a discussion of radial-velocity searches around young nearby stars and example prospects of coupling to direct imaging.

This ends Marleau & Cumming (2014, hereafter MC14). The next two sections present the author's contribution to two publications, one on an updated measurement of β Pic b and the other on κ And b, preceded by their respective abstracts.

5.10. Update to β Pic b

*Section 5.10.2 reproduces the contribution of the author to Bonnefoy, **Marleau** et al., A&A **567**, L9 (2014), "Physical and orbital properties of β Pictoris b" (Bonnefoy et al., 2014b). As a summary of the article, the abstract is first provided. Note that Section 5.10.2 represents a segment of the section "Physical properties and initial conditions" and the entire "Discussion" of Bonnefoy et al. (2014b).*

[21] It was brought to our attention that there is an extension of G04 by Liu et al. (2010), who use updated spectral types and removed binary systems from the sample. However, differences in BC_K only begin appearing later than ≃ L1, whereas the SpT we consider for β Pic b is L1–T0 (Bonnefoy et al., 2011; cf. the constraints of L0–L4 by Bonnefoy et al., 2013 or L2–L5 by Currie et al., 2013). According to the fit of Liu et al. (2010), BC_K(L) = 3.05 mag, while G04 gives 2.99 mag; the difference (0.06 mag) is less than the root-mean-square fit residuals (0.08 mag and 0.13 mag, respectively).

5.10.1. Summary

The intermediate-mass star β Pictoris is known to be surrounded by a structured edge-on debris disk within which a gas giant planet was discovered orbiting at 8–10 au. The physical properties of β Pic b were previously inferred from broad- and narrow-band 0.9–4.8 µm photometry. We used commissioning data of the *Gemini Planet Imager* (GPI) to obtain new astrometry and a low-resolution ($R \sim 35$–39) J-band (1.12–1.35 µm) spectrum of the planet. We find that the planet has passed quadrature. We constrain its semi-major axis to $\leqslant 10$ au (90% prob.) with a peak at $8.9^{+0.4}_{-0.6}$ au. The joint fit of the planet astrometry and the most recent radial velocity measurements of the star yields a planet dynamical mass lower than 20 $M_{\rm J}$ ($\geqslant$ 96% probability). The extracted spectrum of β Pic b is similar to those of young $\mathrm{L1}^{+1}_{-1.5}$ dwarfs. We used the spectral type estimate to revise the planet luminosity to $\log(L/L_\odot) = -3.90 \pm 0.07$. The 0.9–4.8 µm photometry and spectrum are reproduced for $T_{\rm eff} = 1650 \pm 150$ K and a $\log g \leqslant 4.7$ dex by 12 grids of PHOENIX-based and LESIA atmospheric models. For the most recent system age estimate (21 ± 4 Myr), the bolometric luminosity and the constraints on the dynamical mass of β Pic b are only reproduced by warm- and hot-start tracks with initial entropies $S_{\rm i} > 10.5\ k_{\rm B}$ baryon^{-1}. These initial conditions may result from an inefficient accretion shock and/or a planetesimal density at formation higher than in the classical core-accretion model. Considering a younger age for the system or a conservative formation time for β Pic b does not change these conclusions.

5.10.2. Discussion

To derive quantitative constraints on the initial entropy $S_{\rm i}$ of β Pic b, we used the method of MC14 and performed an MCMC in mass and $S_{\rm i}$ using their evolutionary models up to masses of 17 $M_{\rm J}$. The models have gray atmospheres, include deuterium burning, and span in $S_{\rm i}$ the extreme outcomes of any formation process. Figure 5.13 shows the allowed M and $S_{\rm i}$ combinations that match the luminosity and age taking Gaussian errorbars into account.

If the system if truly 21 ± 4 Myr old, shows that β Pic b cannot have formed according to the classic (Marley et al., 2007) parameters of core accretion, which include a supercritical accretion shock (coldest starts) and an initial planetesimal density leading to a 15-$M_\oplus$ core. Indeed, the 95-%-level lower bound[22] on the post-formation entropy of $S_{\rm i,\ min} = 10.4\ k_{\rm B}$ baryon^{-1} is $\approx 2\ k_{\rm B}$ baryon^{-1} warmer than the supercritical 15-$M_\oplus$ prediction.

An on average inefficient shock and/or a higher planetesimal density (Mordasini, 2013) must be invoked to lead to warmer starts. For a completely efficient accretion shock, the predicted core would need to be $\gtrsim 65\ M_\oplus$, which remains possible given the system parameters. These conclusions are nearly unchanged even assuming an extreme duration for the planet's formation phase of 9 Myr (Figure 5.13).

Finally, for masses within the 68.3-% contour, the MC14 cooling curves predict β Pic b to not be affected by deuterium flashes (Bodenheimer et al., 2000), where the luminosity and $T_{\rm eff}$ of massive objects increase, possibly at very late times (MC14; Marleau & Cumming, in prep.). However, due to differences in boundary conditions and nuclear rate details, and given the high precision of the luminosity measurement, using other cooling tracks can somewhat affect the mass constraints and the importance of deuterium burning in the cooling history of β Pic b.

5.11. Analysis of κ Andromeda b

*The contribution of the author to Bonnefoy, Currie, **Marleau** et al., A&A **562**, A111 (2014), "Characterization of the gaseous companion κ Andromedae b" (Bonnefoy et al., 2014a) is presented in Section 5.11.2. First, the abstract is reproduced but slightly expanded, and two relevant figures not prepared by the author are included.*

[22] An upper limit is given by the fact that the radius starts diverging when S increases above $\simeq 16.5$. Varying the upper bound of the cumulative integral barely varies the quoted figures.

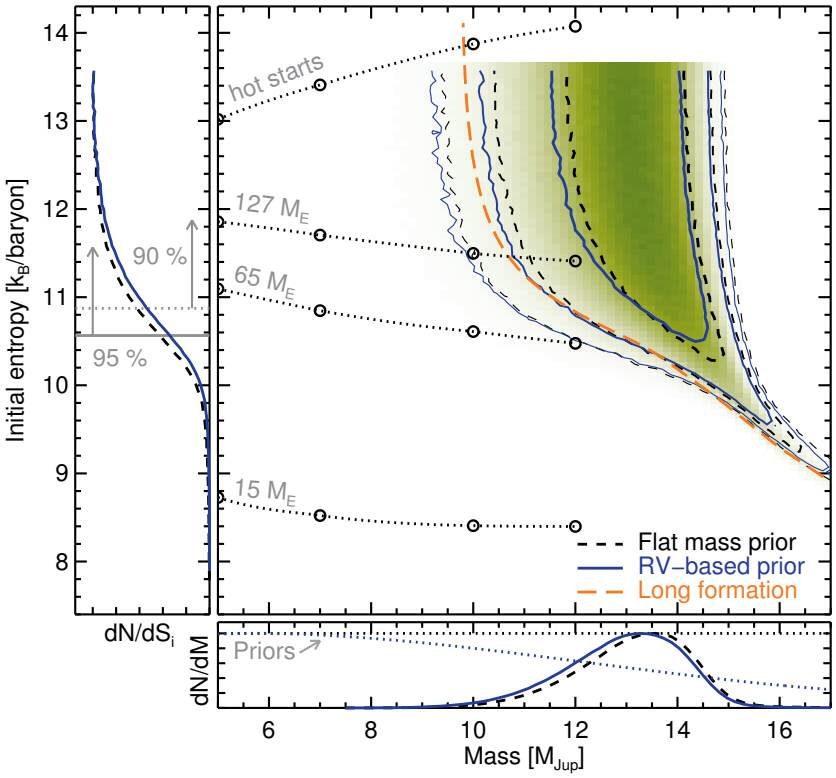

Fig. 5.13.: Joint probability contours (68.3, 95, and 99%) on the mass and post-formation entropy of β Pic b from $\log(L/L_\odot) = -3.90 \pm 0.07$ and an age of 21 ± 4 Myr using a flat prior on S_i and a prior flat in mass (*dashed black curves*) or given by the radial-velocity and astrometry constraints for a linear prior on the radial velocity amplitude K (*solid dark-blue curves*). Using the logarithmic-K prior of Figure 1 gives nearly identical results. The long-dashed orange line shows the combinations matching $\log(L/L_\odot) = -3.90$ at 12 Myr, i.e., allowing for an extreme 9-Myr formation delay. The open circles indicate the cold-start post-formation entropies for different final core masses (*labeled*) or for hot starts (Mordasini, 2013, App. B of MC14). The bottom panel displays the mass priors (*dotted lines*) and the marginalized posterior distributions (*black and blue lines*), whereas the side panel shows the marginalized S_i posterior and the non-flat mass prior's 90- and 95-% lower limits (up to $S_i \sim 14$).

5.11.1. Summary

Context. We previously reported the direct detection of a low-mass companion at a projected separation of 55 ± 2 au around the B9-type star κ Andromedae, the first around such a massive star (2.5 ± 0.1 $M_\odot$). The properties of the system (mass ratio, separation) make it a benchmark for understanding the formation and evolution of gas giant planets and brown dwarfs on wide orbits.
Aims. We present new angular differential imaging (ADI) images of the system at 2.146 (K_s), 3.776 (L'), 4.052 ($NB_{4.05}$), and 4.78 µm (M) obtained with Keck/NIRC2 and LBTI/LMIRCam, as well as more accurate near-infrared photometry of the star with the MIMIR instrument. We aim to determine the near-infrared spectral energy distribution of the companion and use it to characterize the object.
Methods. We used analysis methods adapted to ADI to extract the companion flux. We compared the photometry of the object to reference young and old objects and to a set of seven PHOENIX-based atmospheric models of cool objects accounting for the formation of dust (AMES-DUSTY, AMES-COND, BT-DUSTY, BT-COND, BT-Settl 2010, BT-Settl 2012, DRIFT-PHOENIX). We used evolutionary models to derive mass estimates considering a wide range of plausible initial conditions. Finally, we used dedicated formation models to discuss the possible origin of the companion. For this, we identify regions in the clump-mass–semi-major-axis plane for which (i) the local gravity of a gas clump dominates over the gas pressure (Toomre criterion) and (ii) the cooling

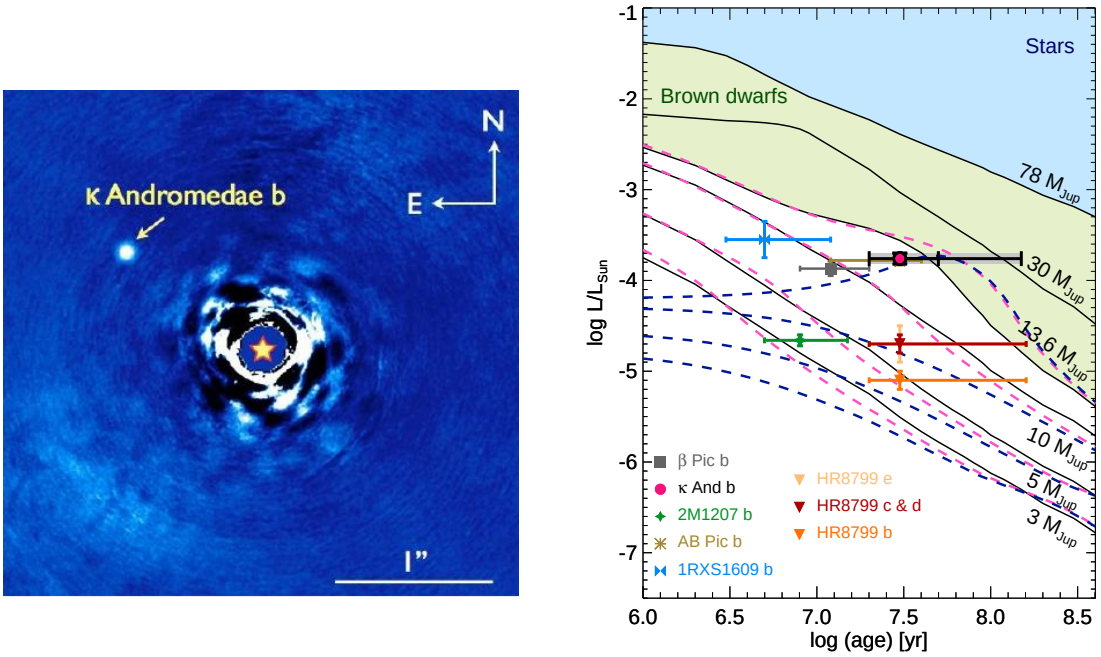

Fig. 5.14.: *Left panel:* LBTI/LMIRCam high-contrast image of the κ And system at M band. The companion is recovered. *Right panel:* Evolution of the luminosity of gaseous objects predicted by the COND models (solid black line) and by the MC14 models with typical 'hot-start' (dashed light pink curve; 3, 5, 10, 13.6 M_J) and 'cold-start' initial conditions (dashed dark blue curve; 3, 5, 10, 13.6 M_J). We overlaid measured luminosity of young low-mass companions. A more complete version of this figure can be found in MC14.

timescale of the clump is smaller than the shearing time, which would allow formation by gravitational instability.

Results. We derive a more accurate $J = 15.86 \pm 0.21$, $H = 14.95 \pm 0.13$, $K_s = 14.32 \pm 0.09$ mag for κ And b. We detect the companion in all our high-contrast observations. We confirm previous contrasts obtained at K_s and L band. We derive $NB_{4.05} = 13.0 \pm 0.2$, and $M = 13.3 \pm 0.3$ mag and estimate $\log(L/L_\odot) = -3.76 \pm 0.06$. Atmospheric models yield $T_{\rm eff} = 1900^{+100}_{-200}$ K but do not set any constraint on the surface gravity. Models with dust in the photosphere of the object better reproduce the SED. 'Hot-start' evolutionary models predict masses of 14^{+25}_{-2} M_J based on the luminosity and temperature estimates, and when considering a conservative age range for the system (30^{+120}_{-10} Myr), 'warm-start' evolutionary tracks constrain the mass to $M \geqslant 10$ M_J.

Conclusions. The mass of κ Andromedae b mostly falls in the brown-dwarf regime, owing to remaining uncertainties in age and in mass-luminosity models. According to the formation models, disk instability in a primordial disk may account for the position and a wide range of plausible masses of κ And b.

Figure 5.14 reproduces figures 2 and 10 of Bonnefoy et al. (2014a) for interest and convenience, respectively.

5.11.2. The mass of κ And b: Warm-start models

This is the author's contribution to section 3.4.2 of Bonnefoy et al. (2014a). Note that it was shortened for publication.

To assess the dependence of the mass–initial-entropy constraints on the choice of the cooling curves, we also used the bolometric luminosity and effective temperature of κ And b to derive joint constraints on its mass and initial entropy using the grid of MC14. As in Spiegel & Burrows

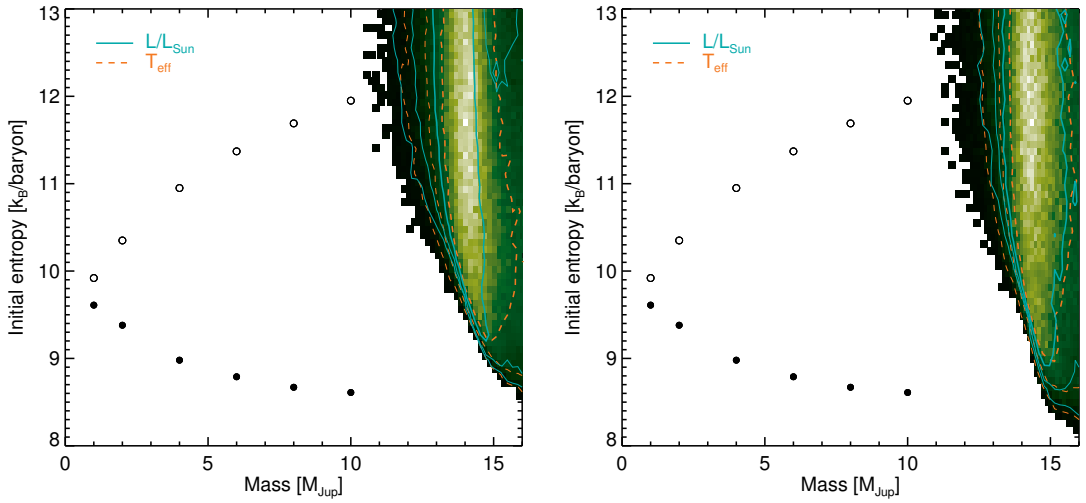

Fig. 5.15.: Joint posteriors on the mass and intial entropy of κ And b obtained through MCMC runs with the models of MC14, which include deuterium burning, from the bolometric luminosity $\log L/L_\odot = -3.76 \pm 0.04$ (solid lines) or effective temperature $T_{\rm eff} = 1800 \pm 100$ K (dashed lines), assuming Gaußian errorbars on either quantity. The colour is proportional to the joint posterior probability at each M and $S_{\rm i}$ location in the $T_{\rm eff}$-based run. The age was taken as $t = 30^{+20}_{-10}$ Myr (top panel) and $t = 30^{+120}_{-10}$ Myr, with Gaußian errorbars in the first case and lognormal ones in the second. Flat priors on the mass and initial entropy were used. Open and closed circles are as in Marley et al. (2007), showing the approximate range of entropies spanned by hot and coldest starts, respectively (the 'tuning fork' diagram of exoplanets), but shifted upwards by +0.38 $k_{\rm B}$/baryon to match the luminosity in the models of MC14, see therein. Similarly, the offset with the models of Spiegel & Burrows (2012) is ca. $\Delta S = +0.45$.

(2012), these models were computed by assuming a constant-entropy interior with a near-solar helium mass fraction $Y = 0.25$ and include deuterium burning. However, they have a much simpler outer boundary condition, using a grey, solar-metallicity atmosphere terminating at the photosphere in the Eddington approximation, instead of calculating the radiative transfer in the upper layers (Burrows et al., 1997). More importantly, the time evolution is handled very differently. Cooling tracks are rapidly calculated by moving in a grid of models labeled by their mass and entropy, in the 'following the adiabats' approach (see MC14 and references therein). This contrasts with the Henyey-based approach of Spiegel & Burrows (2012). Nevertheless, despite the simplicity of the structure and time-evolution calculation, the models of MC14 match within some ten percent independent cold-, warm- and hot-starts models (Burrows et al., 1997; Baraffe et al., 2003; Marley et al., 2007; Spiegel & Burrows, 2012; Paxton et al., 2013).

When comparing the joint constraints on the mass and initial entropy based on the models of Spiegel & Burrows (2012) (shown in Fig. 5.14) with those of MC14, we also took the uncertainty in the age and the luminosity explicitly into account. For this, we ran Markov Chain Monte Carlo simulations (MCMCs) in mass and initial entropy as in MC14 and with their models, drawing at every step a luminosity or effective temperature, as well as an age, according to the values $\log L/L_\odot = -3.76 \pm 0.04$ or $T_{\rm eff} = 1800 \pm 100$ K, and $t = 30^{+20}_{-10}$ Myr or $t = 30^{+120}_{-10}$ Myr. We assumed Gaußian distributions on L and $T_{\rm eff}$ and, respectively, normal or lognormal errorbars for the age, and took flat priors in $S_{\rm i}$ and M. (See MC14 for the effect of a non-flat, radial-velocity-based prior in the case of β Pic b.)

Figure 5.15 displays the 68-, 95- and 99-percent joint confidence regions from the MCMC runs using L or $T_{\rm eff}$, for both age groups. The results are entirely consistent with those of Figure 5.14. Moreover, both L and $T_{\rm eff}$ lead to similar contours, with differences due to the effective temperature $T_{\rm eff} = 1800 \pm 100$ K corresponding to a slightly different luminosity; the mean $\log L/L_\odot$ of the points in the $T_{\rm eff}$ chain is -3.66 instead of -3.72 for the L-based chain, and with a slight skewness.

Even for the low-age group, the phase space for masses below 13 or 14 $M_{\rm J}$ is very small, i.e.,

almost all solutions are in the mass regime where deuterium burning is important for the evolution of the object. A dramatic illustration of this lies in the solutions found at lower entropies. Whereas the models of Spiegel & Burrows (2012) allowed, for an age of 30^{+20}_{-10} Myr, initial entropies down to only 11 k_B/baryon (see Figure 5.14), the models of MC14 find that κ And b could have formed with an entropy as low as $\approx$ 9.0 k_B/baryon, correcting for the entropy offset of $\approx$ 0.5 k_B/baryon between the two models (see MC14).

The low-S_i solutions are possible only if the models include the possibility of a rise in the object's luminosity due to deuterium burning, as mentioned in MC14 and discussed in Marleau & Cumming (in prep.). (As seen in Figure 5.14, these were not found by the models of Spiegel & Burrows (2012) as none of their lightcurves are of this type.) Very recently, Bodenheimer et al. (2013) independently found these 'flashes'[23] occurring in the cooling of objects formed by core accretion for some combinations of parameters, as also seen but in a milder form by Mollière & Mordasini (2012). Figure 5.16 shows cooling tracks for different (M, S_i) combinations which all reach $\log L/L_\odot = -3.76$ at 30 Myr, with the lowest initial-entropy solutions undergoing a flash. While the exact low-entropy solutions can depend on the details of deuterium burning, for instance on the (unknown) initial deuterium content or metallicty of the object (Spiegel et al., 2011; Mollière & Mordasini, 2012), *the main conclusion that the combustion of deuterium plays a significant role in the cooling history of κ And b is a solid one, irrespective of the precise age of the system.* We warn that while the lowest-S_i are comparable to the extrapolation of the coldest starts (Marley et al., 2007) to higher masses, what this implies for the formation mechanism is not clear given the major uncertainties about their outcome.

[23] This term reflects the fact that the entropy increase happens on a relatively short timescale and can lead to a dramatic increase in the luminosity and radius.

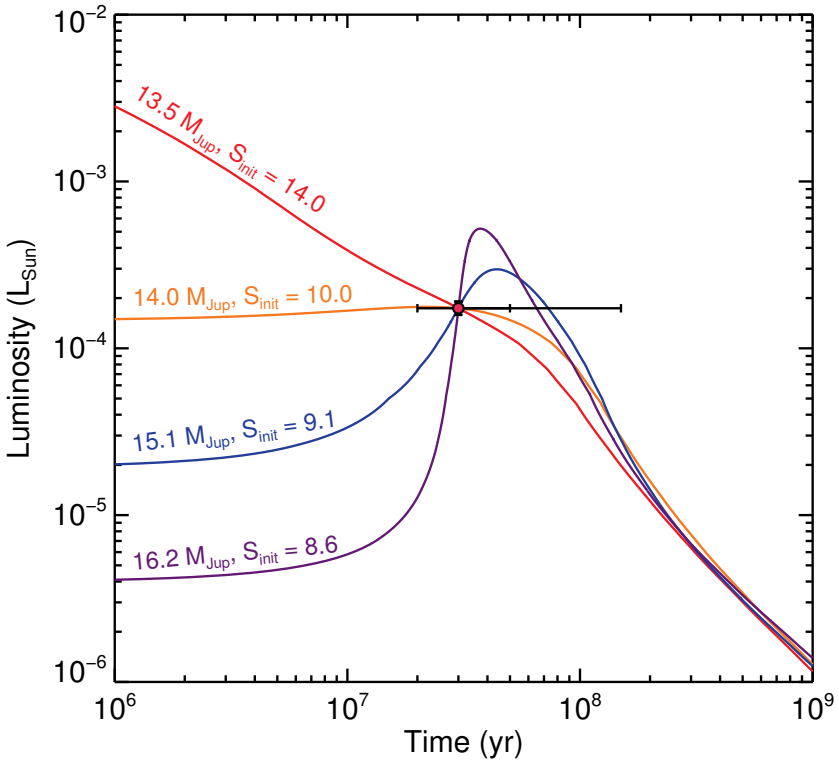

Fig. 5.16.: Examples of possible cooling curves for κ And b using $\log L/L_\odot = -3.76$ at 30 Myr, with the corresponding mass and initial entropy of each curve indicated in the figure; from top to bottom, the mass increases (up to 16.2 M_J) and the initial entropy decreases (down to 8.6 k_B/baryon) to compensate. For the lower entropies, we find that κ And b could be presently undergoing a deuterium 'flash' (Salpeter, 1992; Bodenheimer et al., 2013), where the burning of deuterium drives an increase in its luminosity and radius. Similar curves and a more general discussion of M–S_i constraints from luminosity measurements when considering deuterium-burning masses can be found in Marleau & Cumming (in prep.).

so much depends
upon

a red wheel
barrow

glazed with rain
water

besides the white
chickens.

— William Carlos Williams

6 Conclusion

Up to now, the post-formation thermal state—i.e., entropy and thus luminosity—of gas giant planets was neither predicted by theory nor constrained by observations, yet has significant observational consequences. We addressed this issue from both sides. The modeling effort was directed at the accretion shock at the surface of a forming planet to determine the radiation efficiency, i.e., the fraction of the incoming kinetic energy which is lost as radiation, the rest being added to the planet. We used equilibrium (1-T) flux-limited diffusion in spherical symmetry in Chapter 2 and focussed on cases where the contribution of the internal luminosity is negligible. We found that the shock is always isothermal with a Mach number sufficiently high that almost the entire kinetic energy is radiated away. The fraction brought into the planet was seen to be negligible compared to the planet's internal luminosity and therefore unable to heat the planet up. The ram pressure is much smaller than the photospheric pressure but the shock temperature can be smaller or larger by a factor of several to a few. The implications of this will have to be determined with self-consistent coupling to formation calculations.

For selected cases from the large formation parameter space, we verified in Chapter 3 that the use of non-equilibrium (2-T) radiation transport does not change the Mach numbers as the radiation and gas temperatures were found to be equal. However, it remains to be investigated what the effect of other assumptions is, in particular that of a spherically symmetric geometry and of a constant equation of state. Work concerning the latter is already underway.

In a related aside (Chapter 4), we attempted to produce self-consistent cooling tracks for gas giants using the sophisticated `BT-Settl` atmospheres. However, we found that the only available grid of models which is complete down to sufficienctly low temperatures, `BT-Settl`-2010, has multiple values of $T_{\rm eff}$ corresponding to a given entropy for $T_{\rm eff} \approx 1500$ K. This is due to convergence issues of the models due to hysteresis in the formation and destruction of dust, with the consequence that the grid cannot be used for computing cooling tracks.

On the observational side (Chapter 5), we showed how to convert a measurement of the luminosity and age of a gas giant (planet or brown dwarf) to joint constraints on its mass and initital entropy. The shape of the 'trade-off' curve is set by the behaviour of the cooling curves, which show a constant luminosity (or entropy) at early times before turning off onto the powerlaw cooling track common to hot starts. Useful constraints were derived on a number of objects which showed that most objects form with an entropy clearly above the cold starts predictions of Marley et al. (2007).

Extrapolating our simulation results, we seem to predict only cold starts, while observations seem more favourable to at least warm starts. One possibility of reconciling both statements is if the accretion shock is not the sole or principal physical process setting the initial entropy of a planet. An alternative is provided by the effect of the core mass, as shown in Mordasini (2013).

This is a promising venue as it in turn depends somewhat sensitively on a number of ill-constrained quantities such as the initial planetesimal surface density in the disc. However, it will still be necessary to first clearly isolate the effects of the accretion shock though detailed coupling and, ultimately, full three-dimensional radiation hydrodynamical simulations including the effects of (non-ideal) magnetic fields.

Vernunft und Glaube sind wie die beiden Flügel,
mit denen sich der menschliche Geist
zur Betrachtung der Wahrheit erhebt.

— *Fides et ratio* (1998)

7
Acknowledgements

Mein erster Dank gilt meinem Betreuer Hubert Klahr und unserem Institutsdirektor Thomas Henning, die es mir ermöglichten, bei ihnen spannende Forschung zu betreiben. Außerdem darf ich Christoph Mordasini und Rolf Kuiper für ihre großzügig gespendeten Hilfe und Zeit und Ermutigungen danken.

Einem Leben ohne Freunde und gute Kollegen fehlte etwas, was mich gerne folgenden Personen in alphabetischer Reihenfolge danken läßt: S. Ciceri (grazie!), S. Cielo, K.-M. Dittkrist, A. Gomes (obrigado!), C. Hansen, Th. Hansen (takk!), S. Jin, N. Malygin (spasybi!), J. Menu (dank u!), P. Mollière (danke!), M. Schulik, M. Wöllert (merci!), S.-W. Wu und die vielen anderen, die mir erst nach dem Drucken dieser Arbeit einfallen werden.

Der Exoplanetenkaffee hat mir viel gelehrt, wofür ich unter anderem E. Buenzli, M. Bonnefoy, J. Schlieder, N. Zimmerman, I. Crossfield, V. Jörgens, B. Biller, N. Deacon, A. Bayo, T. Kopytova und F. Rodler danken möchte.

Es war ein großes Privileg, am Max-Planck-Institut zu sein und ein herzliches Dankeschön geht an das ganze Personal für ihren mit Hilfsbereitschaft und Professionalität – und doch Freundlichkeit – ausgeführten Dienst.

Schließlich möge auch Dir, liebe Mona, sowie meinen Eltern und naher Familie und so vielen ‚persönlichen' Bekannten und Freunden für ihre vielfältige und geduldige Unterstützung gedankt werden – merci, danke, thanks!

A

Summary and test of the radiation hydrodynamics code

In this chapter, we briefly list our numerical settings and proceed in Section A.2 to summarise the equations of radiation hydrodynamics solved numerically in Chapters 2 and 3, as implemented in Mignone et al. (2007) and Kuiper et al. (2010). Details of the operator splitting for the energy equation are given in Section A.3 as this differs slightly from Kuiper et al. (2010). We verified our update of the code relative to Kuiper et al. (2010) with the standard Ensman (1994) sub- and supercritical shock tests and present these results in Section A.4.

A.1. Numerical settings

The following settings concern mainly `PLUTO` (see Mignone et al., 2007 and the detailed documentation available under `http://plutocode.ph.unito.it/`). We use the `hll` solver with the default slope limiter and linear interpolation. Time integration is performed with a second-order Runge–Kutta scheme and we take a Courant–Friedrich–Lax number CFL = 0.8 unless indicated otherwise. Thermal conduction and artificial viscosity are switched off.

For the implicit FLD solver (see below), we use the default `PETSc` pre-conditioner and take a relative convergence tolerance on the temperature of $\varepsilon = 10^{-15}$, i.e., the iterations to solve the implicit equation terminate when the relative change in temperature in each grid cell is 10^{-15} or less. Typically, after an adjustment phase, only one iteration is needed.

A.2. Basic equations

The hydrodynamics module of `PLUTO` (Mignone et al., 2007, 2012) solve the Navier–Stokes equations with a finite-difference scheme. In the absence of (explicit) viscosity, these can be written as (see Equations 1.3)

$$\frac{\partial \varrho}{\partial t} + \nabla \cdot (\varrho \mathbf{v}) = 0 \tag{A.1a}$$

$$\frac{\partial \varrho \mathbf{v}}{\partial t} + \nabla \cdot (\varrho \mathbf{v}\mathbf{v} + P\mathbf{1}) = \varrho \mathbf{g} \tag{A.1b}$$

$$\frac{\partial E_{\mathrm{tot}}}{\partial t} + \nabla \cdot ([E_{\mathrm{int}} + E_{\mathrm{kin}} + P]\,\mathbf{v} + \mathbf{F}_{\mathrm{rad}}) = \varrho \mathbf{v} \cdot \mathbf{g}, \tag{A.1c}$$

where symbols have their usual meaning (and in particular $E_{\mathrm{tot}} = E_{\mathrm{int}} + E_{\mathrm{kin}} + E_{\mathrm{rad}}$) and the equations were written in vector form for generality's sake, with $\mathbf{g} = -g\hat{\mathbf{e}}_{\mathbf{r}}$. We now briefly derive the

combined energy equation by deriving the equations for the conservation of internal, mechanical, and radiative energy.

A.2.1. Internal energy equation

The gas energy equation comes directly from the first law of thermodynamics and reads in Lagrangian form (Castor, 2004, and see below):

$$\varrho \frac{De_{\rm int}}{Dt} + \varrho P \frac{D}{Dt}\left(\frac{1}{\varrho}\right) = c(-4\pi\kappa_{\rm P} B + \kappa_E E_{\rm rad}) + \varrho\epsilon, \tag{A.2}$$

where $\epsilon = 0$ is an energy generation rate (e.g., from thermonuclear reactions), and the terms $c(-4\pi\kappa_{\rm P} B + \kappa_E E_{\rm rad})$, which represent respectively absorption of and losses to the radiation field, are defined below. The 'advective derivative' is defined as $D(\cdot)/Dt \equiv \partial(\cdot)/\partial t + \mathbf{v}\cdot\nabla(\cdot)$ and is the derivative at fixed mass element instead of position. Using the continuity equation, one can show that for an arbitrary function f,

$$\varrho \frac{Df}{Dt} = \frac{\partial \varrho f}{\partial t} + \nabla\cdot(\varrho f \mathbf{v})\,; \tag{A.3}$$

with this, the gas energy equation is in Eulerian form

$$\frac{\partial E_{\rm int}}{\partial t} + P\nabla\cdot\mathbf{v} + \nabla\cdot(E_{\rm int}\mathbf{v}) = c(-4\pi\kappa_{\rm P} B + \kappa_E E_{\rm rad}) + \varrho\epsilon, \tag{A.4}$$

where, as defined around Equations (1.3), $E_{\rm int} = \varrho e_{\rm int}$.

A.2.2. Mechanical energy equation

The mechanical energy equation can be derived from the inner product of $\mathbf{v}$ with the momentum equation (Equation A.1b), which yields

$$\varrho \frac{D}{Dt}\left(\frac{1}{2}v^2\right) = \varrho\mathbf{v}\cdot\mathbf{g} - \mathbf{v}\cdot\nabla P \tag{A.5}$$

and thus, using Equation (A.3),

$$\frac{\partial E_{\rm kin}}{\partial t} + \nabla\cdot(E_{\rm kin}\mathbf{v}) + \mathbf{v}\cdot\nabla P = \varrho\mathbf{v}\cdot\mathbf{g}. \tag{A.6}$$

A.2.3. Radiation energy equation

Finally, consider the radiative transfer equation (e.g., Mihalas & Mihalas, 1984)

$$\left(\frac{1}{c}\frac{\partial}{\partial t} + \mathbf{n}\cdot\nabla\right) I = \eta - \chi I, \tag{A.7}$$

where $I = I(\mathbf{x}, t, \mathbf{n}, \nu)$ is the specific intensity, which depends on the position $\mathbf{x}$, time t, propagation direction $\mathbf{n}$, and frequency ν, and where $\eta = \eta_\nu$ and $\chi = \chi_\nu$ are the (in general frequency-dependent) emission and absorption coefficients. In thermodynamic equilibrium, neglecting scattering, emission and absorption of energy must be equal, which leads to the Kirchhoff–Planck relation $\eta_\nu = \kappa_\nu B_\nu$, where B_ν is the Planck function. Taking the angular average of Equation (A.7) then yields the zeroth moment equation,

$$\frac{\partial E_{\rm rad}}{\partial t} + \nabla\cdot\mathbf{F}_{\rm rad} = c\left(4\pi\kappa_{\rm P} B - \kappa_{\rm E} E_{\rm rad}\right), \tag{A.8}$$

where $E_{\rm rad} = \frac{4\pi}{c}J$ and $\mathbf{F}_{\rm rad} = 4\pi\mathbf{H}$ are the (astrophysical) radiation energy density and flux, for a mean intensity $J = \frac{1}{4\pi}\int I\,{\rm d}\Omega$ and mean flux $\mathbf{H} = \frac{1}{4\pi}\int I\mathbf{n}\,{\rm d}\Omega$ (Mihalas & Mihalas, 1984), and

where κ_P and κ_E are, respectively, the Planck and energy mean opacities. The subscript on $\mathbf{F}_{rad}$ is usually dropped for simplicity.

Thus, summing Equations (A.4), (A.6) and (A.8), we obtain the equation for the total energy, Equation (A.1c). The needed closure relation, for instance, an expression for F_{rad} as a function of E_{rad}, was discussed in Section 1.2.

We note in passing that, to have two-temperature radiation transport (where E_{rad} is not necessarily given by the Planck function B), it is necessary to keep seperate the equation for the combined gas internal and kinetic energy from the radiation energy equation to prevent the $\pm\Lambda = \mp c\,(4\pi\kappa_P B - \kappa_E E_{rad})$ terms from cancelling. It is usually assumed that $\kappa_E = \kappa_P$ for convenience.

As it is the main focus of our work (Chapter 2), we next discuss only the 1-T case and refer the interested reader to Klassen et al. (2014) for details of the energy equations when evolving seperately E_{rad} and $E_{int} + E_{kin}$.

A.3. Operator splitting for the energy equation

The energy equation is solved in an operator-split fashion, where the combined internal and kinetic energy are updated in the hydrodynamics module, before the radiation transport modifies the internal energy to account for heating and cooling by the radiation field. Explicitly, the hydrodynamics module updates the kinetic and internal components of the energy at time t^n as

$$\frac{(E_{int} + E_{kin})^\star - (E_{int} + E_{kin})^n}{\Delta t} = -\nabla \cdot ([E_{int} + E_{kin} + P]\,\mathbf{v})^n + (\varrho \mathbf{v} \cdot \mathbf{g})^n\,, \tag{A.9}$$

where the superscripts indicate the time step but $\star$ denote the state after the hydrodynamics but before the radiation transport. This yields the internal and kinetic energies ${E_{int}}^\star$ and ${E_{kin}}^\star$.

To derive the required energy equation for the radiation transport, we first write

$$\frac{\partial\,(E_{int} + E_{rad})}{\partial t} = Q_{hydro} - \nabla \cdot \mathbf{F}, \tag{A.10}$$

where Q_{hydro} is a source term from the hydrodynamics (see below). Since both E_{int} and E_{rad} are power laws of temperature, their derivatives are proportional to $\partial T/\partial t$, so that (holding ϱ constant for radiation transport)

$$\left.\frac{\partial\,(E_{rad} + E_{int})}{\partial t}\right|_\varrho = \left[4aT^3 + \varrho c_v\right]\frac{\partial T}{\partial t} \tag{A.11a}$$

$$= \left[1 + \frac{\varrho c_v T}{4E_{rad}}\right]\frac{\partial E_{rad}}{\partial t} \tag{A.11b}$$

$$\equiv \frac{1}{f_c}\frac{\partial E_{rad}}{\partial t}, \tag{A.11c}$$

where by definition the constant-volume heat capacity is, for a general equation of state (EOS),

$$c_v(\varrho, T) \equiv \left(\frac{\partial(E_{int}/\varrho)}{\partial T}\right)_\varrho. \tag{A.12}$$

Note that Equation (A.11) is valid for an EOS which is not necessarily constant, i.e, when $c_v(\varrho, T)\varrho T$ cannot be automatically identified with E_{int}, and that it implicitly defined the factor f_c. Equation (A.10) then becomes with a first-order time discretisation

$$\frac{1}{f_c}\frac{{E_{rad}}^{n+1} - {E_{rad}}^n}{\Delta t} = Q_{hydro} - \nabla \cdot \mathbf{F}. \tag{A.13}$$

To solve for ${E_{rad}}^{n+1}$, one must choose how to evaluate f_c, Q_{hydro}, and $\mathbf{F}$. The following choices were made (R. Kuiper & H. Klahr, priv. comm.):

- For f_c, the updated density $\varrho^\star$ after the hydrodynamics step but the 'old' temperature T^n are used, yielding:

$$\frac{1}{f_c} = 1 + \frac{c_v(\varrho^\star, T^n)\varrho^\star}{4a(T^n)^3}. \tag{A.14}$$

- The procedure for the flux is similar:

$$\mathbf{F} = -D_F(\varrho^\star, T^n)\nabla {E_{rad}}^{n+1}, \tag{A.15}$$

where writing ${E_{rad}}^{n+1}$ leads to an implicit algorithm, and the diffusion coefficient is calculated as

$$D_F = \frac{\lambda(R(\varrho^\star, T^n))c}{\kappa(\varrho^\star, T^n)\varrho^\star}, \tag{A.16}$$

with λ the flux limiter and R the radiation quantity as discussed in Sections 1.2 and 1.3.

- Finally, the hydrodynamics energy source term Q^n_{hydro} is taken to be

$$Q^n_{hydro} = \bar{\varrho}\left(\frac{E_{int}(\varrho^\star, T^\star)}{\varrho^\star} - \frac{E_{int}(\varrho^n, T^n)}{\varrho^n}\right), \tag{A.17a}$$

$$\bar{\varrho} = \frac{1}{2}\left(\varrho^\star + \varrho^n\right). \tag{A.17b}$$

For a constant-γ and -μ EOS, $Q^n_{hydro} \propto (P^\star/\varrho^\star - P^n/\varrho^n) \propto (T^\star - T^n)$.

Since E_{kin} is not updated during the radiation transport, ${E_{kin}}^{n+1} = {E_{kin}}^\star$, and summing Equations (A.9) and (A.13) gives, using Equation (A.17),

$$\frac{(E_{tot})^{n+1} - (E_{tot})^n}{\Delta t} = -\nabla\cdot([E_{int} + E_{kin} + P]\,\mathbf{v})^n + (\varrho\mathbf{v}\cdot\mathbf{g})^n - \nabla\cdot\left(-D_F\nabla {E_{rad}}^{n+1}\right) + Q^+_{atm}, \tag{A.18}$$

which is a correct discretisation of Equation (A.1c). As mentioned above, since ${E_{rad}}^{n+1}$ appears in Equation (A.13) both on the left-hand side and in a gradient, one must solve Equation (A.13) implicitly. Details are given in Kuiper et al. (2010).

A.4. Radiation-hydrodynamics shock test

As in Kuiper et al. (2010), we perform the classical one-temperature (1-T) radiative shock test described in Ensman (1994, hereafter E94) to test our set-up. Her results are for 2-T radiation transport but she does show that there are only little differences between 1-T and 2-T for these tests. Briefly, we consider a uniformly-spaced spherically-symmetric grid from $r = 8$–8.7×10^6 km. At the inner grid edge, as in the main work, we use reflective boundary conditions in the hydrodynamical quantities and impose zero radiative flux, whereas the outer edge has 'outflow' (i.e., zero-gradient) hydrodynamical boundary conditions and $E_{rad} = 0$. The main differences with the main work are that (i) the accretion boundary conditions are not used, and (ii) the external potential (due to the planet's mass) is set to zero. We neglect self-gravity as in the main study.

We take as in E94 a constant opacity $\kappa = 0.4$ cm^2 g^{-1}, a constant mean molecular weight $\mu = 0.5$, and a constant number of degrees of freedom $f = 3$ (needed for c_V, where $c_V = 1 + 2/f$ in the ideal-gas approximation, used here). We use the simple flux limiter of Equation (1.24) used by E94.

As in E94, the problem is set up with a constant initial density $\varrho_0 = 7.78\times10^{-10}$ g cm^{-3} and a temperature decreasing linearly from 85 K at the inner edge to 10 K at the outer edge. The initial velocity of the gas is -6 or -20 km s^{-1} (i.e., directed towards the left) for the sub- or supercritical case, respectively. Section 1.1.1 reviewed the two shock types, in which the post-shock flux is, respectively, not able or able to heat the pre-shock material to its post-shock value.

The results of the radiative shock tests (sub- and supercritical) are presented in the next subsections along with a comparison to E94.

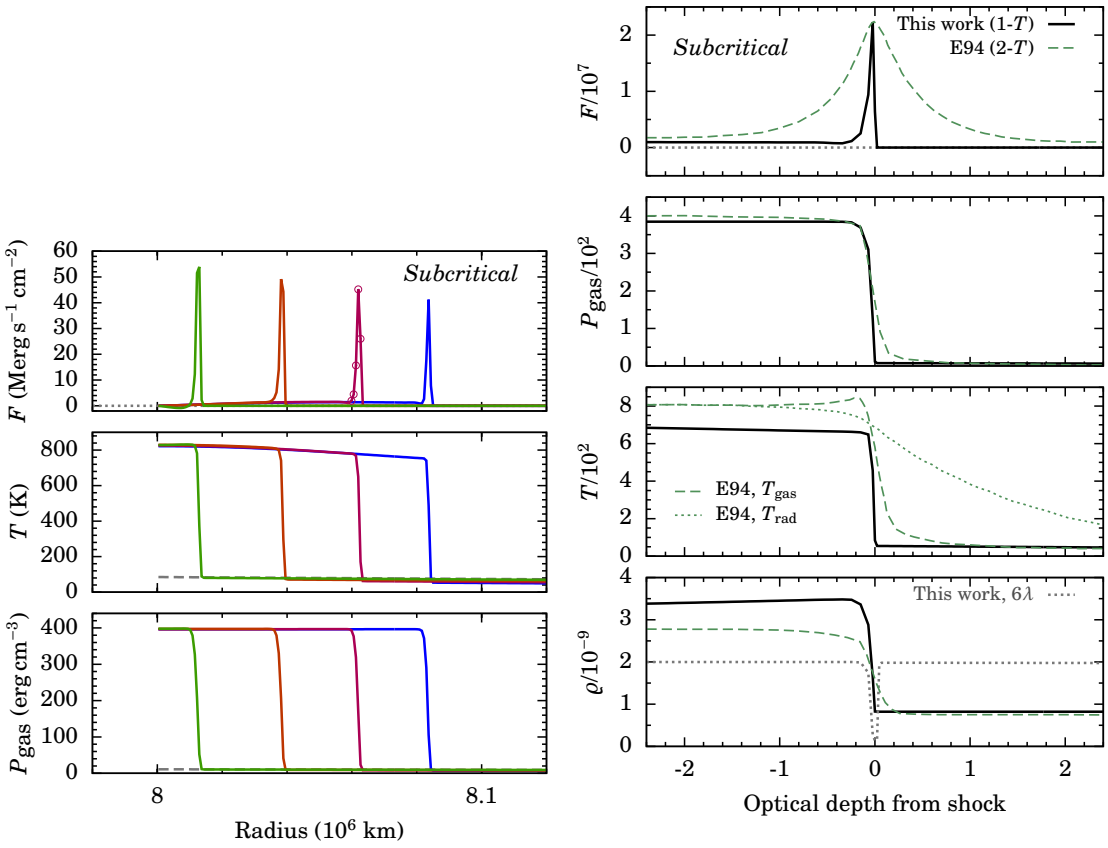

Fig. A.1.: *Left column:* Radial variation of the (*top panel*) flux, (*middle*) temperature, and (*bottom*) gas pressure in the subcritical case ($v_{\rm shock} = 6\ {\rm km\,s^{-1}}$). The four profiles in each panel are, from left to right, taken at 5.4, 17, 28, and 38.3 ks after the initial time, as in figure 8 of E94, while the grey dashed line shows the initial profile. The circles in the third profile of the top panel indicate the grid resolution in the spike. There are 1000 cells in the whole grid. *Right column:* From top to bottom, *(a)* flux, *(b)* gas pressure, *(c)* temperature, and *(d)* density as a function of the optical depth $\int \kappa\rho\,{\rm d}r$ from the shock front for a small region in the subcritical case ($v_{\rm shock} = 6\ {\rm km\,s^{-1}}$) at $t = 3.83 \times 10^4$ s as in figure 9 of E94. Her data (for 2-T radiation transport) is also shown (*green dashed line*). The units are in all cases cgs and are omitted for clarity. The bottom panel also shows as a dashed line six times the flux limiter (see Equation 1.23).

A.4.1. Subcritical case

Figure A.1a shows the radial dependence of the radiative flux, temperature and gas pressure at four different times in the subcritical case with $v_{\rm shock} = 6\ {\rm km\,s^{-1}}$, which corresponds to laboratory-frame Mach numbers $\mathcal{M} \approx 4$–5 at early to late times, respectively. (Note that, in accordance with Equation (1.4), the shock in our reference frame advances with a speed of $v_{\rm front} = 2.1\ {\rm km\,s^{-1}}$.) The results are qualitatively similar to the ones of E94, with (i) some pre-heating but still (ii) $T_- \ll T_1$, reflecting the quick absorption (over only a few grid cells; see also Figure A.1b) of the flux, which leads to a sharp peak, and (iii) the negative flux just after the shock in an early profile, although this is at 17 ks for E94 but in the 5.4 ks-profile for us. Our 1–T diffusion approximation does not let us reproduce the temperature overshoot behind the shock (the Zel'dovich spike; see Chapter 1.1.1) but apart from that the overall shape of the curves is in very good agreement, especially given the differences between 1- and 2-T radiation transport.

There quantitative differences between E94 and our results in the subcritical case are small. The post-temperature ($T_2 \approx 700$ K, with some decay over time due to radiative losses) is similar to within ten per cent, while our peak flux decreases faster over the four snapshots shown, from $F = 3.4$ to $2.2 \times 10^7\ {\rm erg\,s^{-1}\,cm^{-2}}$ compared to her $F = 2.5$ to $2.4 \times 10^7\ {\rm erg\,s^{-1}\,cm^{-2}}$. This is probably due to the much sharper drop in temperature directly upstream of the shock in the 1–T case, as expected from E94.

Figure A.1b shows profiles at $t = 3.83 \times 10^4$ s as a function of the optical depth from the shock. The main difference with the full-radiation transport case or the 2-T approximation is in the thickness, in optical depths, of the flux peak at the shock: in the 1–T case, F decreases within only a few grid cells and in much less than one optical depth, in contrast to E94 where the flux decreases with $F \propto \mathrm{e}^{-\sqrt{3}\Delta\tau \approx 1}$ as a simple semianalytical model predicts (Mihalas & Mihalas, 1984). Temperatures and pressures are however very similar, with also a density jump $\varrho_1/\varrho_- \approx 3.9$. A pure hydrodynamic jump would yield (for a shock-frame Mach number $\mathcal{M}' = 6.6$) a ratio of

$$\frac{\varrho_1}{\varrho_-} = \frac{(\gamma+1)\mathcal{M}'^2}{(\gamma-1)\mathcal{M}'^2+2} \approx 3.7. \tag{A.19}$$

Thus the interaction of the radiation with the gas increases the density jump slightly, as in discussed in Mihalas & Mihalas (1984, see also equation 10 of Commerçon et al., 2011). Notice finally how her artificial viscosity spreads the shock over a few grid cells.

A.4.2. Supercritical case

Figure A.2a shows the radial dependence at four different times of the radiative flux, temperature and gas pressure in the supercritical case ($v_{\mathrm{shock}} = 20$ km s^{-1}, which corresponds to a laboratory-frame $\mathcal{M} \approx 10$–25 at early to late times, respectively). The profiles are very similar to those of E94, with (i) a negative flux directly downstream of the shock (i.e., flowing downstream), (ii) $T_1 \approx T_-$, and (iii) a precursor ahead of the shock stretching out to several optical depths. The Zel'dovich peak is of course absent in our 1-T calculations and the temperature drops sharply at the leading edge of the precursor, as discussed in E94.

The profiles are also quantitatively similar, with only slightly smaller peak temperatures: while E94's peak radiation temperature increases from 3200 to 4900 K over the four snapshots, ours goes from 2800 to 4000 K, which nevertheless represents a similar relative increase. Our peak fluxes are 20 per cent smaller but also roughly constant in time.

At $t = 7.5 \times 10^3$ s, our precursor has a thickness $\Delta r = 0.9 \times 10^{10}$ cm, which is smaller than the $\Delta r = 2.0 \times 10^{10}$ cm, found by E94 but similar to the $\Delta r \approx 1.3 \times 10^{10}$ cm of Kuiper et al. (2010). Nevertheless, as shown in Figure A.2b, the agreement with E94 around the shock is very good. In particular, the pressure structures match almost perfectly, both in the pre- and post-shock regions.

A.4.3. Summary

Overall, our results for the Ensman (1994) radiation-hydrodynamics shocks match her results. Given that the pressure structures are nearly identical, differences in the temperatures translate into differences in the density structure (since $P \propto \varrho T$ for an ideal-gas equation of state). These moderate temperature differences are possibly due to our use of 1-T radiation transport, whereas Ensman (1994) performed 2-T calculations. Note finally that, as used in Chapter 3, the 2-T radiation transport module was tested with the same set-ups by Klassen et al. (2014) and is therefore not discussed here.

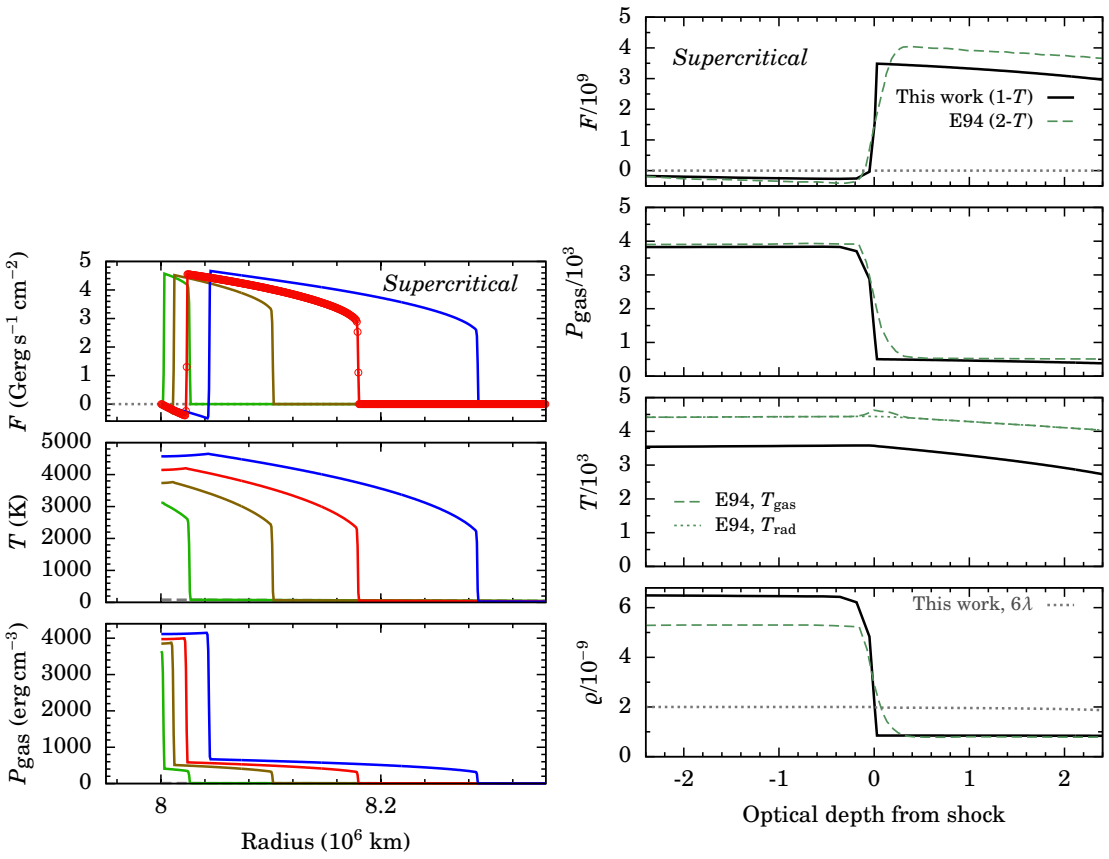

Fig. A.2.: *Left column:* Radial profiles for the supercritical shock ($v_{\rm shock}$ = 20 km s^{-1}). The panels and lines are as in Figure A.1a but for t = 0.9, 4, 7.5, and 13 ks; cf. figure 10 of E94. Note the different reference frame when comparing to E94. *Right column:* As in Figure A.1b (note however the different normalisations) but for the supercritical case ($v_{\rm shock}$ = 20 km s^{-1}) at $t = 7.5 \times 10^3$ s. Compare to figure 13 of E94.

B
Additional material

This chapter provides additional material, mostly figures, which did not fit into the main body of this thesis but which might be useful as reference.

B.1. Flux limiters

The flux limiters of Levermore & Pomraning (1981) and Ensman (1994) are compared in Figure B.1. They differ at most by 20 per cent, at $R \approx 2.5$, and by less than ten per cent for $R \lesssim 0.5$ or $R \gtrsim 15$. Another common choice, the flux limiter of Minerbo (1978), is also shown.

B.2. Effect of the opacity

We compare in Figure B.2 the structures for a constant opacity and using Bell & Lin (1994), as in Section 2.5.2. Only the three last cases of Table 2.1 are considered because of the available data. The results are very similar to Figure 2.9.

B.3. Reduced fluxes for Bell & Lin (1994) opacities

For completeness, Figure B.3 shows the reduced fluxes directly upstream of the shocks for the simulations of Section 2.5.4.

B.4. Parameter exploration

In Figures B.4 and B.5, we vary, respectively, the outer pressure boundary condition as well as the number of grid cells, or the choice of $r_{\min}$. The former is seen to not make a significant difference even when using tabulated opacities.

Due to the inner radiative boundary condition ($\mathrm{d}E_{\mathrm{rad}}/\mathrm{d}r = 0$) and the slight deviation from hydrostatic equilibrium caused by the settling of the gas, planets with a smaller $r_{\min}$ are slightly hotter at the shock. The trend in the shock temperature is $\mathrm{d}T_{\mathrm{shock}}/\mathrm{d}r_{\min} = -1\ \mathrm{K}\,R_{\mathrm{J}}^{-1}$ for $\kappa = 10^{-2}\ \mathrm{cm^2\,g^{-1}}$ around $r_{\min} = 10\ R_{\mathrm{J}}$, with $T_{\mathrm{shock}}(r_{\min} = 20\ R_{\mathrm{J}}, \kappa = 10^{-2}) = 170$ K. The slope is similar for $\kappa = 10^{-1}$ for $r_{\min} = 20$, with $T \approx 170$ K. Thus, taking $r_{\min} \to 0$ here should lead to a difference on the order of 20 K, and probably less for smaller planets. This is a crude estimate but it seems to indicate that the choice of $r_{\min}$ is not crucial; uncertainties in the opacities, for instance, are likely to have much more pronounced consequences.

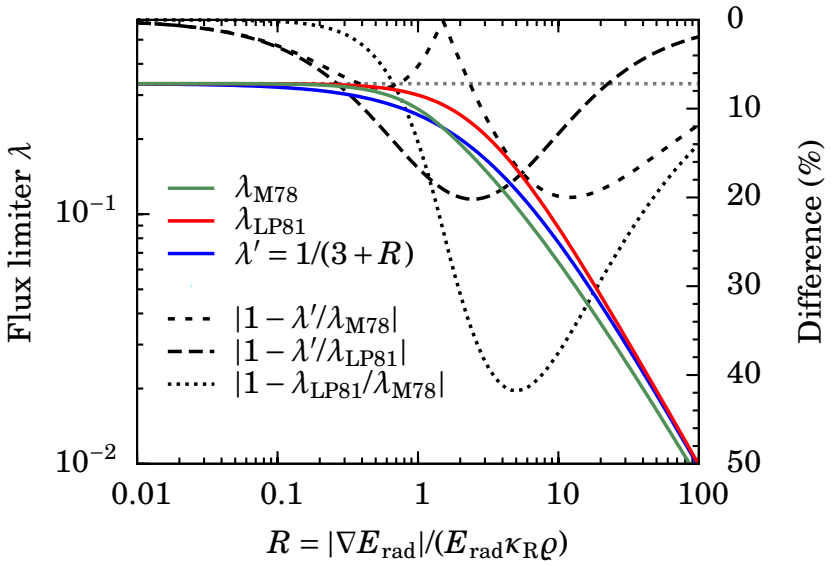

Fig. B.1.: Rational approximation of the Levermore & Pomraning (1981) flux limiter and flux limiter of Ensman (1994) (*solid lines*) as a function of the logarithmic optical derivative of the radiation energy density R. Their ratio is displayed as a dashed curve (with the right axis scale).

Finally, in Figure B.6 we assess the effect of the choice of κ, μ and γ by looking at the shock temperature for a mass and radius grid with $\dot{M} = 10^{-3}\ M_\oplus\,\mathrm{an}^{-1}$ and considering extreme cases: a constant opacity of the BL94 table; $\mu = 1.23$ (appropriate when hydrogen is atomic) or $\mu = 2.353$; and $\gamma = 1.1$ or 1.44. (The number of grid cells is varied simultaneously from $N = 1000$ to 3000 but several other simulations have shown this to be without consequence.) The shock temperature can be seen to not depend at all on N and barely on μ and γ, but noticeably on κ, as found in the main work.

B.5. Estimated Mach numbers for population synthesis planets

Figure B.7 shows the estimated shock temperature and the Mach number obtained with Equation (1.18) and the data of Figures 2.4 and 2.5, as indirectly used in Figure 2.15. The shock temperature increases with planet mass. For the Mach number, we consider two values of μ, where $\mu = 1.23$ is more appropriate at higher temperatures and $\mu = 2.353$ at lower temperatures.

B.6. Density inversions

Since we do not model convection, density inversions can occur. Indeed, considering a profile, for which it holds that

$$P = \frac{\varrho(P)T(P)}{\mu(P)}\frac{k_\mathrm{B}}{m_\mathrm{H}}, \tag{B.1}$$

it is easy to show that the density–pressure stratification is (for a general idea gas with variable mean molecular weight)

$$\left(\frac{\mathrm{d}\ln\varrho}{\mathrm{d}\ln P}\right)_\mathrm{act} = 1 - \nabla_\mathrm{act} + \left(\frac{\mathrm{d}\ln\mu}{\mathrm{d}\ln P}\right)_\mathrm{act}, \tag{B.2}$$

where the actual $T(P)$ gradient is

$$\nabla_\mathrm{act} \equiv \frac{\mathrm{d}\ln T}{\mathrm{d}\ln P}. \tag{B.3}$$

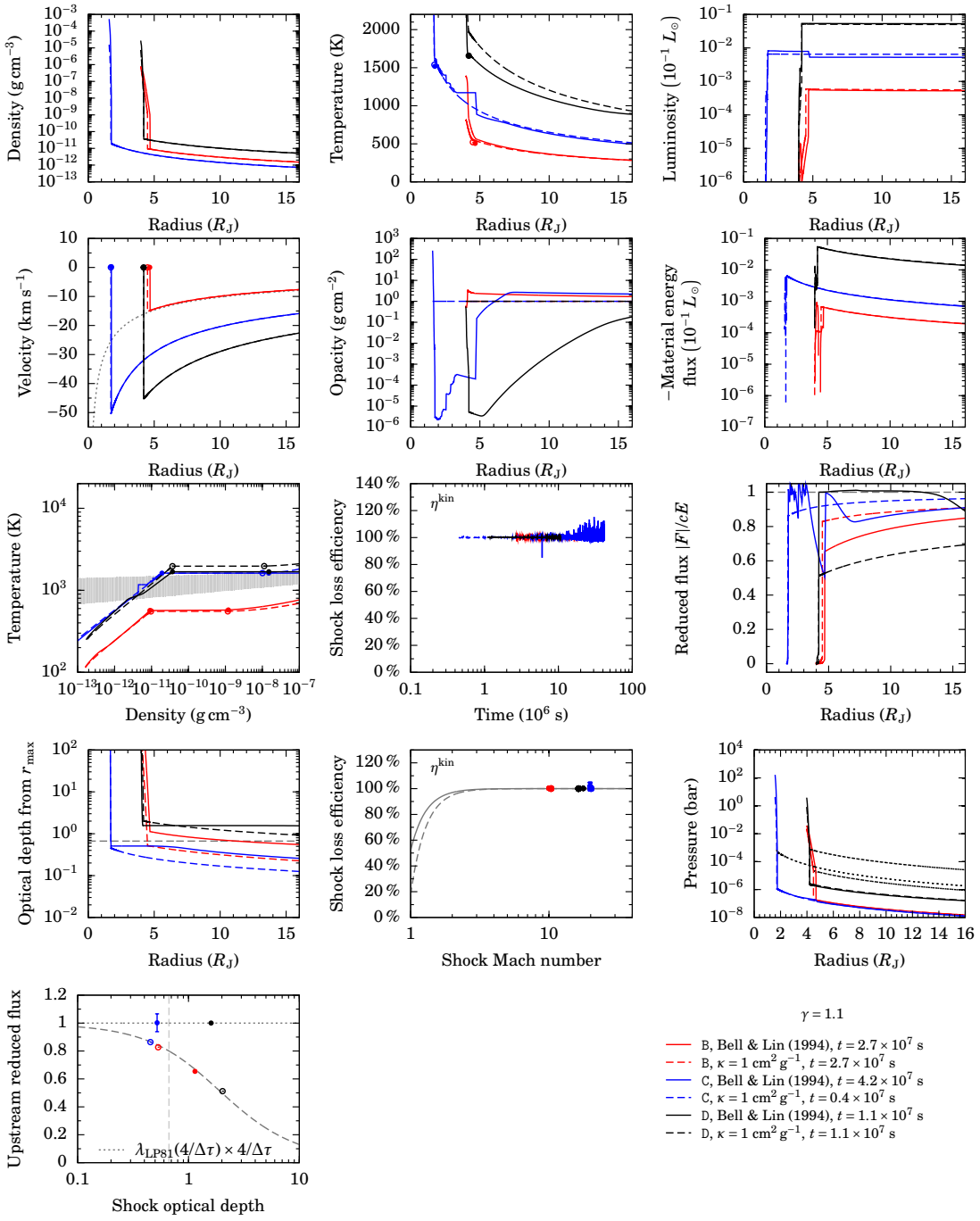

Fig. B.2.: As in Figure 2.9 but for the three last cases of Table 2.1, using $\gamma = 1.1$, and compared to the same cases but using the BL94 opacities. The last panel is as in Figure 2.11, where, as in the efficiency against the Mach number, full (open) circles correspond to solid (dotted) data curves. Only Cases A and B are compared to a free-fall velocity profile (*dashed grey curve*) and only for Case C with BL94 is an errorbar shown for the upstream reduced flux $f_{\rm red}$ (*last panel*), which comes from time averaging. The outer boundary conditions are $\mathrm{d}P/\mathrm{d}r = 0$ and $\mathrm{d}r^2 E_{\rm rad}/\mathrm{d}r = 0$.

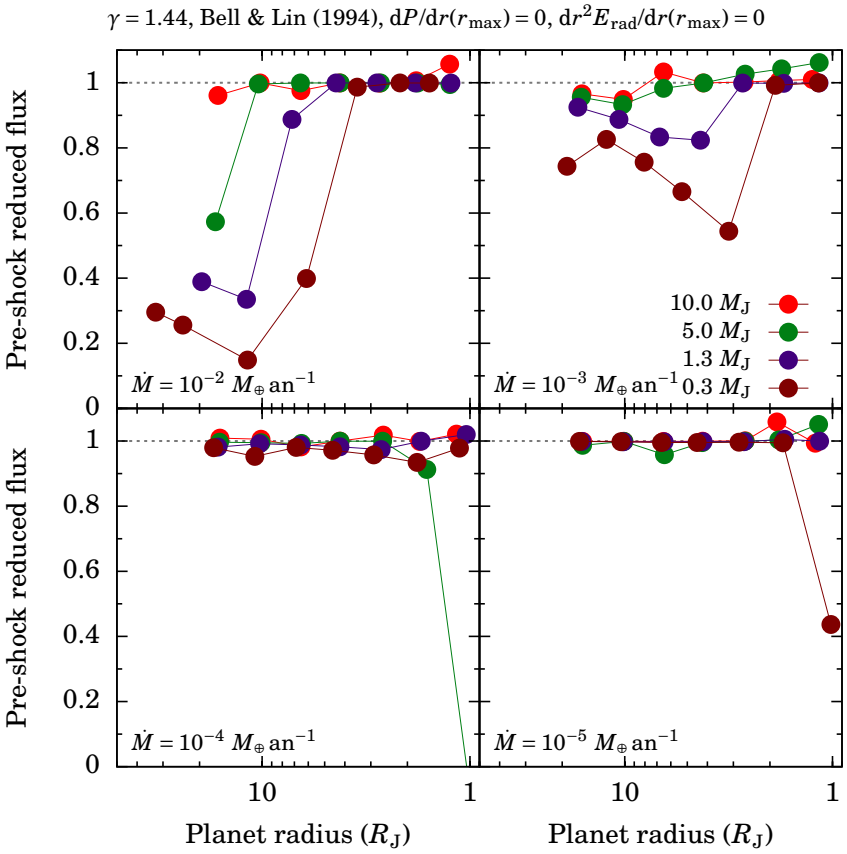

Fig. B.3.: As in Figure 2.10 but for the BL94 opacities and with $\gamma = 1.44$.

The μ derivative being negative but very small (e.g., $\leqslant 0.001$), it is the size of ∇_{act} which is decisive. If one considers convection by the usual Schwarzschild criterion

$$\nabla_{act} = \min(\nabla_{ad}, \nabla_{rad}), \tag{B.4}$$

the fact that ∇_{ad} (which is equal to $1 - 1/\gamma$ for a constant-γ gas) is < 0.5 for hydrogen and helium ensures that $d\varrho/dP > 0$. If however there is no convection and the temperature gradient is given by

$$\nabla_{act} = \nabla_{rad} \equiv \frac{3LP}{64\pi\sigma G m_r T^4}\kappa, \tag{B.5}$$

large enough opacity values will lead to a density inversion.

B.7. Extracting an atmospheric structure from a `Phoenix` log file

The script shown in Listing B.1 was used to extract structures for the coupling work to `BT-Settl` (Chapter 4). It was written by analysing a typical log output file (`http://phoenix.ens-lyon.fr/Grids/BT-Settl/AGSS2009/STRUCTURES/lte006-3.0-0.0.BT-Settl.6`) from the `Phoenix` atmosphere calculator to identify the different parts of the (typically 80000-line long) file and derive criteria to extract the desired blocks. Although not strictly necessary for the coupling, which requires only a single (P, T) point in the convective part, the complete atmospheric structure was extracted to check for anomalities and allow comparisons to other work (see Chapter 4). (It is not available under another form, as confirmed with the author F. Allard.) Note that there are slight differences in the output of different versions of the atmosphere code and that a single log file usually contained all 6 or 12 iterations, which somewhat complexified the extraction process.

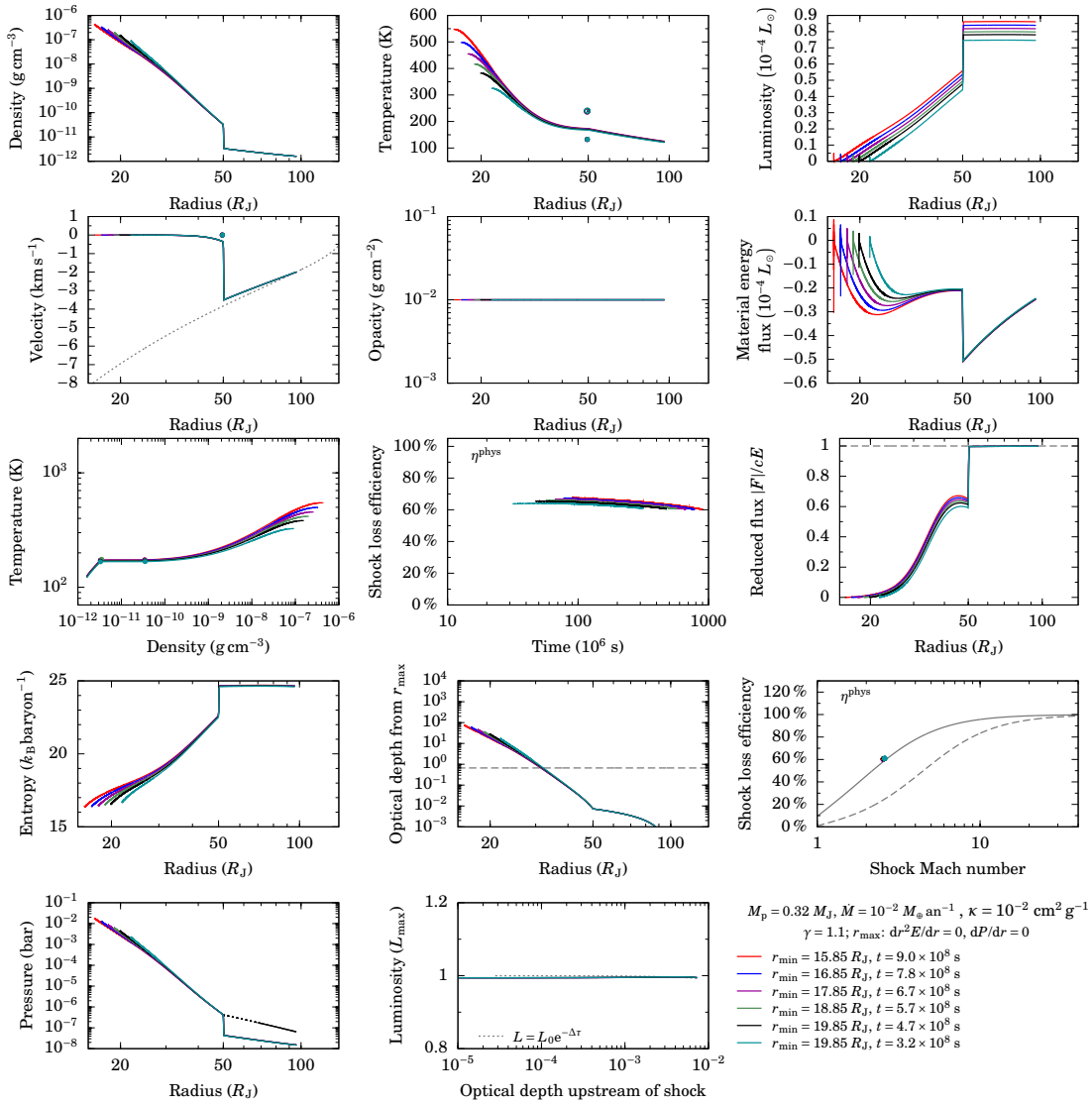

Fig. B.4.: Comparison of the outer boundary conditions. See parameter settings in the caption.

Listing B.1: Code to extract a structure from a `Phoenix` log file.

```
#! /usr/bin/awk -f
# extrahiert die relevanten Blöcke aus PHOENIX-.6-Dateien (z.B. für BT-Settl)
#  - entweder nur die letzte Iteration
#        oder alle Iterationen (mit einer leeren Zeile dazwischen)
#    wird/werden gespeichert
#  - die .7-Dateien enthalten nur eine Iteration
#
# Beispielruf: ./extra.awk           BT-Settl/AGSS2009/lte006-3.0-0.0.BT-Settl.6
#   Die Ausgabedateien lte006-3.0-0.0.BT-Settl.6_Info und lte006-3.0-0.0.BT-Settl.6_Strukt
#   werden in BT-Settl/AGSS2009/ (Vorläufige Dateien aber im gegenwärtigen Verzeichnis) erzeugt
#
# Beispielruf: ./extra.awk -v alle=1 BT-Settl/AGSS2009/lte006-3.0-0.0.BT-Settl.6
#   Die Ausgabedateien lte006-3.0-0.0.BT-Settl.6_Info und lte006-3.0-0.0.BT-Settl.6_Strukt_alleIter
#   werden in BT-Settl/AGSS2009/ (Vorläufige Dateien aber im gegenwärtigen Verzeichnis) erzeugt
#
#
#
# sample call: ./extra.awk somedir/lte006-3.0-0.0.BT-Settl.6
#   The output files lte006-3.0-0.0.BT-Settl.6_Info (not really useful) and lte006-3.0-0.0.BT-Settl.6_Strukt
#   will be created in somedir/ (temporary files however in current directory)
#
# sample call: ./extra.awk -v alle=1 somedir/lte006-3.0-0.0.BT-Settl.6
#   The output files lte006-3.0-0.0.BT-Settl.6_Info (not really useful) and lte006-3.0-0.0.BT-Settl.6_Strukt_alleIter
#   will be created in somedir/ (temporary files however in current directory)
#
#
#  G.-D. Marleau -- MPIA
#               (c)  9.01.2013
#  letzte Änderung: 02.06.2014

BEGIN {

```

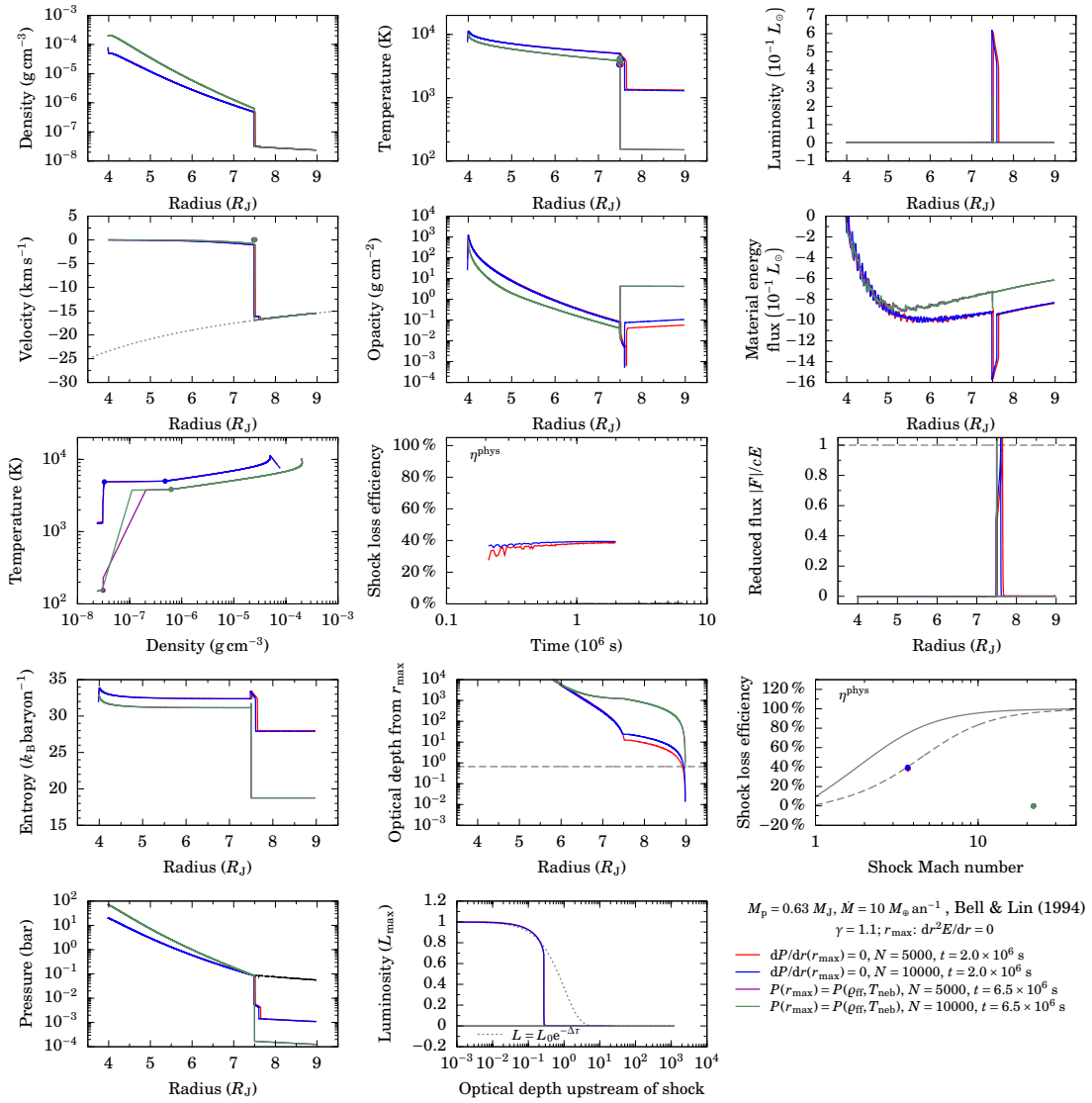

Fig. B.5.: Comparison of the effect of the choice of r_{min}. The time of each simulation snapshot is chosen to yied the same shock position.

```
gewollteIt = 0   # gewollte Iteration: die letzte

# Informationsblock liefert T_eff, R_eff, L (je einen Wert)
InfoText = "This is for effective radius and is physical"     # um den Block zu erkennen
Info = 0

# 1. Block liefert i, tau, T, P, rho, mu
einsText = "i          tau          temp          pg          pe          rho          mu          vel          mdot     lg\\(g_eff\\)
          Nrho      conv"
eins = 0

# 2. Block liefert S, Stgrad (del_rad), gradient, adgrad (del_ad)
zweiText = "i          tau          z          temp          pg          rho          mu          S          Hp       stgrad
      gradient       adgrad       Fconv"
zwei = 0

# 3. Block liefert kappa_Rosseland
#                              (1/cm)                                                (cm**2/g)
dreiText = "layer        tstd      b-mean      j-mean      f-mean    ross-mean      b-mean      j-mean      f-mean    ross-mean
      ross-corr"
drei = 0

# 4. Block liefert tau_Rosseland
vierText = "tau averages"  #layer        tstd      b-mean      j-mean      f-mean    ross-mean"
vier = 0
wartevier = 1

# 5. Block liefert den bolometrischen radiativen FluSS (suf) (tk=tau=taustd: tau bei lambda = 1.25 um)
# ** suf wird mit pi/1e8 multipliziert um den FluSS in erg/s/cm^2 zu bekommen **
# * (F/sigma)^0.25 nicht ganz = Teff weil Fehler != 0 *
fuenfText = "no          tk          sub        subk         suj        sujk         suf        sufk        sulb" # [weniger
      Leerzeichen bei CIFIST 6... der Rest einfach weg]  deltaE\\(%\\)   fehler\\(%\\)   aenderung"
```

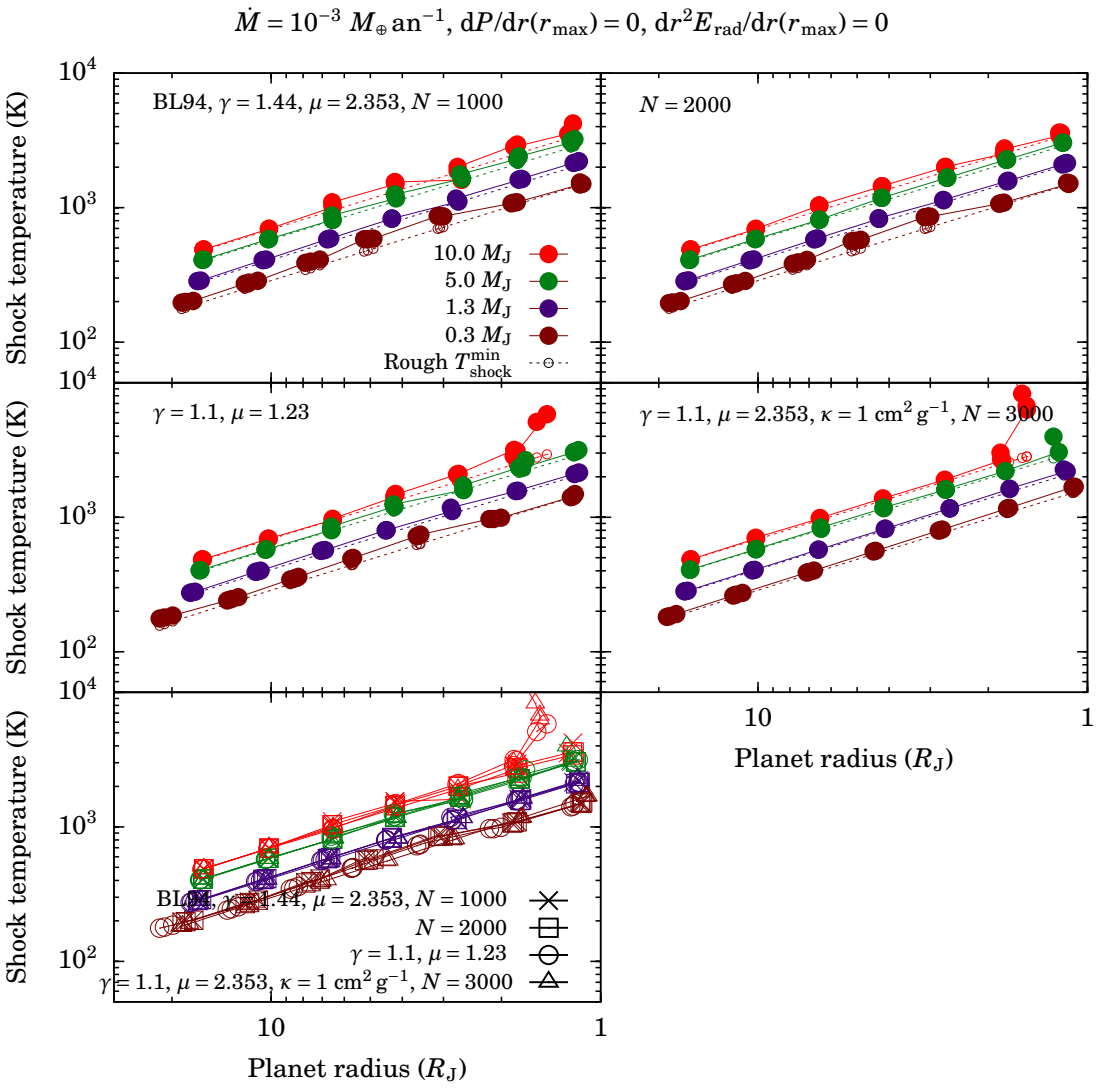

Fig. B.6.: Shock temperatures for different combinations of κ, γ, μ, and number of grid cells N, as indicated in the panels, with only the differences to the top left panel indicated. The last panel combines all results for a direct comparison.

```
61     fuenf = 0
62  }
63
64  {
65    if (NR == 1) {
66       InfoDatei = (FILENAME "_Info")
67       einsDatei = (FILENAME ".TPrhomu")
68       zweiDatei = (FILENAME ".Sdel")
69       dreiDatei = (FILENAME ".kappa")
70       vierDatei = (FILENAME ".tau")
71       fuenfDatei = (FILENAME ".suf")
72       ausDateib  = (FILENAME "_Strukt")   # Basis
73
74       # bei den .spec.6-Datein gibt es nur eine Iteration
75       if ( FILENAME ~ ".spec" ) {
76          gewollteIt = 1
77       }
78
79       if( system( "[ -f " InfoDatei " ] " )  == 0 ) {  system( "rm " InfoDatei )  }
80       print "# i          tau            T              P             rho          mu     log(g_eff)" > einsDatei
81       print "# i\t         tau\t          S\t          Hp\t      delrad\t        del\t      delad" > zweiDatei
82       print "# i         tau        kappa_Rosseland" > dreiDatei
83       print "# i         tau(_std)     tau_Rosseland" > vierDatei
84       print "# i         tau(_std)     bolflux" > fuenfDatei
85    }
86
87    if ( $0 ~ "max. no. of iterations:" ) {
88       Itanz = $(NF);       # Iterationenanzahl
89       print " Iterationenanzahl: " Itanz # "; gewollte Iteration: " Itnum;
90       if ( alle ) {
```

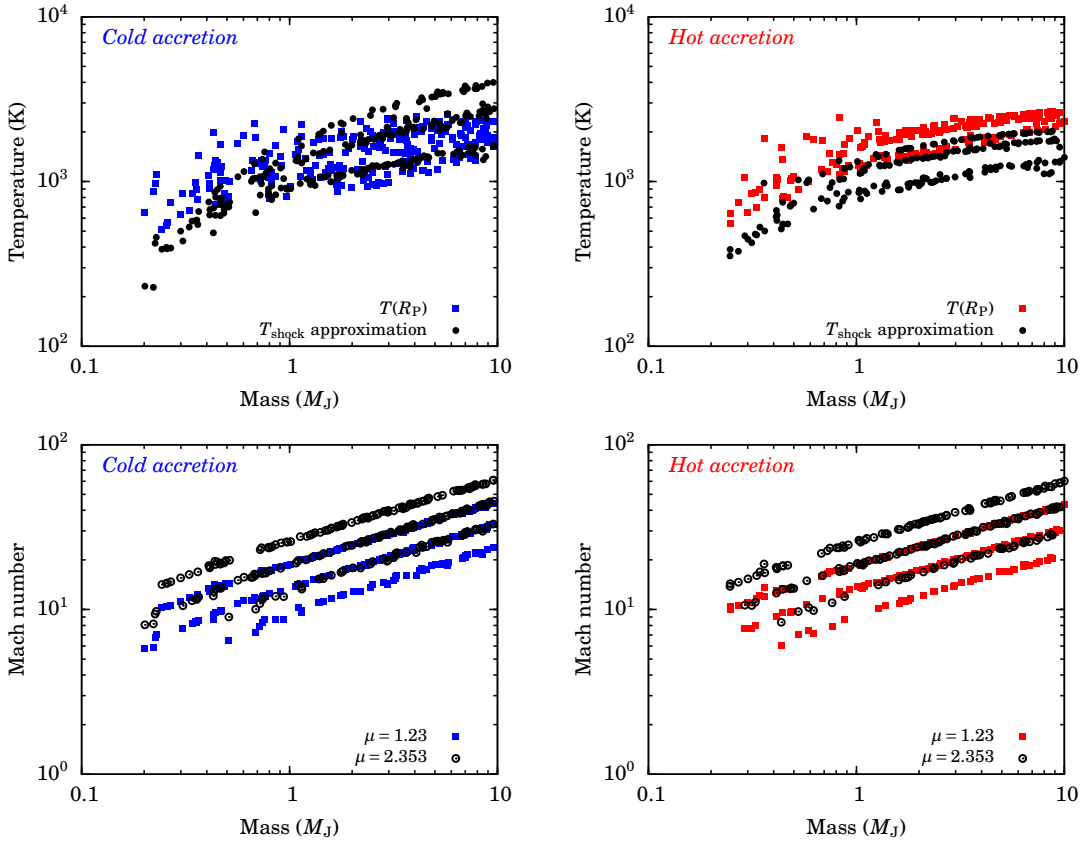

Fig. B.7.: As in Figure 2.15 but showing explicitly the temperatures (*top row*) and Mach numbers (*bottom row*). The effective temperature is shown as $T(R_p)$ and the estimate of the shock temperature as T_{shock}. In the Mach number plots, the groups of points correspond to $\dot{M} = 10^{-2}$ to 10^{-4} $M_\oplus$ an^{-1} (*bottom to top*).

```
        ausDatei = (ausDateib "_alleIter");
        gewollteIt = 1   # wir wollen alle
    } else {
        ausDatei = ausDateib
    }
}

if ( $0 ~ "no. of depth points" ) {  Schichtenanzahl = $(NF)  }  #  ; print " Schichtenanzahl: " Schichtenanzahl;  }

# für den Fall, wo wir nur eine Iteration wollen:
if ( ( $0 ~  "next iteration is no." ) && $0 ~ ( Itanz ) ) {   # man kann nicht "results of iteration no:           8 :" benutzen
      , denn Info, eins und zwei kommen davor
   gewollteIt = 1
}

if (gewollteIt) {

   if ( Info ) {
      print $0 >> InfoDatei
      if ($0 ~ "R_eff is") {  Info = 0  }   # letzter Eintrag des Blockes
   }


   if (eins || zwei || drei || vier || fuenf) {
      gsub(/D/,"E", $0)  # Fortran-Format konvertieren
   }

   if (eins) {
      #     i      tau      T       P       rho      mu     log(g_eff)           # Achtung! log(g_eff) kann mit dem nächsten Feld
          (Nrho) zusammengeschweiSSt sein... deswegen substr
      print $1 "\t" $2 "\t" $3 "\t" $4 "\t" $6 "\t" $7 "\t" substr($10,1,10) >> einsDatei    # log(g_eff) ist 10 breit
   }

   if (zwei) {
      #     i      tau      S      Hp      delrad    del      delad     Fconv          # Achtung! letztes Feld Fconv kann negativ
           sein
      #  Fconv muSS mit 4*pi multipliziert werden

      # wenn del_rad negativ ist:
      if (substr($9,12,1) == "-"){
         Hp = substr($9,1,11)
         strad = "-" substr($9,13,11)
         print " strad = " strad " < 0 bei i = " $1 " ( tau = " $2 ") in " FILENAME
```

```
132             # gradient sollte auch < sein (weil adgrad > 0 und somit > strad bleibt)
133             if (substr($9,24,1) == "-"){
134                gradient = "-" substr($9,25,11)
135 #                print " (gradient = " gradient " bei tau = " $2 " in " FILENAME ")"
136
137                # prüfen, ob Fconv negativ ist
138                if (substr($10,12,1) == "-"){
139                   adgrad = substr($10,1,11)
140                   Fconv = substr($10,12,12)   # mit Vorzeichen
141 #                  print "  Fconv = " Fconv " bei tau = " $2 " in " FILENAME
142                } else {
143                   adgrad = $10
144                   Fconv = $11
145                }
146
147             }else {
148               print "gradient = " gradient " in " FILENAME " aber != " strad " < 0? Problem!"
149               exit
150             }
151
152          # delrad nicht negativ (und somit gradient auch nicht)
153          } else {
154
155                Hp = $9
156                strad = $10
157                gradient = $11
158
159                # prüfen, ob Fconv negativ ist
160                if (substr($12,12,1) == "-"){
161                   adgrad = substr($12,1,11)
162                   Fconv = substr($12,12,12)   # hat Vorzeichen
163 #                  if($1~"77") print "  ** Fconv = " Fconv " bei tau = " $2 " (i=" $1 ") in " FILENAME
164                } else {
165                   adgrad = $12
166                   Fconv = $13
167                }
168
169          }
170
171          print $1 "\t" $2 "\t" $8 "\t" Hp "\t" strad "\t" gradient "\t" adgrad "\t" Fconv >> zweiDatei
172       }
173
174       if (drei) {
175          #     i      tau   kappa_Rosseland  kappa_P  kappa_J   kappa_H
176          ## std: nur kappa_Ross
177          #print $1 "\t" $2 "\t" $10 >> dreiDatei
178          ## Pauls Spezialversion: mit anderen kappas
179          print $1 "\t" $2 "\t" $10 "\t" $7 "\t" $8 "\t" $9 >> dreiDatei
180       }
181
182       if (vier && wartevier == 0) {
183          #     i      tau   tau_Rosseland
184          print $1 "\t" $2 "\t" $6 >> vierDatei
185       } else if (vier) {
186          print "1    0      0.0000E+00" >> vierDatei    # keine 1-Schicht im Block...
187          wartevier = 0                                  # die erste Zeile nach "tau averages" beinhaltet die Spaltennamen
188       }
189
190       if (fuenf) {
191          #     i       tk          suf
192          if ($0 !~ "convection") { print $1 "\t" $2 "\t" $7 >> fuenfDatei }   # Konvektionsanfang und -beginn wird angegeben
193       }
194
195       if ($1 ~ Schichtenanzahl) {
196          if (eins) { print "" >> einsDatei; }
197          if (zwei) { print "" >> zweiDatei; }
198          if (drei) { print "" >> dreiDatei; }
199          if (vier) { print "" >> vierDatei; }
200          if (fuenf) { print "" >> fuenfDatei; }
201
202          if (vier) wartevier = 1   # für die nächste Iteration, falls wir mehrere wollen
203          eins = 0; zwei = 0; drei = 0; vier = 0; fuenf = 0;
204       }
205
206       if ($0 ~ InfoText) {  Info = 1  } #; print "Info  " NR  }
207       if ($0 ~ einsText) {  eins = 1  } #; print "eins " NR  }
208       if ($0 ~ zweiText) {  zwei = 1  }  #; print "2 " NR  }
209       if ($0 ~ dreiText) {  drei = 1  }  #; print "3  " NR  }
210       if ($0 ~ vierText) {  vier = 1  }  #; print "4  " NR  }
211       if ($0 ~ fuenfText) {  fuenf = 1  }  #; print "5  " NR  }
212    }
213 }
214
215 END {
216     N = split(FILENAME,Vorl,"/")   # Vorläufige Dateien im gegenwärtigen Verzeichnis speichern
217     Name = Vorl[N]
218     system( "join --header " einsDatei " " zweiDatei " > vorl1." Name )
219     system( "join --header vorl1."Name " " dreiDatei  " > vorl2." Name )
220     system( "join --header vorl2."Name " " vierDatei  " > vorl3." Name )
221     system( "join --header vorl3."Name " " fuenfDatei  " > vorl4." Name )
222      # die Reihenfolge von vorl4 ist (mit ,join' wird das Vergleichsfeld nur einmal gedruckt!):
223      #     i      tau      T       P       rho      mu      log(g_eff)       tau       S       Hp        delrad    del      delad
               Fconv    tau   kappa_Rosseland    tau   tau_Rosseland    tau    suf
224      #     1       2       3       4       5        6        7               8       9       10       11        12        13
                      14     14+1         15+1             1+16        17           1+18     1+19
225 ## Pauls Spezialversion:
226      #     i      tau      T       P       rho      mu      log(g_eff)       tau       S       Hp        delrad    del      delad
               Fconv    tau   kappa_Rosseland         kappa_P  kappa_J   kappa_H   tau   tau_Rosseland    tau    suf
227      #     1       2       3       4       5        6        7               8       9       10       11        12        13
                      14     14+1         15+1              17      18          19      20      21             22      23
228      system( "awk 'BEGIN{print \"" \
```

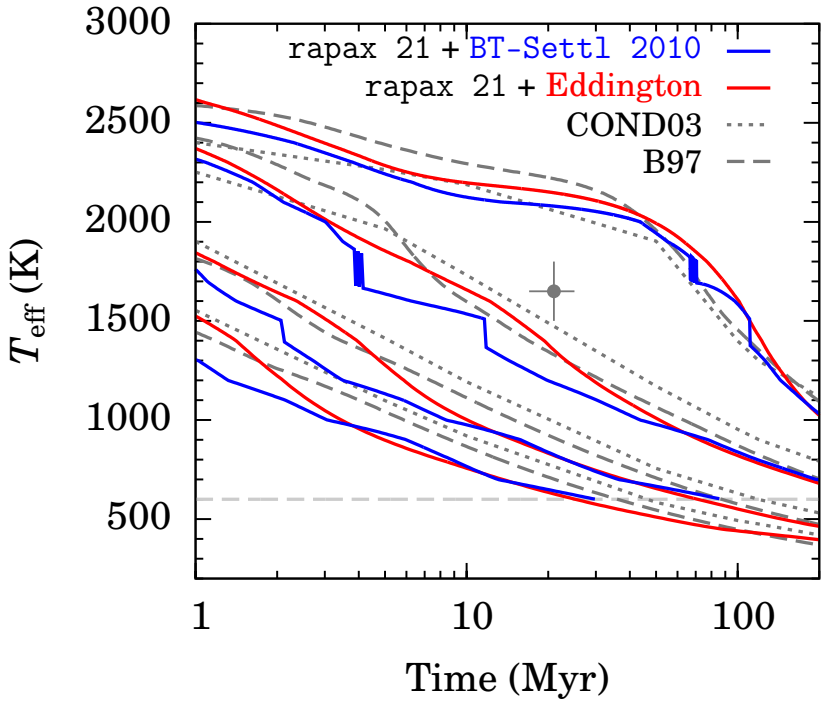

Fig. B.8.: As in Figure 4.3, hot-start cooling tracks for $M_{\rm p}$ = 3, 5, 10, 15 $M_{\rm J}$ (*bottom to top*) for different models including our self-consistent coupling. The lower edge of the grid is marked (*pale grey dashed line*).

```
229             "# 1             2               3               4               5               6               7               8
                              9              10              11              12              13              14              15
                                 16              17              18           19\"; print \"" \
230             "# i          tau               P               T     log(g_eff)              Hp             rho               S
                      mu       kappaRoss          delrad          del          delad        tauRoss       bolradflux         convflux
                           kappa_P       kappa_J       kappa_H\"; b = \"     \";}; " \
231             "(NR >= 2) { if(NF){ print $1 b $2 b $4 b $3 b $7 b $10 b $5 b $9 b $6 b $16 b $11 b $12 b $13 b $21 b $23/1e8
                      *3.1415926 b $14*4*3.1415926 b $17 b $18 b $19 } else { print $0 } }' vorl4." Name " > " ausDatei )  # NF (leere
                      Zeile): um nicht " "/4e8 = 0 zu bekommen
232
233     Befehl = ("wc -l < " ausDatei)
234     Befehl | getline Zeilenanz
235     close(Befehl)
236
237     if ( (!alle && abs(Zeilenanz-Schichtenanzahl) > 4) || (alle && abs(Zeilenanz - Itanz*(Schichtenanzahl+1)) > 4) ) {   # einige
            zusätzliche Zeilen ist nicht unbedingt ein Problem
238        print
239        print " *** Seltsam! `" ausDatei "' hat " Zeilenanz " Zeilen für eine " Schichtenanzahl "schichtige Atmosphäre... *** = "
240     } else {
241        Teff = substr(Name, 4, 3)*100   # ohne die Verzeichnisnamen davor; Name = lte***-***-...
242        if (substr(Name, 8, 3) !~ "-")  # die neueren haben eine genauere Teff
243           logg = substr(Name, 8, 3)
244        else
245           logg = substr(Name, 10, 3)
246        if ( Zeilenanz < 100 ) {
247           print " ** [ " Teff " K, " logg " dex ] ** Etwas ist schief gelaufen! < 100 Zeilen"
248        } else {
249           print " [ " Teff " K, " logg " dex ] Struktur extrahiert und in " ausDatei " gespeichert! " Itanz " Iterationen und "
                  Schichtenanzahl " Schichten"
250        }
251     }
252     system( "rm vorl1." Name " vorl2." Name " vorl3." Name " vorl4." Name " " einsDatei " " zweiDatei " " dreiDatei " " vierDatei "
            " fuenfDatei )
253 }
254
255 function abs(value) { return (value<0?-value:value); }
```

B.8. Coupled cooling tracks: Effective temperature evolution

Figure B.8 shows the effective temperature as a function of time for the coupled cooling tracks with `BT-Settl`-2010 and compares to the simple Eddington boundary conditions and other commonly-used tracks (Baraffe et al., 2003; Burrows et al., 1997). The effects of the non-converged atmospheres around $T_{\rm eff} \approx$ 1300–1700 K are clearly visible.

References

Ackerman A. S., Marley M. S., 2001, ApJ, 556, 872

Alibert Y., Mordasini C., Benz W., Winisdoerffer C., 2005, A&A, 434, 343

Allard F., Guillot T., Ludwig H.-G., Hauschildt P. H., Schweitzer A., Alexander D. R., Ferguson J. W., 2003, in Martín E., ed., IAU Symposium Vol. 211, Brown Dwarfs. p. 325

Allard F., Hauschildt P. H., Alexander D. R., Starrfield S., 1997, ARA&A, 35, 137

Allard F., Hauschildt P. H., Alexander D. R., Tamanai A., Schweitzer A., 2001, ApJ, 556, 357

Allard F., Homeier D., Freytag B., 2011, in Johns-Krull C., Browning M. K., West A. A., eds, Astronomical Society of the Pacific Conference Series Vol. 448, 16th Cambridge Workshop on Cool Stars, Stellar Systems, and the Sun. p. 91

Allard F., Homeier D., Freytag B., 2012, Philosophical Transactions of the Royal Society of London Series A, 370, 2765

Allard F., Homeier D., Freytag B., Schaffenberger W., Rajpurohit A. S., 2013, Memorie della Societa Astronomica Italiana Supplementi, 24, 128

Allard F., Homeier D., Freytag B., Sharp C. M., 2012, in Reylé C., Charbonnel C., Schultheis M., eds, EAS Publications Series Vol. 57, Low-Mass Stars and the Transition Stars/Brown Dwarfs (EES2011). pp 3–43

Allers K. N. et al., 2007, ApJ, 657, 511

Arras P., Bildsten L., 2006, ApJ, 650, 394

Asplund M., Grevesse N., Sauval A. J., Scott P., 2009, ARA&A, 47, 481

Ayliffe B. A., Bate M. R., 2009, MNRAS, 393, 49

Baines E. K. et al., 2012, ApJ, 761, 57

Baraffe I., 2014, in Joergens V., ed., Astrophysics and Space Science Library Vol. 401, 50 Years of Brown Dwarfs. p. 141

Baraffe I., Chabrier G., Allard F., Hauschildt P. H., 1998, A&A, 337, 403

Baraffe I., Chabrier G., Allard F., Hauschildt P. H., 2002, A&A, 382, 563

Baraffe I., Chabrier G., Barman T., 2010, Reports on Progress in Physics, 73, 016901

Baraffe I., Chabrier G., Barman T. S., Allard F., Hauschildt P. H., 2003, A&A, 402, 701

Baraffe I., Chabrier G., Fortney J., Sotin C., 2014, Protostars and Planets VI, pp 763–786

Baraffe I., Homeier D., Allard F., Chabrier G., 2015, A&A, 577, A42

Baraffe I., Vorobyov E., Chabrier G., 2012, ApJ, 756, 118

Barman T. S., Macintosh B., Konopacky Q. M., Marois C., 2011a, ApJ, 733, 65

Barman T. S., Macintosh B., Konopacky Q. M., Marois C., 2011b, ApJ, 735, L39

Bell K. R., Lin D. N. C., 1994, ApJ, 427, 987

Bergfors C., Brandner W., Janson M., Köhler R., Henning T., 2011, A&A, 528, A134

Beuzit J.-L. et al., 2006, The Messenger, 125, 29

Biller B. A., Close L. M., 2007, ApJ, 669, L41

Biller B. A. et al., 2013, ApJ, 777, 160

Black D. C., Bodenheimer P., 1975, ApJ, 199, 619

Bodenheimer P., D'Angelo G., Lissauer J. J., Fortney J. J., Saumon D., 2013, ApJ, 770, 120

Bodenheimer P., Hubickyj O., Lissauer J. J., 2000, Icarus, 143, 2

Bonnefoy M. et al., 2013, A&A, 555, A107

Bonnefoy M., Chauvin G., Lagrange A.-M., Rojo P., Allard F., Pinte C., Dumas C., Homeier D., 2014, A&A, 562, A127

Bonnefoy M. et al., 2014a, A&A, 562, A111

Bonnefoy M. et al., 2011, A&A, 528, L15

Bonnefoy M. et al., 2014b, A&A, 567, L9

Boss A. P., 1997, Science, 276, 1836

Bowler B. P., Liu M. C., Shkolnik E. L., Dupuy T. J., 2013, ApJ, 774, 55

Brandt T. D. et al., 2014, ApJ, 794, 159

Burgasser A. J. et al., 2010, ApJ, 725, 1405

Burrows A., Hubbard W. B., Lunine J. I., Liebert J., 2001, Reviews of Modern Physics, 73, 719

Burrows A., Liebert J., 1993, Reviews of Modern Physics, 65, 301

Burrows A. et al., 1997, ApJ, 491, 856

Caffau E., Ludwig H.-G., Steffen M., Freytag B., Bonifacio P., 2011, Sol. Phys., 268, 255

Callen H. B., 1985, Thermodynamics and an Introduction to Thermostatistics, 2nd edn. John Wiley & Sons, New York

Calvet N., Gullbring E., 1998, ApJ, 509, 802

Carson J. et al., 2013, ApJ, 763, L32

Cassisi S., Potekhin A. Y., Pietrinferni A., Catelan M., Salaris M., 2007, ApJ, 661, 1094

Castor J. I., 2004, Radiation Hydrodynamics. Cambridge University Press

Chabrier G., Baraffe I., 1997, A&A, 327, 1039

Chabrier G., Baraffe I., Allard F., Hauschildt P., 2000a, ApJ, 542, L119

Chabrier G., Baraffe I., Allard F., Hauschildt P., 2000b, ApJ, 542, 464

Chauvin G. et al., 2012, A&A, 542, A41

Chauvin G. et al., 2010, A&A, 509, A52

Chauvin G., Lagrange A.-M., Dumas C., Zuckerman B., Mouillet D., Song I., Beuzit J.-L., Lowrance P., 2004, A&A, 425, L29

Chauvin G., Lagrange A.-M., Dumas C., Zuckerman B., Mouillet D., Song I., Beuzit J.-L., Lowrance P., 2005, A&A, 438, L25

Close L. M., Males J. R., 2010, ApJ, 709, 342

Commerçon B., Audit E., Chabrier G., Chièze J.-P., 2011, A&A, 530, A13

Cox J. P., Giuli R. T., 1968, Principles of Stellar Structure. Gordon and Breach, New York

Crifo F., Vidal-Madjar A., Lallement R., Ferlet R., Gerbaldi M., 1997, A&A, 320, L29

Cumming A., Butler R. P., Marcy G. W., Vogt S. S., Wright J. T., Fischer D. A., 2008, PASP, 120, 531

Currie T. et al., 2011, ApJ, 729, 128

Currie T. et al., 2013, ApJ, 776, 15

Currie T., Cloutier R., Debes J. H., Kenyon S. J., Kaisler D., 2013, ApJ, 777, L6

Currie T. et al., 2012, ApJ, 760, L32

Currie T., Fukagawa M., Thalmann C., Matsumura S., Plavchan P., 2012, ApJ, 755, L34

D'Angelo G., Bodenheimer P., 2013, ApJ, 778, 77

Delorme P. et al., 2013, A&A, 553, L5

Deloye C. J., Bildsten L., 2003, ApJ, 598, 1217

Dieterich S. B., Henry T. J., Golimowski D. A., Krist J. E., Tanner A. M., 2012, AJ, 144, 64

Dodson-Robinson S. E., Veras D., Ford E. B., Beichman C. A., 2009, ApJ, 707, 79

Drake R. P., 2006, High-Energy-Density Physics: Fundamentals, Inertial Fusion, and Experimental Astrophysics, with 172 figures. Springer

Drake R. P., 2007, Physics of Plasmas, 14, 043301

Ducourant C., Teixeira R., Chauvin G., Daigne G., Le Campion J.-F., Song I., Zuckerman B., 2008, A&A, 477, L1

Eisner J. A., 2015, ApJ, 803, L4

Ensman L., 1994, ApJ, 424, 275

Esposito S. et al., 2013, A&A, 549, A52

Fabrycky D. C., Murray-Clay R. A., 2010, ApJ, 710, 1408

Faherty J. K. et al., 2012, ApJ, 752, 56

Ferguson J. W., Alexander D. R., Allard F., Barman T., Bodnarik J. G., Hauschildt P. H., Heffner-Wong A., Tamanai A., 2005, ApJ, 623, 585

Fernández D., Figueras F., Torra J., 2008, A&A, 480, 735

Ford E. B., 2014, Proceedings of the National Academy of Science, 111, 12616

Fortney J. J., Hubbard W. B., 2004, ApJ, 608, 1039

Fortney J. J., Ikoma M., Nettelmann N., Guillot T., Marley M. S., 2011, ApJ, 729, 32

Fortney J. J., Marley M. S., Hubickyj O., Bodenheimer P., Lissauer J. J., 2005, Astronomische Nachrichten, 326, 925

Fortney J. J., Marley M. S., Saumon D., Lodders K., 2008, ApJ, 683, 1104

Freedman R. S., Marley M. S., Lodders K., 2008, ApJS, 174, 504

Freistetter F., Krivov A. V., Löhne T., 2007, A&A, 466, 389

Freytag B., Allard F., Ludwig H.-G., Homeier D., Steffen M., 2010, A&A, 513, A19

Fung J., Artymowicz P., Wu Y., 2015, ArXiv e-prints

Galicher R., Marois C., Zuckerman B., Macintosh B., 2013, ApJ, 769, 42

Gizis J. E., 2002, ApJ, 575, 484

Gizis J. E., Jao W.-C., Subasavage J. P., Henry T. J., 2007, ApJ, 669, L45

Golimowski D. A. et al., 2004, AJ, 127, 3516

Gough D. O., 1996, The Observatory, 116, 313

Goździewski K., Migaszewski C., 2009, MNRAS, 397, L16

Goździewski K., Migaszewski C., 2014, MNRAS, 440, 3140

Gregory P. C., 2005, Bayesian Logical Data Analysis for the Physical Sciences: A Comparative Approach with Mathematica Support. Cambridge University Press, Cambridge, UK

Grether D., Lineweaver C. H., 2006, ApJ, 640, 1051

Guillot T., Chabrier G., Morel P., Gautier D., 1994, Icarus, 112, 354

Hansen C. J., Kawaler S. D., 1994, Stellar Interiors. Physical Principles, Structure, and Evolution.. Springer-Verlag

Hartmann L., Cassen P., Kenyon S. J., 1997, ApJ, 475, 770

Heaslet M. A., Baldwin B. S., 1963, Physics of Fluids, 6, 781

Helling C. et al., 2008, MNRAS, 391, 1854

Helling C., Casewell S., 2014, A&A Rev., 22, 80

Helling C., Jardine M., Witte S., Diver D. A., 2011, ApJ, 727, 4

Helling C., Winters J. M., Sedlmayr E., 2000, A&A, 358, 651

Henyey L. G., Forbes J. E., Gould N. L., 1964, ApJ, 139, 306

Hinkley S., Carpenter J. M., Ireland M. J., Kraus A. L., 2011, ApJ, 730, L21

Hinkley S. et al., 2011, PASP, 123, 74

Huang X., Cumming A., 2012, ApJ, 757, 47

Hubbard W. B., 1977, Icarus, 30, 305

Hubickyj O., Bodenheimer P., Lissauer J. J., 2005, Icarus, 179, 415

Ida S., Lin D. N. C., 2004, ApJ, 604, 388

Ida S., Lin D. N. C., Nagasawa M., 2013, ApJ, 775, 42

Janson M., Bonavita M., Klahr H., Lafrenière D., 2012, ApJ, 745, 4

Janson M., Bonavita M., Klahr H., Lafrenière D., Jayawardhana R., Zinnecker H., 2011, ApJ, 736, 89

Janson M., Carson J. C., Lafrenière D., Spiegel D. S., Bent J. R., Wong P., 2012, ApJ, 747, 116

Kalas P., Graham J. R., Fitzgerald M. P., Clampin M., 2013, ApJ, 775, 56

Keith S. L., Wardle M., 2015, MNRAS, 451, 1104

Kennedy G. M., Wyatt M. C., Bryden G., Wittenmyer R., Sibthorpe B., 2013, MNRAS

Kenworthy M. A., Meshkat T., Quanz S. P., Girard J. H., Meyer M. R., Kasper M., 2013, ApJ, 764, 7

Kippenhahn R., Weigert A., 1990, Stellar Structure and Evolution. Astron. Astrophys. Lib. Ser., Springer-Verlag, Berlin

Klassen M., Kuiper R., Pudritz R. E., Peters T., Banerjee R., Buntemeyer L., 2014, ApJ, 797, 4

Kuiper R., Klahr H., Dullemond C., Kley W., Henning T., 2010, A&A, 511, A81

Kuzuhara M. et al., 2013, ApJ, 774, 11

Lafrenière D., Jayawardhana R., van Kerkwijk M. H., 2008, ApJ, 689, L153

Lafrenière D., Marois C., Doyon R., Barman T., 2009, ApJ, 694, L148

Lagrange A.-M. et al., 2012, A&A, 542, A40

Lagrange A.-M. et al., 2011, in Sozzetti A., Lattanzi M. G., Boss A. P., eds, IAU Symposium Vol. 276, IAU Symposium. pp 60–63

Lagrange A.-M., De Bondt K., Meunier N., Sterzik M., Beust H., Galland F., 2012, A&A, 542, A18

Lagrange A.-M. et al., 2009, A&A, 493, L21

Lagrange A.-M., Meunier N., Chauvin G., Sterzik M., Galland F., Lo Curto G., Rameau J., Sosnowska D., 2013, A&A, 559, A83

Larson R. B., 1969, MNRAS, 145, 271

Leconte J., Chabrier G., 2012, A&A, 540, A20

Leconte J., Chabrier G., 2013, Nature Geoscience, 6, 347

Lee J.-M., Heng K., Irwin P. G. J., 2013, ApJ, 778, 97

Levermore C. D., Pomraning G. C., 1981, ApJ, 248, 321

Liu M. C. et al., 2011, ApJ, 740, 108

Liu M. C., Dupuy T. J., Leggett S. K., 2010, ApJ, 722, 311

Lodato G., Delgado-Donate E., Clarke C. J., 2005, MNRAS, 364, L91

Lodders K., 2003, ApJ, 591, 1220

Lovelace R. V. E., Covey K. R., Lloyd J. P., 2011, AJ, 141, 51

Luhman K. L., 2012, ARA&A, 50, 65

Luhman K. L., Burgasser A. J., Labbé I., Saumon D., Marley M. S., Bochanski J. J., Monson A. J., Persson S. E., 2012, ApJ, 744, 135

Luhman K. L., Joergens V., Lada C., Muzerolle J., Pascucci I., White R., 2007, Protostars and Planets V, pp 443–457

Lunine J. I., Hubbard W. B., Burrows A., Wang Y.-P., Garlow K., 1989, ApJ, 338, 314

Malo L., Doyon R., Lafrenière D., Artigau É., Gagné J., Baron F., Riedel A., 2013, ApJ, 762, 88

Malygin M. G., Kuiper R., Klahr H., Dullemond C. P., Henning T., 2014, A&A, 568, A91

Mamajek E. E., 2005, ApJ, 634, 1385

Mamajek E. E., Meyer M. R., 2007, ApJ, 668, L175

Marcy G. W., Butler R. P., 2000, PASP, 112, 137

Marleau G.-D., 2012, M. Sc. thesis, Univ. McGill

Marleau G.-D., Cumming A., 2014, MNRAS, 437, 1378

Marley M. S., Fortney J. J., Hubickyj O., Bodenheimer P., Lissauer J. J., 2007, ApJ, 655, 541

Marley M. S., Robinson T. D., 2015, ARA&A, 53, 279

Marley M. S., Saumon D., Cushing M., Ackerman A. S., Fortney J. J., Freedman R., 2012, ApJ, 754, 135

Marois C., Macintosh B., Barman T., Zuckerman B., Song I., Patience J., Lafrenière D., Doyon R., 2008, Science, 322, 1348

Marois C., Zuckerman B., Konopacky Q. M., Macintosh B., Barman T., 2010, Nature, 468, 1080

Marshak R. E., 1958, Physics of Fluids, 1, 24

Mayor M., Queloz D., 1995, Nature, 378, 355

McBride J., Graham J. R., Macintosh B., Beckwith S. V. W., Marois C., Poyneer L. A., Wiktorowicz S. J., 2011, PASP, 123, 692

McElwain M. W. et al., 2012, in Society of Photo-Optical Instrumentation Engineers (SPIE) Conference Series.

Meshkat T. et al., 2013, ApJ, 775, L40

Mignone A., Bodo G., Massaglia S., Matsakos T., Tesileanu O., Zanni C., Ferrari A., 2007, ApJS, 170, 228

Mignone A., Zanni C., Tzeferacos P., van Straalen B., Colella P., Bodo G., 2012, ApJS, 198, 7

Mihalas D., Mihalas B. W., 1984, Foundations of radiation hydrodynamics. Oxford University Press

Minerbo G. N., 1978, J. Quant. Spec. Radiat. Transf., 20, 541

Mizuno H., 1980, Prog. Th. Phys., 64, 544

Mohanty S., Basri G., Jayawardhana R., Allard F., Hauschildt P., Ardila D., 2004, ApJ, 609, 854

Mohanty S., Jayawardhana R., Basri G., 2004, ApJ, 609, 885

Mohanty S., Jayawardhana R., Huélamo N., Mamajek E., 2007, ApJ, 657, 1064

Mollière P., Mordasini C., 2012, A&A, 547, A105

Mollière P., van Boekel R., Dullemond C., Henning T., Mordasini C., 2015, ApJ, 813, 47

Moór A., Ábrahám P., Derekas A., Kiss C., Kiss L. L., Apai D., Grady C., Henning T., 2006, ApJ, 644, 525

Mordasini C., 2013, A&A, 558, A113

Mordasini C., 2014, A&A, 572, A118

Mordasini C., Alibert Y., Benz W., Naef D., 2009, A&A, 501, 1161

Mordasini C., Alibert Y., Klahr H., Henning T., 2012, A&A, 547, A111

Mordasini C., Mollière P., Dittkrist K.-M., Jin S., Alibert Y., 2015, International Journal of Astrobiology, 14, 201

Morley C. V., Marley M. S., Fortney J. J., Lupu R., Saumon D., Greene T., Lodders K., 2014, ApJ, 787, 78

Moro-Martín A., Rieke G. H., Su K. Y. L., 2010, ApJ, 721, L199

Morzinski K. M. et al., 2015, ApJ, 815, 108

Moses J. I., 2014, Philosophical Transactions of the Royal Society of London Series A, 372, 30073

Moya A., Amado P. J., Barrado D., García Hernández A., Aberasturi M., Montesinos B., Aceituno F., 2010, MNRAS, 405, L81

Moya A., Amado P. J., Barrado D., Hernández A. G., Aberasturi M., Montesinos B., Aceituno F., 2010, MNRAS, 406, 566

Neuhäuser R., Schmidt T. O. B., 2012, arXiv:1201.3537

Nielsen E. L., Close L. M., 2010, ApJ, 717, 878

Oppenheimer B. R., Kulkarni S. R., Matthews K., Nakajima T., 1995, Science, 270, 1478

Ormel C. W., Shi J.-M., Kuiper R., 2015, MNRAS, 447, 3512

Patience J., King R. R., de Rosa R. J., Marois C., 2010, A&A, 517, A76

Patience J., King R. R., De Rosa R. J., Vigan A., Witte S., Rice E., Helling C., Hauschildt P., 2012, A&A, 540, A85

Paxton B., Bildsten L., Dotter A., Herwig F., Lesaffre P., Timmes F., 2011, ApJS, 192, 3

Paxton B. et al., 2013, ApJS, 208, 4

Pecaut M. J., Mamajek E. E., Bubar E. J., 2012, ApJ, 746, 154

Pollack J. B., Hollenbach D., Beckwith S., Simonelli D. P., Roush T., Fong W., 1994, ApJ, 421, 615

Pollack J. B., Hubickyj O., Bodenheimer P., Lissauer J. J., Podolak M., Greenzweig Y., 1996, Icarus, 124, 62

Quanz S. P., Amara A., Meyer M. R., Girard J. H., Kenworthy M. A., Kasper M., 2015, ApJ, 807, 64

Quanz S. P. et al., 2010, ApJ, 722, L49

Rafikov R. R., 2011, ApJ, 727, 86

Rameau J. et al., 2013, ApJ, 772, L15

Ramsey J. P., Dullemond C. P., 2015, A&A, 574, A81

Rebolo R., Zapatero Osorio M. R., Martín E. L., 1995, Nature, 377, 129

Reidemeister M., Krivov A. V., Schmidt T. O. B., Fiedler S., Müller S., Löhne T., Neuhäuser R., 2009, A&A, 503, 247

Riaz B., Lodato G., Stamatellos D., Gizis J. E., 2012a, MNRAS, 424, L74

Riaz B., Lodato G., Stamatellos D., Gizis J. E., 2012b, MNRAS, 422, L6

Rossow W. B., 1978, Icarus, 36, 1

Sallum S. et al., 2015, Nature, 527, 342

Salpeter E. E., 1992, ApJ, 393, 258

Saumon D., Bergeron P., Lunine J. I., Hubbard W. B., Burrows A., 1994, ApJ, 424, 333

Saumon D., Chabrier G., van Horn H. M., 1995, ApJS, 99, 713

Saumon D., Guillot T., 2004, ApJ, 609, 1170

Saumon D., Hubbard W. B., Burrows A., Guillot T., Lunine J. I., Chabrier G., 1996, ApJ, 460, 993

Saumon D., Marley M. S., 2008, ApJ, 689, 1327

Schneider J., Dedieu C., Le Sidaner P., Savalle R., Zolotukhin I., 2011, A&A, 532, A79

Semenov D., Henning T., Helling C., Ilgner M., Sedlmayr E., 2003, A&A, 410, 611

Skemer A. J., Close L. M., Szűcs L., Apai D., Pascucci I., Biller B. A., 2011, ApJ, 732, 107

Soderblom D. R., 2010, ARA&A, 48, 581

Song I., Schneider G., Zuckerman B., Farihi J., Becklin E. E., Bessell M. S., Lowrance P., Macintosh B. A., 2006, ApJ, 652, 724

Spiegel D. S., Burrows A., 2012, ApJ, 745, 174

Spiegel D. S., Burrows A., Milsom J. A., 2011, ApJ, 727, 57

Stahler S. W., Shu F. H., Taam R. E., 1980, ApJ, 241, 637

Stelzer B., Scholz A., Jayawardhana R., 2007, ApJ, 671, 842

Stephens D. C. et al., 2009, ApJ, 702, 154

Stevenson D. J., 1979, MNRAS, 187, 129

Stevenson D. J., 1982, Planet. Space Sci., 30, 755

Su K. Y. L. et al., 2009, ApJ, 705, 314

Sudol J. J., Haghighipour N., 2012, ApJ, 755, 38

Tanigawa T., Ohtsuki K., Machida M. N., 2012, ApJ, 747, 47

Tomida K., Tomisaka K., Matsumoto T., Hori Y., Okuzumi S., Machida M. N., Saigo K., 2013, ApJ, 763, 6

Tsuji T., Ohnaka K., Aoki W., Nakajima T., 1996, A&A, 308, L29

Turner N. J., Stone J. M., 2001, ApJS, 135, 95

Uribe A. L., Klahr H., Henning T., 2013, ApJ, 769, 97

Vaidya B., Mignone A., Bodo G., Massaglia S., 2015, ArXiv e-prints

van Leeuwen F., 2007, A&A, 474, 653

Vaytet N., Chabrier G., Audit E., Commerçon B., Masson J., Ferguson J., Delahaye F., 2013, A&A, 557, A90

Vaytet N., González M., Audit E., Chabrier G., 2013, J. Quant. Spec. Radiat. Transf., 125, 105

Vaytet N., Tomida K., Chabrier G., 2014, A&A, 563, A85

Vigan A., Moutou C., Langlois M., Allard F., Boccaletti A., Carbillet M., Mouillet D., Smith I., 2010, MNRAS, 407, 71

Vigan A. et al., 2012, A&A, 544, A9

Wahhaj Z. et al., 2013, ApJ, 773, 179

Weingartner J. C., Draine B. T., 2001, ApJ, 548, 296

Yamamoto K. et al., 2013, PASJ, 65, 90

Zapolsky H. S., Salpeter E. E., 1969, ApJ, 158, 809

Zel'dovich Y. B., Raizer Y. P., 1967, Physics of shock waves and high-temperature hydrodynamic phenomena. Academic Press

Zhou Y., Herczeg G. J., Kraus A. L., Metchev S., Cruz K. L., 2014, ApJ, 783, L17

Zhu Z., 2015, ApJ, 799, 16

Zuckerman B., Song I., Bessell M. S., Webb R. A., 2001, ApJ, 562, L87

Declaration

I hereby declare that, except where reference to the work of others is made, this thesis and its contents represent my own and original work. It was conducted at the Max-Planck-Institut für Astronomie (Heidelberg) under the supervision of Priv. Doz. H. Klahr and therefore benefited from his assistance and suggestions, as well as from those of Prof. Dr. Ch. Mordasini and Dr. R. Kuiper. As carefully detailed there, a fraction of the work presented in Chapter 5 was submitted as part of the requirements for the obtention of the degree of M. Sc. at McGill University (Montréal, Canada), but no other part of the present thesis has been submitted at any other institution for any degree or qualification.

Heidelberg, 7 December 2015